UNIVERSITÀ DEGLI STUDI DI PALERMO
Dottorato in Scienze della Terra e del Mare
Dipartimento di Scienze della Terra e del Mare
GEO 07

Experimental investigation on peralkaline silicic magmas of Pantelleria Island: inferences on pre-eruptive conditions, magma evolution and water solubility

IL DOTTORE
Pierangelo Romano

IL COORDINATORE
Prof. Alessandro Aiuppa

IL TUTOR
Prof. Silvio G. Rotolo

CICLO XXIX_ -
2016/2017

Index

Abstract

Trachytes and pantellerites usually represent the felsic end-member in continental rift systems and oceanic island settings characterized by peralkaline silicic magmatism. At Pantelleria Island pantellerites are by far the most abundant rocks, followed by trachytes and subordinate basalts. Recent experimental and analytical investigations have laid down the storage and evolution conditions of pantellerite magmas, while less attention has been paid to the pre-eruptive conditions of trachytic magmas, such as the storage pressure, crystallization temperature, redox conditions or solubility of volatiles.

To fill this gap, we have performed several phase equilibrium and water solubility experiments primarily on two trachytic compositions, with a three-fold aim: (i) determination of pre-eruptive conditions of trachyte magma; (ii) to experimentally constrain the liquid line of descent towards pantellerite melts, (iii) to determine water solubility, in such a kind of melts, where small bulk chemical variations (chiefly alkali and alumina) reflect in non-trivial variations is water solubility.

A secondary line of experiments was dedicated to phase equilibrium experiments on two pantellerite composition, with the aim to add further constraints to the existing experimental data set, in particular to define the bulk compositional control on phase equilibria, among pantellerite magmas with different degree of evolution (i.e. Na+K/Al ratio) and the inferences on determination of pre-eruptive conditions.

The rocks chosen as starting material for experiments cover the last period of activity at Pantelleria (45 to 10 ka) and include in decreasing age order: (i) the Green Tuff plinian eruption, in particular the opening fallout (pantelleritic) and the topmost trachytic member; a (ii) voluminous trachyte lava flow, erupted soon after the caldera collapse related to the GT eruption, (iii) a 10 ka old violent strombolian pantellerite eruption. Crystallization experiments were performed in the temperature range 750-950°C, pressure 0.5-1.5 kbar and fluid saturation conditions with XH_2O ($=H_2O/H_2O+CO_2$) ranging between 0 and 1. Redox conditions were fixed around the FMQ buffer. On the contrary, solubility experiments were realized in a pressure range 0.5 – 3 kbar supra liquidus temperature and water saturation conditions.

Comparing the experimental results with the natural products we have defined the pre-eruptive conditions of trachytic magmas at Pantelleria island. Experiments corroborated the well known role of alkali feldspar role in the low pressure differentiation of trachytic

magmas toward a pantelleritic residual liquid and hence in the transition from a metaluminous to a peralkaline melt.

Crystallization experiments on pantelleritic compositions demonstrated the control that melt peralkalinity has on the mineral assemblages observed in peralkaline rhyolite of Pantelleria, in particular, the presence of fayalitic olivine in the mineral assemblage occurs when melt peralkalinity index lower than 2. Moreover, the crystallization experiments allowed to define the pre-eruptive conditions of Green Tuff eruptions at temperature=750°C pressure= 1.0 kbar and H_2O_{melt} ~ 4 wt%.

Water solubility experiments on trachytic allowed to expand the small existing experimental data in metaluminous trachyte compositions. Experiments show remarkable deviation with popular solubility models, in particular at 1.5 kb, the H_2O experimental solubilized was 4.97 wt.% while the Papale et al., (2006) model predicted value was slightly higher than 6 wt%; this bias translates in depth variation of around 1 km.

INTRODUCTION

This study focuses on the peralkaline silicic magmatism of Pantelleria Island, Strait of Sicily, Italy. Pantelleria is the emerged portion of a Quaternary volcano located in the Sicily Channel Rift Zone, a domain belonging to African Plate constituted of thinned continental crust. In the petrological literature Pantelleria is well known as the type locality for pantellerite, an iron-rich peralkaline rhyolite. Pantelleria, along its volcanological history, erupted a vast majority of pantellerite and trachyte magmas, and only a small volume of alkali basalts.

The debate on the origin of peralkaline silicic magmas dates back to the end of 18^{th} century and nowadays, although numerous advances have been made, some opinion still remain contrasting. In the literature Pantelleria magmas have been chosen as case study because Pantelleria is one of the best example of peralkaline silicic volcanism in the world and the sole in the Mediterranean area. Furthermore, the eruptive products outcropping in the island reflect the intriguing and debated issues of (i) the origin of Daly Gap in eruptive sequences and (ii) the transition from metaluminous (trachyte) to clearly peralkaline (pantellerite) magmas.

At Pantelleria, pantellerite magmas were erupted as pyroclastic flows or pumice fall deposits or lava flows, while trachytes almost exclusively as lava flows. Several studies used geochemical and petrological arguments to constrain the origin of trachytes and pantellerites, but less attention was paid to the reconstruction of the pre-eruptive conditions of these magmas.

Recently, thermodynamic and experimental studies have systematically studied the pre-eruptive conditions of pantellerites and despite the significant progresses done, some aspect still remain unclear. Among these the pre-eruptive conditions, the petrological evolution and composition-specific study on solubility of H_2O in trachyte magma.

This project focuses on the petrological aspects of trachytes and pantellerites, exploring with the tools of experimental petrology three principal aspects: (i) pre- eruptive temperature, pressure, redox conditions of the peralkaline magmas erupted during some key eruptions, (ii) the origin of peralkaline rock from a metaluminous parental magma, (iii) H_2O solubility in both magma types.

To achieve these objectives, several phase equilibrium and solubility experiments have been performed on representative trachyte and pantellerite starting compositions. Crystallisation experiments are recognized as an excellent method to establish precisely the intensive parameters of pre-eruptive magma. Phase equilibria are indeed composition specific even for subtle variations in major elements composition that might result in some loss of accuracy in thermodynamic geothermo-baro-oxy-hygro-meters (and this is particularly true for very particular compositions such as pantellerites).

More in detail this experimental study has several targets:

(i) to establish ***the pre-eruptive conditions*** of trachytic magma of Pantelleria erupted during two very different eruptions, the upper member of the plinian Green Tuff eruption (age 45 ka) and the lava flow that followed the caldera collpase after the GT .

(ii) to constrain the petrogenetic relationships between trachytic and pantellerite magmas in order to bind experimentally the parent/daughter relationships,

(iii) to add further constrain on the pre-eruptive conditions of Pantelleria peralkaline rhyolite,

(iv) to experimentally investigate the water solubility on Pantelleria trachytes, another point where often an experimental benchmark is needed for thermodynamic or empirical solubility models.

Phase equilibria experiments were carried out for 4 starting compositions (two pantellerites with different (Na+K)/Al and two trachyte) in the pressure range 0.5 – 1.5 and kbar and temperature range 750-950 °C. The explored redox conditions were fixed around the FMQ oxygen buffer, maintaining always fluid saturation conditions but exploring different fluid phase composition [XH_2O= 0-1 i.e. exploring different activities of H_2O (aH_2O)] in equilibrium with trachytic and pantelleritic experimental charges.

Solubility experiments were realized in a pressure range 0.5 – 3 kbar and temperature of 950 – 975°C on the trachyte starting compositions.

The experimental results and the comparison with the natural trachyte and pantellerite allowed to add new and valuable constraints regarding: (i) the storage conditions of trachyte magmas at Pantelleria, (ii) the magma differentiation mechanisms and the origin of the different mineral assemblages found in metaluminous to peralkaline rocks with different degrees of evolution (iii) the H_2O solubility in trachytic magmas.

The thesis is thus divided in six principal sections.

In **Chapter 1** we introduce the reader in the principal geological features of Pantelleria Island and on the general petrological characteristic of the peralkaline silicic magmas. In **Chapter 2** we describe the experimental machines and the experimental methods used to carry out this study. In **Chapter 3** we present the starting materials for experiments within the frame of their original eruptive units and describing also the main petrological features.

Chapter 4 focuses on the results obtained from the petrological and experimental study of the trachytes, which have been synthetized in a paper submitted to Journal of Petrology.

In **Chapter 5** we report the results of phase equilibrium experiments on pantellerites focusing the attention on the influence that very tiny compositional differences produce in phase relationships, hence in volcanological inferences. These latter centred on the magma storage conditions of the highest magnitude eruption at Pantelleria, and eventual modification of the plumbing system at the resurgence of magmatism after the caldera collapse.

In **Chapter 6** we present the result of water solubility experiment on trachytic melt, compared to other (few) experimental works and thermodynamic models. This latter point is particularly useful for melt inclusion studies in metaluminous trachytes, which suffer the almost absence of a specific study on the specific composition.

Chapter 1

Geological and petrological background

1.1 Geological background of Pantelleria island

1.1.1 Regional geology

Pantelleria island is located in the Strait of Sicily (Fig.1.1), at approximately 120 km south-west of the Sicilian coast and 70 km east the coast of Tunisia. The island, approximately 80 km^2, is the emerged part of a large volcanic complex associated with the continental rift system of the Sicily Channel, which includes other small volcanic islands such as Linosa and Graham Bank. The Sicily Channel Rift Zone (SCRZ) is developed within the Pelagian Block, which underwent a tectonic stretching since the Late Miocene – Early Pliocene (Civile et al., 2008). The major tectonic features consist of NW-SE trending faults that originated a series of depression such as the Pantelleria, Malta and Linosa graben. Magmatic activity of the Sicily Channel displays an alkaline affinity (Carapezza et al., 1979; Rossi et al., 1996; Rotolo et al., 2006), beside Pantelleria and Linosa indeed the Sicily Channel is characterized by several submarine edifices (Beccaluva et al., 1981)

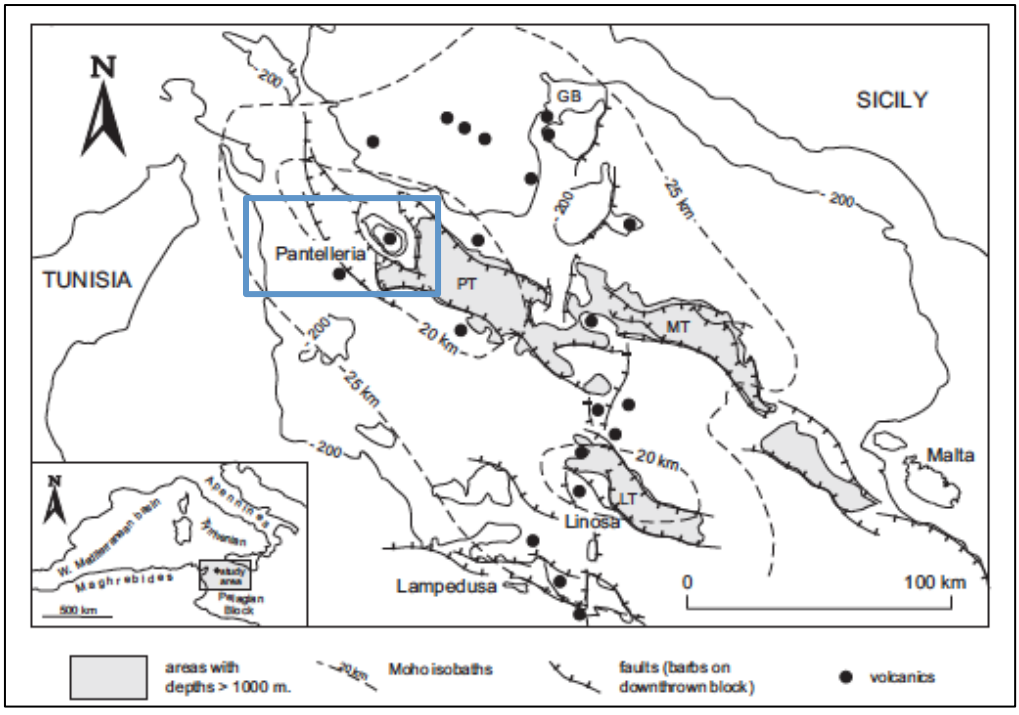

Figure 1.1: Geological sketch of the Sicily Channel Rift Zone. Modified from Catalano et al. (2014)

1.1.2 Magma Source region at Pantelleria

Several studies have focused on the geochemical characteristics of mafic products of Pantelleria. The isotopic data indicate both a DMM (depleted MORB) and an HIMU oceanic mantle source with trace of EM1-type of asthenospheric origin (Esperanca & Crisci, 1995; Civetta et al., 1998). A mixing model of differently enriched asthenospheric melts has been proposed to explain the isotopic features of mafic magmas in the Sicily Channel. The signature of a HIMU-EM1 magmatic activity of Pantelleria island was evidenced also by He isotopes in volcanic fluids (Parello et al., 2000). The hypothesis of a contribution of a mantle plume in the magmas of Sicily Channel agrees with a more general geodynamics vision regarding the contribution of an enriched intraplate mantle source on the south-eastern sicilian volcanoes (Schiano et al., 2004). As regard the generation of magmas below Pantelleria, Neave et al., (2012), inverting REE, explained (i) the melt generation below Pantelleria with 1.7% melting of primitive mantle source at depth of 60-80km and (ii) the generation of Pantelleria basalts after ~35% of fractional crystallization of a primitive melt.

1.1.3 Geological and volcanological background

Pantelleria Island is entirely constituted of volcanic rocks and the beginning of emerged activity is dated at around 300 ka (Mahood & Hildreth, 1986). The majority of the island is composed by pantellerites and trachytes, basalts represent less of 10% of the exposed rocks. The volcanological history of Pantelleria can be divided in three main cycle. The *first cycle* of activity (324-180 ka) is characterized by pantelleritic lava flow, welded tuffs and pumice fallout (Mahood & Hildreth, 1986). During the *second cycle* of activity (180-45 ka) at least nine ignimbrite forming eruption occurred, the majority of them with pantelleritic composition. Among these, at least two eruptions are linked to the two visible calderas formation, that originated the La Vecchia Caldera 140 ka (Rotolo et al., 2013, and references therein) and then the Cinque Denti Caldera, this latter (45 ka) nested in the older caldera (Fig 2). The Green Tuff and the related caldera collapse marked the end of the second cycle of activity. *The third cycle* of activity (45-8 ka), begun soon after the Green Tuff eruption, with the eruption of voluminous trachytic lavas that constitute the Mt. Gibele-Mt. Grande complex (Mahood & Hildreth, 1986), which is then followed by more than 40 low-energy eruptions (pumice fall, lava flows and lava domes) with pantelleritc composition (Rotolo et al., 2007, Scaillet et al., 2011). The third cycle of activity ends with the eruption

of extracaldera basalts (scoria cones and lava flows) limited to the northwest sector of the island. The most recent eruption of Pantelleria occurred on 1891 and was localized in the sea 5 km off (NW) the main village (Ricco 1892). The eruptive products, with basaltic composition, were found floating (basalt ballons) in the sea in front of Pantelleria (Washington 1909; Conte et al., 2014; Kelly et al., 2014).

The estimation of magma erupted during the first cycle of activity resulted difficult because most of the eruptive unit are covered by the Green Tuff ignimbrite. Rotolo et al. (2013) recently revised the pre- Green Tuff activity, estimating also the cumulative erupted magma volume. They recognize during the volcanalogical history of Pantelleria eruptive climax, after inter-eruptive period, in which the highest amount of cumulative magma coincide with the maximum degree of magma evolution. Although the assessment of the erupted volumes is still discussed, the Green Tuff eruption is an important maker in the geological history of Pantelleria. The Green Tuff eruption, recently dated at 45 ka (Scaillet et al., 2013), indeed blanked the entire island covering all the pre-existing geological features. The early works on the Green Tuff eruption (Wolff & Wright 1981; Civetta et al., 1988) estimated a volume included between 1.5 km^3 and 7 km^3 dense rock equivalent (D.R.E), the incertitude arises from the difficult to estimate the volume of material deposited in the sea. Recently, through an high-resolution analysis of the depositional architecture, Williams et al., (2014) described the Green Tuff eruption as a catastrophic event during which the pyroclastic density current gradually covered the entire island in a limited time span (estimated < 2 h). In addition, Catalano et al (2013) suggested that the Green Tuff eruption developed from fissural sources controlled by the tectonic trend acting at the time of the eruption in the island. From a petrological point of view, the Green Tuff represent the sole ignimbrite, chemically zoned from a crystal poor pantellerite at the bottom to a crystal rich trachyte at the top (Mahood & Hildreth, 1986, Williams 2010).

Post-Green Tuff activity and stratigraphy have been thoroughly studied defining age and location relationship (Civetta et al., 1988; Orsi et al., 1991; Mahood & Hildreth 1986; Rotolo et al., 2007; Scaillet et 2011). During the post-Green Tuff activity (third cycle) a total volume ≤ 5 km^3 DRE was erupted (Civetta et al., 1988). The reappraisal of activity, was with the eruptions that formed Mt Gibel, whose age (37- 44 +/- 10 ka) is following (virtually overlapping due to the large error implicit in K/Ar ages) the Green Tuff , (Mahood & Hildreth 1986). This probably implies that the volcanic system continued in the production of trachyte magma, but only at least 15 ka later produced pantellerites (the 23 ka

Gelkhmar shield volcano). One possible hypothesis is that the plumbing system that fed the GT, was not severely modified after the caldera collapse, and continued to produce felsic magmas. The third cycle of activity was grouped by Civetta et al.,(1988) and Orsi et al., (1991) into six sub-cycles and one of the main difference with the precedent cycles is that this cycle begun with explosive phases and ended with effusive activity.

Among the relevant tectonic features of Pantelleria are included the Zighidi fault (Catalano et al., 2009), which divides the island in the basaltic domain (north west) and trachyte-pantellerite domain (south east) and the trapdoor faults of Mt.Grande representing the preferential path to magmas extrusion during the third cycle of activity (Mahood & Hildreth 1983; 1986).

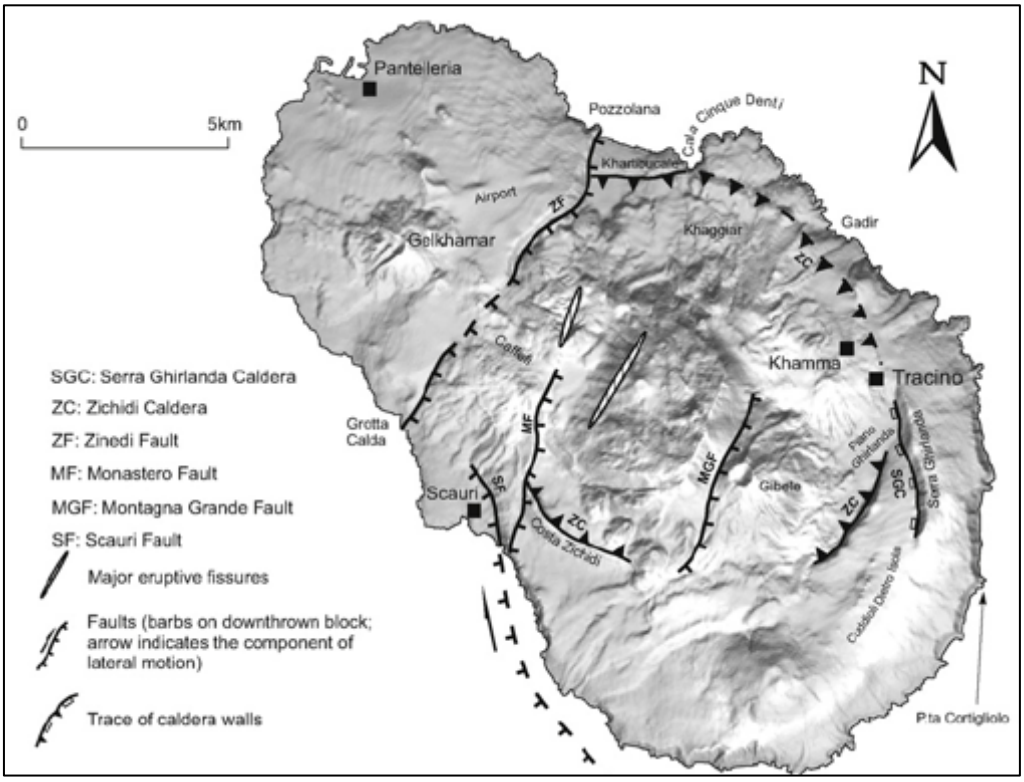

Figure 1.2: Structural map of Pantelleria island on digital elevation model generated on a geographic grid 40x40point per km^2 (modified from Civile et al., 2008).

1.2 Petrological background

1.2.1 Petrogenesis of peralkaline silicic magmas (at Pantelleria and worldwide)

The origin of peralkaline silicic magmas is a petrological issue debated from many years and some aspects still remain unclear. Peralkaline silicic magmas are often associated with a compositional gap in the eruptive sequence (Daly Gap) that makes yet more puzzling the origin of these magmas. At Pantelleria and other localities as well, eruptive products with silica content in the range 52- 63wt% are missing or rarely found as mixing products between a mafic and a felsic member (Ferla & Meli, 2006; Romengo et al., 2011). Bowen (1937) was the first to propose the transition from metaluminous to peralkaline as consequence of massive crystallization of calcic plagioclase ("*plagioclase effect*"). Bailey & Schairer, (1964) attributed the genesis of peralkaline silicic magmas to the crystallization of an alkali feldspar, less peralkaline than the coexisting melt, this is known in literature as "*orthoclase effect*". Afterwards, several studies have focused on the origin of peralkaline silicic magmas and different models have been proposed on the basis of petrological and geochemical arguments. The petrogenesis of peralkaline magmas by protracted crystal fractionation from a transitional basalt parent was successfully documented in several volcanic system where alkali basalts are ubiquitous with peralkaline silicic magmas, such as the Ethiopian Rift (Barberi et al., 1975; Gasparon et al., 1993; Peccerillo et al., 2003; MacDonald et al., 2012; MacDonald 2012), Galapagos Archipelago (Geist et al., 1995) or Azores (Mungall & Martin 1995), Paisano Volcano, Texas (Parker, 1983). An other model suggests that peralkaline silicic magmas are genetically independent from basalts and consequently they derive by melting of old continental crust (Davies & MacDonald, 1987; Lightfoot et al., 1987; MacDonald et al., 1987, Lewis et al., 2016) or alkali gabbro (Bohrson & Reid, 1997; Trua et al., 1999). This model is supported by the relative low abundance or absence of basalt associated with peralkaline silicic magmas. A third model proposed Bailey & MacDonald, (1987) and Black et al., (1998) for Kenya magmatism (Eburru and Olkaria) concerns the volatiles-fluxed partial melting of continental crust.

As regard Pantelleria island, the petrogenetic models proposed to explain the origin of trachytes and pantellerites are: (i) protracted crystal fractionation from a mafic parental magma (Civetta et al., 1998, White et al., 2009; Neave et al., 2012) (ii) partial melting of alkali gabbro to generate first a trachyte liquid, which in turn evolves to pantellerite by low-pressure crystal fractionation (Lowenstern & Mahood, 1991; Avanzinelli et al., 2004). The

first model is supported by major and trace element mass balances and principal component analysis (PCA) fitting as well as from the large volume of mafic rocks submerged below Pantelleria island. In detail, major and trace elements modelling suggest that trachyte can be generated by 70-75% fractional crystallization of plagioclase olivine, clinopyroxene and magnetitie, from hydrous basalts, and pantellerites after an additional 80% of fractional crystallization of alkali feldspar, clinopyroxene, Fe-rich olivine and oxides. On the contrary, Lowenstern & Mahood, (1991) proposed a model based on partial melting model of mafic cumulates to generate trachytic melts which evolve to pantellerites by low-pressure crystal fractionation; this model was partly based on the supposed low H_2O measured at that time in melt inclusion of pantellerites: the fractional crystallization of an alkali basalt to produce a pantellerite would result in 8wt% of H_2O in the pantelleritc melts, in contrast to the 2.1 wt% determined in melt inclusions (Lowenstern & Mahood, 1991). All the recent experimental studies (Scaillet and MacDonald, 2006; Di Carlo et al. 2010) and melt inclusions (see 1.2.2) proved instead that pantellerites are H_2O-rich magmas.

1.2.2 Peralkaline silicic magmas at Pantelleria

Following the classification of MacDonald (1974), peralkaline silicic magmas, include comentic trachytes, comendites, pantellerites and pantelleritic trachytes. This classification is based on the variation in FeO_{tot} and Al_2O_3 the best suited chemical components to discriminate the different peralkaline rocks.

At Pantelleria island the felsic end-member is composed almost exclusively by trachytes and pantellerites (Fig 1.3). From a mineralogical point of view ***trachytes*** are constituted by abundant (Na,K)-feldspar, Fe-rich olivine, clinopyroxene, Fe-Ti oxides and apatite as accessory phase, quartz and amphibole sometimes are present as residual phases in groundmass. From the compositional viewpoint, trachytes are rather homogeneous with only small variations in major and trace element until now reported (White et al., 2009; Romengo 2011). The mineral assemblage of ***pantellerites*** instead is constituted by (Na,K)-feldspar, Na-rich clinopyroxene, fayalite, aenigmatite and quartz; amphibole and ilmenite, even though rare, can also be present. White et al. (2005) discussed in detail the variation in mineral assemblage observed in pantellerites from Pantelleria, in particular they reported the presence of fayalite as function of peralkalinity and whole rock SiO_2 content besides the intensive parameters such as temperature and fO_2.

Minor and trace elements analyses in trachyte and pantellerite have been reported by Civetta et al., (1998), White et al., (2009) and Williams (2010). Trachyte and pantellerite are characterized by an increase of REE respect to mafic member and in particular LREE increases most respect HREE; Ba, Sr, Co, Ni decrease during the differentiation from trachyte to pantellerite. Another particular feature is the europium behaviour in trachyte and pantellerites, which shows a progressive anomaly, increases in the most evolved pantelleritic members; this in turn is consequence of the massive crystallization of alkali feldspar. Trachyes were divided in two groups by White al., (2009) on the basis of incompatible trace elements (ITE): low-ITE trachyte and high-ITE trachyte; the first, characterized also by high Ba (1300-1900 ppm) and positive Eu anomalies (1.11-1.37), were interpreted as result of a crystal accumulation process while the second is thought to be consanguineous with pantellerites. Pantellerites reach maximum concentration in Zr and Nb respectively of 2000 ppm and 400 ppm, and minimum in Sr of 5 ppm.

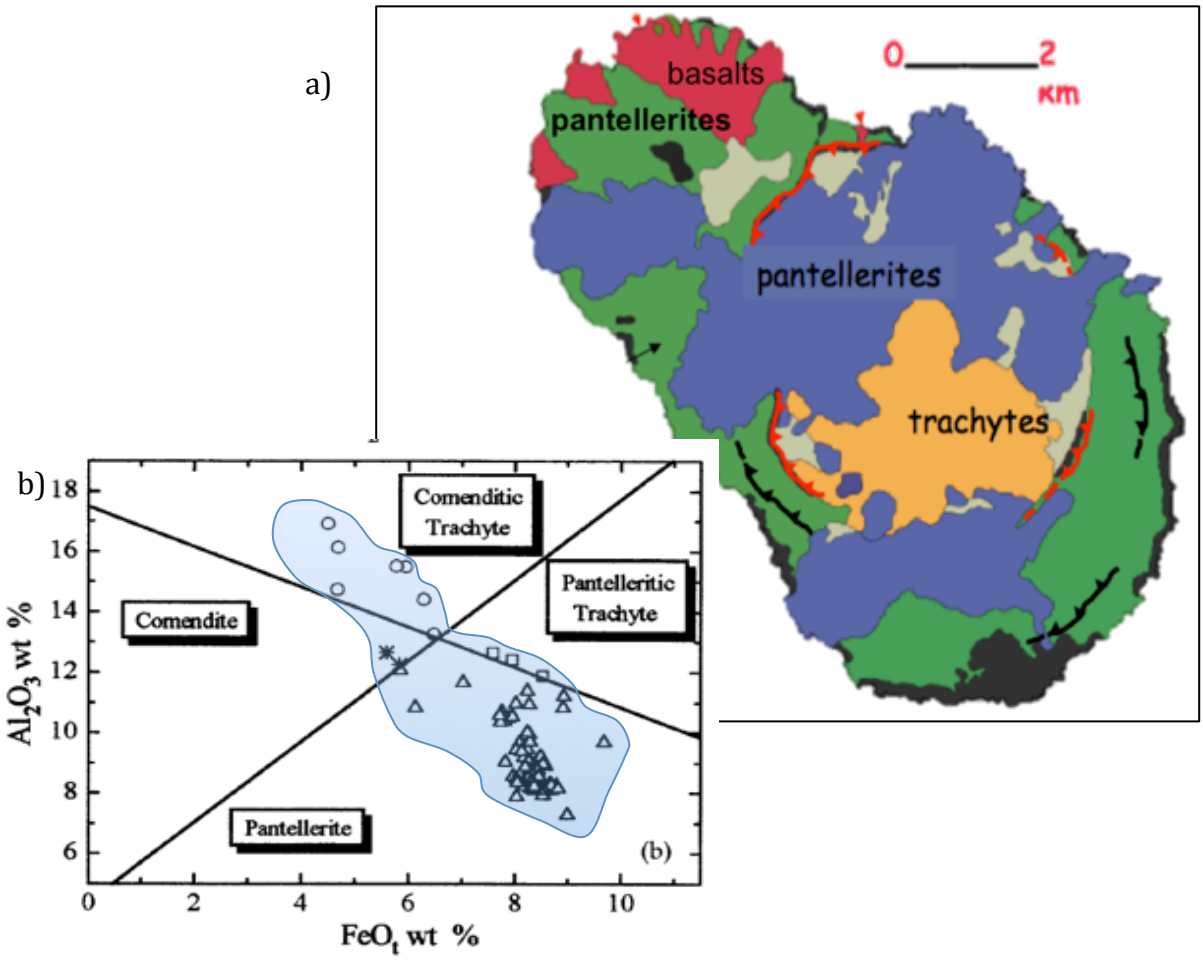

Figure 1.3: a) Simplified geological map of Pantelleria island. b) Classification diagram for peralkaline silicic magams (MacDonald, 1974) modified from Civetta et al., 1998 for Pantelleria rocks.

Recently, several studies have focused on the volatiles contend dissolved in pantellerites and all studies have reported high chlorine concentration (up 1wt%) dissolved in pantelleritic melt, with flour and sulphur respectively around 0.3wt% and 0.03wt%, both much higher than those found in metaluminous rhyolites (Gioncada & Landi 2010; Neave et al., 2012; Lanzo et al., 2013).As regards the water content in pantelleritic melt, it have been largely investigated and debated because the results obtained were not always coherent. Lowenstern & Mahood (1991) and Metrich et al., 2006 reported a maximum water content of 2.5wt% while the recent studies of Gioncada & Landi (2010), Neave et al., (2012), Lanzo et al., (2013) agree for a maximum water content dissolved in the melt of 4.5 wt%. As regard the CO_2 content, Neave et al., (2012) have reported a maximum content of 150 ppm.

Excess of alkali over aluminium strongly affect the physical characteristics (viscosity, density, diffusivities) of magma. Physical characteristics of magma in turn influence the eruptive style (Mahood 1984). The first effect of the excess of alkali over alumina is the decreases of melt viscosity, indeed, despite the high SiO_2 content peralkaline rhyolite are 2-3 orders of magnitude less viscous respect to a metaluminous rhyolite (Mahood & Hildreth, 1986). Moreover, peralkaline silicic magmas have moderate to high water dissolved in the melt as well as high halogen content. Both acts as network modifiers and the final result is a further decrease in melts viscosity. The high rheomorphism observed in pantellerites ignimbrites once were interpreted as consequence of the relatively high temperature (Schmincke 1974; Wolff & Wright 1981b) of the magma, but recent experimental studies have demonstrated that pantellerites magmas evolve at T≤ 750°C (see below). One of the first order consequences of low viscosities is the high rheomorphism and welding in ignimbrites in peralkaline deposits. Moreover, Stabile et al., (2016) evidenced how the low Fe^{3+} /Fe^{2+}ratio in the melt, hence low fO_2, reduces the melt viscosity, and this is likely to contribute in a further decrease of melt viscosity, given the low fO_2 of peralkaline magmas at Pantelleria.

1.2.3 Experimental constraints on peralkaline silicic magmas: a review

In the last fifteen years several studies have used a phase equilibrium approach to study peralkaline silicic magmas, most of them with the objective of knowing the pre-eruptive conditions of such magmas. Experiments that have achieved to generate peralkaline silicic magmas from alkali basalt are not presents in the petrological literarure. Nevertheless Mahood & Baker (1986) on Pantelleria basalt and Caricchi et al., (2006) on Ethiopian basalts concluded that low pressure conditions jointly to hydrous conditions are needed to drive an evolutionary trend of alkali basalt toward the peralkaline felsic member.

The "no-oxide field" in pantellerites (Nicholls & Carmichael, 1969) prevented the application of Fe-Ti oxide thermobaromether to study the redox conditions of magmas as well as the temperature ranges of storage and evolution. Many progress to understand the pre-eruptive condition of peralkaline silicic magmas have been made by Scaillet & MacDonald (2001, 2003, 2006) on the Kenya rift valley silicic magmatism (Eburru and Olkaria volcanic complexes). First of all, it was found that comendite and pantellerite of Kenya rift valley have pre-eruptive conditions lower than 750°C, in conflict with the early view that considered peralkaline silicic magmas among the highest temperature rhyolites, which explained certain volcanological features such as the high rheomorphism in the deposits. Furthermore, they (i) evidenced the reducer character of these magmas despite the relative high water content and (ii) showed experimentally for first time, how a pantelleritic melt can be originated from fractional crystallization of a comendite.

Di Carlo et al., (2010) constrained experimentally for first time the pre-eruptive conditions of pantelleritic magmas at Pantelleria Island. They evidenced that temperature, pressure and redox conditions of pantelleritic magmas at Pantelleria are broadly similar to those of Kenya peralkaline magmas despite the difference in phase relationship that derive from appreciable difference in rock chemistry. The experiments corroborate the results of White et al., (2005), which through thermodynamic calculations inferred the temperature of Pantelleria rhyolite in the range 680-800°C and redox conditions around the FMQ buffer. Furthermore, phase equilibria experiments shed light the H_2O-rich character of peralkaline rhyolite of Pantelleria, in accord with the recent studies on melts inclusion in pantelleritic rocks (Gioncada & Lando, 2010; Neave et al., 2012; Lanzo et al., 2013).

The pressure conditions explored experimentally ($P< 2.0$ kbar) for peralkaline silicic magmas reflect the low pressure conditions inferred for this category of magmas mainly

from petrological observation (Mahood 1986). In the case of Pantelleria, melt inclusion studies and geophysical observation agree for a storage region of felsic magmas around 4 km that converted into pressure (considering an average density of 2.6 kg/cm^3) result in a maximum pressure of 1.5 kbar.

Chapter 2

Experimental and analytical techniques

In this section will be described the general principles of the experimental and analytical protocol used to carry out this study. Experiments were performed at CNRS-Institut des Sciences de la Terre d' Orleans (ISTO, France) while the analytical part was realised both at University of Palermo, Dipartimento di Scienze della Terra e del Mare (DiSTeM) and at CNRS-ISTO. However, in each following chapter will be added further detail in relation to the experiments performed, in general two type of experiments have been performed: (i) phase equilibria experiments and (ii) solubility experiments.

2.1 Experimental methods

2.1.1 Starting material preparation

All experiments were performed using as starting material, either (i) a glass prepared from the starting rock or (ii) a fine powder obtained crushing the natural rock. The initial glass was obtained grounding the natural rock in agate mortar under acetone and then melting the powder in a high temperature furnace at 1300°C in a platinum crucible, assuming total oxidation. Two melting cycle of 3 hours were realized and at the end of each cycle the crucible was rapidly cooled in water in order to obtain an homogeneous glass with the composition of the natural rock. This technique allows eliminating the presence of "*resistate*" crystals from the starting rock, and was successfully used in several experimental works (Di Carlo et al., 2006; Andujar et al., 2016). On the contrary, the fine powder of natural rock has been largely used (Scaillet & MacDonald 2001; 2003; 2006) when the crystal content of the rock is low (≤ 10%).

2.1.2 Experimental containers and charges preparation

Experiments were performed using gold capsules as containers in order to to minimize the iron loss from the staring material. Iron loss to the capsule material during the high T/P experiments is well-know problem especially when using platinum or gold-palladium capsules (Au_{80}-Pd_{20}) a problem that results amplified at reducing redox conditions Kawamoto & Hirose (1994). Iron loss to Au capsules appears less problematic, even if at high T (≥ 950°C) and low redox conditions iron loss can be significant (Ratajeski & Sisson 1999). However, The use of gold capsule was possible because the temperature during the

experiments was lower than the gold melting temperature (positive Clapeyron slope: T_m= 1063 °C at P= 1 bar; T_m= 1125 °C at P= 10 kbar)

Experimental charges for phase **equilibrium experiments** were prepared loading 30 mg of starting material in Au capsules with size 16 mm length, 2.5 mm inner diameter, 2.9 outer diameter. Together with the starting material were loaded water or water and $Ag_2C_2O_4$ (as a source of CO_2) and the amount of fluid within the capsule were maintained constant at 10wt% of the starting material. The different component were loaded in sequence, first water then $Ag_2C_2O_4$ and finally the starting material. Once loaded the capsule were weighted, welded and left in a oven at 100°C to homogenize the fluid phase within the capsules; before the experiment in order to check any volatiles lost. Each experiment consisted of several capsules (3 to 5) loaded in the same sample holder, and in these capsules the molar fraction of water [$XH_2O = H_2O/(H_2O+CO_2)$] was varied between 0-1. Experimental charge **for solubility experiments** were instead prepared loading in gold capsules (20 mm length, 2.5-2.9mm respectively inner and outer diameter) 50-100 mg of starting material and distilled water, the latter loaded in amount equal to the 10 wt% of the starting material (5-10 mg) in order to ensure volatile saturation at the experimental conditions. Only in the lowest pressure experiment (0.5 kbar) the water loaded was lower than 10%, to avoid the risk of capsule explosion.

2.1.3 Experimental equipment

All experiments were carried out in *Internally Heated Pressure Vessel* (**IHPV**) working vertically and pressurized with Ar-H_2 gas mixture (Fig. 2.1). The IHPV allows performing experiments up to temperature of 1300°C and pressure 4 kbar. Furthermore, the use of a fixed Ar/H_2 ratio allows imposing variable fH_2 within the vessel (Scaillet et al., 1992; 1995) and consequently it is possible to impose different fO_2 within the different capsules loaded in each experiment (see next paragraph).

The vessel was equipped with an inner furnace (Molybdenum and Kantal furnace) and the temperature was continuously controlled by S-type thermo-couples (± 5°C of precision) while the pressure was recorded by a trasducer calibrated against a Heise-Bourdon tube gauge (precision ± 15-20 bat). The IHPV are also equipped with a fast quench device (Roux & Lefevre 1992), which allows a nearly isobaric quench of the experimental charge. The drop quench technique consists in melting with an electric current the sample holder

wire, in this way the sample holder passes through an alumina tube from the hotspot zone to the cold part of the vessel (Fig.2.1); quench rate is around 100°C/s. The experiments at temperature lower than 800°C were terminated by switching off the power supply and keeping constant the pressure (isobaric quench). Run duration varied between 146 and 552 hours, depending on the temperature at which experiments were performed.

The experimental procedure consists of different steps: (i) loading the sample holder together with the furnace within the vessel (ii) closure of the vessel and sequential loading of H_2 (in accord to the desired fO_2 target) and pressurize with Ar (iii) heating up to experimental temperature.

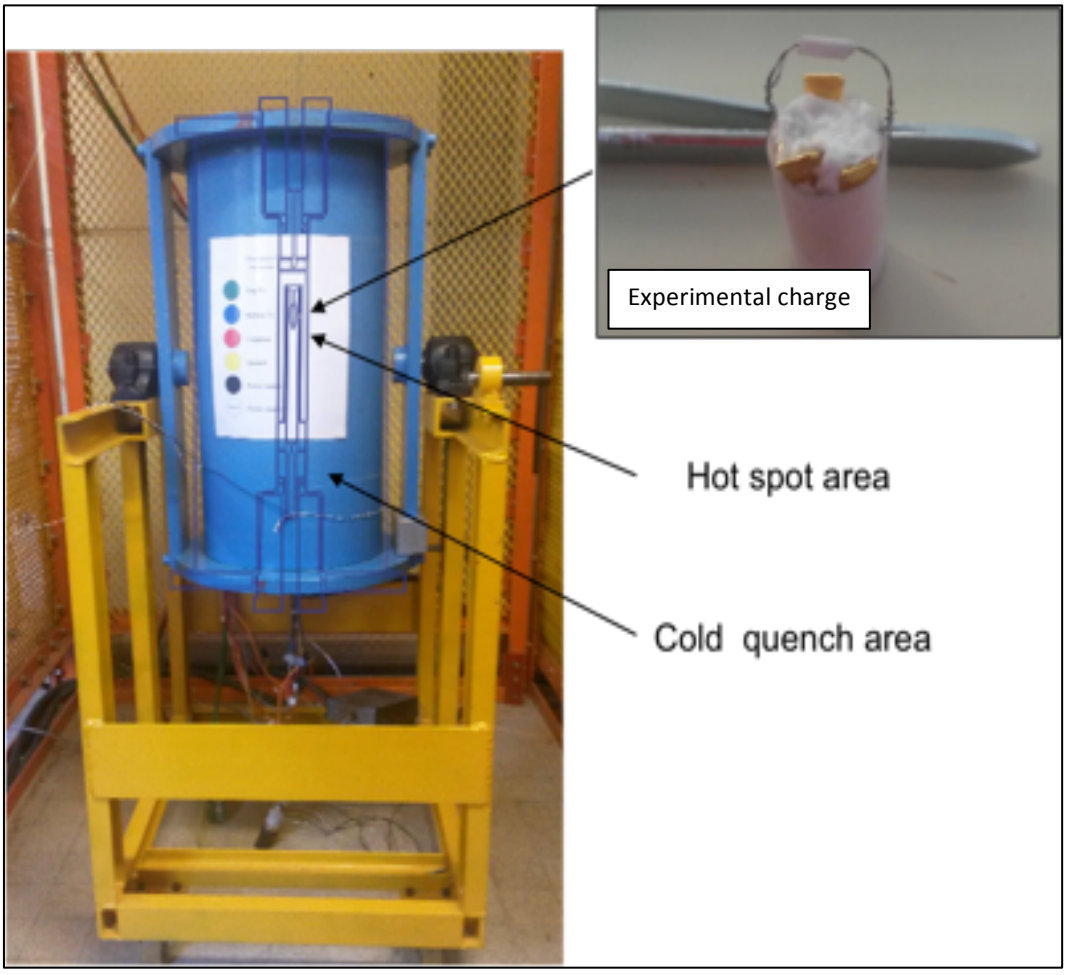

Figure 2.1: Scheme of Internal Heated pressure vessel (IHPV).

2.1.4 Control and monitoring of oxygen fugacity

Imposing a know Ar/H_2 ratio within the vessel allows to fix the redox conditions within the capsules. The noble metal of the capsule behaves as an ideal semipermeable membrane to H_2 (Chou 1986), which diffuses relative fast across the membrane and establishing the following equilibrium with the H_2O present in the capsules

$$H_2+\tfrac{1}{2}\,O_2 \leftrightarrow H_2O \quad \textit{(eq. 2.1)}$$

The equilibrium constant of this reaction at a given temperature and pressure allows knowing the oxygen fugacity (fO_2) if the hydrogen fugacity (fH_2) is known.

$$K_w = f°H_2O/(fH_2 * \tfrac{1}{2}O_2) \quad \textit{(eq. 2.2)}$$

$$\log K_w = \log f°H_2O - \log fH_2 - \tfrac{1}{2}\log fO_2 \quad \textit{(eq. 2.3)}$$

where the $f°H2O$ is the fugacity of pure H_2O, at the given pressure and temperature (derived from from Burnham 1969). The fO_2 during experiments was indirectly measured ex-post through the *solid sensor technique* (Taylor et al., 1992). The solid sensor consists of two pellet of a binary alloy, such as CoPd (using in this study) that form a continuous solid solution between 500°C and 1237°C, water and ZrO_2 powder; the latter to prevent contamination with capsule material. Previous calibration (Schwerdtfeger & Muan 1965) related the sensor composition and fO_2 following the equation:

$$Co+½\ O2 \leftrightarrow CoO$$

$$\log K_{(P,T)} = \log (a\text{CoO}) - [\log (a\text{Co}) + ½ \log fO_2] \quad \textit{(eq. 2.4)}$$

given that for pure phases (or end members in ideal solid solutions) a =1, the 2.4 reduces to:

$$\log K_{(P,T)} = -½ \log fO_2 \quad \textit{(eq. 2.5)}$$

If another metal oxide component (i.e PdO) that display a continuous solid solution is added, the end-member buffer equilibria is displaced to higher fO_2 so that at any given T and P

$$\log fO_2 = -2\,[\log K_{(T,P)} + \log (\text{aCo})] \quad \textit{(eq. 2.6)}$$

The equation calibrated at temperatures between 700°C and 1200°C for the Co-Pd alloy (Taylor et al., 1992) is:

$\log fO_2$ (CoPd) = -2 log X_{Co} – 1/(2.3025 RT) [(491649 – 508.527T + 122.6909T log T – $0.02518T^2$) + $[2(1-X_{Co})^2$ *(-9.76T + 16445 ($4X_{Co}$-1)] *(eq. 2.7)*

where T is the temperature of the experiment and X_{Co} is the molar fraction of Co in the alloy [XCo= Co/(Co+Pd)] obtained analysing the metal alloy . The graphical expression of the equation 2.7 is reported in Fig. 2.2. In this study the starting metal mixture had composition $Co_{0.15}$-$Pd_{0.85}$ and $Co_{0.5}$-$Pd_{0.5}$.

In synthesis, from the solid sensor is possible to obtain the fO_2 in the vessel then using the equation 2.2 the fH_2 within the vessel, which is calculated using the log Kw from Robie et al., (1979) and $f°H2O$ from Burnham et al., (1969).

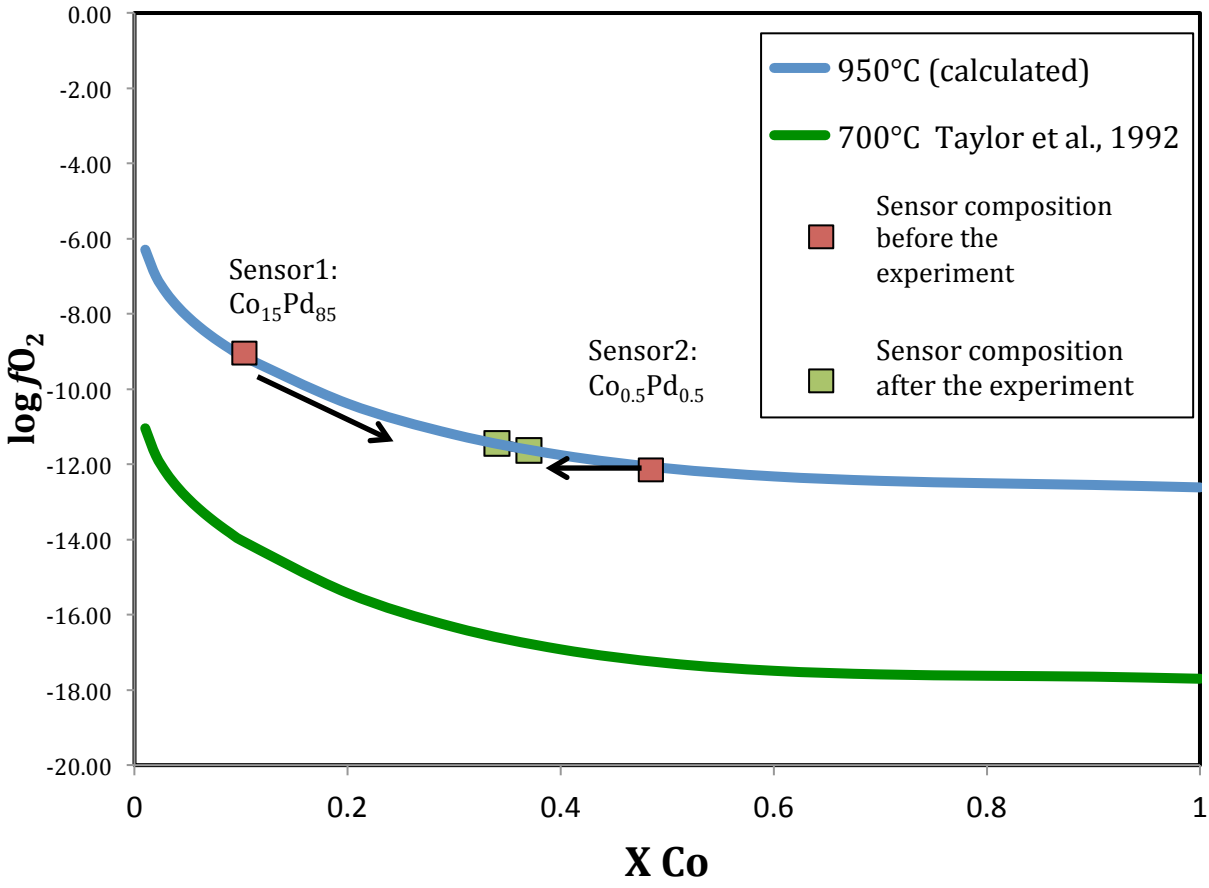

Figure 2.2: Variation of fO_2 with XCo [=Co/(Co+Pd)]. In the graphic is also reported the composition of the 2 CoPd alloys before the experiments and the composition after the experiment obtained from microprobe analysis, the arrows indicate the direction of the compositional change.
The use of 2 alloys is required to better constrain the final alloy composition

2.2 Analytical techniques

2.2.1 Scanning electron Microscope and Electron Microprobe

Small fragments of experimental products were embedded in epoxy resin and polished carefully. The preliminary studies were carried out using a *Scanning Electron Microprobe* (SEM-EDS) identifying the mineral phase and glass portions. It was used a SEM Cambridge LEO 440 housed at DiSTeM, University of Palermo and a TESCAN Mira 3 XMU hosted at ISTO, analytical conditions were 20keV electron energy and 600pA beam current.

Quantitative analysis of mineral phases and glasses were carried out using an *Electron Microprobe CAMECA SX FIVE* hosted at CNRS-ISTO, the analytical conditions were: acceleration voltage 15 kV, current 6 nA and counting time 10s for peak for all elements and 10 s for background. The analytical conditions of solid sensor (Co-Pd alloy) were: acceleration voltage 15 kV and beam current 20 nA. Experimental mineral phases were analysed with a focused beam while the experimental glasses were analysed using a defocused beam of 10x10μm.

The glasses analysed by Electron Microprobe in some case showed alkali values lower than those usually measured in felsic rock of Pantelleria. Alkali loss in hydrous glass has extensively discussed by Morgan & London, (1996, 2005). They suggested to use a current density of 0.006 nA/μm^2 corresponding to a beam size of 20x20μm with the analytical conditions used in this study. Nevertheless, Na and K were analysed first and a ZAF correction was applied so that the Na loss from the glasses analysed using a defocused beam of 10x10 resulted negligible. Some experimental products presented high crystal contents that prevented the use of a 10x10μm defocused beam and it was necessary use a beam size of 5x5 or 2x2 μm. In these latter cases, the Na loss resulted amplified, so that hydrous glasses where used to quantify the Na loss in the experimental products during the analysis and to calibre a correction factor.

Chapter 3

The trachytic and pantelleritic starting materials: field relationships and petrographic features

In this chapter will be described the main characteristics of the rocks used as starting material in this experimental study. In the first part will be presented the eruptive units sampled, with the aim of introducing the field relationships and the volcanological features of the deposit. The second part instead will focus on the petrographic and compositional aspects of the sample used as starting material that belongs to the target eruptive units, the purpose is to describe the natural phase relationships and the composition of the mineral phases. It is important to note that the efficacy of an experimental study through the use of experimental phase equilibria is consequent to an accurate characterization of the natural rocks.

3.1 Three target eruptions

The samples studied in this work belong to three eruptive units emplaced during the **second** and **third cycle** of volcanic activity at Pantelleria (paragraph 1.1.3). The oldest unit is the (i) *Green Tuff eruption*, the last caldera forming eruption at Pantelleria, (ii) the second eruptive unit is representative of the *post Cinque Denti Caldera magmatism*, while the third (iii) eruptive unit belongs to one of the most energetic eruptive event during the third cycle of activity at Pantelleria, the *Fastuca eruption*. It is worth to note that these three eruptive units cover the last period of activity at Pantelleria (45 to 10 ka) and include the most common eruptive styles at Pantelleria for felsic magmas: (i) high energy eruption with consequent emplacement of pyroclastic density current, (ii) violent strombolian eruption and (iii) lava flows.

3.1.1 The Green Tuff eruption ($^{40}Ar/^{39}Ar$ age : 45 ka)

The Green Tuff eruption is a low aspect-ratio rheomorphic ignimbrite with an internal chemical zoning from pantellerite at the bottom to trachyte at the top of the eruptive sequence. Previous works have considered the Green Tuff as a lava flow (Washington, 1913-1914) then a welded ignimbrite (Villari, 1974), a welded air fall (Wolff and Whright 1981)

or a combination of pyroclastic flow, welded fall and surge ignimbrite (Orsi & Sheridan 1984). Recently, Williams 2010, describing extensively and in detail the Green Tuff stratigraphy and lithofacies, has interpreted the Green Tuff as a single pyroclastic flow unit with a slightly diachronic distribution of the density currents.

Based on variation of mesoscopic features of the deposit, such as welding and crystal content, the Green Tuff eruption can be roughly divide in five members (Fig. 3.1), in detail:

-The **member A** (basal pumice), Fig. 3.1 is a **pumice fall** deposit 70-80 cm thick, with pumice clasts of maximum 5cm length and pantelleritic compositions (Na+K)/Al~ 1.80, lithic fragments with length lower than 1 cm are also present. The pumice fall lies directly on a palaeosol and it is preserved only in few sector of the island and it have been interpreted as the beginning of the eruption with a sustained strombolian-scale column (William 2010).

-The **member B** is an unsorted deposit (40-60 cm thick) of elongated pumice clasts (6 cm long) and abundant fine-grained material. This deposit has been interpreted as a **pumice flow** reflecting the first phases of the column collapse. The whole rock composition of the pumice is almost the same of the basal pumice of member A.

- The **member C** (70-90 cm) is the first **welded** member and it is characterized by a 10 cm thick vitrophyre at its base. This member is the most welded of the Green Tuff sequence and the upper portion is variably laminated with elongated fiamme e vesicles. This member has still pantelleritic compositions with peralkalinity index 1.62.

- The **member D** is a crystal-poor **rheomorphic** tuff 1 m thick characterized by a basal vitrophyre that grades into a massive and welded ash-rich portion with a pistachio-green colour. The uppermost portion is more scoriaceous with crystal content slightly higher of the lower members. The chemical composition of the juvenile fragments is similar to the previous member.

- The **member E** is the last member of the Green Tuff sequence and it is constituted by 2 m thick **crystal rich welded tuff** (up to 30%). This member has a pronounced trachytic composition with peralkalinity index (Na+K)/Al= 1.05 lower than the previous members.

The majority of the magma volume erupted has pantelleritic composition while the trachyte volume is only an hundredth of the total volume (3-7 km^3 D.R.E) and it outcrops only in some sector of the island. The stratigraphic sequence described reflects a zoned

magma reservoir that fed the Green Tuff eruption. The pumices of the basal member of the Green Tuff used in this study were sampled in the north-east side of the island while the trachytic member was sampled in the south-western part of the island (Fig. 3.1), in these two location member A and E are best exposed.

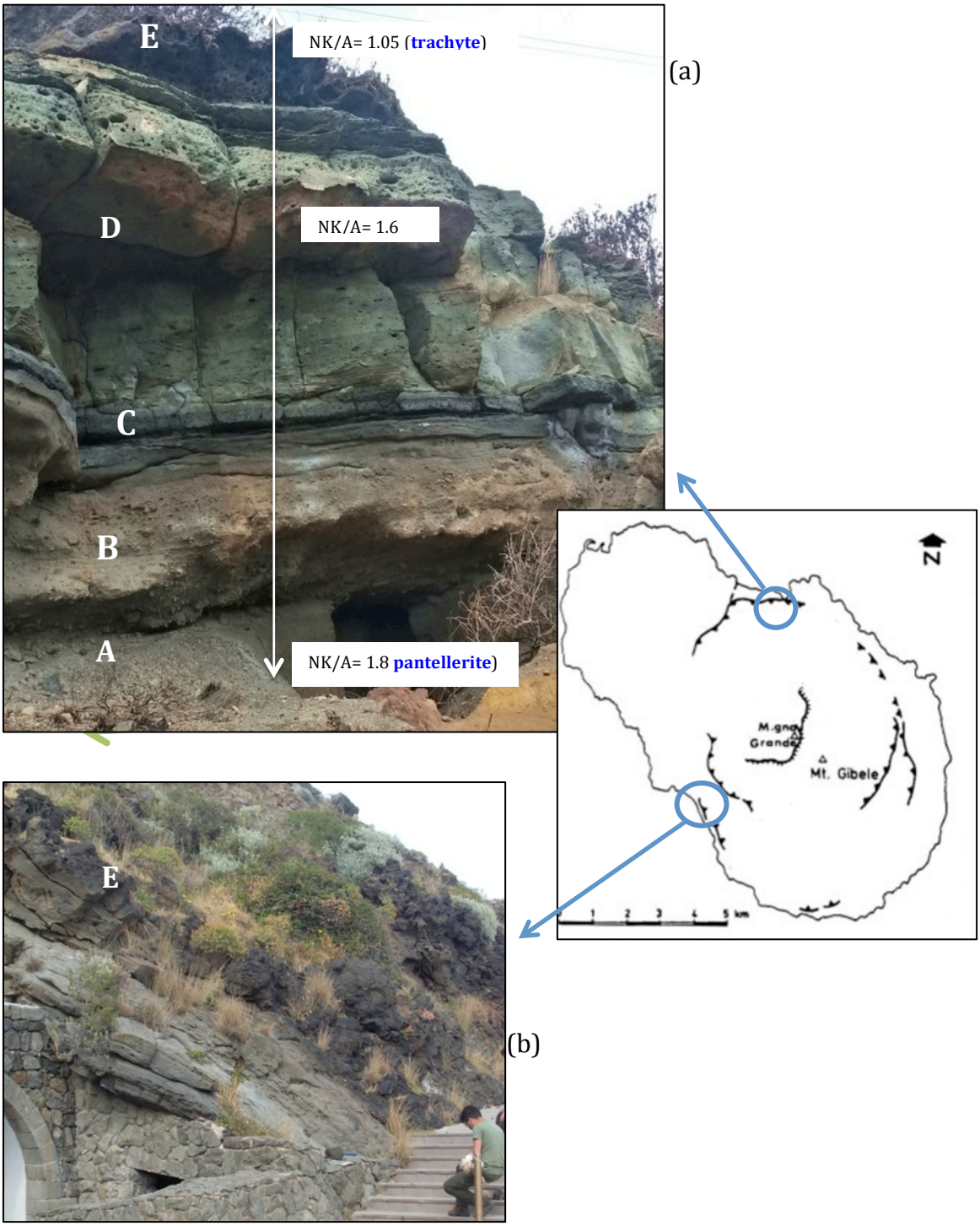

Figure 3.1 : Close view of the stratigraphic section of the Green Tuff eruption at (a) Calda Cinque Denti where the basal fallout is well exposed (sample GTP, Table 3.1) and (b) Porto di Scauri where the trachye top member of the Green Tuff (Sample GTT) outcrops. White capital letters indicate the different member described in the text.

3.1.2 Post Cinque Denti caldera trachyte (K/Ar age = 37-44 ka)

The large volume of trachyte erupted soon after the Green Tuff eruption, beside a lithostatic adjustment after the caldera-forming event it is interpreted as a prosecution of the emptying process of the compositionally zoned magma reservoir that fed the Green Tuff eruption (Mahood & Hildreth 1986). The Montagna Grande and Monte Gibele complex (Fig. 3.2) constitutes a compound of lava flow units and minor pyroclatisc flows. The stacked lava-flows units have a strongly porphyric texture (alkali feldspar phenocrysts up to 5 mm length) and the composition is similar to the trachytic member (E) of the Green Tuff. The Mt Grande-Mt Gibile complex has been interpreted as an homogeneous body although some small differences in major and trace elements have been recently evidenced by White et al., (2009) and Romengo (2010). The trachyte used as starting material in this study have been sampled at Contrada Monastero and belongs to the Case Ricco unit identified by Romengo (2010) (Fig. 3.3) and correspond to an high-incompatible trace elements trachyte of White et al., (2009).

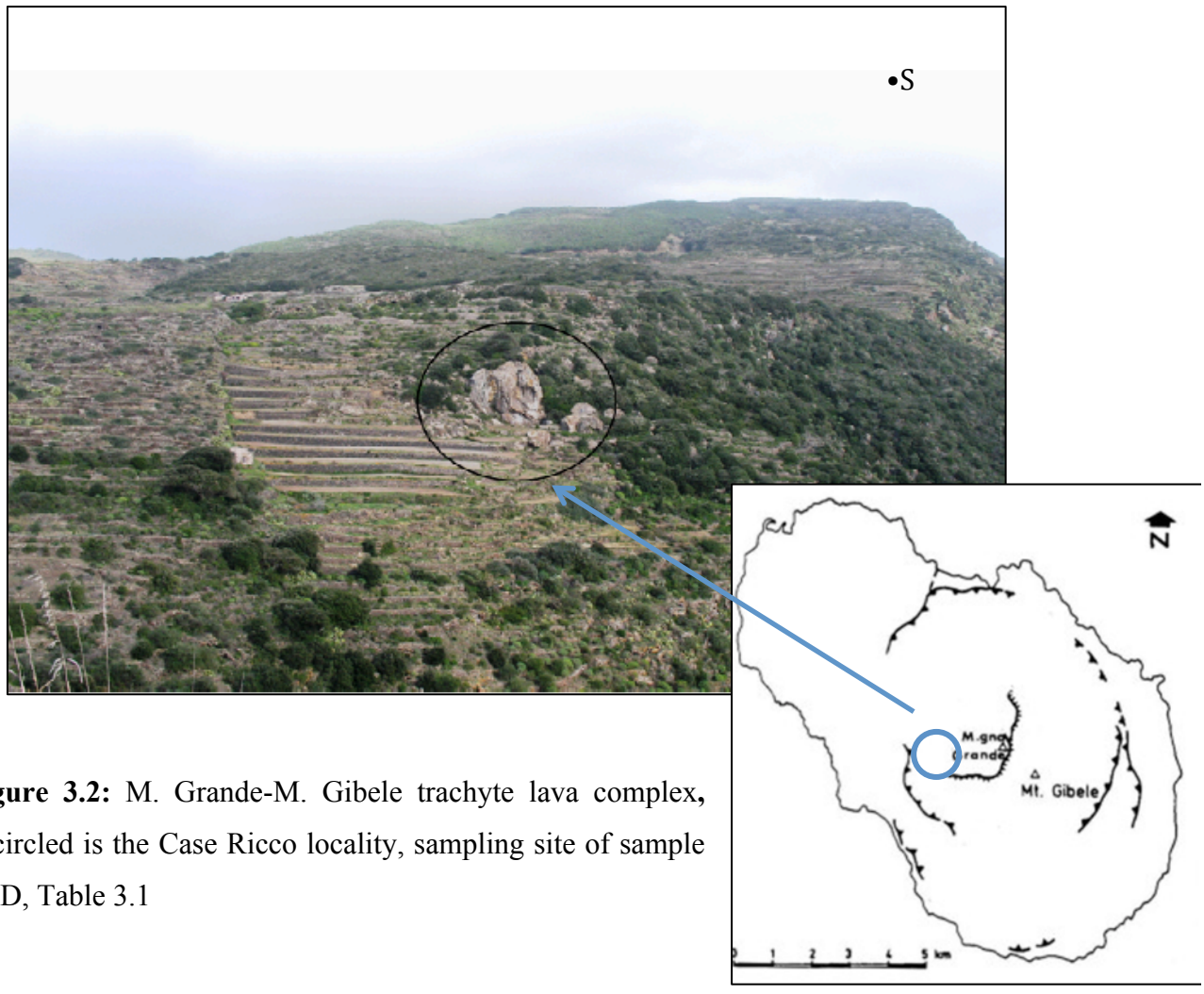

Figure 3.2: M. Grande-M. Gibele trachyte lava complex**,** encircled is the Case Ricco locality, sampling site of sample PCD, Table 3.1

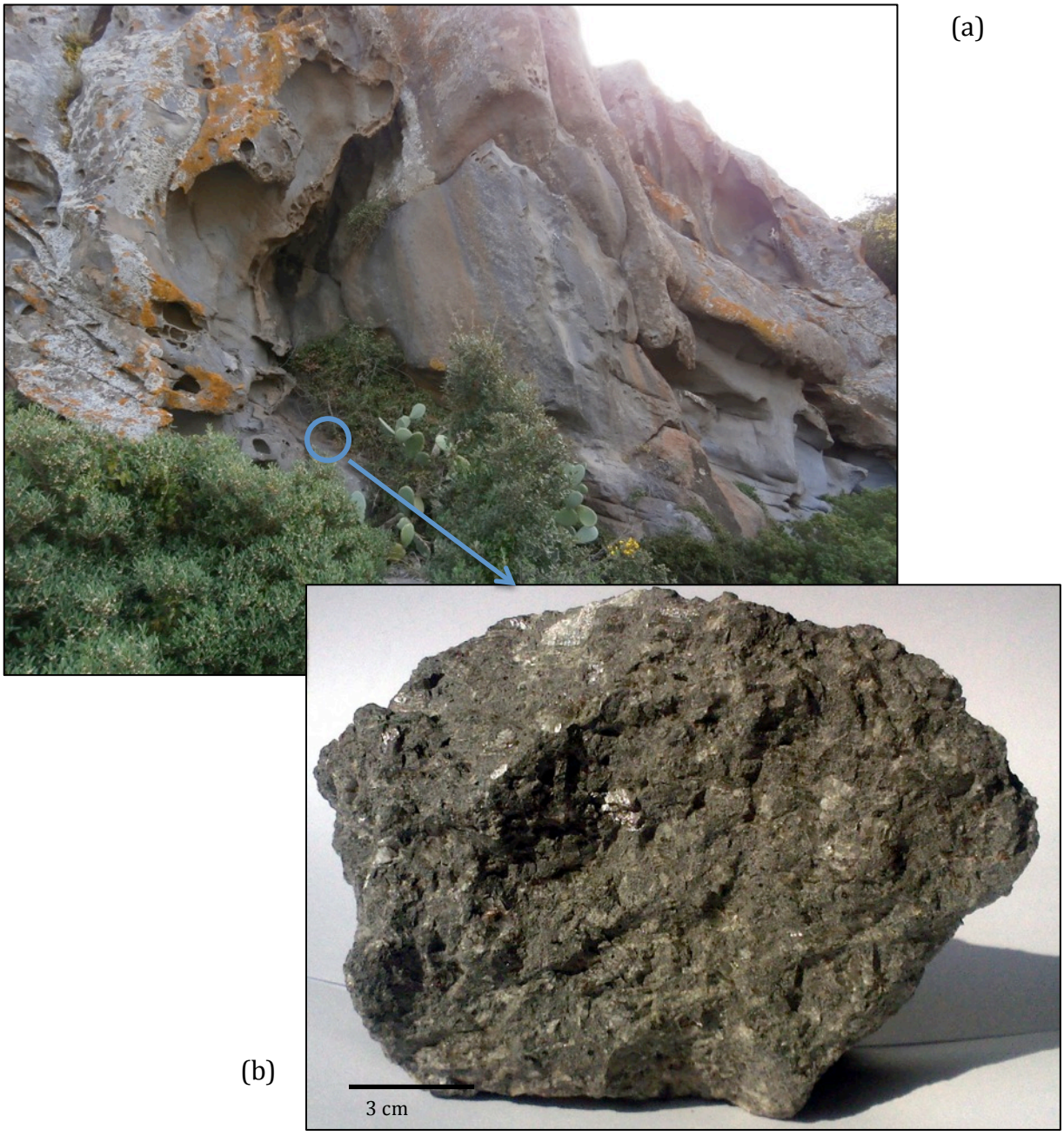

Figure 3.3: a) Close up view of the trachyte lava-flow at Case Ricco locality. b) Hand specimen image of trachyte rock, must be noted the high crystal content typical of Pantelleria trachytes.

3.1.3 Fastuca eruptive unit ($^{40}Ar/^{39}Ar$ age : 9.7 ka)

The Fastuca eruptive unit is the result of one of the most powerful pantelleritic eruption during the third cycle of activity at Pantelleria classified as a sub-plinian eruption by Orsi et al., (1989). The complete section is exposed near Case Siracusa (Fig.3.4) and is described by Orsi et al., (1989) and Rotolo et al., (2007); it consists of :

-a basal member of 3 m thick of **massive pumice fall** with pumice clasts up 15cm length and rare hyalopantelleritic lithics fragments, pumice are locally agglutinated to form lava like layers.

-a median portion 1.2 m thick composed by **well sorted pumice** clasts (up to 4 cm in diameter) and hyalopantelleritic lithics which reach a maximum content (~ 10%) in the uppermost portion of the member,

-a massive top member with **coarse pumice clasts** (up to 80 cm in diameter) and large hyalopantelleritic lithic fragments (up to 30 cm in length).

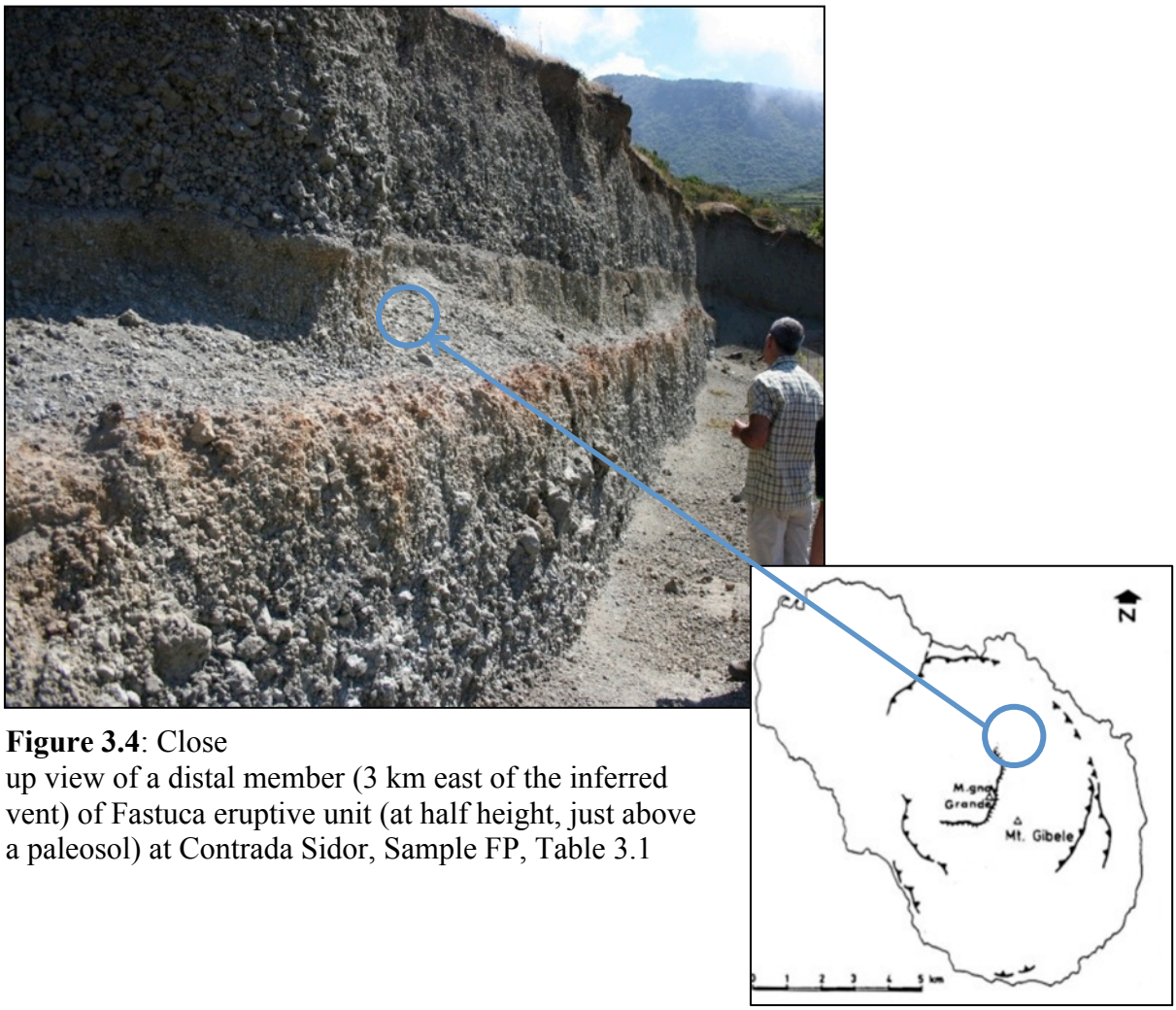

Figure 3.4: Close up view of a distal member (3 km east of the inferred vent) of Fastuca eruptive unit (at half height, just above a paleosol) at Contrada Sidor, Sample FP, Table 3.1

3.2 Petrographic and compositional characteristics of the rocks studied and used as starting material

The rocks studied have trachytic and pantelleritic composition and in general they are representative of the felsic pole of Pantelleria rocks. Pantellerites are the most abundant rocks at Pantelleria while trachytes, despite the smaller volume erupted represent the link between the mafic and felsic pole. In the section below will be described the petrographic and compositional aspect of the rocks sampled and then used as stating materials for the experiments. The whole rock composition (XRF analyses) of the rocks is listed in table 3.1 while in table 3.2 are summarized crystal modal abundances of each rock.

Table 3.1: Major element composition of the natural rocks used in this study. The acronym reported will be used also in the following paragraphs

Bulk rock	Green Tuff Pantellerite	Fastuca Pantellerite	Green Tuff Trachyte	Post Cinque Denti Caldera trachyte
Cycle of activity	II	III	II	III
Sample	**GTP (PAN 1201)**	**FP (PAN 0113)**	**GTT (pan 1401)**	**PCD (PAN 0718)**
SiO_2 (wt%)	70.15	70.4	63.07	63.78
TiO_2	0.46	0.43	0.82	0.75
Al_2O_3	8.27	8.74	15.66	15.83
FeO_{tot}	8.55	9.02	*7.06*	*5.61*
MnO	0.29	0.28	0.25	0.19
MgO	0.62	0.31	0.27	0.52
CaO	0.95	0.44	0.93	1.87
Na_2O	6.77	5.96	7.05	6.63
K_2O	3.88	4.43	4.72	4.22
P2O5	0.05	0.00	0.23	0.18
sum	99.21	100.1	100.06	99.58
P.I	1.86	1.67	1.07	0.97

P.I: peralkalinity index molar $(Na_2O+K_2O)/Al_2O_3$

Table 2: Modal phenocryst and microphenocryst abundances (vol%) inferred form SEM-BSE Images in natural trachyte and pantellerite

Sample	Green Tuff Pantellerite	Green Tuff Trachyte	Post Cinque Denti Caldera trachyte	Fastuca Pantellerite
Cycle of activity	II	II	III	III
Acronym	GTP	GTT	PCD	FP
Alkali felspar	7	30	32	15
Clinopyroxene	2	4	4	1.7
Fe-rich olivine	<1	3	3	<1
Fe-Ti oxides	<1	1	1	-
Aenigmatite	2	-	-	2.3
Amphibole	-	-	<0.5	<1
Quartz	<0.5	-	<0.5	0.1
Total crystals content	11%	34%	45%	20%
Ground mass	28%	61%	50%	64%

Vesicles	61%	5%	<5%	16%

*3.2.1 The Green Tuff basal pumice (**GTP**)*

The pumice composing the Green Tuff basal member presents an high vesiculated texture with crystal content that does not exceeded the 10% in volume (Fig. 3.5). The matrix glass is totally glassy and does not present any microlites while the mineral assemblage is dominated (in order of abundance) by alkali feldspar, aenigmatite, clinopyroxene and trace amount of olivine and quartz; rare ilmenite crystal are also presents, in groundmass or included in aenigmatite. Alkali feldspars phenocrysts, with ehuedral habitus and maximum length of 1 mm, have homogeneous composition $Ab_{65\text{-}69}Or_{35\text{-}38}$, clinopyroxene are riches in Na and Fe with composition Wo_{40}-En_{10}-Fs_{50} while olivines can be classified as fayalite with composition $Fa_{89\text{-}93}$. Aenigmatites have homogeneous compositions with XTi=[XTi=Ti/(Ti+Fe)]= 0.16-0.17.

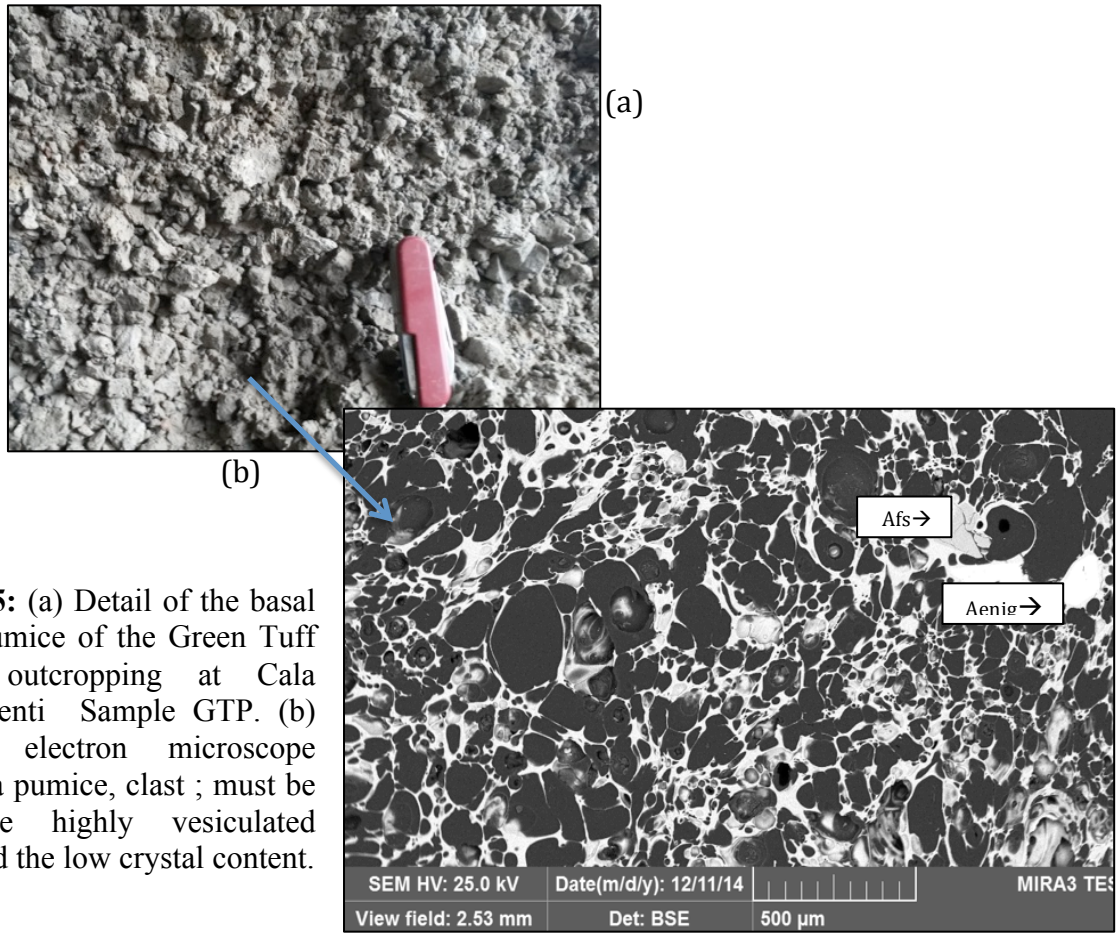

Figure 3.5: (a) Detail of the basal fall-out pumice of the Green Tuff eruption outcropping at Cala Cinque Denti Sample GTP. (b) Scanning electron microscope image of a pumice, clast ; must be noted the highly vesiculated texture and the low crystal content.

*3.2.2 The trachytic member of the Green Tuff (**GTT**)*

The trachytic member of the Green tuff eruption eruptions is constituted by abundant and large (up to 25 mm in length) alkali feldspar phenocrysts, microphenocrysts of clinopyroxene, Fe-rich olivine and Fe-Ti oxides. The groundmass is almost totally crystallised with abundant alkali feldspar and Fe-Ti oxides microlites, whereas clinopyroxene and olivine results rare or absent. Few glass pockets (< 10% vol) are present although difficult to be probed. As regards the crystallisation sequence, the textural features highlight a co-precipitation of clinopyroxene and olivine followed the (large) alkali feldspar phenocrysts, which often enclose other mineral phases originating glomerophyric textures (Fig. 3.5). Fe-Ti oxides are present both included in mafic minerals and in groundmass and often they present an oxy-exsolution texture. In mafic mineral phases are often included acicular apatite crystal and small sulphides (pyrrhotite) . Alkali feldspars (anorthoclase) phenocrysts show disequilibrium textures, such as resorbed cores and embayments with large corrosion gulfs, sometimes filled by glass.

Despite the almost uniform contrast in BSE images, cathodoluminescence (CL) imaging (Fig. 3.6) evidenced the presence of a weak concentric zoning, that together with EMPA chemical imaging and quantitative analyses reveal a slight variation in major elements CaO (0.4-2.5wt.%) and K_2O (4-5.5 wt.%) and trace elements BaO (0.18-0.65 wt%) as well, in anorthoclase phenocrysts. Olivine, clinopyroxene and Fe-Ti oxides are usually unzoned. Alkali feldspars have compositions in the range $An_{01-09}Ab_{64-74}Or_{16-34}$, clinopyroxene $En_{26-28} – Fs_{27-29} – Wo_{42-44}$) with XFe [=Fe/(Fe+Mg)]=0.52, while Fe-rich olivine is Fo_{23-27}.

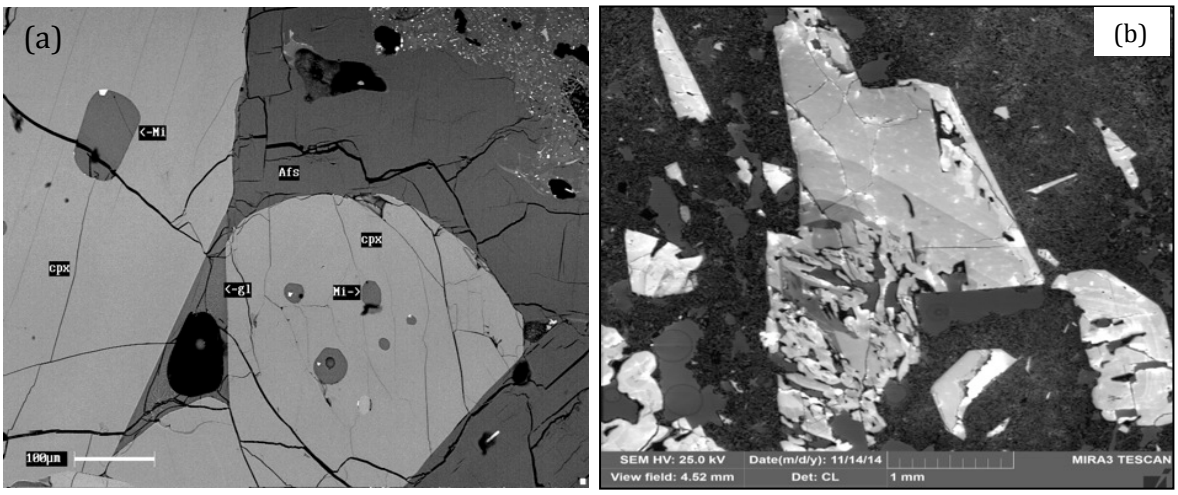

Figure 3.6: (a) Scanning electron microscope image of glomerophyric texuture in Green Tuff trachyte (Sample GTT) , Afs , alkali feldspar; cpx, clinopyroxene; MI, melt inclusions (b) Selected cathodoluminescence image of alkali feldspar characterized by concentric zoning.

3.2.3 The Post Cinque Denti Caldera trachyte (**PCD**)

Textures and minerals composition of the post Cinque Denti Caldera trachyte lavas (erupted from the M.gna Grande-M.Gibele complex) are similar to the Green Tuff trachyte (Fig. 3.7). Alkali feldspar is the most abundant mineral phase, follow clinopyroxene, olivine microphenocrysts and Fe-Ti oxides. Rare amphibole and quartz have been found as residual phases in groundmass, which is completely crystallised with alkali feldspar and clinopyroxene microlite. Respect to the Green Tuff member, alkali feldspar does not show deep resorbed or sieved textures but present also oscillatory zoning and patchy textures. The composition of alkali feldspars (anorthoclase) is in the range $An_{03\text{-}10}Ab_{65\text{-}69}Or_{22\text{-}29}$ while clinopyroxene and olivine, similarly to the trachyte of the Green Tuff top member, have composition respectively $En_{26\text{-}28} - Fs_{27\text{-}29} - Wo_{42\text{-}44}$ with XFe=0.49 and $Fo_{23\text{-}27}$.

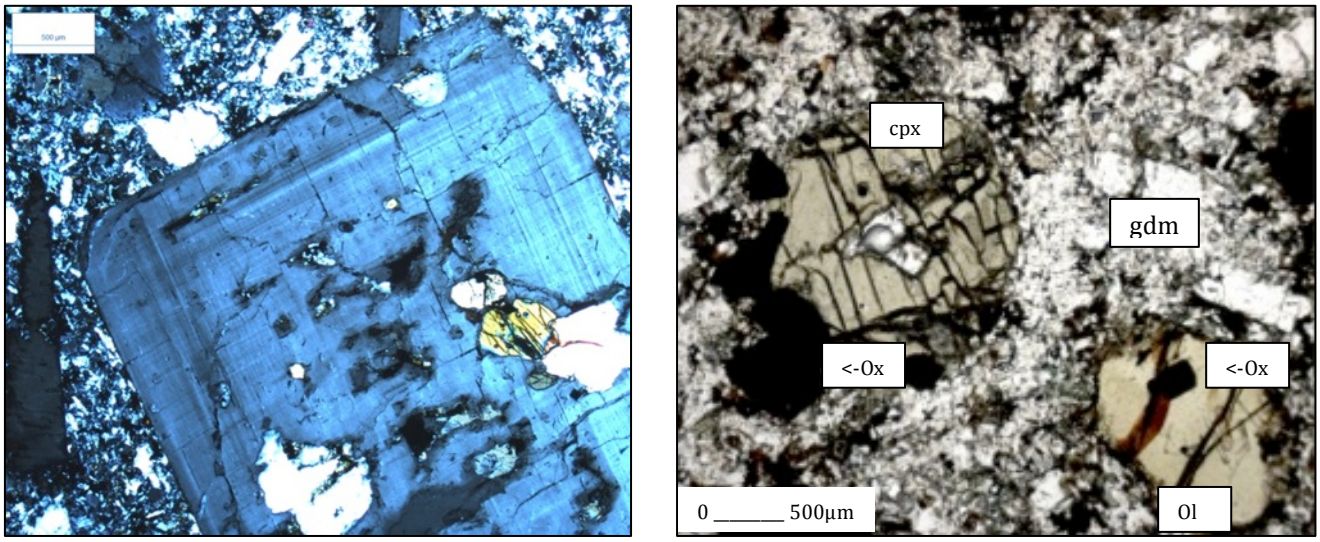

Figure 3.7: (a) Detail of the large alkali feldspar phenocryst of the post Cinque Denti Caldera trachytes (Sample PCD, Table 3.1). (b) Detail of the other mineral phases in paragenesis with alkali feldspar in post Cinque Denti Caldera trachyte.

*3.2.4 The Fastuca Pantellerite (**FP**)*

Fastuca pumices were sampled in the bottom portion of the fallout deposit. Pumices are dense and on average vesciculated. Similarly to other pantellerite, alkali feldspar, clinopyroxene, aenigmatite and trace proportions of fayalitic olivine, ilmenite and quartz constitute the mineral assemblage; although in small proportion also amphibole is present in the mineral assemblage as microphenocryst or microlite. The crystal content is close to the

20 vol. % and the most abundant mineral phase, also in this case, is alkali feldspar (15 vol. %), followed by aenigmatite, clinopyroxene in proportion lower than 5 vol%. Alkali feldspar tends to form glomerocrystic clots with aenigmatite and clinopyroxene (Fig.3.8). The groundmass is not totally glassy and contains alkali feldspar microlites.

Alkali feldspars phenocrysts and microlites have homogenous composition (Ab_{63} Or_{36}). Clinopyroxene microphenocrysts have compositions Wo_{43} Fs_{53} En_4 and XFe=0.93 while amphibole composition varies in the range ferrorichterite-arfvedsonite; rare microlite of aegirine are also present in groundmass. Olivines composition is in the range $Fa_{90\text{-}93}$, typical of the olivine found in pantellerites while aenigmatite has homogeneous composition with XTi=[XTi=Ti/(Ti+Fe)]= 0.16-0.17 similarly to the aenigmatite found in the pumice of the Green Tuff basal member.

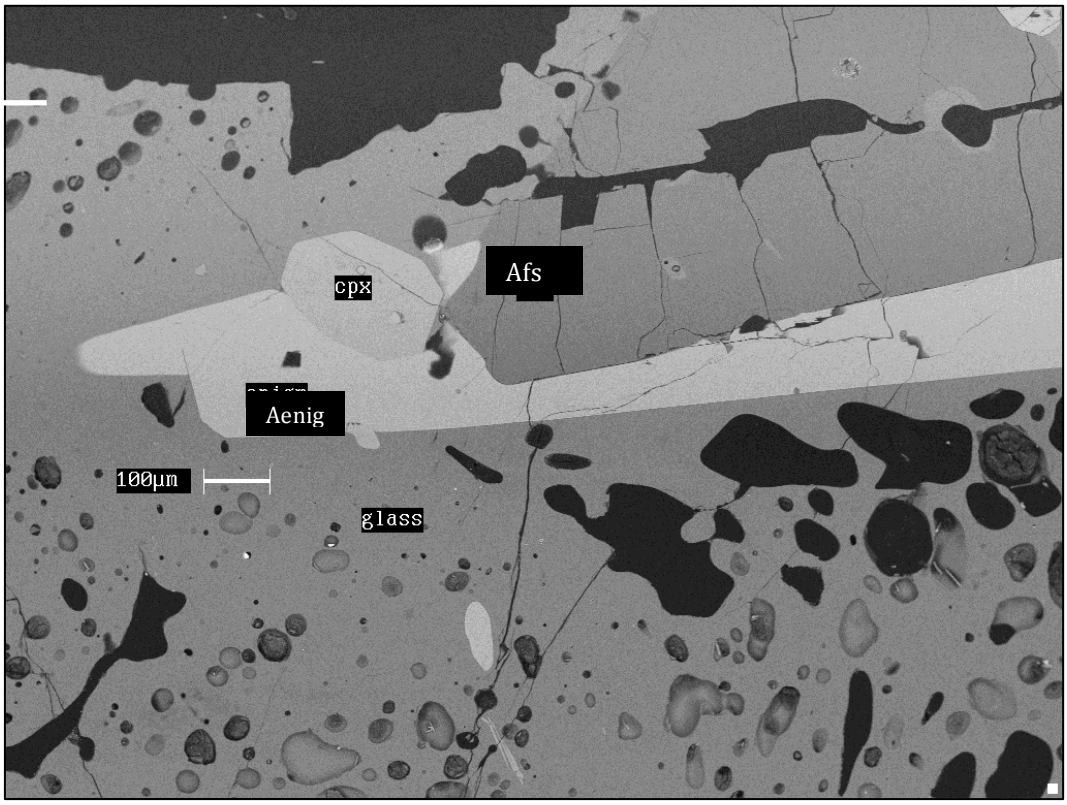

Figure 3.8: Scanning electron microscope image of the Fastuca pumice (Sample FP, Table 3.1), in detail the low-vesicularity texture and the glomerophyric crystal clots with alkali feldspar (Afs), clinopyroxene (Cpx) and aenigmatite (Aenig)

Chapter 4:

Phase equilibria of Pantelleria trachytes (Italy): constraints on pre-eruptive conditions and on the metaluminous to peralkaline transition in silicic magmas.

(paper accepted to Journal of Petrology)

Authors: Pierangelo Romano[1] *, Joan Andujar [2], Bruno Scaillet [2], Nunzia Romengo [1], Ida di Carlo [2], Silvio G. Rotolo [1,3]

1: UNIVERSITÀ DEGLI STUDI DI PALERMO- DIPARTIMENTO DI SCIENZE DELLA TERRA E DEL MARE- VIA ARCHIRAFI, 36 – 90123 PALERMO, ITALY

2:UNIVERSITÉ D'ORLÉANS, ISTO, UMR 7327, 45071 ORLÉANS, FRANCE; CNRS/INSU, ISTO, UMR 7327, 45071 ORLÉANS, FRANCE; BRGM, ISTO, UMR 7327, BP 36009, 45060 ORLÉANS, FRANCE

3 ISTITUTO NAZIONALE DI GEOFISICA E VULCANOLOGIA, SEZIONE DI PALERMO, VIA UGO LA MALFA 153, 90146 PALERMO, ITALY

Affiliations:

P. Romano (corresponding author) – Università degli Studi di Palermo- Dipartimento di Scienze della Terra e del Mare (DiSTeM)- Via Archirafi, 26 – 90123 Palermo, Italy – pierangelo.romano@unipa.it

J. Andujar: juan.andujar@cnrs-orleans.fr

B. Scaillet: bscaille@cnrs-orleans.fr

I. di Carlo: ida.di-carlo@cnrs-orleans.fr

S. G. Rotolo: silvio.rotolo@unipa.it

Draft Manuscript for Review

Phase equilibria of Pantelleria trachytes (Italy): constraints on pre-eruptive conditions and on the metaluminous to peralkaline transition in silicic magmas.

Journal:	*Journal of Petrology*
Manuscript ID	Draft
Manuscript Type:	Original Manuscript
Date Submitted by the Author:	n/a
Complete List of Authors:	Romano, Pierangelo; Università degli Studi di Palermo, Scienze della Terra e de Mare Andújar, Joan; ISTO- CNRS, Scaillet, Bruno; CNRS/ISTO, Di Carlo, Ida Romengo, Nunzia Rotolo, Silvio; Universita degli Studi di Palermo, Scienze della Terra e del Mare (DiSTeM)
Keyword:	peralkaline silicic magmatism, experimental petrology, trachyte, pantellerite, liquid line of descent, Pantelleria

Abstract

Trachytes and peralkaline rhyolites (i.e pantellerite and comendite) usually represent the felsic end-member in continental rift systems and oceanic island settings characterized by peralkaline silicic magmatism. Recent experimental investigations on both Pantelleria Island and Kenya Rift Valley have laid down the general conditions of storage and evolution of comenditic and pantelleritic magmas at these locations (Di Carlo et al., 2010; Scaillet & Macdonald, 2001, 2003, 2006). However, the parent-daughter relationship between trachyte and pantellerite still awaits experimental investigation. To fill this gap, we have performed phase equilibrium experiments on two representative trachytes from Pantelleria in order to determine both their pre-eruptive conditions (pressure, temperature, volatile fugacities) and differentiation conditions. Experiments were performed in the temperature range 750-950°C, pressure 0.5-1.5 kbar and fluid saturation conditions with XH_2O (=H_2O/H_2O+CO_2) ranging between 0 and 1. Redox conditions were fixed below the nickel-nickel oxide buffer (NNO). The results show that at 950°C and melt water content (H_2O_{melt}) close to saturation, trachytes are at liquidus conditions at all pressures. Clinopyroxene is the liquidus phase, being followed by iron-rich olivine and alkali feldspar. Comparison of experimental and natural phase abundances and compositions yields the following pre-eruptive conditions: T=900±50°C, H_2O_{melt} = 1-3 wt%, and fO_2 between NNO-0.5 to NNO-2. A decrease in temperature from 950°C to 750°C as well as of H_2O_{melt} promotes a massive crystallization of alkali feldspar to over 80 wt%. Iron-bearing minerals show gradual iron enrichment when T and fO_2 decrease, trending towards the compositions of crystals in natural pantellerites. Despite the metaluminous character of the bulk rock composition, residual glasses obtained after 80 wt% crystallisation evolve toward a comenditic composition, owing to profuse alkali feldspar crystallization, which decreases the Al_2O_3 of the melt, leading to a consequent increase in the peralkalinity index [=molar $(Na_2O+K_2O)/Al_2O_3$]. Our results show that peralkaline felsic magmas of basalt-trachyte-rhyolite rock suites require at least 95 wt% of basalt crystallisation, in agreement with trace element evidence. Redox conditions, through their effect on Fe-Ti oxide stabilities, control the final iron content of the evolving melt. Considering the time interval since the Green Tuff eruption, an average basalt intrusive rate of 10^{-3} km^3/year, and the amount of fractionation required to produce felsic derivatives from basalt crystallisation, we suggest that any present-day pantelleritic reservoir beneath Pantelleria cannot exceed a few km^3 in volume.

KEY WORDS: peralkaline silicic magmatism; experimental petrology; trachyte; pantellerite; liquid line of descent; Pantelleria;

INTRODUCTION

Pantelleria Island is the type locality of pantellerite, an iron and alkali-rich rhyolite (P.I=molar Na_2O+K_2O/Al_2O_3 >1.2). Peralkaline rhyolites (i.e pantellerite and comendite) and trachytes usually represent the felsic end-members in continental rift systems (e.g., Pantelleria, Tibesti, Ethiopia, Afar, Kenya, Basin and Range, South Greenland) and in oceanic island settings (Socorro Is., Easter Is., Iceland and Azores). The origin of peralkaline rhyolites in the different tectonic settings is still a matter of debate and three hypotheses have been suggested: (a) crystal fractionation of alkali-basalt in a shallow reservoir to produce a trachyte which subsequently gives rise to a pantellerite (e.g., Barberi et al., 1975, Mungall & Martin 1995, Civetta et al., 1998,) (b) partial melting of cumulate gabbros to form a trachyte which then produces pantellerite (e.g., Lowenstern & Mahood 1991; Bohrson & Reid 1997), (c) partial melting of different lithospheric sources fluxed by volatiles which add the excess alkalies to the melt (Bailey & Macdonald, 1975, 1987). Recent petrological work has helped to define the temperature range and redox conditions of pantellerite magmas (Scaillet & Macdonald 2001, 2003, 2006; White et al., 2005, 2009; Di Carlo et al., 2010,) as well as their pre-eruptive volatile contents (e.g., Gioncada & Landi 2010, Neave et al., 2012, Lanzo et al., 2013). In contrast little is known about the conditions of storage and evolution of the associated trachytes. At Pantelleria, trachytes and pantellerites constitute most of the outcropping rocks, the former being erupted dominantly as lava flows while pantellerites are erupted either explosively or effusively.

We have experimentally investigated the phase relationship of two representative trachytes from Pantelleria island in order to shed light on their pre-eruptive conditions (pressure, temperature, H_2O_{melt}, oxygen fugacity) and define their liquid lines of descent toward more evolved compositions. We have established the phase relationships over a P-T-fO_2-H_2Omelt range of T=750-950°C, P=0.5-1.5 kbar, fO_2=~FMQ and XH_2O_{fluid} (H_2O/H_2O+CO_2, in moles) between 1 and 0. By comparing the experimental phase assemblages, abundances and compositions with the natural products we set constraints on the storage conditions of trachytic magmas at Pantelleria and more generally, on the putative parent-daughter relationship between trachytic and pantelleritic magmas. Our results lay the

basis to understand the long debated petrological issue regarding the link between silica-oversaturated peralkaline and metaluminous magmas.

GEOLOGICAL SETTING

Eruptive history

The island of Pantelleria is the emerged portion of a Quaternary large volcanic edifice rising up from the Sicily Channel rift zone (e.g, Fig.1 Rotolo et al., 2006, Catalano et al., 2009). The eruptive products of Pantelleria draw a bimodal suite that consists of a mafic (mildly alkali basalts) and felsic (metaluminous or slightly peralkaline trachytes and pantellerites) end-members (Washington,1913–1914)???. From the volcanological point of view, the eruptive history of Pantelleria is characterized by large explosive ignimbritic eruptions, low-energy Strombolian eruptions and lava flows. The eruptive history can be divided into three major periods. During the first period (324-180 ka) were ejected mostly pantelleritic lava flows with alternating welded tuffs and pumice fallout deposits, (Mahood & Hildreth, 1986, Civetta et al., 1988, Rotolo et al., 2013). The second period (180-45 ka) was characterized by more than eight ignimbrite-forming eruptions including the La Vecchia caldera-forming eruption and the Green Tuff eruption (GT). The GT eruption, recently dated at 44.1±0.6 ka (Scaillet et al., 2013) is the last highly energetic eruption and the sole that blanketed the entire island (at least 7 km^3 D.R.E of tephra erupted). Moreover it is thought to be the cause of the Cinque Denti Caldera, which is nested within La Vecchia caldera collapse (Fig. 1) (Mahood & Hildreth, 1986, Speranza et al., 2012). During the third period (45-8 ka), the activity consisted of felsic resurgent volcanism confined almost entirely inside the Cinque Denti caldera. Initially, a long period of effusive activity produced at least ~ 3 km^3 of trachytic magmas which formed the present-day Montagna Grande-Monte Gibele system, a large volcanic complex tectonically uplifted and tilted to form the island's highest elevation. Subsequently, the activity continued with low-energy Strombolian eruptions associated with effusive events, yielding pumice fall sequences, lava flows and lava domes with pantelleritic composition (Mahood & Hildreth, 1986, Civetta et al., 1998, Rotolo et al., 2007). In the late stage of the third period, simultaneously to pantelleritic magmatism, extracaldera basaltic volcanism occurred in the North-West side of the island (Fig 1). The last eruptive episode (1891) is located offshore of the island, at about 5 km of the northwest coast and the lava balloons erupted were basaltic-hawaiitic in compositions.

Petrological background: the origin of pantellerites and previous constraints on storage conditions

Pantelleria is very well known in the petrological literature for the presence of a typical compositional gap (Daly Gap) in the eruptive sequence between the mafic products and the felsic member. Intermediate products are however sporadically found as enclaves within the felsic rocks and as a single small-volume lava flow with benmoreitic bulk rock composition. In both cases, these rocks show the characteristics of a product originated from basalt-rhyolite mixing (Ferla & Meli, 2006; Romengo et al., 2012). The petrogenesis of pantelleritic rocks at Pantelleria has been explained through two models: (1) protracted fractional crystallization from alkali basalt parental magma, (2) low-degree partial melting of alkali gabbroic cumulates. The first model argues for the fractional crystallization of a mineral assemblage made of plagioclase, clinopyroxene, and olivine at an oxygen fugacity around FMQ-1, which produced a metaluminous trachyte residual liquid, which then crystallised (~ 90%) to yield a pantellerite melt (Civetta et al., 1998; White et al.,2009; Neave et al., 2012). Alternatively, on the basis of the low water contents found in the melt inclusion of pantelleritic composition, Lowenstern & Mahood (1991) proposed the partial melting of gabbroic cumulates as the source of trachytic magma, which then produces pantellerites by low-pressure fractional crystallization. As regard the pre-eruptive conditions of the mafic suite, Civetta et al., (1998) reported Fe-Ti oxides based temperatures in the range 940-1079°C. These values are similar to the 1091±45°C obtained by Neave et al., (2012) using mineral-liquid equilibria. For the metaluminous trachyte, based on mineral-mineral or mineral-liquid equilibria, White et al. (2005, 2009) reported temperatures ranging from 858 to 922°C, while for pantellerites they found a temperature range of 650-750°C. Estimates of redox conditions for Pantelleria magmas yield a fO_2 around the FMQ buffer. Such T-fO_2 estimates for pantelleritic melts are corroborated by Di Carlo et al., (2010) phase equilibrium experiments which in addition demonstrate the water-rich character (up to 4 wt.%) of these magmas. Water contents of mafic to felsic melt inclusions (MI) have been also investigated through Fourier transform infrared spectroscopy (FT-IR) and SIMS. Melt inclusions trapped in phenocrysts of alkali basalts yield water contents (H_2O melt) ranging from 0.8 to 1.6 wt.% and CO_2 up to 980 ppm (Gioncada & Landi 2010). Water contents in MI of phenocrysts of pantelleritic magmas vary between 2 and 4.5 wt.% (Lowenstern & Mahood 1991, Gioncada & Landi 2010, Neave et al., 2012, Lanzo et al., 2013). The corresponding pressures of volatile saturation are < 2 kbar, being consistent with both

experimental (Di Carlo et al., 2010) and geophysical (Mattia et al., 2007) constraints, altogether suggesting the existence of a magma reservoir at a depth of 4 km (1000 bar for an average crustal density of 2.6 g cm^{-3})

ROCKS STUDIED AND CHOICE OF THE EXPERIMENTAL CONDITIONS

Despite of much smaller volume than pantellerite, trachytic magmas were erupted during the entire volcanological history of Pantelleria as lava flows (Civetta et al., 1998, White et al., 2009, Romengo, 2011), ignimbrite units (Mahood et al., 1986, Rotolo et al., 2013) and magmatic enclaves (Prosperini et al., 2000, Landi & Rotolo, 2015). We have performed phase equilibrium experiments on two trachytic samples representative of the trachytic rocks at Pantelleria which are spatially and temporally related to pantelleritic eruptions. One of the samples comes from the trachytic (top-) member of the Green tuff (GTT) formation (36°49′10.90′′N, 11°59′49.71′′E) while the other belongs to one of post-GT lava flows filling the Cinque Denti caldera (36°46′46.72′′N, 11°58′47.23′′E), here named PCD. The Green Tuff formation, apart form the initial pumice fallout, is considered a single pyroclastic flow unit (for a complete and detailed report about lithofacies and zoneography see Williams, 2010) which displays a continuous chemical zoning from pantellerite at the bottom to comenditic trachyte at the top. Pantellerite was the dominant magma erupted but a small volume of trachytic magma was emplaced at the top of the GT sequence, possibly reflecting a zoned reservoir (Mahood & Hildreth, 1986; Civetta et al., 1998; Williams 2010). The trachytes of M.Grande-M. Gibele (starting sample, PCD) which erupted immediately after the Cinque Denti caldera collapse, form a complex system of lava flows that constitute a broadly homogeneous body, with minor differences in major and trace element between units (White et al., 2009, Romengo 2011). In accord to Mahood & Hildreth (1986), the Green Tuff trachyte and the post Cinque Denti trachytes are genetically linked, the latter representing the deeper part of a zoned reservoir which have been depleted of the pantelleritic fraction during the Green Tuff eruption.

This large volume of trachyte follows the Green Tuff eruption but also precedes the last explosive post-caldera pantelleritic eruptions (Scaillet et al., 2011).

Bulk rock compositions of both rocks were obtained by XRF analyses (Tables 1). The mineralogy was determined using both petrographic and electron (SEM) microscopies while the compositions of mineral phases were determined by electron microprobe analyses

(EPMA) (Tables 1). The selected samples are trachytes in compositions (Le Bas et al., 1986) with a peralkalinity index (molar Na_2O+K_2O/Al_2O_3) of 0.98 (GTT) and 0.92 (PCD). Crystal contents, based on point counting in thin sections, are ~34 vol% for Pan1410 and ~37 vol% for PCD. Large alkali feldspars (0.6 mm) make up ~32 vol% of the phenocrysts content in GTT and 34 vol% in PCD. Clinopyroxene and olivine have generally dimensions ranging from 250 to 500 μm, representing 1.5 and 2.8 vol%, respectively, of the crystal content. The occurrence of large glomerophenocrysts of alkali feldspar and mafic minerals suggests that olivine and clinopyroxene co-precipitated along with alkali feldspar. Microphenocrysts of Ti-magnetite and ilmenite occur in sample GTT, either in the groundmass or in glomerophenocrysts (with alkali feldspar and pyroxene) but also within clinopyroxene and olivine. In GTT, Fe-Ti oxides are either homogeneous or display oxy-exsolution textures with inter-growing lamellae of ilmenite in magnetite, whereas in PCD all oxides exhibit oxy-exsolution textures. As for oxides, apatite crystals are often included in olivine and clinopyroxene. The groundmass in both samples consists predominantly of alkali feldspar microlite (<0.05 mm), clinopyroxene, oxides and trace of olivine, but PCD presents also traces of quartz and amphibole. A few pockets of residual glass were found only in the sample GTT, which is probably due to the different cooling rate between ignimbrite deposits (GTT) and lava flows (PCD). The scarcity of quenched glass in trachytes, also reported by Gioncada & Landi (2010), explains the lack of volatile data for trachytic magmas. Alkali feldspar phenocrysts display compositions ranging from $An_{01\text{-}09}Ab_{64\text{-}74}Or_{16\text{-}34}$ (GTT) to $An_{03\text{-}10}Ab_{65\text{-}69}Or_{22\text{-}29}$ (PCD). Clinopyroxenes in both rocks are augite ($En_{26\text{-}28} - Fs_{27\text{-}29} - Wo_{42\text{-}44}$) with XFe [=Fe/(Fe+Mg), calculated using FeO_{tot}]=0.52 in GTT and XFe=0.49 in PCD while olivine is $Fo_{23\text{-}27}$. In GTT ilmenite has a TiO_2 content of 44.1% and magnetite has an FeO content of 66.1 wt.%

The choice of experimental conditions was guided by the results of previous investigations carried out at Pantelleria. The range of pressure explored in this study reflects broadly the low pressure inferred for the magma reservoir at Pantelleria (≤ 2 kbar; Gioncada & Landi 2010, Di Carlo et al., 2010, Neave et al., 2012), which is typical of this category of magmas (Mahood 1984, Scaillet & Macdonald 2001, 2006). Temperature constraints come from the results of White et al. (2009) for the metaluminous trachyte (900 ± 50°C) filling the Cinque Denti Caldera, and from those estimated with the few oxide-pairs in GTT. Using the formulation of Sauerzapf et al. (2008) the latter give a temperature of 932 ± 68°C and a fO_2 of NNO-1.31 ±0.09 (ie 1.31 log unit below the Ni-NiO buffer). The low temperature

experiments were performed in order to investigate the relationships between trachyte and pantellerite.

EXPERIMENTAL STRATEGY

Charge preparation

The rocks chosen as starting materials were initially crushed and about 10 g of the resulting powders were fused twice in a Pt crucible at 1300 °C in air for 3-4 hours. Some chips of glasses were analysed by electron microprobe and found to be homogeneous and similar to the X-ray fluorescence bulk rock analyses of the natural rocks (Tables 1). The glasses were then ground in an agate mortar under acetone to 10-40 μm mesh size and utilized as starting materials for the experiments. Au capsules (1.5 cm in length, inner diameter 2.5 mm and outer diameter 2.9 mm) were used in order to minimize iron loss. Capsules were loaded first with distilled water, then silver oxalate as a CO_2 source, and finally with 30 mg of powdered glass. The amount of fluid (H_2O+CO_2) loaded into each capsule was 3±0.5 mg (the 10% of the starting material) ensuring always fluid saturation conditions (e.g., Scaillet et al., 1995, Andujar et al., 2015). Each capsule was arc-welded with weighing before and after the welding to check for water loss; afterwards the capsules were left in an oven at 100°C to homogenize the water distribution along capsule length before the experiment and to check further for leaks. After the experiment, capsules were reweighed and each capsule was considered successful if the pre-post run weight difference was less than 0.4 mg, which is the precision of the analytical balance. Each run consisted of several capsules loaded together to the vessel, each capsule having different H_2O/CO_2 ratios so as to vary XH_2O (=molar H_2O/H_2O+CO_2) between 1 and 0.12 (Table 2) at any explored P and T. Vesicle size and proportion vary with melt water content and the presence of vesicles in all charges bears evidence for fluid saturation condition during the experiment.

Experimental equipment

All experiments were performed at the Institut des Sciences de la Terre d'Orleans using Internally Heated Pressure Vessels (IHPV) working vertically and equipped with either a Molybdenum or a Kanthal furnace. The pressuring medium was an H_2-Ar mixture (loading sequentially H_2 and then Ar at room temperature), the Ar/H_2 ratio used to reach the desired target fO_2 being based on previous experiments (Scaillet et al., 1992). Total pressure

was recorded by a transducer calibrated against a Heise-Bourdon tube gauge (uncertainty ± 20 bars), while temperature was permanently measured by 2 S-type thermocouples (accuracy ± 5°C). The fO_2 prevailing during the experiment was determined *a posteriori* through redox sensors, which consist of two pellets of hand-pressed Co-Pd-CoO powder loaded into Au capsules with distilled water embedded within a ZrO_2 powder to prevent alloying with Au (Taylor et al., 1992). Run duration varied between 60 h and 180 h (Table 2) depending on temperature. Experiments at T>800°C were terminated using a drop-quench device (Di Carlo et al., 2006) which allows to reach a quench rate > 100°C s^{-1}. The transient increase in total pressure during the drop-quench was taken as evidence that the sample holder had successfully fallen into the bottom cold part of the vessel. Low temperature experiment (T≤800°C) were terminated by switching off the power supply while maintaining the experimental pressure at the target value until about 300°C. After the experiment, the capsules were weighted to check for leaks and opened: some pieces of run products were mounted in epoxy resin and polished for SEM-EDS phase identification and EMP analyses.

fH_2, fO_2 and water content in the experimental charges

The fO_2 recorded by redox sensors allows obtaining the fH_2 at T-P during the experiment. This fH_2 was calculated from the water dissociation constant K_w ($=f°H_2O/fH_2 * fO_2^{1/2}$) from Robie et al., (1997) using the $f°H_2O$ (fugacity of pure water at P and T of interest, Burnham et al., 1969) and the fO_2 of the sensor. For H_2O-saturated charges (i.e XH_2O=1), the fO_2 is that of the sensor. The fO_2 of each single H_2O-undersaturated charge was calculated using the water dissociation equilibrium, the fH_2 as given by the sensor, and the fH_2O of the charge, which was determined using the relationship: $fH_2O = f°H2O * XH_2O_{in}$ (moles). The fO_2 obtained using such a method ranges from NNO-0.17 to NNO-3.16, the spread reflecting essentially the fO_2 decrease with decreasing XH_2O (e.g., Scaillet et al., 2006, Di Carlo et al., 2010 Cadoux, et al., 2014).

Most charges are characterized by high crystal contents preventing the use of techniques such as FT-IR to determine directly the dissolved water content. Consequently, the water content in all charges was computed using the following approach: we first derived an empirical relationships between $f°H_2O$ and H_2O content (at saturation) in the melt ie, $f°H_2O = a(H_2O\ wt.\%)^b$. To derive the *a* and *b* coefficients, we used the results of a series of water-saturated experiments conducted on the sample GTT and the values found are $a=72.612$ and $b=1.8615$. Then the H_2O_{melt} of each charge was computed from the equation $H_2O_{melt}(wt.\%) = (fH_2O/72.612)^{1/1.8615}$ (obtained by inverting the previous equation between

fH_2O and H_2O_{melt}), where fH_2O is given by using the relationships $fH_2O = f°H2O * XH_2O_{in}$. It is important to note that this procedure is equivalent to assuming ideal behaviour in the H_2O-CO_2 fluid phase so that the values obtained must be considered as maximum dissolved water contents. All results are listed in Table 2.

ANALYTICAL TECHNIQUES

A total of 68 charges were observed by SEM-EDS (Cambridge Leo 440 at University of Palermo and Tescan Mira 3, XMU at ISTO-BRGM Orleans joint facility) for preliminary phase identification and textural analysis. Experimental phases and glasses were analysed by electron microprobe (CAMECA SX-Five at ISTO) using an acceleration voltage of 15 kV, sample current 6 nA and counting time of 10 s on peak and background for all elements; Na and K were analysed first and a ZAF correction was applied. Co-Pd-O solid sensors were analysed at 20 kV and 20 nA, with 10 s on each peak and 5 s on background. Mineral phases were analysed with a focused beam while glasses were analysed with 10x10, 5x5 and 2x2 μm defocused beams as well as with a focused beam. Minerals and glass compositions of the natural rocks were determined using the same analytical conditions.

In our experimental glasses Na was affected by migration under the microprobe beam. (e.g., Hanson et al., 1996, Spray & Rae 1995 Morgan & London 1996, 2005). The local heating accompanied by the flux of beam energy is the most important factor in controlling the Na mobility, which becomes severe in hydrous glasses and peralkaline composition, where some fraction of Na forms a terminal species on non-bringing O atoms associated with Si (Mysen 1983; McMillan & Wolf 1995; Morgan & London 2005). As shown by Morgan & London 2005, using a current density close to 0,006 nA/μm^2 the Na loss is lower than 2 % in hydrous haplogranitic glass. For our analytical conditions, a current density close to 0,006 nA/μm^2 corresponds to a 20x20μm defocused beam which was inappropriate for most of the experimental charges. Hence, in order to obtain reliable data on Na concentration of our experimental glasses, we calibrated the beam size effect (i.e the current density) using different hydrous glasses standard prepared from the starting material.

ATTAINMENT OF EQUILIBRIUM

The experimental strategy adopted in this work is well known for favouring crystal nucleation in aluminosilicates glasses (e.g., Clemens &Wall, 1981; Pichavant 1987) as well

as the attainment of crystal-liquid equilibrium on laboratory time-scales (Pichavant et al., 2007). Previous works performed on haplogranite compositions (equivalent to high-silica rhyolites), have shown that crystal nucleation is promoted if a fine-grained dry glass is used as starting material, as in our case. Our compositions are less silicic than the haplogranite one and richer in alkali elements. Both factors imply a lower melt viscosity and consequently component diffusivities significantly higher than in high-silica rhyolites for which crystal-liquid equilibrium has been demonstrated (e.g., Scaillet et al., 1995).

As evidenced in other experimental works on intermediate compositions (e.g., Martel et al., 1999), when drop-quench failed our compositions ended up producing abundant quench minerals showing that activation energy for crystal nucleation was not insurmountable. More specifically, the experiments from this study are of crystallization-type and the condition of near-equilibrium crystallization reached in the experimental products is suggested by several observations, in particular: (i) the euhedral shape of the crystals; (ii) the homogeneous distribution of phases within the charges; (iii) low residuals of mass-balance calculations; (iv) the fact that crystal abundances and compositions vary regularly as function of T and H_2O_{melt}. Altogether, this suggests that run durations were long enough (>60 h) to ensure close attainment of crystal-melt equilibrium, in agreement with previous work on broadly similar intermediate compositions (e.g., Martel et al, 1999; Scaillet & Evans, 1999).

IRON LOSS TO THE CAPSULE MATERIAL

Iron loss to the capsule material is a well known problem with Pt and Au_{80}-Pd_{20} containers (Green & Ringwood 1967), but is strongly minimised when Au capsules are used (e.g., Sisson & Grove, 1993). In our experiments we did not observe large iron-loss, except in charges GT R9-3, GT R9-4 which were run at 950°C and in which estimated FeO loss ranges between 33% and 40%. In other charges ran at the same temperature and similar fO_2 no iron loss was observed.

EXPERIMENTAL RESUTS

General observations

Our crystallization experiments show textural features similar to those observed in

several crystallization experiments carried out at similar temperatures on intermediate to felsic compositions (e.g Scaillet & Evans 1999; Martel et al., 1999; Cadoux et al., 2014). Run products include mineral phases, glass and vesicles. Crystals have euhedral to sub-euhedral shapes and generally, at T>900°C their size ranges between 10 and 15 μm whereas at lower temperature they rarely exceeds 10 μm (Fig. 2). The mineral phases identified are clinopyroxene, olivine, feldspar, Ti-magnetite, ilmenite and quartz (the latter only in charge #GTR3-7). Glass was present in all charges except #GTR3-7. In successfully drop-quenched runs, no evidence of quench textures was found confirming that cooling rates were fast enough to prevent quench crystallisation. Overall, crystallization experiments reproduce the natural phase assemblage observed in the targeted rocks.

Mineral and glass analyses were used in mass-balance calculations (Albarède 1995) in order to obtain phase proportions for each charge (Table 2). Phase compositions are reported in Tables 3-7. Square residuals of mass-balance calculations are generally < 1 suggesting that: (i) no major phases were overlooked, (ii) the Na contents of experimental glasses have been correctly evaluated and (iii) the iron loss to the capsule container was negligible. The relationships between mineral phases are shown in two projections of direct petrologic use: T-H_2O_{melt} sections (Fig 5) allow constraining the cooling history of trachytic magma whereas isothermal P-H_2O_{melt} sections (Fig. 6) show the effect of decreasing P and H_2O_{melt} on crystallization during magma ascent.

The experiments produced homogeneous phases and variations of the main intensive variables T, XH_2O, fO_2 are well displayed in the compositions of solid-solution phases. For example, small changes in fH_2O (i.e H_2O_{melt}) produce variations in fO_2 that affect all iron-bearing minerals (i.e clinopyroxene, olivine and oxides). Microprobe analyses of alkali feldspar were difficult to achieve due to the poor contrast in back-scattered (BSE) electron images with residual glasses. Moreover alkali feldspars often present small oxides inclusions, which increase their iron-content. Some iron-rich analyses were recalculated assuming a maximum iron content of 1.5 wt.% and subtracting the average composition of a Ti-magnetite. Ti-magnetite and ilmenite were always small (< 8 μm) and in some cases glass contamination during EMP analyses was inevitable. When glass contamination was reasonably low the glass contribution was calculated out, otherwise Fe-Ti analyses were not taken in account. Similarly, the analysis of residual glasses in some crystal-rich charges was not possible even with a focused beam.

Phase proportions

Phase proportions obtained from mass balance calculations show that the amount of liquid varies from 98 wt.% to less than 20 wt.%, decreasing with degreasing H_2O_{melt} and temperature. Liquidus conditions were attained at 950°C and $H_2O_{melt} \geq 3.5$ wt.% whereas the highest crystal contents (~ 80 wt.%) were obtained at temperatures ≤ 800°C (Fig. 3a). At 750°C and nominally dry condition no glass was detected in the charge so that solidus condition for the trachytic magma is close to this temperature (a small amount of water can be present because of the reduction of Fe_2O_3 by the hydrogen of the pressure medium, which produces water). In charges where alkali feldspar does not crystallize, the crystal content never exceeds 12 wt.%. Alkali feldspar, whenever present, increases linearly as the melt fraction decreases, becoming rapidly the dominant mineral phase (Fig 3b). At any given temperature and pressure, the amount of alkali feldspar tends to increase with decreasing H_2O_{melt}, but a large increase in alkali feldspar content is also observable when temperature decreases (Fig. 4a, Table 2). Clinopyroxene never exceeds 9 wt.% while the amount of olivine is usually below 4 wt.%. In charges with alkali feldspar, the afs/(cpx+ol) mass ratio ranges between 4 and 15, increasing when H_2O decreases (Fig. 4b). These afs/cpx+ol values for experimental charges broadly bracket the value of the natural rocks, which is around 4-6. Fe-Ti oxides proportion ranges between 2 and 5 wt.%. It is worth noting that the experiments performed on both starting materials show the same phase proportion variation with respect to P-T-H_2O_{melt}. The small compositional difference between the two starting materials affects the crystal contents, and, under similar P-T- H_2O_{melt} conditions, the Post Cinque Denti Caldera (PCD) charges have a sligthly higher crystal load than those of GTT (Fig. 4).

Phase relationships

Phase relationships are shown in Fig. 5-7. The Green Tuff trachytic phase equilibria were established between 750°C-950°C and 0.5 - 1.5 kbar, whereas for the Post Cinque Denti Caldera Trachyte a more narrow range of temperature (850-950°C) and pressure (1.0-1.5 kbar) was explored (Table 2). Isobaric phase relationships as a function of temperature and H_2O_{melt} are shown at 1.5, 1.0, 0.5 kbar for the GT trachytic member and at 1.5 and 1 kbar for the post Cinque Denti Caldera Trachyte, while the effect of decreasing pressure is shown at 950°C (Fig. 7). In both compositions, the stability fields of clinopyroxene, olivine and alkali feldspar are well defined, whereas oxides stability fields are only constrained in broad outline. Magnetite is always present in charges below 950°C at 1.5 kbar while ilmenite

occurs sporadically only in few charges. In the following, we describe in detail the phase relationship for each composition.

Green tuff trachytic member (GTT)

At 1.5 kbar clinopyroxene is the liquidus phase appearing at 950°C and H_2O_{melt} < 4 wt%. At 900°C clinopyroxene becomes stable at H_2O-saturation at all investigated pressures and is followed by olivine then by alkali feldspar when H_2O_{melt} is lower than 3.5 wt.% (Fig. 5a). Ilmenite and Ti-magnetite appear at T < 950°C regardless H_2O_{melt}. Clinopyroxene, olivine and Fe-Ti oxide are the liquidus phases at 1 kbar, 950°C and H_2O_{melt} close to 3 wt.%, followed by alkali feldspar for $H_2O_{melt} \leq 2.5$ wt%. Alkali feldspar stability field expands with decreasing temperature, becoming stable at H_2O-saturation at T≤ 800°C (Fig. 5b) At 0.5 kbar and 950°C olivine replaces pyroxene as the liquidus phase (Fig. 5c) becoming stable at H_2O saturation at 900°C. The isothermal P-H_2O_{melt} projections show that a near-isothermal ascent at either 950°C or 900°C (Fig. 6a-b) promote crystallization and consequently an increase in crystal content with decreasing melt water content.

Post Cinque Denti Caldera trachyte (PCD)

The phase diagrams of the post Cinque Denti Caldera trachyte show some differences with respect to those of the Green Tuff trachytic member (Fig. 7a). At 1.5 kbar, 950°C and H_2O_{melt} < 4 wt.% clinopyroxene is the liquidus phase, being followed by olivine and alkali feldspar at H_2O_{melt} < 3 wt%. Phase relationships at 1.0 kbar (Fig. 7b) show that clinopyroxene is the liquidus phase, as observed in the Green Tuff trachytic member (Fig. 5b), but is followed first by alkali feldspar, then by olivine. Alkali feldspar shows the same behaviour than in the Green tuff trachytic member but it becomes stable at H_2O-saturation at a slightly higher temperature, around 850°C. The effect of pressure is shown in the isothermal section at 950°C (Fig. 7c), also in this case a near isothermal ascent of a trachytic melt would thus promote crystallization of the three principal mineral phases.

Phase compositions

Experimental phase compositions of both compositions studied are similar, and they are reported in Tables 3 and 7. The variation with P-T-fO_2 and H_2O_{melt} of GT experimental phases is shown in Fig. 7-13 and discussed below.

Clinopyroxene

Experimental clinopyroxenes are augites with composition in the range $En_{26-42} - Fs_{17-58} - Wo_{26-42}$ and XFe [=Fe/(Fe+Mg), calculated using FeO_{tot}] ranging between 0.27- 0.75 (Table 3). Compositional trends of experimental clinopyroxenes are governed by variation in T, H_2O_{melt} and fO_2. At a given temperature, the Wo content of clinopyroxene decreases by 10 mol% when H_2O_{melt} decreases by 1.5-2 wt.%, whereas the Fs content shows the opposite behaviour, tending to increase when H_2O_{melt} decreases (Fig. 8a-b). Clinopyroxene becomes progressively richer in Na_2O and FeO_{tot} and poorer in Mg with melt evolution (and hence with decreasing temperature and melt water content) (Fig. 8c-d). At 950°C clinopyroxenes have an XFe ranging between 0.27 and 0.50 while below 850°C, XFe reaches values up 0.75, displaying a good correlation with H_2O_{melt} and fO_2 (Fig 8e).

The average clinopyroxene liquid exchange coefficient Kd^{Fe-Mg} (calculated with FeO=FeOtot) is 0.15±0.06. This value is very similar to that found by Di Carlo et al., (2010) and Scaillet & Macdondald (2003).

The covariation of XFe_{tot} with both temperature, fO_2, pressure and melt water content can be parametrized with the following empirical equation:

$$XFe = -0.0024 \times T(°C) + 0.0002 \times P\ (bar) - 0.2044 \times H_2O_{melt}\ (wt\%) + 0.0718\ NNO + 3.117 \quad (R^2=0.92) \qquad \text{(Eq. 1)}$$

Equation (1) back-calculates the experimental XFe to within ± 0.02. Due to its empirical nature, the use of such an equation, and of all similar equations that follow, is strictly recommended for compositions similar to those of Pantelleria trachytes.

Olivine

The composition of olivine falls in the range Fo_{46} -Fo_{12} [calculated as Mg/(Fe+Mg+Mn)] and it can be classified as ferrohortonolite (Table 4). In the experimental T-P-H_2Omelt-fO_2 range explored, the highest Fo contents were reached at 950°C whereas the lowest Fo content occurs at 750°C and low fO_2 (Fig. 9). Olivine composition, as for clinopyroxene, varies systematically with temperature, H_2O_{melt} and fO_2, becoming richer in iron content with melt evolution. The more Fe-rich olivine occurs in H_2O_{melt}-poor, or low temperature, charges (i.e T<850°C) where alkali feldspar dominates over clinopyroxene and olivine. The composition of experimental olivine is hence strongly affected by H_2O_{melt} and consequently by fO_2. At constant T and P, a difference of 1.5 wt% of H_2O_{melt} (i.e the average variation of water content along a given experimental series) produces a decrease of about 1.5-2 log units in fO_2 (Table 4) which is accompanied by a decrease of fayalitic content of 5-10 mole % (Fig.

9c-d). The average olivine-liquid exchange coefficient Kd^{Fe-Mg}, calculated considering FeO=FeOtot, is 0.37±0.12, which is broadly similar to the K_d of previous works although most of them concern Mg-richer olivine in equilibrium with more mafic melts.

The influence of T, P, H_2O_{melt} and fO_2 on olivine composition has been also parameterised, with the following simple empirical equation:

Fa (mol%)=-0.1973 x T(°C)+0.0134 x P(bar)+1.7118 x DNNO-11.9175 x H_2O_{melt} (wt%)+262.2215 (R^2=0.95) (Eq. 2)

Equation (2) back-calculates the Fa content of experimental olivine to within 1.2 mol %.

Alkali feldspar

Microprobe analyses of alkali feldspar were considered acceptable when the structural formula fulfilled the following criteria: 3.050 < (Si+Al+Fe) < 4.050 and 0.950 < (Ca+Na+K) < 1.050 on a 8 oxygen basis. Analyses of alkali feldspar are listed in Table 5. Alkali feldspar in single charges usually displays a small compositional variation of 1-3 mol % An, which is considered to be within the analytical uncertainty given the problems mentioned before. In our experiments only anorthoclase feldspars crystallized, with compositions in the range $An_{2-10}Ab_{63-68}Or_{20-28}$ (Fig. 10a). In detail, the An content ranges between 10 mol % at 950°C to 2 mol % at 750°C while the Or content ranges between 28 mol% at 750°C and 20 mol% at 950°C, ie similar to those observed in other compositionally similar systems (e.g., Scaillet & Evans 1999; Scaillet & Macdonald 2003). At fixed T, the Or content in alkali feldspar tends to increase with increasing H_2O_{melt} while the An content seems to increase when water content decreases (Fig.10b-e), the latter trend being opposite to that observed in Ca-richer compositions in which An-richer plagioclase crystallizes under H_2O-rich conditions (e.g. Scaillet & Evans, 1999; Martel et al., 1999).

The compositional variation of experimental alkali feldspars has been parameterised with the temperature and water content obtaining the following empirical equation:

An (mol%)= 0.0244 x T (°C)-1.3456xH_2O_{melt} (wt%)-10.2855 R^2=0.86 (Eq. 3)

The equation back-calculate the An content to within 0.6 mol %.

Fe-Ti oxides

In Table 6 are reported the analyses of Fe-Ti oxides after calculating out glass contamination and computing Fe^{3+} from formula constraints. Ti-magnetite is present in almost all charges but its small size prevented its analysis, whereas ilmenite was analysed only in charges

GTR-7-1, GTR-7-2, GT R10-3. For both oxides, analyses having total outside the 96.5% and 102% range were excluded. Contents of FeO_{tot} and TiO_2 in Ti-magnetite range between 63.5-71.1 wt.% and 15.4-26.3 wt.% respectively, while in ilmenite FeOtot varies between 39.7-41.4 wt.% and TiO_2 ranges between 48 and 48.5 wt.%. Contents in Mn and MgO are generally comparable with those of the natural rocks, whereas Al_2O_3 is slightly larger. Ulvospinel content in Ti-magnetite reflects changes in oxygen fugacity, decreasing when fO_2 decreases. Ilmenite and Ti-magnetite usually coexist in charges at water under-saturated conditions. However, reliable analyses of coexisting ilmenite and magnetite were obtained only for three charges (GT R-7-1; GT R-7-2; GTR-10-3, Table 6). In these three charges there is an excellent agreement between the experimental T- fO_2 conditions and those derived from coexisting oxides using the formulation of Sauerzapf et al. (2008); the formulation of Ghiorso & Evans 2008 tends instead to underestimate both temperature and oxygen fugacity (Fig. 11).

Glass

Glass compositions of experimental charges recalculated on anhydrous basis are listed in Table 7 and plotted in Fig. 12. At T ≥ 900°C glass compositions are close to the starting materials, evolving when melt fraction decreases with falling temperature and H_2O_{melt}. Compositional changes with respect to T and H_2O_{melt} are obviously due to the crystallization of clinopyroxene, olivine and alkali feldspar. Residual liquids are marked by a progressive increase in SiO_2 with respect to the starting material (Fig. 12a), SiO_2 content ranging between 65 wt.% and 72.8 wt% in the most crystallized charges. In near-liquidus charges, crystallization of clinopyroxene, olivine and Fe-Ti oxides, produces a decrease in FeO_{tot} and a slight increase in Al_2O_3. The decrease of temperature and H_2O_{melt} promotes the massive crystallization of alkali feldspar causing a decrease in Al_2O_3 content, which drops from 15.7 wt% in near liquidus charges down to 11.8 wt% in crystal-rich charges (Fig. 12b). In contrast, the FeO_{tot} content, after a first decrease to 2.3 wt.%, increases up to 4.7 wt.% in some highly crystallized charges. A similar behaviour is also observable for the TiO_2 content, whereas other major elements (MnO, MgO, CaO) tend to decrease with crystallisation (Fig 12d-f). Both Na_2O and K_2O tend to remain roughly constant with Na_2O around 5.5-6 wt% and K_2O at 3.8-4.4 wt%. Variations in peralkalinity index (Fig. 12c) are thus primarily related to variations in Al_2O_3 content: when melt fraction decreases (i.e at low temperature and low H_2O_{melt}) Al_2O_3 tends to decrease and the peralkalinity index increases up to 1.21 with respect to that of the starting material (0.98)

DISCUSSION

Comparison with other intermediate magmas

Intermediate magmas are characterized by variable silica contents, at 62-69 wt.% SiO_2. Dacitic and trachytic magmas have similar SiO_2 and Al_2O_3 contents but they differ in other major elements, in particular alkalies and MgO, CaO, FeO_{tot} contents. These apparently small differences influence notably the stability of mineral phases. The range of temperature explored in our study is similar to that investigated to constrain phase relationships of broadly similar trachytic magmas (Martel et al, 2013) or common dacitic magmas, such as Pinatubo (Scaillet & Evans 1999), San Pedro (Costa et al., 2004) and Fish Canyon Tuff (Johnson & Rutherford 1989, Caricchi & Blundy 2015a) rocks. In contrast, the range of pressure and fO_2 explored in previous studies both tend to be higher, around 2-3 kbar and above the NNO buffer. Yet the liquidus temperature for dacitic magmas is estimated to be around 900-950°C for water content between 4-6 wt%, similar to our findings.

In dacitic magmas (Pinatubo, San Pedro and Fish Canyon tuff dacite) the falling temperature from 950°C (near liquidus conditions) to 800°C at H_2O_{melt} close to saturation (~ 7 wt% at 2 kbar) increases progressively the crystal content up to 60 wt%. In our run products, for a similar decrease of temperature at H_2O saturation (~4 wt% at 1 kbar), the crystal content remains broadly constant (and low) until 850°C (0-10 wt%) but it rapidly increases up to 75 wt% at temperature ≤ 800°C.

A similar behaviour is also observed in the experiments of Martel et al., (2013) wherein the crystal content increases over the 50 wt% only at T≤ 750°C and water saturation. At 900°C and 3 wt% H_2O_{melt} (i.e undersaturated conditions) dacitic charges (Scaillet & Evans 1999; Costa et al., 2004) have crystal content slightly higher than 50 wt% whereas trachytic charges held at the same conditions have crystal content close to the 30 wt%. However when the temperature decreases to 850°C both compositions end up with a crystal content ≥ 60 wt%. Decreasing further the temperature to 800°C, the dacite gets close to its solidus (Scaillet & Evans 1999) whereas for our trachyte at the same temperature and similar water content a residual liquid is still present in relatively large amount. Such a difference in melt fraction between metaluminous and peralkaline magmas has been also found for rhyolites (Scaillet & Macdonald 2001, 2006; Di Carlo et al., 2010). The lower solidus

temperature of peralkaline systems suggests that they may survive (as molten bodies) longer times in the cold upper crust relative to those metaluminous.

As regard mineral phases, trachyte and dacite compositions present remarkable differences. The Pinatubo, San Pedro and Fish Canyon tuff dacites all crystallize plagioclase, clinopyroxene and magnetite as near-liquidus phases. In contrast, in trachytes alkali feldspar is the only tectosilicate mineral phase (except for quartz crystallizing at near solidus condition). The absence of plagioclase in trachyte can be attributed to its lower CaO content (~2 wt.%) compared to that of dacitic magmas (~5 wt.%). This has been already highlighted by the experiments of Martel et al. (2013) wherein small variation in CaO content of trachytic starting rocks affects plagioclase stability. The presence of alkali feldspar in dacitic magmas has been reported only at high degree of melt evolution (i.e low temperature and low melt water content) (Scaillet & Evans 1999; Caricchi & Blundy 2015a). In our run products, clinopyroxene is the liquidus phase and is stable all over the temperature range investigated. However, in dacite magmas clinopyroxene is stable only at T≥ 800°C (Scaillet & Evans, 1999; Costa et al., 2004; Caricchi & Blundy 2015) whereas this phase persists below 800°C in trachytes (Martel et al., 2013). Clinopyroxene lower stability maybe related to the MgO/FeO_{tot} of the starting material, increasing when MgO/FeO increases. In trachytes sensu latu (this work and Martel et al., 2013) this ratio is much lower compared to that of common dacitic magmas, and clinopyroxene is present over all the temperature range investigated even if, in detail, small variations in CaO and alkalis can affect the stability of clinopyroxene (Martel et al., 2013). The MgO and FeO_{tot} contents, and perhaps pressure, control also the stability of othopyroxene, which has a large stability field in dacites in particular in those with higher MgO/FeO_{tot} ratio such as the Pinatubo dacite, while othopyroxene is conspicuously absent in trachytes.

The high FeO (and low MgO) content in Pantelleria trachytes is highlighted by the occurrence of fayalitic olivine, a mineral phase common only in high-Fe intermediate and felsic magmas (i.e in Iceland trachyte, Selbek & Tronnes, (2007) and Yellowstone rhyolite, Almeev et al., (2012)). This in large part reflects the effect of low fO_2, that promotes Fe^{2+} over Fe^{3+}, hence stabilises olivine, which accommodates only Fe^{2+}, in lieu of pyroxenes. Considering now the hydrous phases, in our run products as well as in the natural rocks, neither biotite nor amphibole (either calcic or sodic) have been detected. In contrast, biotite in dacitic (e.g., Costa et al., 2004) and other more aluminous (and iron-poorer) trachytic (Martel et al., 2013) melts is stable at T< 875°C, depending in particular on potassium content. We suggest that the lack of biotite in our experiments is primarily due to the

peralkaline nature of the residual liquid, though biotite has been shown to crystallise in comendites, but only at very low temperature (< 700°C, Scaillet & Macdonald, 2001). As regard amphibole, the relative CaO-rich character of the bulk compositions together with the high-pressure conditions (P≥ 2 kbar), allow stabilizing hornblende in dacititic magmas as well as in the trachytes of Martel et al. (2013). In the latter, however, Ca-amphibole crystallised only in trachytes with at least 2 wt% CaO. The low-pressure conditions (P≤ 1.5 kbar) investigated in this study are in addition more favourable for the crystallization of clinopyroxene, which, in dacitic magmas replaces amphibole at low pressure (Scaillet et al, 2016). The above comparison serves primarily to illustrate how small differences in major element contents such as CaO and FeO, along with different redox conditions, influence the stability of the main mineral phases characterizing intermediate magmas (see also Cadoux et al., 2014).

Pre-eruption conditions of trachytic magmas at Pantelleria

We now turn to the pre-eruptive conditions of trachytic magmas at Pantelleria Island, combining the results of phase equilibrium experiments with petrological data. The mineral assemblage of both samples is well reproduced in the P-T-H_2O_{melt}-fO_2 range investigated. However, the large coexistence field of clinopyroxene, olivine and alkali feldspar requires other considerations to identify at which conditions phase proportions and chemical compositions similar to those observed in natural rocks can be reproduced. As mentioned above, White et al., 2009 (using QUILF) calculated for the metaluminous trachytes a temperature range from 858°C to 922°C at an fO_2 close to FMQ. In detail, for the Green Tuff trachytic member they found a temperature of 904°C and fO_2 around FMQ-1. Considering crystals content and phase proportions (Fig.13) only the charges at 900-950°C and H_2O_{melt} between 1.5 wt% and 3.5 wt% have crystal contents comparable to that of the natural rock. Run products at T≥ 900°C or T≤ 850°C with H_2O_{melt} close to saturation have crystals content either too low (T≥ 900°C) or too high (T≤ 850°C) to match those of the natural rocks. This is strongly dependent on the alkali feldspar behaviour, which at T≥ 900°C crystallizes at H_2O_{melt}-poor conditions (i.e H_2O_{melt}≤ 3wt.%) while at T< 850°C it joins the crystallization sequence close or at H_2O-saturation (Fig. 6a, b) causing a large increase in crystal content (Fig 3a).

Additional constraints on pre-eruptive conditions are provided by considering the effect of intensive variables on mineral chemistry. Besides P-T-H_2O_{melt}, fO_2 changes arising from fH_2O melt variations, also affect the compositions of the experimental mineral phases.

Clinopyroxene and olivine compositionally similar to that of the natural trachyte were reproduced in the temperature range 850°-950°C, over a fairly wide range melt water content (1.1 wt% and 3 wt%). If we consider a pressure of 1.0 kbar, a temperature of 900°C and oxygen fugacity of around NNO-1.31, as already determined for the natural trachyte (this work, White et al., 2009), using equations 1 and 2 with the composition of natural clinopyroxene and olivine ($XFe_{0,50}$, Fa_{70-72}) allow to retrieve a water content of 2.2-2.5 wt.%. In the same range of temperature and H_2O_{melt}, alkali feldspar joins the crystallization sequence and its composition falls within the compositional range of the less evolved alkali feldspars, typical of the natural trachyte phenocrysts.

Using such a water content with a temperature of 900°C as inputs for equation 3 yields an anortithe content of An_{8-10} similar to that of natural alkali feldspar phenocrysts. Moreover, in the range of temperature 900-950°C, experimental Fe-Ti oxides also present a composition similar to those of the natural rock (Fig. 11).

As regard the storage pressure, the topology of phase diagram (Fig. 6a) relevant to alkali feldspar stability concurs to establish a limit pressure of 1.5 kbar to reproduce the paragenesis found in the trachytic rocks of GT eruption. This is in agreement with geophysical constraints, which suggest the existence of a magma reservoir at a depth of about 4 km at Pantelleria Island. Considering an average crustal density of 2.6 g cm^{-3}, such a depth corresponds to a lithostatic pressure between 1 and 1.5 kbar at best (Mattia et al., 2007). Although we cannot compare the water content inferred from our experimental study with natural data (i.e melt inclusion or groundmass) the topology of phase diagram as well as crystal content and crystal composition suggest an H_2O_{melt} in equilibrium with clinopyroxene, olivine, alkali feldspar and Fe-Ti oxides of 3.5 wt.% maximum. Moreover, our estimates of H_2O_{melt} at near liquidus conditions (~ 4 wt%) compare favourably with the value (~ 4 wt%) calculated via MELTS by White et al., 2009 for the metaluminous trachytes obtained after 64% fractional crystallization of a parental basalt (with a starting H_2O_{melt} of 1.0-1.5 wt%)

To summarise, combining experimental and petrological results constrains the pre-eruptive condition of Pantelleria trachytic magma at 900±50°C, 0.5-1.5 kbar, H_2O_{melt} 1-3 wt.% and an fO_2 in the range NNO-0.5 to NNO-2. These constraints are in agreement with available thermodynamic and geophysical data (White et al., 2009; Mattia et al., 2007). The GT trachytes were erupted during the last caldera forming event at Pantelleria island (Williams et al., 2010) and the pressure inferred from melt inclusions trapped in phenocrysts of the GT pantelleritic basal member (i.e first ejected) is 0.5-0.6 kbar (Lanzo et al., 2013). On the other hand, the Post Cinque Denti Caldera trachytes were erupted immediately after

the Green Tuff eruption and, as suggested by Mahood & Hildreth (1986), they are related to isostatic readjustment in response to the caldera-forming event.

Relation between trachytes and pantellerites

A central issue in the study of magmatism at Pantelleria, as well as in other peralkaline settings, is the origin of the more differentiated rocks (i.e pantellerites and comendites). Crystal fractionation and partial melting or a combination of both processes have been invoked to explain the genesis of pantellerite in different settings (Macdonald 1987; Mungal & Martin 1995; Scaillet & Macdonald 2003). On the basis of major and trace element modelling, most of the recent studies on Pantelleria magmatism (Civetta et al., 1998, White et al., 2009, Neave et., 2012), have argued for a fractional crystallization process to produce pantellerite melts from a metaluminous parental trachyte, although Avanzinelli et al., (2004) proposed an origin by partial melting of gabbroid cumulates .

Civetta et al. (1998), using mass balance calculations, proposed a crystallization as high as 77-82% from a comenditic trachytic magma, with a mineral assemblage dominated by anorthoclase and subordinate aenigmatite, olivine, clinopyroxene or amphibole and apatite. Similarly, by combining mass-balance calculations and thermodynamic modelling White et al. (2009) proposed that pantellerites are produced by 80-85% crystallization of a metaluminous trachyte in the temperature interval 700-940°C, with a mineral assemblage dominated by alkali feldspar, clinopyroxene, Fe-Ti oxides, aenigmatite, and apatite. Neave et al. (2012) proposed a liquid line of descent trachyte-pantellerite through a principal component analysis using natural glasses (i.e melt inclusions and matrix glasses) and whole-rock data. They too come to the conclusion that pantellerite form via the removal of 89 wt.% alkali feldspar (Or_{38}), 5 wt.% clinopyroxene ($En_4Fs_{45}Wo_{35}Ae_{16}$), 6 wt.% aenigmatite and 0·2 wt.% ilmenite of a trachyte magma.

In our study, phases controlling the trends of glass major elements are clinopyroxene, olivine, Fe-Ti oxides and alkali feldspar, as inferred from the above mentioned geochemical modelling. If we first consider phase proportions, a decrease in temperature from 950 to 750 °C at 1 kbar, increases the crystal content up to 85 wt%, alkali feldspar being the dominant phase (25-80 wt.% of solids) while the amount of olivine, clinopyroxene and oxides remain lower than 15 wt.% (Fig.3b). These results are coherent with the paragenesis of the natural trachyte and pantellerite as well as with the geochemical constraints. Moreover, the results of Di Carlo et al. (2010) show that pantelleritic melts crystallize alkali feldspar at

near liquidus conditions, which is consistent with their extraction from a parental melt saturated in alkali feldspar.

Considering now the composition of the experimental minerals, with decreasing temperature and fO_2 clinopyroxene have XFe > 0.75 approaching that of the natural pantellerite (XFe> 0.80), showing also a general Na_2O enrichment (Fig. 8c). The near liquidus (at 800°C NNO-1.87) experimental clinopyroxene of Di Carlo et al. (2010) has an XFe=0.82, which is close to that produced after extensive trachyte crystallization in our experiments. Similarly, the olivine crystallizing at 750°C in trachyte has a fayalitic content (Fa_{83-89}) very similar to that of pantelleritic olivine (Fa_{90}). Finally, alkali feldspars also show an evolutionary trend from anorthoclase to alkali feldspar wherein the anorthitic content is lower than 2 mol%, i.e similar to that of pantelleritic alkali feldspar. Altogether, our results reproduce the expected mineralogical attributes of pantellerites, being also in very good agreement with those of Di Carlo et al., 2010, in which mineral compositions of pantelleritic rocks have been reproduced at temperatures ≤ 750°C and redox conditions at, or below the, FMQ buffer.

As stressed above, the crystallising experimental phases obviously influence the residual glass composition. In particular, the crystallisation of mafic phases leads first to a decrease of melt iron content along with an increase in Al_2O_3 with respect to the starting material, lying mostly within the comenditic trachyte field in the projection scheme of Macdonald (1974) (Fig. 13b). At temperatures below 850°C, the trend reverses, and liquids of increasing FeO and decreasing Al_2O_3 contents are produced, plotting clearly within the comendite field, and trending toward the pantellerite field where Pantelleria rhyolites occur (Fig. 13b). Although our experimental liquids are not as iron-rich as true pantellerites, production of liquids more enriched in iron is possibly achieved by a slight decrease in fO_2 during the evolution of trachyte to pantellerite stage, which would suppress magnetite from the crystallising assemblage. For trachytes, our data suggest redox conditions akin to magnetite crystallisation (NNO-0.5 to NNO-1.5), while in pantellerites, redox conditions are too low (<NNO-1.5) for this oxide to be stable, as observed in many strongly peralkaline rhyolites (Nicholls & Carmichael 1969). The decrease in Al_2O_3 is primarily driven by the massive crystallisation of alkali feldspar, whose amount reaches up to 80 wt% of the crystallizing assemblage at temperatures below 850°C. As a result, the peralkalinity index of the residual liquid progressively increases as crystallisation proceeds, from 0.98 to 1.21 (Fig. 12c, Table 7), while the Al_2O_3 melt content decreases from 14.8 wt.% to 11.8 wt.% (Fig.

12b). This demonstrates unambiguously, and for the first time, that peralkaline felsic derivatives can be produced from a metaluminous, more mafic, parental magma crystallizing at low pressure. The fact that both trachyte and pantellerite magmas record similar pressure of magma storage is an additional evidence of their parent-daughter relationships. In terms of volatile content, it is worth noting that both trachyte and pantellerite magmas have significant amounts of dissolved water, the estimated H_2O_{melt} for trachyte being slightly lower than that of Pantellerite. This reinforces a genetic link between the two magmas but also presumably reflects the shallow conditions of magma storage, which constrain melt water content of silicate melts close to water saturation conditions.

CONCLUSIONS

Our experiments on trachytes from Pantelleria island extend and complement our previous experimental study on Pantelleria peralkaline silicic magmatism (Di Carlo et al., 2010). Phase equilibrium experiments on trachytic sample of Green Tuff eruption and Post Cinque Denti Caldera have allowed us to constrain the pre-eruptive conditions of trachytic magmas at Pantelleria that bridge the compositional gap with basalts. The inferred conditions of storage are all the more similar, save for the higher temperature that reflects the maficity of the magma, to those inferred for the more silicic members, in particular for pressure. The last fact shows that fractionation leading to peralkaline felsic derivatives is a process that occurs at shallow crustal level (e.g., Mahood, 1984). To the best of our knowledge, this is the first time that the transition between a metaluminous magma and a peralkaline derivative is experimentally achieved at low pressure, confirming previous suggestions regarding the origin of peralkaline rhyolite by low-pressure fractional crystallization of a metaluminous, more mafic, parental magma (ie, Civetta et al., 1988), though they do not rule out other mechanisms.

Of particular interest in the context of volcanic hazard assessment is the large amount of crystallisation which is required to produce a peralkaline rhyolite, when starting from a transitional parental basalt. Given that about 50-70 wt% crystallisation is needed to produce a trachytic (intermediate) magma from basalt, and that an additional 80 wt% (at least) crystallisation of such a trachyte is required to produce a comendite-pantellerite, as our results show, it turns out that every single parcel of basalt injected beneath Pantelleria will produce at best 5-10 wt% peralkaline felsic liquid. Hence the production of the voluminous Green Tuff eruption (7 km^3) needs at least 10 times more of non erupted basalt stored at

depth. The construction of a large felsic reservoir via such a mechanism will necessarily require a prolonged time for maturation/cooling of basalt, in addition to feeding rates necessary to supply the mafic parent. Assuming an average basalt feeding rate of 10^{-3} km^3/year (1000 years for every km^3), the time needed to build a 70-100 km^3 basalt body is 70-100 ky, which is about twice the time interval since the Green Tuff eruption. A basalt body 7x10 km of surface area in size would be approximately 1 km thick, and it could cool down by conduction in about 80 ky (estimated using the simple relationships $t=x^2/k$, where t is time in s, x the half thickness of the cooling body in m (ie 500 m) and *k*, heat diffusivity ($=10^{-7}$ s/m^2)). In 40 ky, the amount of accumulated basalt magma could be therefore around 40 km^3. On this basis, assuming that in the meantime the basalt has significantly cooled (ie by 90-95 wt%, or close to its solidus), any pantelleritic reservoir present nowadays beneath Pantelleria is unlikely to exceed more than a few km^3 (about 3 km^3 or a sphere with 0.8 km radius), inasmuch that pantelleritic eruptions have occurred during this period (ie the system has lost some of its felsic derivatives). These estimates are obviously subject to caution owing to the errors attached to input parameters (feeding rates, cooling time, extraction rates of derivative liquids, etc..). Considerations of those is, however, well beyond the scope of our paper, and will require a detailed thermal modelling investigation. Instead, the aim is simply to illustrate that the occurrence of a pantelleritic magma reservoir is a possibility that cannot be excluded for Pantelleria.

Figure captions

Figure 1: (a) Tectonic sketch of the Sicily Channel continental rift zone (modified from Catalano et al., 2009) showing the location of Pantelleria and other volcanic islands (Graham Bank, Linosa) in the rift zone between Sicily and Tunisia. (b) Simplified geological map of Pantelleria Island: the stars mark the sampling site of the starting materials used in the experiments.

Figure 2: Selected scanning electron microscope images of run products obtained in crystallization experiments at (a) 950°C, 1 kbar H_2O_{melt} = 3 wt% and (b) 800°C, 1 kbar and H_2O_{melt}-saturated conditions. ol, olivine; cpx, clinopyroxene; Fe-Ti ox, Fe-Ti oxide; Afs, alkali feldspar; gl, glass.

Figure 3: (a) Variation of crystal and melt proportions with temperature at 1 kbar and XH_2O ($=H_2O/H_2O+CO_2$) =1 for GTT experiments. Note that the increase in crystal content corresponds to the crystallization of alkali feldspar at H_2O-saturation; (b) variation of crystal, alkali feldspar and clinopyroxene (cpx) + olivine (ol) proportions as a function of melt %

Figure 4: (a) Variation of crystal content vs H_2O_{melt}. The arrow indicates the large increase in crystal content when temperature decreases; (b) variation of alkali feldspar / (clinopyroxene + olivine) ratio (wt%) in experimental charges. In both panels diamonds indicate experiments on Green Tuff trachyte (GT) while circles show experiments on Post Cinque Denti Caldera trachyte (PCD); the horizontal grey bar corresponds to the crystal loads of the natural rock.

Figure 5: Phase relationships of the Green Tuff trachyte in T-H_2O_{melt} projections at (a) 1.5 kbar, (b) 1 kbar, and (c) 0.5 kbar, all at fO_2 ~QFM. L, liquid; Cpx, clinopyroxene; Ol, olivine; ox, Fe-Ti oxides; Afs, alkali feldspar; Qz, quartz. The tick on a phase boundary marks the side on which an experimental phase is stable. Dashed lines are estimated phase boundaries.

Figure 6: Phase relationships of the Green Tuff trachyte as a function of pressure and H_2O_{melt} at (a) 950°C, (b) 900°C and at fO_2 ~QFM. L, liquid; Cpx, clinopyroxene; Ol, olivine; ox, Fe-Ti oxides; Afs, alkali feldspar. The grey dashed lines indicate the crystal content (Φ, wt%).

Figure 7: Phase relationships of Post Cinque Denti Caldera trachyte at fO_2 ~QFM as a function of temperature and H_2O_{melt} at (a) 1.5 kbar, (b) 1 kbar, (c) 950°C, and (c) pressure and H_2O_{melt} at 950°C. L, liquid; Cpx, clinopyroxene; Ol, olivine; ox, Fe-Ti oxides; Afs, alkali feldspar. The tick on phase boundary marks the side on which an experimental phase is stable. Dashed lines are estimated phase boundaries. The grey dashed lines indicate the crystal content (Φ, wt%).

Figure 8: Composition of experimental clinopyroxene. (a) Wo and (b) Fs contents in mole % vs H_2O_{melt}. (c) Na vs total iron content (expressed as $XFe=Fe_{tot}/(Fe_{tot}+Mg)$, the arrow showing the direction of decreasing temperature. (d) Mg# vs SiO_2 (wt%) of coexisting

melt (e) Variation of XFe with oxygen fugacity (expressed as ΔNNO) and H_2O_{melt} in the pressure-temperature range investigated. In all panels the grey box represents the natural clinopyroxene composition while in (c) the white box indicates natural clinopyroxene composition in pantellerites.

Figure 9: Composition of experimental olivine. (a) Fa content vs melt fraction. (b) Fa content vs MgO content of coexisting melt. (c) Fa content vs H_2O_{melt}. (d) Fa content vs oxygen fugacity expressed as ΔNNO.

Figure 10: (a) Composition of experimental alkali feldspar plotted onto the classification diagram of Deer et al., 1992. All alkali feldspars fall in the field of anorthoclase. Compositional variation of experimental alkali feldspar with temperature and H_2O_{melt}. (b) An content (mol %) vs temperature. (c) An content vs H_2O_{melt}. (d) Or content (mol%) vs temperature. (e) Or content vs H_2O_{melt}.

Figure 11: Composition of experimental Fe-Ti oxides. (a) Ulvospinel content vs fO2 expressed as ΔNNO. (b) ilmenite content vs oxygen fugacity expressed as ΔNNO. In both projections is also plotted the calculated oxygen fugacity (see text) calculated following the formulation of Sauerzapf et al. (2008) and Ghiorso & Evans 2008, for the given % of ulvospinel or ilmenite components. The grey band corresponds to the composition of the natural Fe-Ti oxides. The vertical bar is the average of standard deviation of experimental oxide analyses; the horizontal bar is the maximum uncertainty on fO_2.

Figure 12: Glass compositions. (a-e) Variation of major and minor oxides of experimental glasses vs either melt fraction (a,b) or SiO_2 (c-f).

Figure 13: (a) Phase relationships at 1 kbar of the Green Tuff trachytic member with superimposed contours (dashed lines) of crystal content (Φ, wt%). (b) MacDonald (1974) diagram [FeO_{tot} vs Al_2O_3 (wt%)] for peralkaline rocks. In the diagram are reported the experiments of this study and for comparison the experiments of Scaillet & MacDonald (2003), Di Carlo et al., (2010) as well as literature data taken from Civetta et al. (1998), Ferla & Meli (2006), Rotolo et al. (2007) and White et al. (2009).

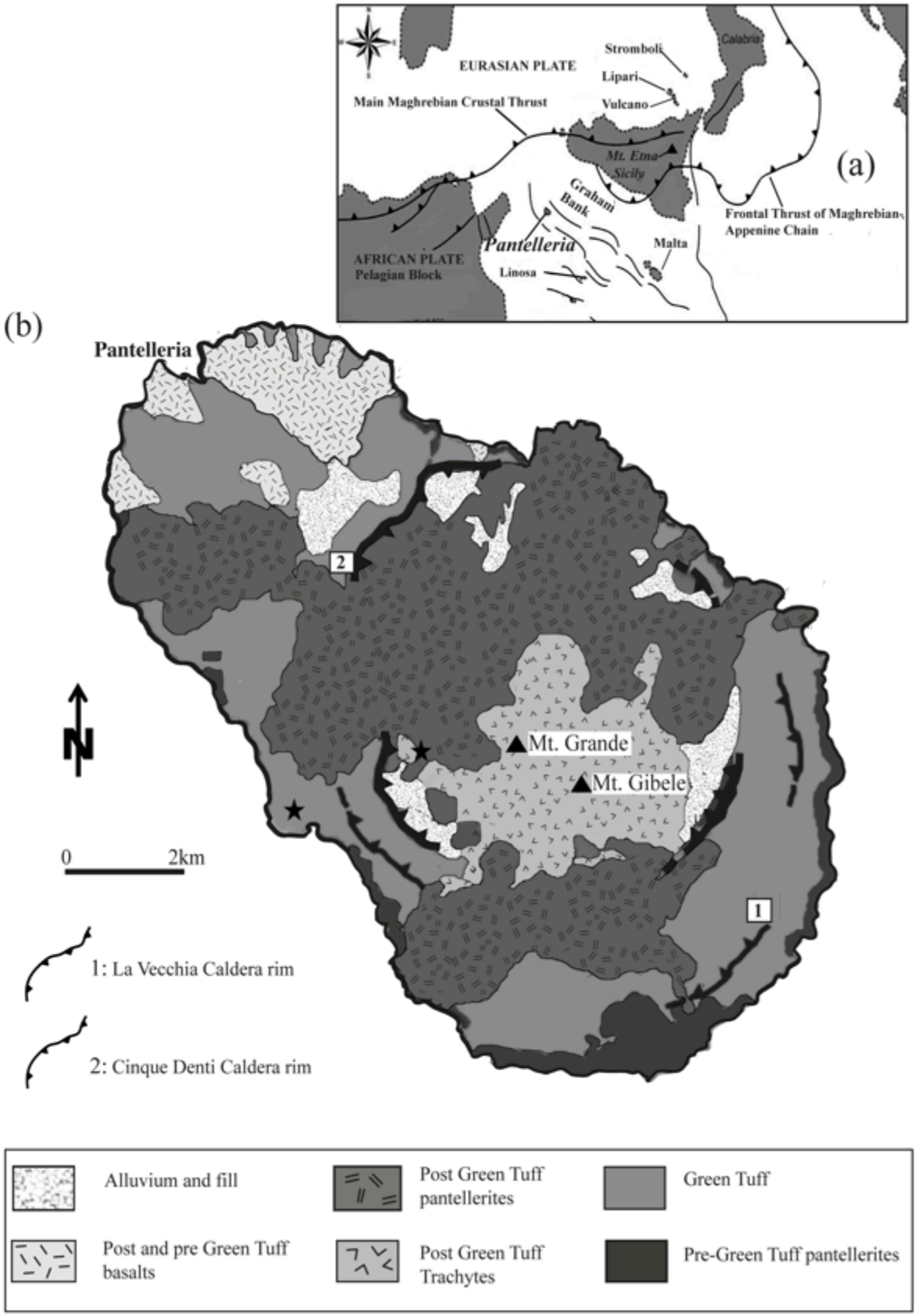
(a)
EURASIAN PLATE
Stromboli
Lipari
Vulcano
Calabria
Main Maghrebian Crustal Thrust
Mt. Etna
Sicily
Graham Bank
Pantelleria
Malta
Linosa
AFRICAN PLATE
Pelagian Block
Frontal Thrust of Maghrebian Appenine Chain
(b)
Pantelleria
2
1
Mt. Grande
Mt. Gibele
N
0
2km
1: La Vecchia Caldera rim
2: Cinque Denti Caldera rim
Alluvium and fill
Post Green Tuff pantellerites
Green Tuff
Post and pre Green Tuff basalts
Post Green Tuff Trachytes
Pre-Green Tuff pantellerites

Fig.1

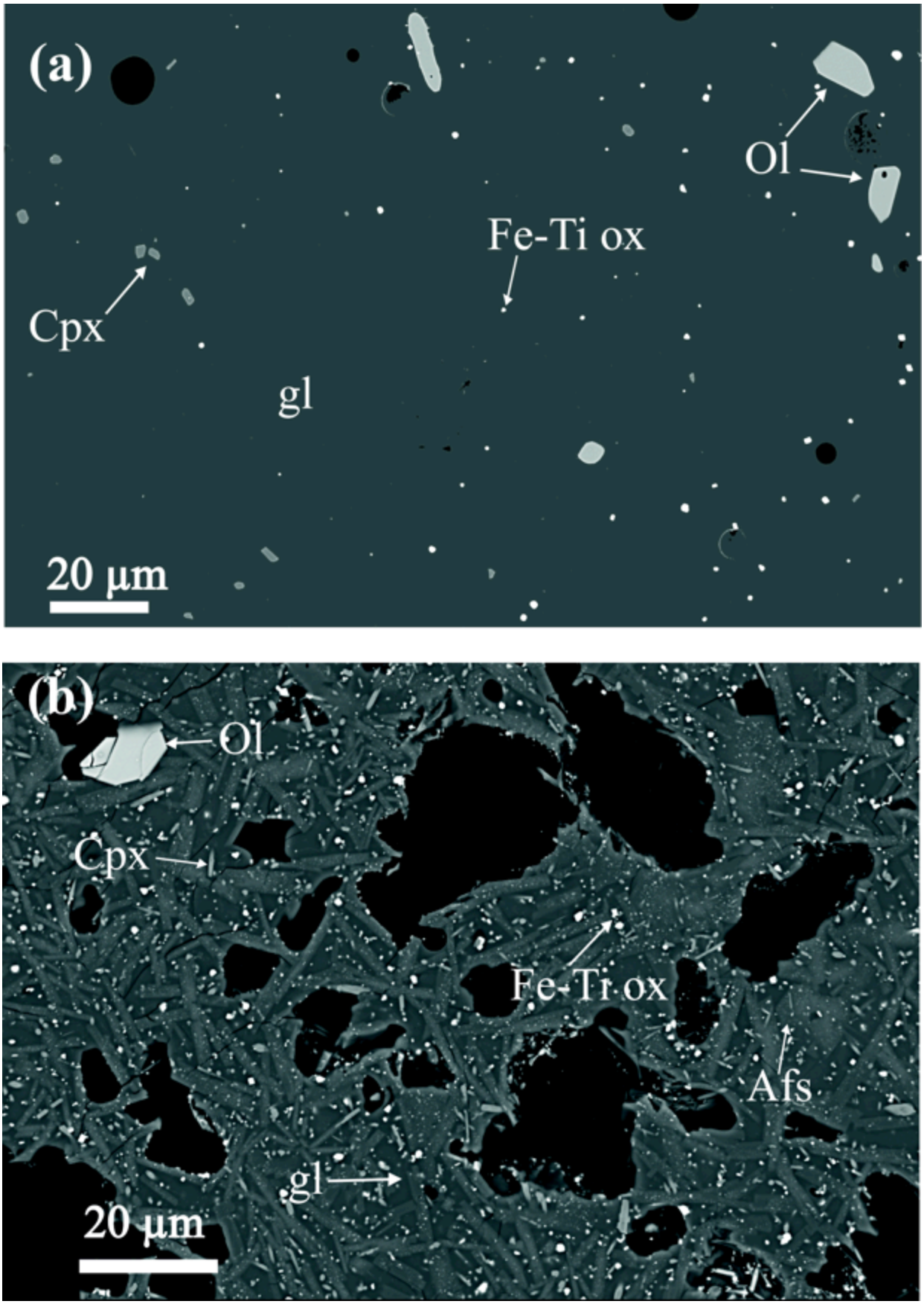

Fig.2

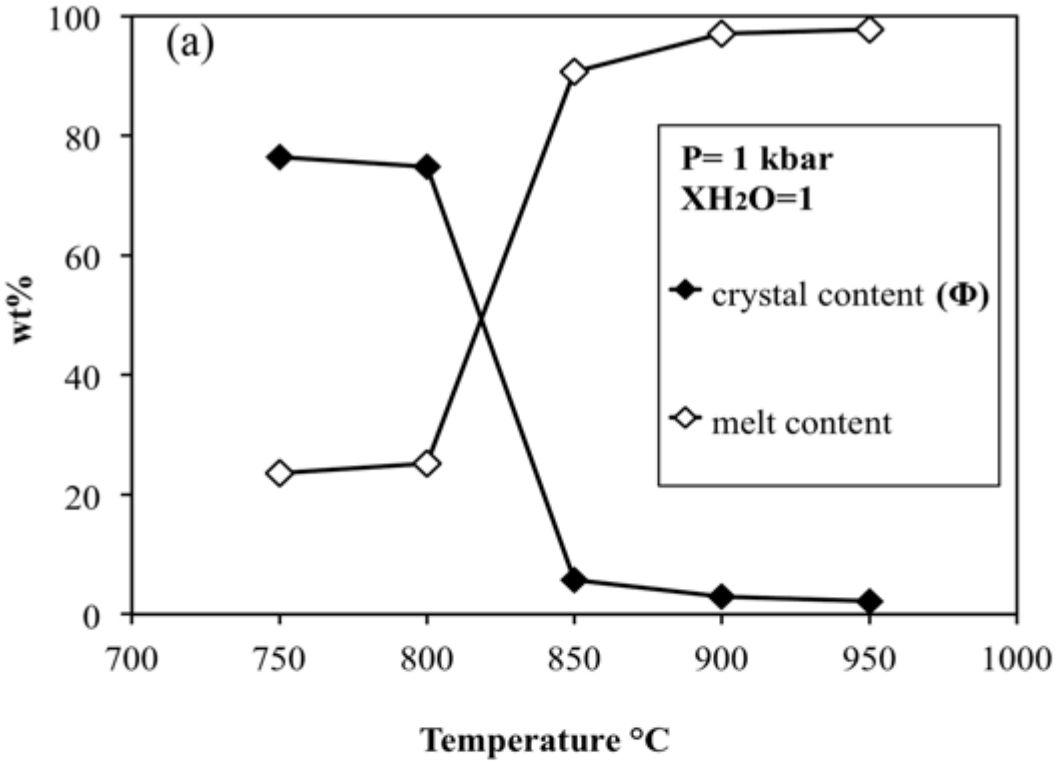
(a)
P= 1 kbar
XH2O=1
crystal content (Φ)
melt content
wt%
Temperature °C
100
80
60
40
20
0
700
750
800
850
900
950
1000

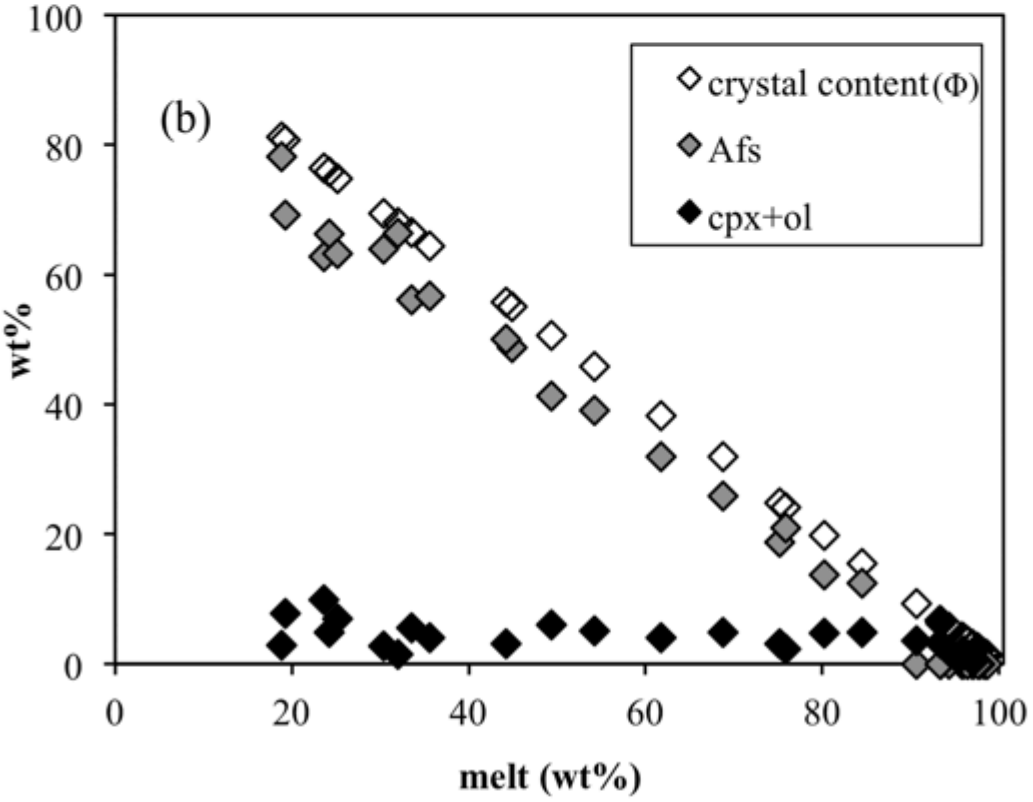
(b)
crystal content (Φ)
Afs
cpx+ol
wt%
melt (wt%)
100
80
60
40
20
0
0
20
40
60
80
100

Fig.3

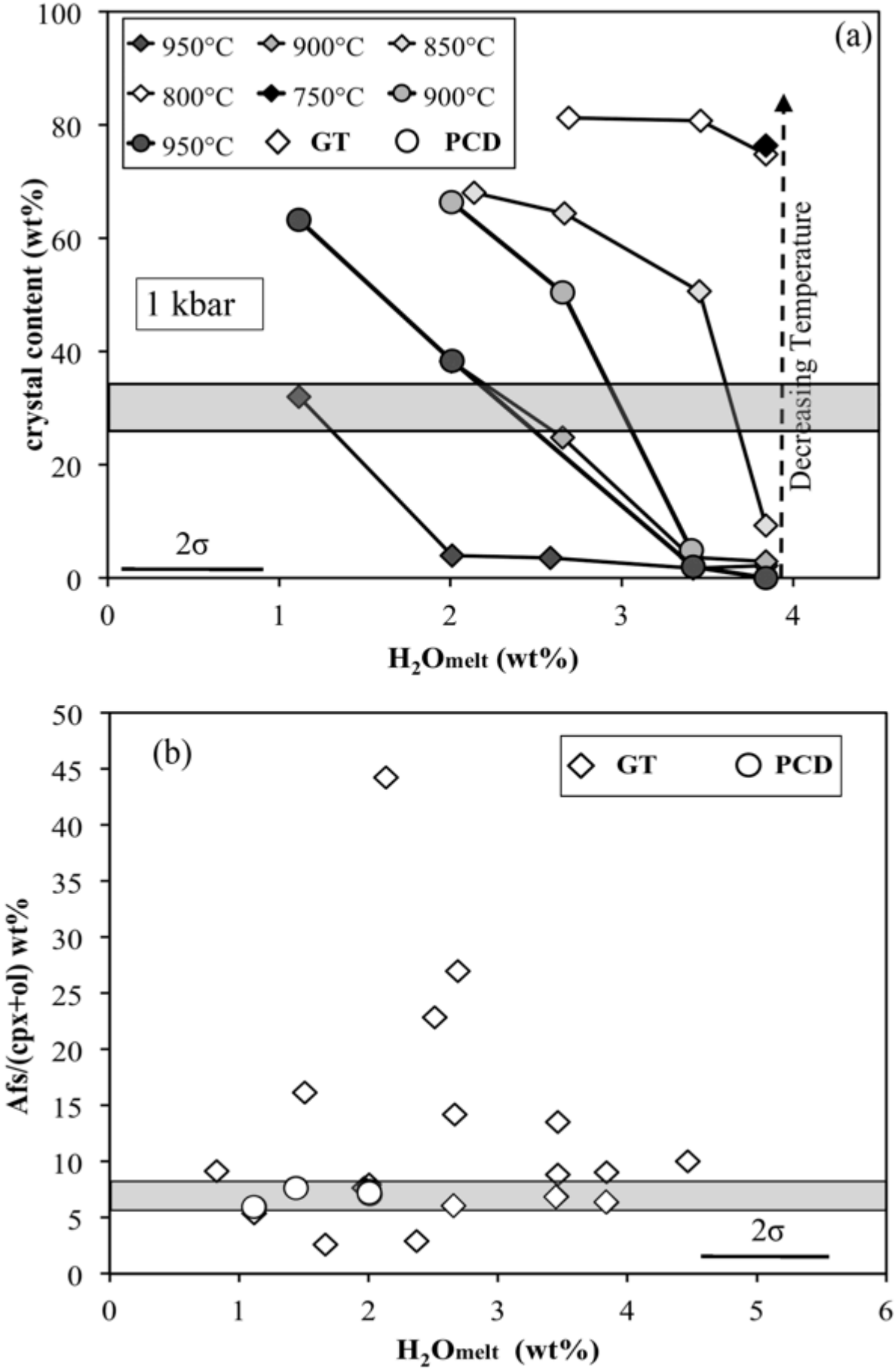
(a)
950°C
900°C
850°C
800°C
750°C
900°C
950°C
GT
PCD
1 kbar
2σ
Decreasing Temperature
crystal content (wt%)
H2Omelt (wt%)
(b)
GT
PCD
2σ
Afs/(cpx+ol) wt%
H2Omelt (wt%)

Fig. 4

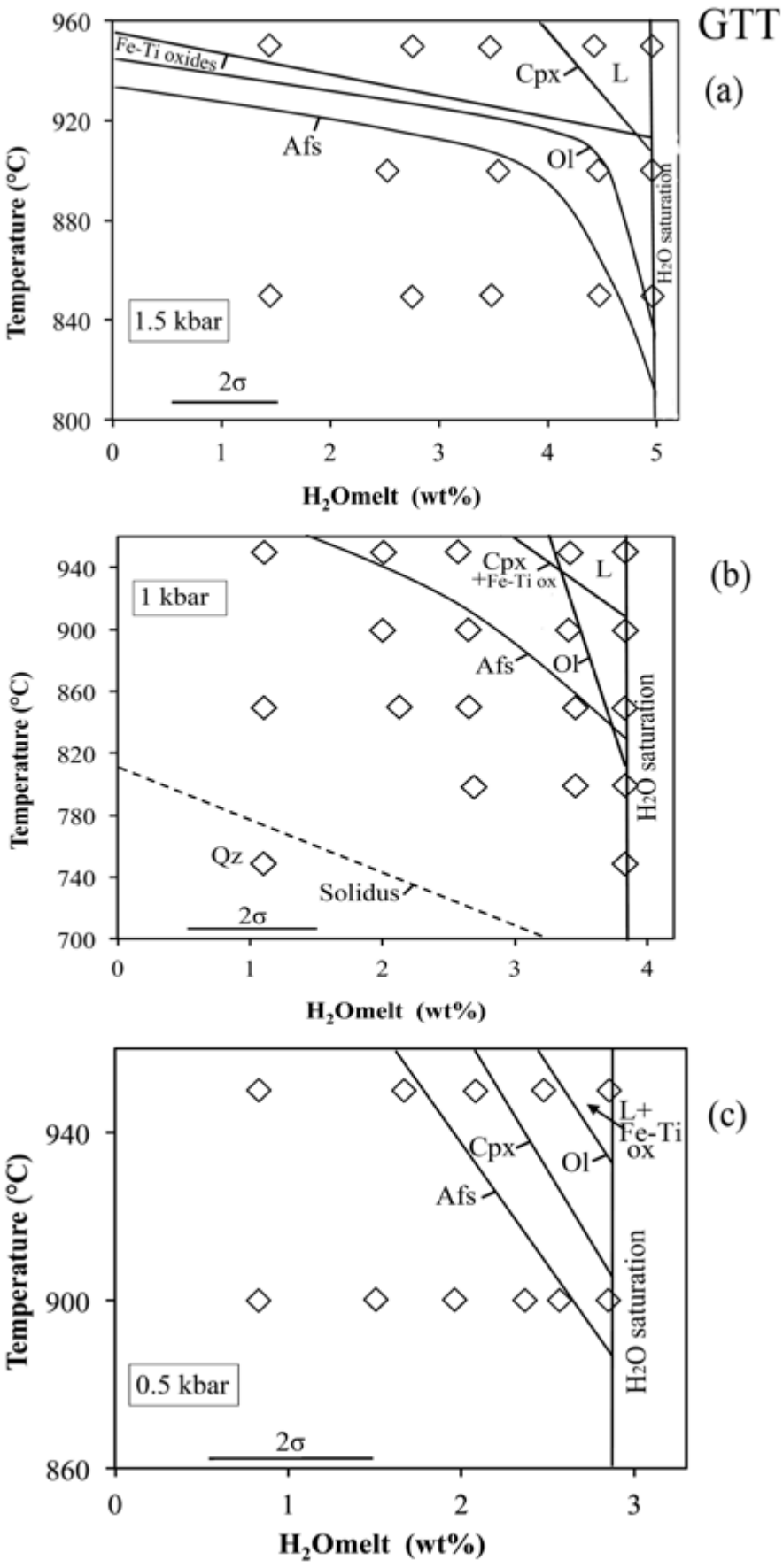
GTT
(a)
Fe-Ti oxides
Cpx
L
Afs
Ol
H2O saturation
1.5 kbar
2σ
Temperature (°C)
H2Omelt (wt%)
(b)
1 kbar
Cpx
+Fe-Ti ox
L
Afs
Ol
H2O saturation
Qz
Solidus
2σ
Temperature (°C)
H2Omelt (wt%)
(c)
L+
Fe-Ti
ox
Cpx
Ol
Afs
H2O saturation
0.5 kbar
2σ
Temperature (°C)
H2Omelt (wt%)

Fig.5

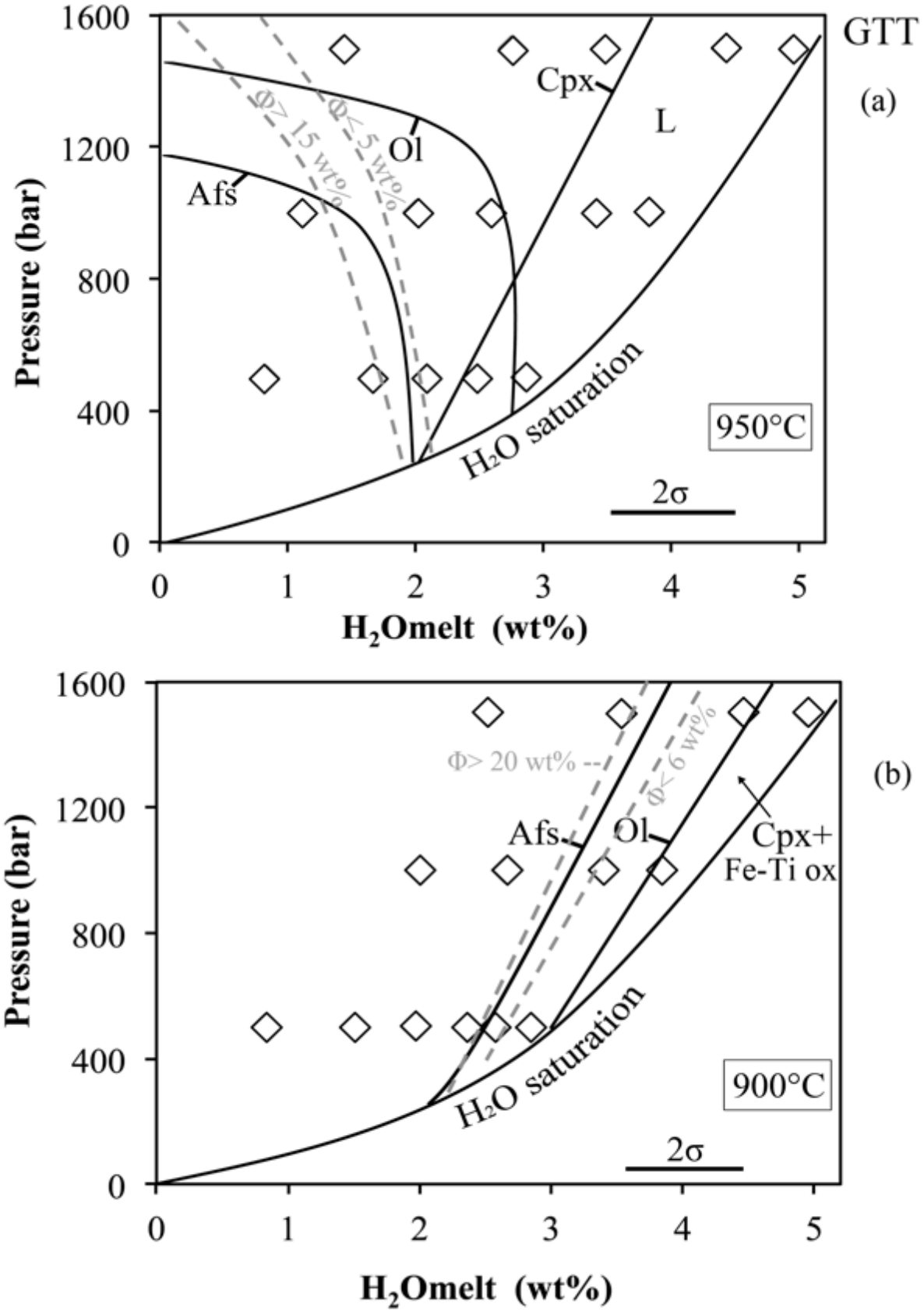
GTT
(a)
Pressure (bar)
H2Omelt (wt%)
Cpx
L
Ol
Afs
Φ> 15 wt%
Φ< 5 wt%
H2O saturation
950°C
2σ
(b)
Φ> 20 wt% --
Φ< 6 wt%
Afs
Ol
Cpx+
Fe-Ti ox
900°C

Fig.6

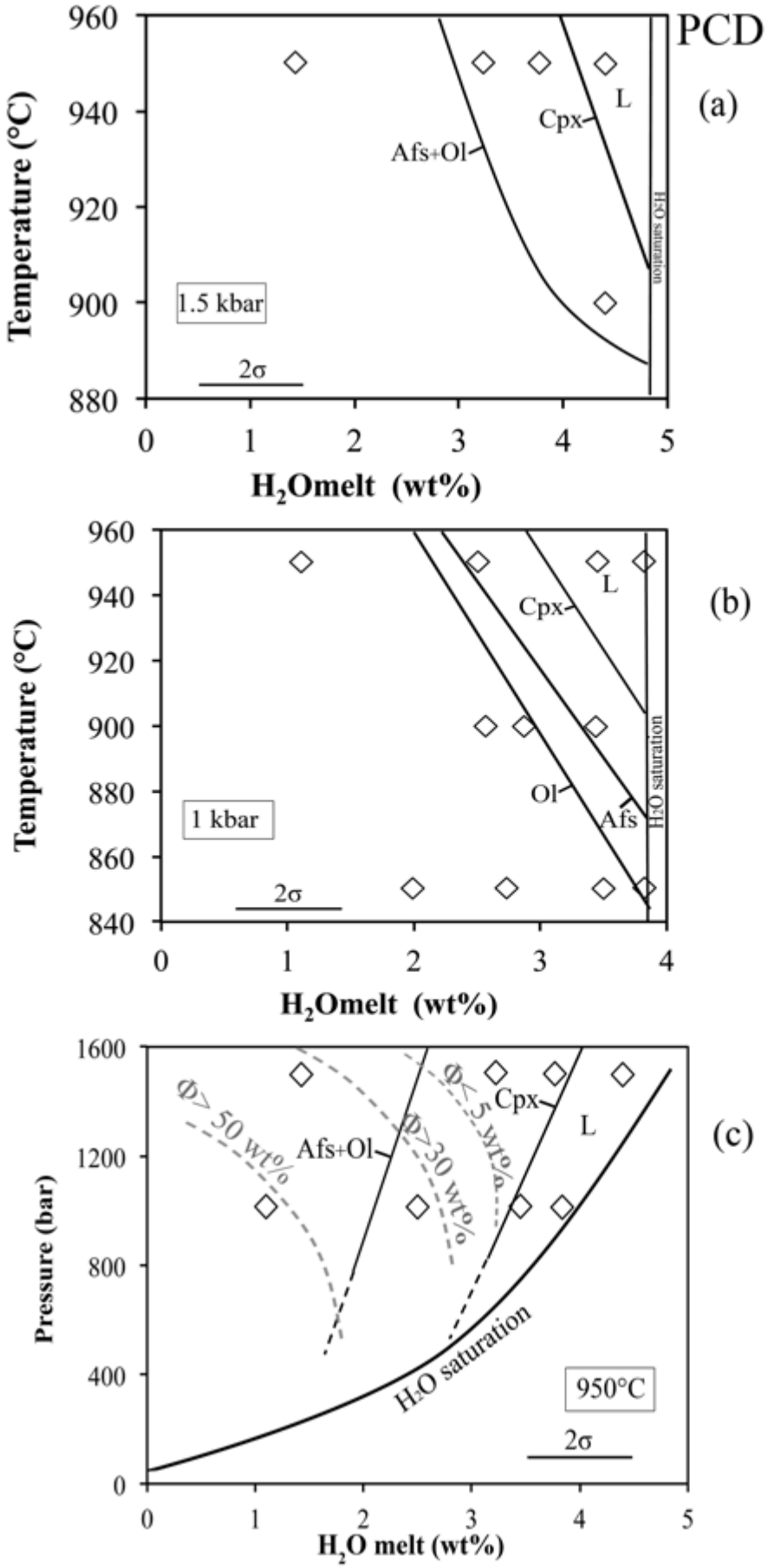
PCD
(a)
Temperature (°C)
960
940
920
900
880
Afs+Ol
Cpx
L
H2O saturation
1.5 kbar
2σ
0
1
2
3
4
5
H2Omelt (wt%)
(b)
Temperature (°C)
960
940
920
900
880
860
840
Cpx
L
Ol
Afs
H2O saturation
1 kbar
2σ
0
1
2
3
4
H2Omelt (wt%)
(c)
Pressure (bar)
1600
1200
800
400
0
Ø> 50 wt%
Afs+Ol
Ø>30 wt%
Ø< 5 wt%
Cpx
L
H2O saturation
950°C
2σ
0
1
2
3
4
5
H2O melt (wt%)

Fig.7

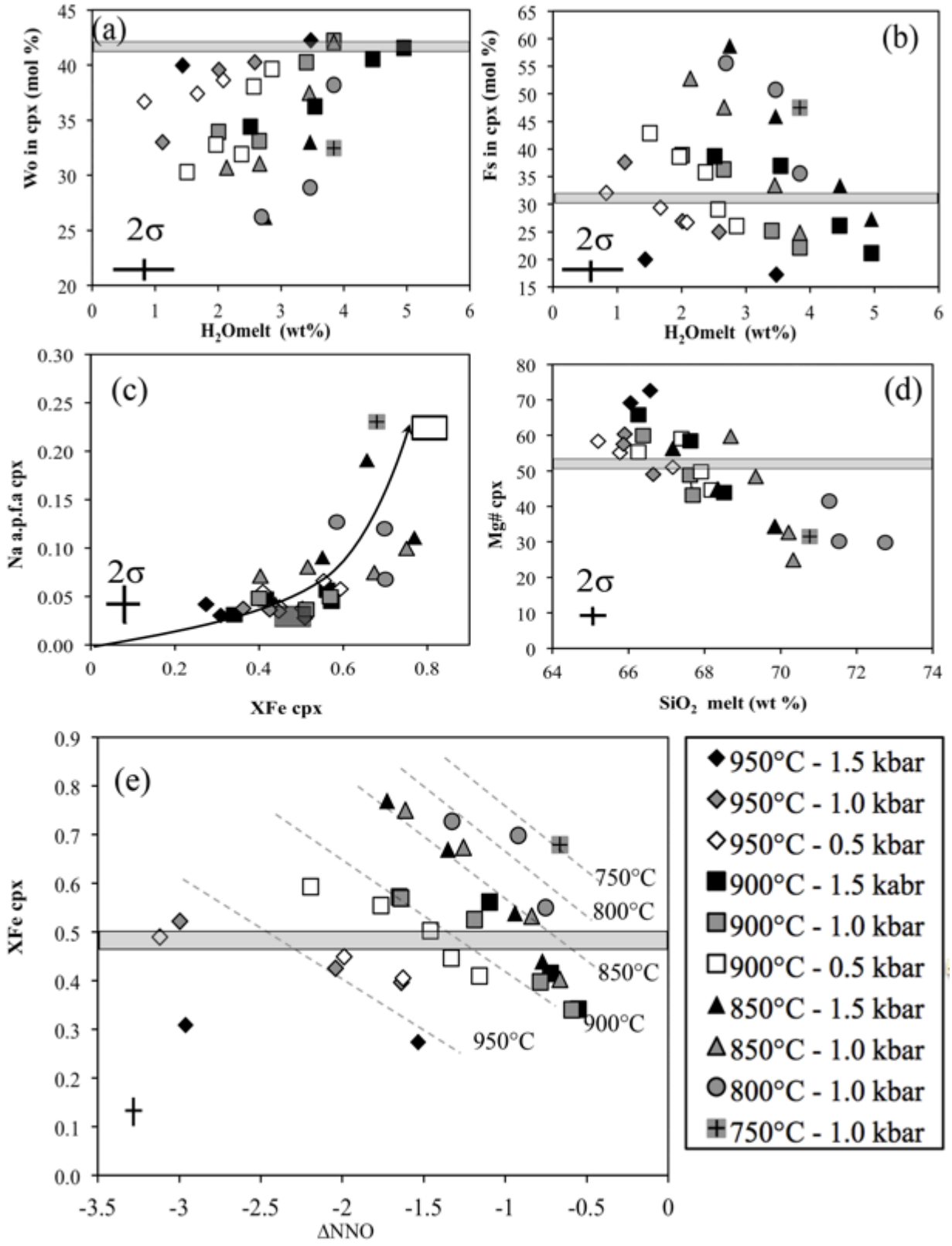
(a)
Wo in cpx (mol %)
H2Omelt (wt%)
2σ
(b)
Fs in cpx (mol %)
H2Omelt (wt%)
2σ
(c)
Na a.p.f.a cpx
XFe cpx
2σ
(d)
Mg# cpx
SiO2 melt (wt %)
2σ
(e)
XFe cpx
ΔNNO
750°C
800°C
850°C
900°C
950°C
950°C - 1.5 kbar
950°C - 1.0 kbar
950°C - 0.5 kbar
900°C - 1.5 kabr
900°C - 1.0 kbar
900°C - 0.5 kbar
850°C - 1.5 kbar
850°C - 1.0 kbar
800°C - 1.0 kbar
750°C - 1.0 kbar

Fig.8

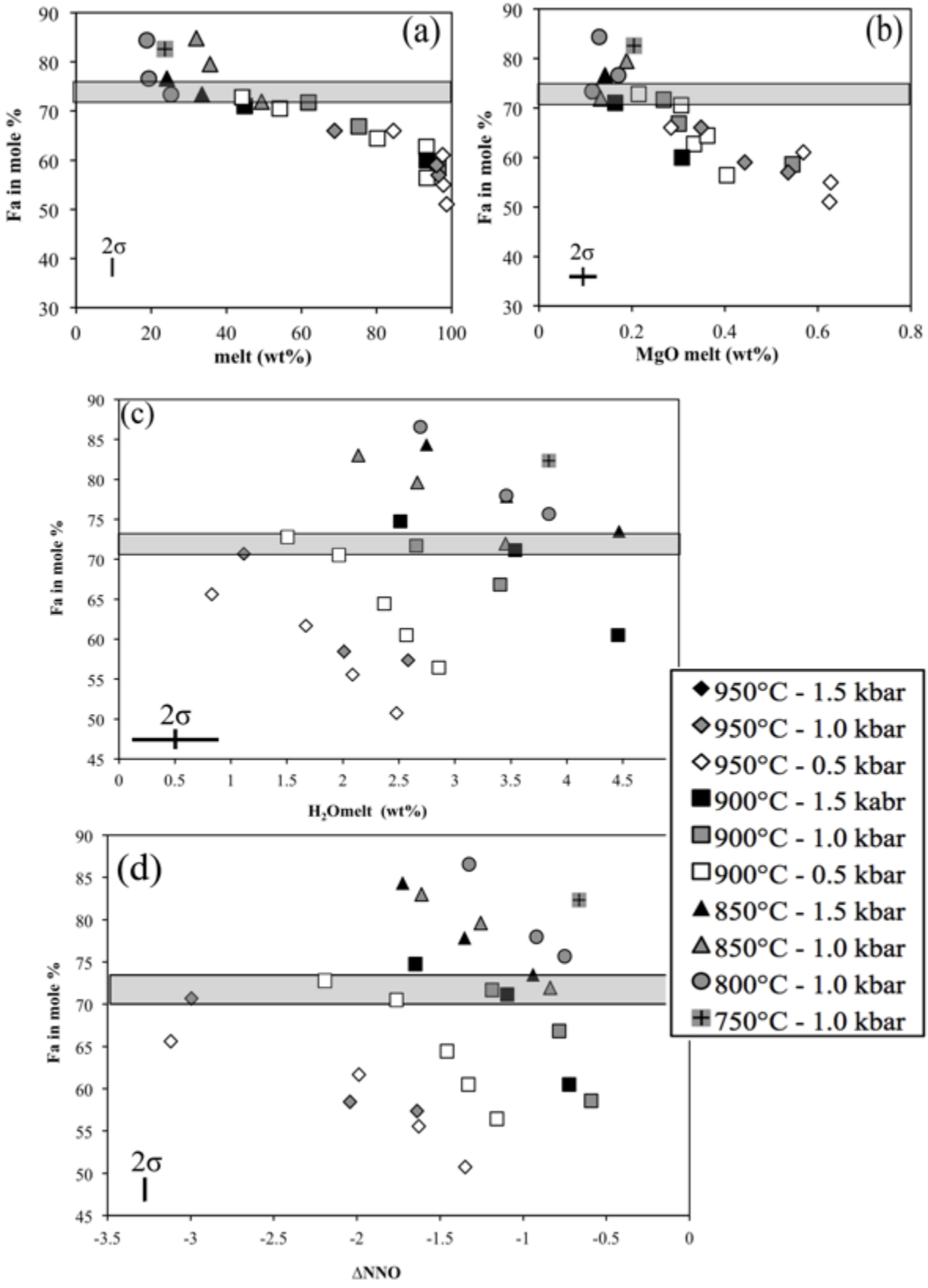
(a)
(b)
(c)
(d)
Fa in mole %
melt (wt%)
MgO melt (wt%)
H2Omelt (wt%)
ΔNNO
2σ
950°C - 1.5 kbar
950°C - 1.0 kbar
950°C - 0.5 kbar
900°C - 1.5 kabr
900°C - 1.0 kbar
900°C - 0.5 kbar
850°C - 1.5 kbar
850°C - 1.0 kbar
800°C - 1.0 kbar
750°C - 1.0 kbar

Fig. 9

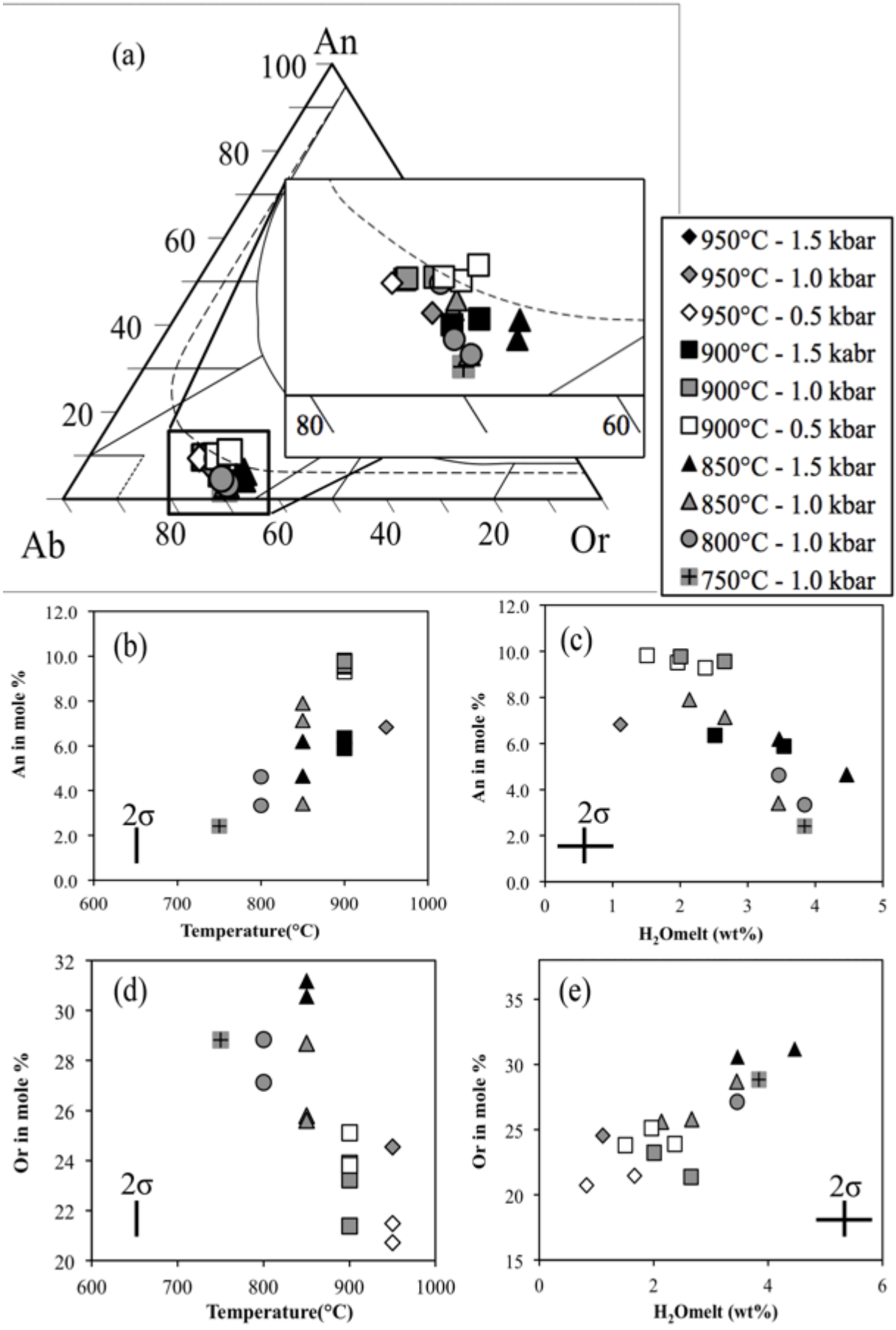
(a)
An
Ab
Or
100
80
60
40
20
80
60
40
20
950°C - 1.5 kbar
950°C - 1.0 kbar
950°C - 0.5 kbar
900°C - 1.5 kabr
900°C - 1.0 kbar
900°C - 0.5 kbar
850°C - 1.5 kbar
850°C - 1.0 kbar
800°C - 1.0 kbar
750°C - 1.0 kbar
(b)
An in mole %
Temperature(°C)
2σ
(c)
An in mole %
H2Omelt (wt%)
2σ
(d)
Or in mole %
Temperature(°C)
2σ
(e)
Or in mole %
H2Omelt (wt%)
2σ

Fig.10

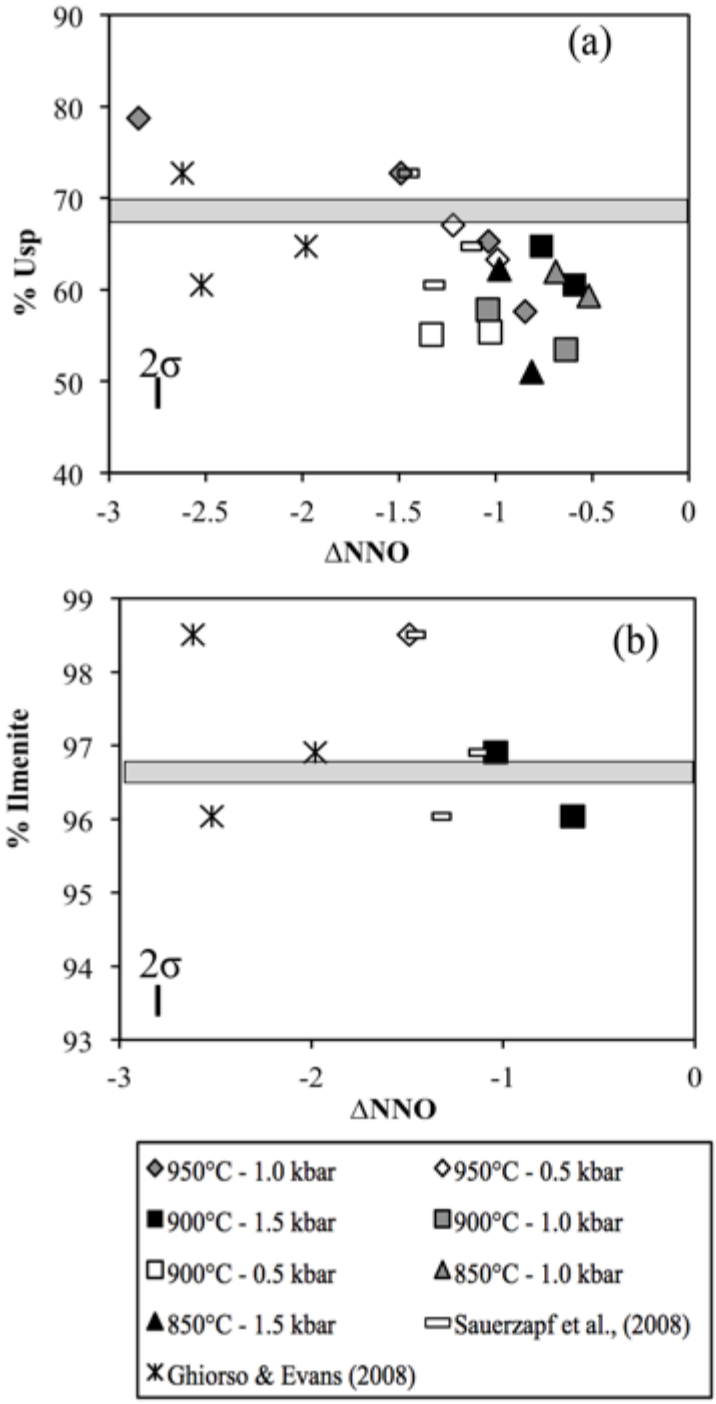
(a)
% Usp
ΔNNO
2σ
(b)
% Ilmenite
ΔNNO
2σ
950°C - 1.0 kbar
950°C - 0.5 kbar
900°C - 1.5 kbar
900°C - 1.0 kbar
900°C - 0.5 kbar
850°C - 1.0 kbar
850°C - 1.5 kbar
Sauerzapf et al., (2008)
Ghiorso & Evans (2008)

Fig.11

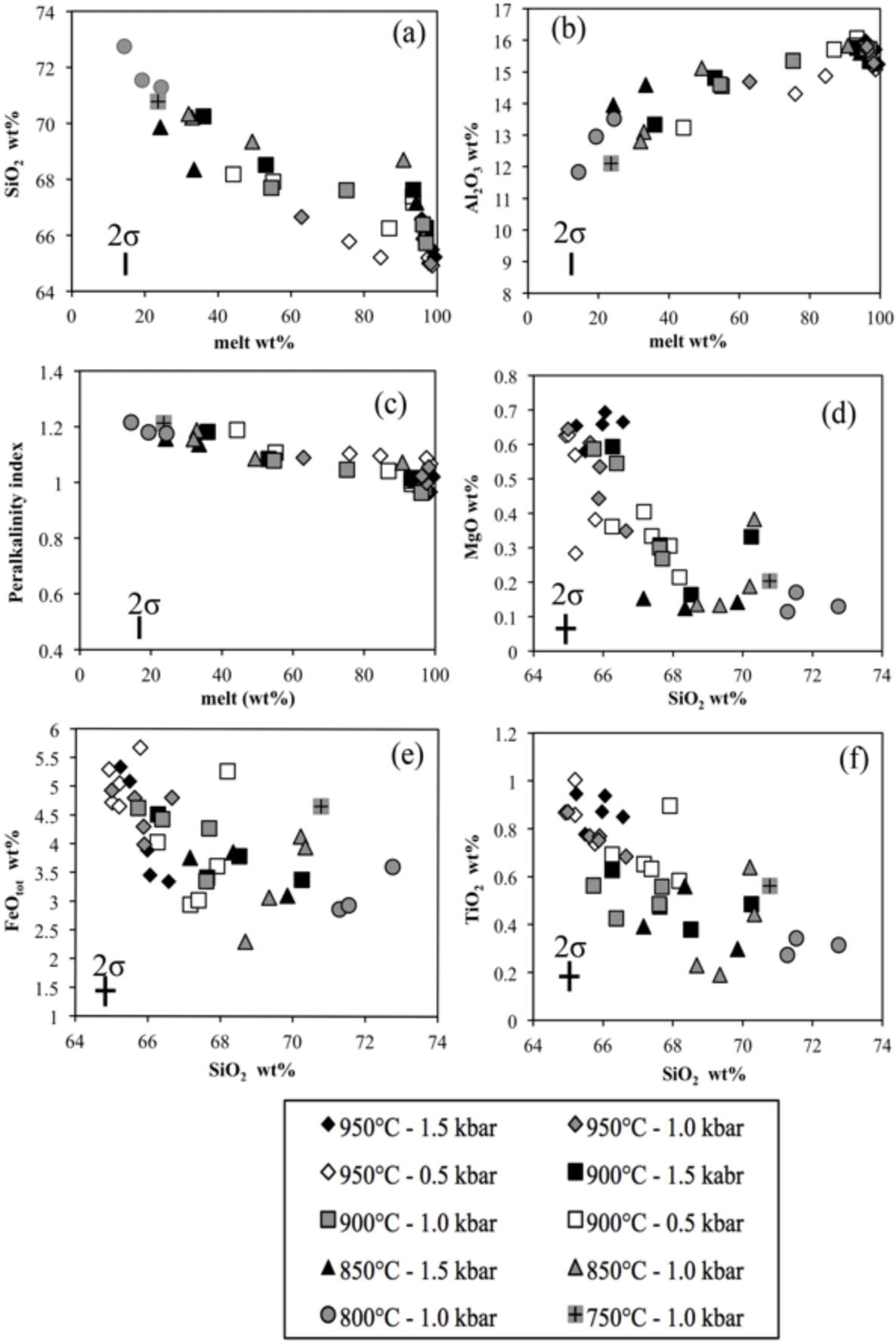
(a)
SiO2 wt%
melt wt%
2σ
(b)
Al2O3 wt%
melt wt%
2σ
(c)
Peralkalinity index
melt (wt%)
2σ
(d)
MgO wt%
SiO2 wt%
2σ
(e)
FeOtot wt%
SiO2 wt%
2σ
(f)
TiO2 wt%
SiO2 wt%
2σ
950°C - 1.5 kbar
950°C - 1.0 kbar
950°C - 0.5 kbar
900°C - 1.5 kabr
900°C - 1.0 kbar
900°C - 0.5 kbar
850°C - 1.5 kbar
850°C - 1.0 kbar
800°C - 1.0 kbar
750°C - 1.0 kbar

Fig.12

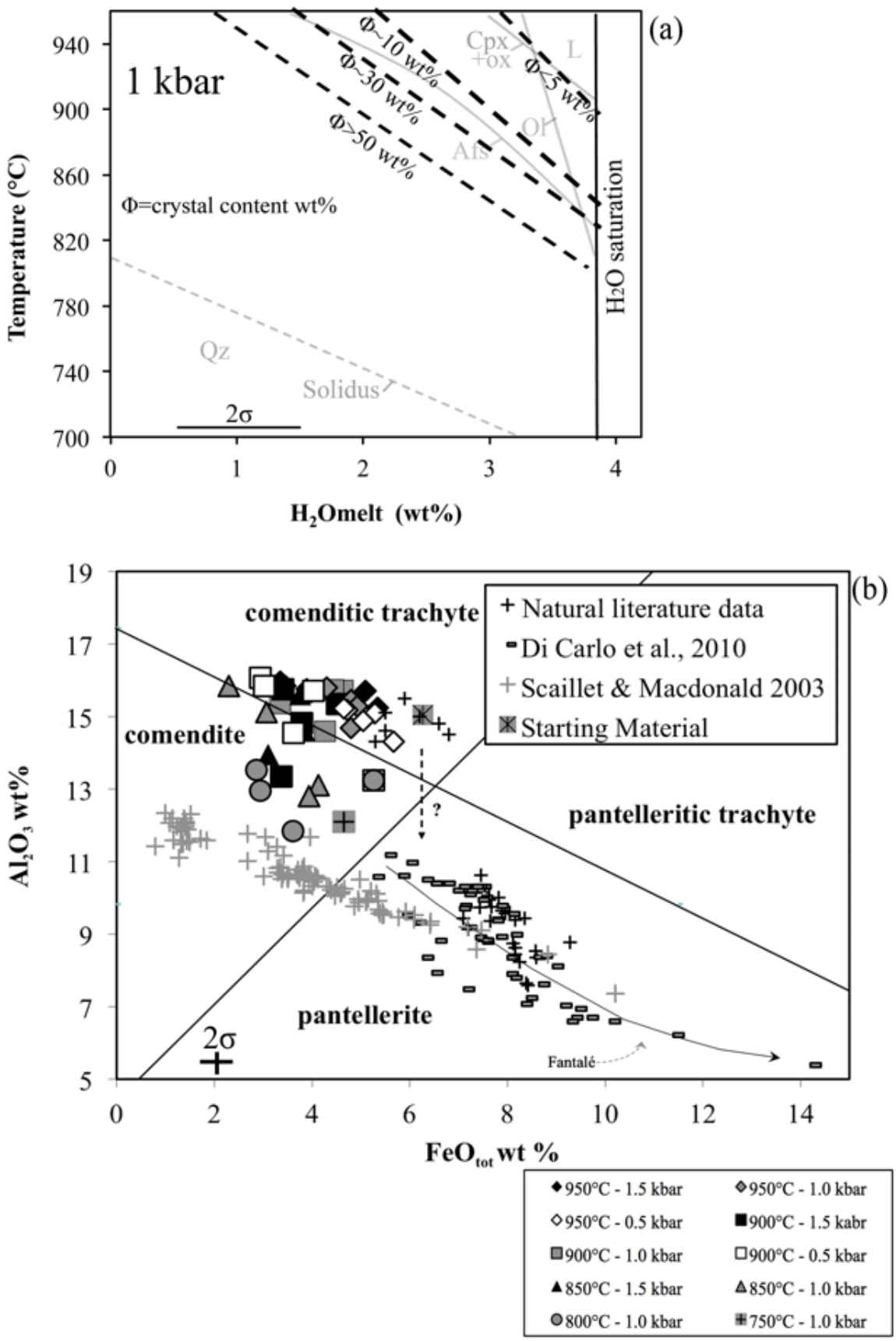
(a)
1 kbar
Φ=crystal content wt%
Φ~10 wt%
Φ~30 wt%
Φ>50 wt%
Φ<5 wt%
Cpx
+ox
L
Ol
Afs
Qz
Solidus
2σ
H2O saturation
Temperature (°C)
H2Omelt (wt%)
(b)
comenditic trachyte
comendite
pantelleritic trachyte
pantellerite
Natural literature data
Di Carlo et al., 2010
Scaillet & Macdonald 2003
Starting Material
Fantalé
Al2O3 wt%
FeOtot wt %
950°C - 1.5 kbar
950°C - 1.0 kbar
950°C - 0.5 kbar
900°C - 1.5 kabr
900°C - 1.0 kbar
900°C - 0.5 kbar
850°C - 1.5 kbar
850°C - 1.0 kbar
800°C - 1.0 kbar
750°C - 1.0 kbar

Fig.13

Table 1: Major element composition of natural Green Tuff (GT) and Post Cinque Denti Caldera (PCD) trachytes: bulk rock (XRF), mineral phases (EMP) and starting materials (glasses, EMP)

GTT n:	Bulk rock	Starting material 20	sd	Cpx 10	sd	Ol 4	sd	Afs pheno 20	sd	Afs microlite 12	sd	Mt 3	sd	Ilm 3.	sd
SiO_2 (wt%)	63.07	64.12	0.39	50.02	0.50	31.72	0.12	65.46	0.54	66.68	0.54	0.06	0.00	0.00	0.01
TiO_2	0.82	0.85	0.09	0.56	0.15	0.00	0.00	0.00	0.00	0.00	0.00	24.62	0.76	49.72	0.59
Al_2O_3	15.66	15.04	0.14	0.60	0.08	0.00	0.00	19.57	0.36	18.57	0.22	0.62	0.13	0.15	0.13
FeO_{tot}	7.06	6.27	0.23	16.96	0.53	52.42	1.84	0.24	0.09	0.79	0.20	66.05	2.58	44.09	0.25
MnO	0.25	0.27	0.08	1.03	0.13	2.84	0.13	0.00	0.00	0.00	0.00	1.59	0.11	1.88	0.45
MgO	0.27	0.62	0.04	9.41	0.22	10.75	0.07	0.00	0.00	0.00	0.00	0.80	0.53	1.02	0.88
CaO	0.93	1.48	0.05	20.12	0.19	0.47	0.01	0.95	0.06	0.56	0.09	0.01	0.01	0.05	0.01
Na_2O	7.05	6.58	0.22	0.54	0.04	0.00	0.00	7.70	0.13	8.11	0.15	0.00	0.00	0.00	0.00
K_2O	4.72	4.60	0.11	0.00	0.00	0.00	0.00	4.13	0.17	4.86	0.09	0.00	0.00	0.00	0.00
P2O5	0.23	0.17	0.09	0.00	0.00	0.00	0.00	0.00	0.00	0.00	0.00	0.00	0.00	0.00	0.00
BaO				0.00	0.00	0.00	0.00	0.63	0.04	0.24	0.17	0.00	0.00	0.00	0.00
sum	100.06	100.00	0.00	99.24	0.92	98.20	1.95	98.69	0.96	99.58	0.44	93.75	0.01	96.91	0.01
P.I	1.07	0.98													
Mg#															
Fa mole(%)						70.38	0.50								
Wo				43.17	0.33										
En				28.08	0.57										
Fs				28.75	0.59										
An								4.80	0.33	2.67	0.79				
Ab								70.39	0.95	69.79	0.49				
Or								24.82	0.92	27.54	0.70				

PCD n:	Bulk rock	Starting material 20	sd	Cpx 8	sd	Ol 6	sd	Afs pheno 10	sd	Afs microlite	sd	Mt	sd	Ilm	sd
SiO_2 (wt%)	63.78	64.42	0.43	48.79	0.59	30.72	0.63	64.64	2.02						
TiO2	0.75	0.68	0.14	0.57	0.20	0.00		0.06	0.06						
Al_2O_3	15.83	15.90	0.22	0.79	0.40	0.00		19.23	1.12						
FeO_{tot}	5.61	5.40	0.31	16.15	0.85	54.84	2.83	0.40	0.20						
MnO	0.19	0.20	0.08	0.98	0.14	2.79	0.30	0.05	0.06						
MgO	0.52	0.59	0.03	10.28	0.62	10.47	2.51	0.01	0.01						
CaO	1.87	2.06	0.08	20.41	0.19	0.41	0.10	1.59	1.48						
Na_2O	6.63	6.01	0.32	0.46	0.20	0.00		7.49	0.73						
K_2O	4.22	4.38	0.11	0.00	0.02	0.00		4.03	1.76						
P2O5		0.15	0.07		0.04			0.02	0.04						
BaO		0.12	0.06					0.20	0.16						
sum		100.00	0.00	98.42	0.90	99.24	0.68	97.71	1.01						
P.I	0.97	0.92	0.04												
Mg#															
Fa mole(%)						71	3.4								
Wo				43.76	1										
En				30.68	3										

Fs	25.56	3			
An			7.96	3	
Ab			67.99	2	
Or			24.05	5	

n, number of analyses; sd, standard deviation; FeOtot total iron reported as FeO.
Ol, olivine; cpx, clinopyroxene; afs, alkali feldspar, mt, magnetite; ilm, ilmenite.
Fa (mol%)=100(Mg/Mg+FeOtot) in olivine. Wo, En and Fs were calculated as in the study by Morimoto (1989). P.I = peralkalinity index (molar Na_2O+K_2O/Al_2O_3).
An=100[Ca/(Ca+Na+K)]; Ab=100[Na/(Ca+Na+K)]; Or=100[K/(Ca+Na+K)]. End-members calculated as in the study by Deer et al., (1992).

Table 2: Experimental run conditions and results

Green Tuff trachyte (GTT)

Run	XH_2O_{in} moles [1]	H_2O_{melt} (wt%)[2]	log fO_2[3] (bar)	Δ QFM[4]	Δ NNO[5]	Phase assemblage and abundances (wt%)	Crystal (wt%)	R^2
GT-R 9, 950°C, 1500 bar, PH_2 [6]=6,5 bar (target: FMQ buffer), 96h								
1	1.00	4.95	-12.09	-0.47	-0.96	Gl only	0.7	1.07
2	0.81	4.42	-12.23	-0.61	-1.14	Gl only	0.0	0.78
3	0.52	3.47	-12.62	-1.00	-1.53	Gl (95.8), Cpx (1.1)	4.2	0.46
4	0.34	2.76	-12.99	-1.38	-1.91	Gl (97), Cpx (0.5)	3.0	0.42
5	0.10	1.44	-14.04	-2.43	-2.96	Gl (96.8), Cpx (0.3)	3.2	0.30
GT-R 7, 900°C, 1500 bar, PH_2= 6,5bar, 115h								
1	1.00	4.95	-12.55	-0.10	-0.55	Gl (97.1), Cpx (0.1), Mt (3.4), Ilm (0.61)	2.9	0.31
2	0.82	4.46	-12.66	-0.21	-0.72	Gl (93.5), Cpx (3.7), Mt (6.83), Ilm (1.65)	6.5	0.45
3	0.53	3.54	-13.03	-0.58	-1.10	Gl (50.8), Cpx (3.5), Ol (2.3) Mt (2.9), Afs (40.5)	49.2	0.13
4	0.28	2.51	-13.58	-1.13	-1.65	Gl (36.0), Cpx (2.4), Ol (3), Mt (3.3), Afs (55.3)	64.0	0.27
GT-R 8, 850°C, 1500 bar, PH_2=6bar, 125h								
1	1.00	4.95	-13.73	-0.37	-0.77	Gl (94.3), Cpx (1.9), Mt (3.8)	5.7	0.81
2	0.82	4.47	-13.80	-0.44	-0.94	Gl (33.4), Cpx (5.2), Ol (0.4), Mt (4.9), Afs (56.1)	66.6	0.30
3	0.51	3.46	-14.21	-0.85	-1.35	Gl (24.2), Cpx (3.8), Ol (1.1), Mt (6.7), Afs (66.3)	75.8	0.46
4	0.33	2.75	-14.59	-1.22	-1.73	Gl, Cpx, Ol, Mt, Afs	n.d	n.d
5	0.10	1.44	-15.63	-2.27	-2.77	Gl, Cpx, Ol, Mt, Afs	n.d	n.d
GT-R 10, 950°C, 1000 bar, PH_2=5,5bar, 96h								
1	0.99	3.84	-12.06	-0.44	-1.00	Gl (97.8), Mt (2.2)	2.2	0.30
2	0.80	3.42	-12.28	-0.66	-1.19	Gl (98.3), Mt (1.7)	1.7	0.29
3	0.48	2.58	-12.73	-1.12	-1.64	Gl (96.5), Cpx (0.6), Ol (0.4), Mt (4.57), Ilm (2.04)	3.5	0.07
4	0.30	2.01	-13.14	-1.52	-2.04	Gl (96.0), Cpx (1.2), Ol (0.8), Mt (3.4), Ilm (1.3)	3.8	0.24
5	0.10	1.11	-14.09	-2.47	-3.00	Gl (68.0), Cpx (2.2), Ol (2.6), Mt (1.4), Afs (25.8)	32.0	0.15
GT-R 2, 900°C, 1000 bar, PH_2=5,5bar, 86 h								
1	1.00	3.84	-12.52	-0.07	-0.59	Gl (97.1), Cpx (0.4), Mt (2.5)	2.9	0.39
2	0.80	3.41	-12.73	-0.28	-0.78	Gl (95.6), Cpx (0.9), Ol (0.4) Mt (3.1)	4.4	0.91
3	0.50	2.65	-13.13	-0.68	-1.19	Gl (75.2), Cpx (0.8), Ol (2.3) Mt (3.0), Afs (18.7)	24.8	0.19
4	0.30	2.01	-13.58	-1.13	-1.64	Gl (61.8), Cpx (1.0), Ol (3.0), Mt (2.2) Afs (32.0)	38.2	0.15
GT-R 4, 850°C, 1000 bar, PH_2=5,5bar, 120h								
6	1.00	3.84	-13.54	-0.18	-0.66	Gl (90.7), Cpx (3.6), Mt (5.7)	9.3	0.64
7	0.82	3.45	-13.71	-0.35	-0.84	Gl (48.9), Cpx (5.2), Ol (0.8), Mt (3.4), Afs (41.7)	51.1	0.07
8	0.51	2.66	-14.13	-0.76	-1.26	Gl (35.9), Cpx (2.3), Ol (1.7), Mt (3.7), Afs (56.7)	64.1	0.23
9	0.34	2.14	-14.48	-1.12	-1.61	Gl (30.2), Cpx (0.9), Ol (0.6), Mt (1.9), Afs (66.4)	69.8	0.94
10	0.10	1.11	-15.54	-2.17	-2.66	nd	n.d	n.d
GT-R 14, 800°C, 1000 bar, PH_2=6bar, 150h								
1	1.00	3.84	-14.68	-0.32	-0.75	Gl (25.2), Cpx (6.1), Ol (0.9), Mt (4.5), Afs (63.3)	74.8	0.14
2	0.82	3.46	-14.80	-0.45	-0.92	Gl (19.3), Cpx (7.3), Ol (0.5), Mt (4.7), Afs (69.2)	80.7	0.31
5	0.52	2.69	-15.21	-0.85	-1.33	Gl (18.7), Cpx (1.2), Ol (2.0), Mt (4.0), Afs (71.2)	81.2	1.83
GT-R 3, 750°C, 1000 bar, PH_2=5,5bar, 170h								
6	1.00	3.84	-15.74	-0.30	-0.66	Gl (23.8), Cpx (8.9), Ol (1.4), Mt (3.1), Afs (62.8)	76.2	0.20
7	0.10	1.11	-17.66	-2.21	-2.66	Gl, Cpx, Ol, Qz	100.0	nd
GT-R 11, 950°C, 500 bar, PH2=5,5bar, 96h								
1	1.00	2.86	-12.22	-0.61	-1.12	Gl (98.7), Mt (1.3)	1.3	0.13

2	0.77	2.48	-12.45	-0.84	-1.35	Gl (97.9), Ol (0.7), Mt (1.4)	2.1	0.44
3	0.56	2.08	-12.73	-1.11	-1.63	Gl (97.6), Cpx (0.6), Ol (1.9), Mt (1.1)	2.4	0.30
4	0.37	1.67	-13.09	-1.47	-1.99	Gl (84.8), Cpx (0.6), Ol (3.5), Mt (0.13), Afs (12.2)	15.2	0.54
5	0.10	0.83	-14.22	-2.61	-3.12	Gl (75.9), Cpx (0.1), Ol (2.1), Mt (1.1), Afs (20.9)	24.1	0.06
GT-R 12, 900°C, 500 bar, PH_2=5,5bar, 110h								
1	1.00	2.86	-13.11	-0.66	-1.16	Gl (93.4), Cpx (1.6), Ol (1.5), Mt (3.5)	6.6	0.63
2	0.82	2.57	-13.28	-0.83	-1.33	Gl (93.3), Cpx (1.3), Ol (2.0), Mt (3.4)	6.7	0.78
3	0.71	2.37	-13.41	-0.96	-1.46	Gl (80.2), Cpx (2.2), Ol (2.5), Mt (1.4), Afs (13.7)	19.8	0.49
4	0.50	1.96	-13.72	-1.27	-1.76	Gl (54.2), Cpx (1.7), Ol (3.4), Mt (1.6), Afs (39.1)	45.8	0.28
5	0.30	1.51	-14.15	-1.69	-2.19	Gl (42.7), Cpx (0.5), Ol (3.0), Mt (2,7), Afs (52.1)	57.3	0.22
6	0.10	0.83	-15.11	-2.66	-3.16	Gl, Cpx, Ol, Afs, Mt	nd	nd

Post Cinque Denti Caldera trachyte (PCD)

Run	XH_2Oin moles [1]	H_2O_{melt} (wt%)[2]	log fO_2[3] (bar)	Δ QFM[4]	Δ NNO[5]	Phase assemblage and abundances (wt%)	Crystal (wt%)	R^2
R 1 950°C, 1500 bar, PH_2=6,5 bar (target: FMQ buffer) , 60 h								
1	1.00	4.95	-11.45	0.16	-0.33	leaked		
2	0.80	4.41	-11.41	0.21	-0.28	Gl (97.2)	2.8	1.29
3	0.60	3.77	-11.66	-0.04	-0.54	Gl (95.7), Cpx (1.1) Mt (3.2)	4.3	1.35
4	0.45	3.23	-11.91	-0.29	-0.79	Gl (95.2), Cpx (1.5), Mt (3.3)	4.8	1.7
5	0.10	1.44	-13.22	-1.60	-2.09	Gl (54.3), Cpx (5.8), Ol (1.5), Mt (1.0), Afs (37.4)	45.7	0.12
R2 900°C, 1500 bar, 96 h, PH_2=5,5bar, 86 h								
1	1.00	4.95	-12.93	-0.47	-0.93	leaked		
2	0.80	4.40	-12.31	0.14	-0.38	Gl (94.3), Cpx (2.2), Mt (3.4)	5.6	0.94
3	0.57	3.68	-12.61	-0.15	-0.67	leaked		
4	0.46	3.28	-12.79	-0.34	-0.86	leaked		
5	0.10	1.44	-14.12	-1.67	-2.19	n.d	~100%	
R4 950°C, 1000bar, PH_2=5,5bar 86 h								
1	1.00	3.84	-11.59	0.86	-0.53	Gl (100)	0	0
2	0.83	3.47	-11.79	0.66	-0.70	Gl (98), Cpx (2)	2	0.68
3	0.71	3.20	-11.92	0.53	-0.82	leaked		
4	0.45	2.50	-12.32	0.14	-1.22	Gl (62.4), Cpx (3.9), Mt (3.0) Afs (30.8),	37.6	0.82
5	0.10	1.11	-13.63	-1.17	-2.53	Gl (33.3), Cpx (6.6), Ol (3.2), Mt (3.0), Afs (60.4)	63.2	0.37
R3 900°C, 1000 bar, PH_2=5,5bar, 86 h								
1	1.00	3.84	-12.36	0.09	-0.43	leaked		
2	0.82	3.44	-12.61	-0.15	-0.66	Gl (95.4), Cpx (2.3), Mt (2.3)	4.6	1.13
3	0.58	2.86	-12.91	-0.45	-0.96	Gl (57.5), Cpx (4.0), Ol (1.9), Mt (1.7), Afs (34.9)	42.5	0.83
4	0.47	2.56	-13.09	-0.64	-1.14	Gl (39.4), Cpx (5.1), Ol (1.2), Mt (0.93), Afs (53.4)	60.6	0.52
5	0.10	1.11	-14.43	-1.98	-2.49	Gl, Cpx, Ol, Mt, Afs	n.d	n.d
R10 850°C, 1000bar, PH_2=6 bar, 120h								
1	1.00	3.84	-13.54	-1.09	-0.66	Gl, Cpx, Mt, Afs	n.d	n.d
2	0.85	3.51	-13.04	-0.59	-0.17	Gl, Cpx, Ol, Mt, Afs	n.d	n.d
3	0.53	2.72	-13.45	-1.00	-0.58	Gl, Cpx, Ol, Mt, Afs	n.d	n.d
4	0.29	1.99	-13.96	-1.51	-1.09	Gl, Cpx, Ol, Mt, Afs	n.d	n.d

[1] $XH_2O_{in,}$ initial mole fraction of H_2O of the C-H-O fluid loaded in the capsule.

[2] H_2O_{melt} (wt%), dissolved melt water content determined following the method of Scaillet & Macdonald 2006 and Andujar et al., 2016.

[3] fO_2, logarithm of the oxygen fugacity (bar) calculated from the experimental fH_2 obtained from the solid sensors (see the text).
[4]Δ QFM, [5] Δ NNO log fO_2-logfO_2 of the NNO and QFM buffer calculated at P and T respectively from Pownceby & O'Neill 1994 and Chou 1978.
[6] PH_2, hydrogen pressure loaded in the vessel at room temperature. Crystal content, values indicate the phase abundance in the charge (in wt %). Gl, glass; Cpx, clinopyroxene; Ol, olivine; Mt, magnetite; Afs, alkali feldspar; Ilm, ilmenite; Qz, quartz.
Leaked: capsule that lost the fluid phase during the experiment

Table 3: Composition of experimental clinopyroxenes (wt%)

Green Tuff trachyte (GTT)

Run	n.	SiO_2	TiO_2	Al_2O_3	FeO_{tot}	MnO	MgO	CaO	Na_2O	K_2O	P_2O_5	Total	XFe
GT-R 9, 950°C, 1500 bar													
3	1	52.11	0.90	1.18	9.27	1.16	13.79	20.00	0.57	0.10	0.01	98.98	0.27
5	5	52.36	0.83	1.01	10.96	1.26	13.75	19.09	0.42	0.10	0.00	99.69	0.31
sd		0.26	0.23	0.42	1.08	0.23	0.62	0.82	0.15	0.07	0.00	0.55	0.03
GT-R 7, 900°C, 1500 bar													
1	6	52.38	0.50	0.69	11.83	1.10	12.79	19.84	0.42	0.07	0.03	99.66	0.34
sd		0.46	0.13	0.21	0.68	0.11	0.44	0.31	0.07	0.03	0.04	0.44	0.02
2	7	51.77	0.52	1.29	14.00	1.39	11.05	18.68	0.64	0.12	0.02	99.48	0.42
sd		0.51	0.17	0.42	1.64	0.17	0.63	0.69	0.08	0.04	0.04	0.49	0.04
3	7	51.54	0.59	1.59	19.35	1.46	8.49	15.96	0.75	0.42	0.06	100.20	0.56
sd		0.29	0.19	0.63	1.78	0.28	0.64	0.55	0.21	0.28	0.04	1.41	0.01
4	2	49.82	0.49	0.65	21.15	1.52	8.86	15.76	0.59	0.06	0.05	98.95	0.57
sd		0.82	0.01	0.21	0.62	0.06	0.21	0.68	0.09	0.00	0.00	0.20	0.06
GT-R 8, 850°C, 1500 bar													
1	3	52.95	0.24	1.40	14.38	1.60	10.38	19.16	0.53	0.02	0.01	100.67	0.44
sd		0.51	0.06	0.11	1.53	0.57	0.34	0.54	0.25	0.04	0.06	0.79	0.03
2	7	53.46	0.68	3.90	15.89	1.48	7.26	15.67	1.25	0.20	0.03	99.09	0.54
sd		1.15	0.35	0.63	1.17	0.17	0.67	0.97	0.15	0.20	0.09	1.24	0.03
3	6	50.19	0.66	1.22	21.97	1.93	6.45	15.46	0.80	0.13	0.08	98.81	0.67
sd		0.76	0.16	0.33	1.86	0.43	0.31	0.91	0.12	0.11	0.18	0.70	0.02
4	3	50.63	0.52	2.48	29.31	1.67	4.48	10.80	0.93	0.47	0.28	99.51	0.79
sd		0.29	0.16	0.42	0.62	0.62	0.21	0.09	0.15	0.20	0.00	0.63	0.05
GT-R 10, 950°C, 1000 bar													
3	11	52.29	0.51	1.23	13.66	1.21	11.66	18.75	0.51	0.18	0.08	99.82	0.40
sd		0.61	0.11	0.44	0.99	0.15	0.34	0.81	0.12	0.13	0.09	0.00	0.02
4	15	51.71	0.71	1.22	14.68	1.22	11.12	18.26	0.49	0.14	0.03	99.41	0.43
sd		0.82	0.12	0.88	1.14	0.20	0.76	1.04	0.28	0.10	0.05	0.96	0.02
5	7	52.14	0.82	1.41	18.56	1.60	9.62	15.48	0.56	0.26	0.29	100.19	0.52
sd		1.40	0.29	0.93	2.01	0.23	0.76	1.94	0.08	0.13	0.11	1.07	0.04
GT-R 2, 900°C, 1000 bar													
1	4	51.10	0.49	1.19	12.40	1.19	12.20	20.10	0.60	0.09	0.03	99.40	0.36
sd		0.87	0.12	0.12	0.90	0.40	0.32	0.87	0.13	0.02		0.90	0.02
2	10	52.02	0.43	1.71	13.79	1.25	11.59	18.78	0.65	0.22	0.03	100.47	0.40
sd		0.89	0.12	0.87	1.05	0.48	0.34	0.89	0.11	0.18	0.04	1.32	0.02
3	5	50.82	0.81	1.51	19.68	1.75	10.27	15.54	0.54	0.13	0.14	101.19	0.53
sd		0.61	0.87	0.27	1.67	0.12	0.42	1.26	0.16	0.03	0.08	0.39	0.03
4	5	50.67	0.59	1.15	20.72	1.65	8.78	15.26	0.65	0.26	0.10	99.48	0.57
sd		0.62	0.12	0.39	1.95	0.28	0.41	0.98	0.17	0.10	0.17	1.31	0.01
GT-R 4, 850°C, 1000 bar													
6	10	51.48	0.49	1.57	13.04	1.42	10.83	19.13	0.96	0.00	0.00	98.92	0.40
sd		0.92	0.33	0.97	1.11	0.41	0.72	0.32	0.20	0.07	0.05	1.49	0.03
7	2	50.78	0.54	2.58	16.99	1.56	8.35	16.04	1.43	0.02	0.03	98.34	0.53
sd		0.58	0.17	1.09	0.28	0.28	0.99	0.29	0.54	0.54	0.18	0.80	0.02

8	6	50.24	0.52	1.18	24.37	1.93	6.62	13.41	0.96	0.02	0.03	1.32	0.67
sd		0.95	0.34	0.37	1.44	0.47	0.21	1.33	0.23	0.19	0.33	0.78	0.01
9	1	49.58	0.73	1.50	27.64	1.70	5.16	13.32	1.30	0.40	0.06	100.92	0.75
sd		0.58	0.41	0.97	0.28	0.21	0.32	0.21	0.16	0.00	0.00	0.90	
GT-R 14, 800°C, 1000 bar													
1	4	51.54	0.95	4.01	16.56	1.83	7.61	15.43	1.69	0.49	0.05	100.32	0.55
sd		0.87	0.23	1.40	0.93	0.32	0.92	1.23	0.24	0.30	0.10	0.70	0.03
2	4	52.52	0.44	2.73	24.72	1.89	6.00	11.83	1.60	0.68	0.12	102.40	0.70
sd		0.99	0.05	0.58	0.54	0.18	0.24	0.82	0.43	0.30	0.10	52.52	0.01
5	5	49.86	0.38	1.41	26.86	2.07	5.66	11.31	1.04	0.33	0.11	99.12	0.73
sd		1.01	0.01	0.49	0.66	0.20	0.40	1.65	0.41	0.15	0.14	0.70	0.02
GT-R 3, 750°C, 1000 bar													
6	3	50.05	1.27	3.61	21.48	1.54	5.70	12.66	2.00	0.60	0.11	99.01	0.68
sd		1.45	0.52	0.94	1.24	0.19	0.37	1.03	0.45	0.40	0.09	1.33	0.07
GT-R 11, 950°C, 500 bar													
3	10	52.07	0.76	1.78	14.45	1.19	11.38	17.67	0.67	0.19	0.20	99.98	0.41
sd		1.20	0.23	0.69	0.98	0.14	0.44	0.90	0.27	0.06	0.07	0.90	0.01
4	13	52.31	0.71	1.63	15.73	1.29	10.82	16.94	0.53	0.35	0.02	99.95	0.45
sd		1.26	0.19	1.32	2.31	0.23	1.07	1.78	0.32	0.27	0.02	0.67	0.04
5	2	52.20	0.83	2.24	16.79	1.16	9.81	16.02	0.83	0.51	0.02	99.88	0.49
sd		1.62	0.07	1.49	2.10	0.05	0.58	0.59	0.69	0.32	0.02	1.75	0.02
GT-R 12, 900°C, 500 bar													
1	10	51.63	0.57	1.45	13.99	1.31	11.32	18.19	0.74	0.26	0.08	99.19	0.41
sd		1.19	0.34	0.87	1.47	0.13	0.34	0.66	0.34	0.18	0.13	1.51	0.02
2	11	52.44	0.43	1.00	15.77	1.50	10.95	17.65	0.47	0.15	0.08	100.21	0.45
sd		0.89	0.11	0.27	1.27	0.18	0.27	0.91	0.11	0.09	0.11	1.04	0.02
3	8	51.48	0.38	1.20	18.82	1.74	10.44	14.33	0.50	0.30	0.13	98.89	0.50
sd		0.58	0.10	0.23	0.68	0.18	0.26	0.65	0.13	0.09	0.07	0.58	0.01
4	7	52.24	0.42	1.67	19.66	1.68	8.88	14.15	0.87	0.44	0.15	99.57	0.55
sd		1.09	0.19	0.65	1.65	0.32	0.59	0.58	0.29	0.15	0.12	0.87	0.01
5	2	51.98	0.39	1.45	21.93	2.00	8.43	13.22	0.76	0.30	0.06	100.16	0.59
sd		0.11	0.24	0.41	0.07	0.10	0.14	1.46	0.09	0.00	0.00	0.78	0.00

Post Cinque Denti (PCD)

Run	n.	SiO_2	TiO_2	Al_2O_3	FeO_{tot}	MnO	MgO	CaO	Na_2O	K_2O	P_2O_5	Total	XFe
R 1 950°C, 1500 bar													
3	6	51.14	0.75	1.93	15.36	0.84	10.31	19.64	0.49	0.16	0.16	100.79	0.45
sd		0.59	0.13	0.26	0.88	0.14	0.20	0.30	0.07	0.20	0.20	0.28	0.02
4	4	49.76	0.77	1.81	16.78	0.90	9.60	19.82	0.55	0.39	0.39	99.99	0.49
sd		0.39	0.10	0.14	1.03	0.08	0.14	0.28	0.05	0.26	0.26	0.50	0.01
5	4	50.78	0.67	1.99	23.59	1.36	7.48	14.14	0.77	0.37	0.05	100.79	0.64
sd		1.17	0.30	0.49	1.40	0.14	0.23	0.84	0.15	0.04	0.04	1.74	0.02
R2 900°C, 1500 bar													
2	5	50.56	0.56	1.81	13.11	1.00	10.38	20.98	0.61	0.16	0.13	99.01	0.41
sd		0.89	0.08	0.49	0.66	0.17	0.17	0.44	0.10	0.32	0.04	1.04	0.01
R4 950°C, 1000bar													

2	4	51.83	0.59	1.91	13.41	0.78	10.79	20.06	0.56	0.22	0.10	99.93	0.41
sd		0.14	0.23	0.99	0.26	0.18	1.05	0.63	0.09	0.15	0.10	0.63	0.03
4	6	49.28	0.63	1.30	18.04	1.20	10.23	17.25	0.51	0.16	0.05	98.64	0.50
sd		0.47	0.19	0.32	1.17	0.10	0.52	1.08	0.10	0.11	0.08	0.65	0.03
5	2	48.53	0.86	2.20	22.03	1.52	8.20	15.23	0.66	0.30	0.04	99.56	0.60
sd		1.77	0.20	0.28	1.85	0.05	0.63	2.08	0.22	0.29	0.06	0.82	0.03
R3 900°C, 1000 bar													
2	4	51.13	0.48	1.41	14.79	0.92	10.24	20.16	0.48	0.10	0.04	99.74	0.45
sd		0.62	0.16	0.37	0.52	0.19	0.23	0.31	0.09	0.04	0.04	0.60	0.01
3	5	50.36	0.45	0.94	21.35	1.63	9.15	15.35	0.46	0.14	0.11	99.92	0.57
sd		0.82	0.10	0.25	1.02	0.09	0.27	1.05	0.08	0.17	0.11	0.64	0.01
4	3	49.70	0.50	1.09	24.28	1.68	7.45	14.17	0.49	0.55	0.04	99.94	0.65
sd		0.67	0.16	0.62	2.58	0.23	0.89	0.84	0.12	0.08	0.07	1.04	0.05

n: number of analysis;
sd: standard deviation;
FeOtot: Total Iron reported as FeO;
XFe is molar Fe/(Fe+Mg) in clinopyroxene

Table 4: Composition of experimental olivines (wt%)

Green Tuff (GTT)

Run	n.	SiO_2	TiO_2	Al_2O_3	FeO_{tot}	MnO	MgO	CaO	Na_2O	K_2O	P_2O_5	Total	Fa mole%
GT-R 7, 900°C, 1500 bar													
2	4	33.16	0.03	0.02	46.78	2.98	15.45	0.33	0.03	0.03	0.16	98.96	60.49
sd		0.27	0.04	0.04	0.29	0.06	0.28	0.01	0.03	0.05	0.22	0.45	0.27
3	6	32.11	0.05	0.03	51.33	3.17	9.97	0.49	0.03	0.00	0.00	97.57	71.14
sd		0.53	0.13	0.33	0.87	0.19	0.31	0.10	0.10	0.08	0.11	1.09	0.59
4	3	30.78	0.13	0.04	56.37	3.32	8.78	0.43	0.04	0.04	0.24	100.19	74.77
sd		0.06	0.08	0.05	0.61	0.16	0.08	0.08	0.04	0.03	0.26	0.75	0.33
GT-R 8, 850°C, 1500 bar													
2	8	31.38	0.22	0.07	51.73	3.58	8.44	0.34	0.07	0.07	0.17	95.76	73.48
sd		0.44	0.17	0.03	0.65	0.42	0.17	0.05	0.08	0.05	0.14	0.97	0.54
3	5	31.04	0.04	0.12	53.43	3.42	6.59	0.33	0.12	0.08	0.18	95.40	77.83
sd		0.82	0.90	0.73	0.95	0.29	0.78	0.05	0.34	0.18	0.16	0.75	1.44
4	4	30.72	0.10	0.09	57.51	2.70	4.44	0.32	0.04	0.10	0.12	96.15	84.36
sd		0.19	0.05	0.16	0.83	0.19	0.19	0.03	0.03	0.08	0.08	0.71	0.33
GT-R 10, 950°C, 1000 bar													
3	12	33.65	0.00	0.00	43.36	2.46	17.23	0.36	0.01	0.00	0.00	97.42	57.37
sd		0.42	0.04	0.12	0.87	0.31	0.37	0.04	0.03	0.07	0.16	0.83	0.31
4	12	33.42	0.02	0.01	44.22	2.73	16.50	0.40	0.00	0.00	0.00	97.70	58.45
sd		0.34	0.09	0.04	0.70	0.12	0.55	0.08	0.08	0.04	0.19	0.68	1.02
5	2	32.56	0.00	0.00	48.85	3.00	12.17	0.00	0.00	0.00	0.20	99.70	70.71
sd		0.77	0.04	0.03	0.93	0.36	1.22	0.14	0.02	0.02	0.12	1.05	0.47
GT-R 2, 900°C, 1000 bar													
2	7	32.90	0.01	0.00	46.64	2.95	16.81	0.31	0.05	0.02	0.19	100.29	59.05
sd		0.35	0.04	0.02	0.79	0.19	0.40	0.03	0.03	0.02	0.09	0.93	0.74

3	6	32.02	0.18	0.11	49.96	3.11	12.15	0.38	0.07	0.06	0.16	97.75	66.63
sd		0.51	0.09	0.44	1.05	0.21	0.29	0.03	0.06	0.10	0.19	1.40	0.56
4	5	32.43	0.14	0.30	51.00	2.60	9.59	0.46	0.10	0.21	0.15	96.52	71.59
sd		0.52	0.08	0.17	0.69	0.64	0.68	0.09	0.08	0.15	0.09	0.63	0.12
GT-R 4, 850°C, 1000 bar													
7	7	31.32	0.10	0.04	52.73	3.76	9.40	0.28	0.04	0.08	0.27	98.03	71.93
sd		0.40	0.09	0.05	1.84	0.43	0.59	0.04	0.07	0.05	0.21	1.95	0.86
8	5	30.86	0.13	0.01	56.89	3.22	6.34	0.30	0.06	0.02	0.13	97.41	79.61
sd		0.76	0.07	0.01	0.85	0.20	0.40	0.06	0.04	0.03	0.16	0.50	0.78
9	2	32.92	0.05	0.03	57.13	2.95	5.09	0.35	0.03	0.00	0.00	98.55	85.10
sd		1.23	0.15	0.28	2.39	0.03	0.56	0.02	0.24	0.03	0.08	0.01	1.67
GT-R 14, 800°C, 1000 bar													
1	9	31.33	0.05	0.02	52.61	3.84	7.30	0.25	0.04	0.07	0.15	95.39	75.69
sd		0.30	0.09	0.03	0.62	0.24	0.30	0.10	0.05	0.04	0.09	0.42	0.80
2	1	31.66	0.04	0.30	56.11	3.67	6.72	0.24	0.19	0.12	0.13	97.14	77.99
sd		0.60	0.06	0.48	1.07	0.47	1.11	0.05	0.21	0.12	0.10	0.00	0.90
5	3	31.14	0.06	0.01	55.90	3.31	4.43	0.27	0.06	0.05	0.13	95.36	83.26
sd		0.27	0.06	0.02	0.94	0.28	0.40	0.03	0.03	0.06	0.12	0.83	0.73
GT-R 3, 750°C, 1000 bar													
6	5	30.70	0.26	0.43	58.11	3.06	5.26	0.25	0.14	0.12	0.23	98.03	82.32
sd		1.12	0.40	0.70	1.65	0.08	0.18	0.07	0.17	0.11	0.08	1.59	0.27
7	2	31.49	0.12	0.72	59.17	2.23	3.04	0.34	0.41	0.19	0.03	97.73	88.53
sd		2.01	0.03	0.93	2.65	0.30	0.24	0.17	0.58	0.23	0.05	1.21	0.62
GT-R 11, 950°C, 500 bar													
2	2	33.40	0.04	0.07	40.14	2.61	20.36	0.32	0.04	0.08	0.15	97.20	50.75
sd		1.09	0.01	0.05	0.28	0.06	0.10	0.05	0.01	0.01	0.04	1.35	0.25
3	7	33.73	0.28	0.04	43.38	2.50	18.05	0.37	0.04	0.08	0.19	98.66	55.55
sd		0.73	0.37	0.04	1.09	0.17	0.64	0.01	0.04	0.03	0.22	0.56	1.28
4	8	32.35	0.08	0.05	46.42	2.59	14.69	0.44	0.06	0.08	0.22	96.98	61.70
sd		1.24	0.10	0.02	0.60	0.23	0.43	0.04	0.07	0.05	0.17	0.87	0.94
5	3	32.30	0.11	0.01	49.91	2.87	13.03	0.45	0.03	0.07	0.16	97.84	65.63
sd		1.70	0.05	0.03	1.22	0.24	0.18	0.03	0.04	0.07	0.09	0.60	1.70
GT-R 12, 900°C, 500 bar													
1	2	33.64	0.05	0.01	44.09	3.11	17.34	0.32	0.01	0.05	0.22	98.85	56.42
sd		0.28	0.08	0.01	0.67	0.17	0.44	0.05	0.02	0.05	0.15	0.11	1.03
2	7	33.31	0.07	0.02	45.92	3.27	14.95	0.37	0.05	0.06	0.13	98.15	60.52
sd		0.70	0.07	0.03	1.18	0.18	0.77	0.07	0.03	0.04	0.09	0.74	1.63
3	5	33.08	0.07	0.04	47.92	3.35	12.93	0.38	0.06	0.05	0.14	98.01	64.44
sd		0.38	0.07	0.04	0.63	0.20	0.45	0.05	0.05	0.03	0.08	0.55	0.70
4	6	32.13	0.06	0.04	51.00	3.35	10.05	0.41	0.07	0.08	0.19	97.37	70.54
sd		1.31	0.06	0.03	0.78	0.23	0.35	0.05	0.10	0.04	0.09	1.04	0.57
5	7	32.08	0.15	0.06	52.27	3.38	9.05	0.46	0.06	0.05	0.22	97.76	72.78
sd		0.42	0.11	0.07	1.10	0.28	0.93	0.08	0.05	0.06	0.10	0.33	1.40

Post Cinque Denti Caldera (PCD)

Run	n.	SiO_2	TiO_2	Al_2O_3	FeO_{tot}	MnO	MgO	CaO	Na_2O	K_2O	P_2O_5	Total	Fa mole%

R 1 950°C, 1500 bar													
5	4	31.59	0.11	0.17	55.57	2.70	8.57	0.85	0.06	0.11	0.57	100.30	75.00
sd		0.69	0.05	0.25	1.10	0.08	0.50	0.45	0.06	0.09	0.55	0.71	0.68
R4 950°C, 1000bar													
5	7	31.01	0.05	0.18	55.62	2.62	10.00	0.44	0.06	0.08	0.12	100.19	73.00
sd		0.62	0.04	0.18	0.54	0.15	0.67	0.09	0.04	0.02	0.12	0.97	1.17
R3 900°C, 1000 bar													
3	5	31.96	0.03	0.14	54.38	2.93	9.48	0.47	0.05	0.09	0.10	99.38	73.00
sd		0.44	0.03	0.20	0.90	0.20	0.34	0.21	0.04	0.08	0.08	1.53	0.47
4	5	30.84	0.10	0.06	57.97	3.00	6.65	0.43	0.05	0.08	0.12	99.05	80.00
sd		0.55	0.09	0.06	0.47	0.17	0.31	0.07	0.03	0.04	0.04	0.63	0.42

n: number of analysis;
sd: standard deviation;
FeO_{tot} Total Iron reported as FeO;
Fa mol(%)=100 Fe/(Fe_{tot}+Mg+Mn) in olivine

Table 5: Composition of experimental alkali feldspar (wt%)

Green Tuff (GTT)

	n.	SiO2	TiO_2	Al_2O_3	FeO_{tot}	MnO	MgO	CaO	Na_2O	K_2O	P_2O5	Total	An-Or (%)
GT-R 7, 900°C, 1500 bar													
3	3	65.84	0.22	18.10	1.12	0.02	0.07	0.97	7.61	4.75	0.10	99.02	5.88-26.33
sd		1.21	0.06	1.20	0.61	0.06	0.06	0.26	0.36	0.23	0.09	0.43	
4	1	64.48	0.38	16.31	3.07	0.20	0.21	1.08	7.44	4.79	0.03	97.87	6.35-27.85
GT-R 8, 850°C, 1500 bar													
2		68.48	0.30	17.83	1.37	0.14	0.15	0.89	6.76	4.99	0.22	101.12	4.65-31.18
sd		1.05	0.01	0.36	0.76	0.10	0.07	0.06	0.74	0.45	0.12	0.00	
3		68.00	0.15	17.79	1.31	0.12	0.30	1.22	6.88	5.06	0.19	101.03	6.20-30-57
sd		0.21	0.03	0.34	0.06	0.00	0.06	0.39	0.25	0.29	0.01	0.16	
GT-R 10, 950°C, 1000 bar													
5	2	64.78	0.31	19.02	1.05	0.02	0.04	1.04	8.01	4.33	0.00	98.60	6.82-24.54
sd		0.27	0.29	0.20	0.20	0.00	0.02	0.00	0.24	0.30	0.00	0.92	
GT-R 2, 900°C, 1000 bar													
3	5	65.09	0.44	18.46	1.25	0.07	0.35	1.88	7.51	3.54	0.17	98.96	9.57-21.39
sd		1.72	0.17	0.37	1.35	0.06	0.12	0.37	0.82	0.25	0.22	0.85	
4	10	64.96	0.50	18.72	1.00	0.00	0.05	2.00	7.50	4.01	0.13	98.87	9.78-21.23
sd		1.30	0.10	0.51	0.92	0.06	0.13	0.33	0.41	0.14	0.01	0..67	
GT-R 4, 850°C, 1000 bar													
7	8	66.44	0.51	17.96	1.59	0.15	0.06	0.67	7.40	4.75	0.06	99.58	3.41-28.69
sd		1.64	0.19	0.79	1.06	0.08	0.06	0.21	0.81	0.35	0.06	1.75	
8	2	65.97	0.23	17.98	1.32	0.09	0.45	1.53	7.93	4.64	0.09	99.56	7.13-25.80
sd		0.16	0.04	0.20	0.44	0.08	0.16	0.28	0.59	0.25	0.13	1.71	
9	1	66.77	0.17	16.71	1.32	0.11	0.47	1.64	7.62	4.46	0.17	97.83	7.90-25.61
GT-R 14, 800°C, 1000 bar													
1	4	67.34	0.20	18.10	1.66	0.03	0.06	0.71	7.60	4.18	0.10	100.64	3.34-28.84
sd		0.49	0.25	0.67	0.76	0.05	0.05	0.22	0.18	0.00	0.09	1.28	

2	4	65.29	0.58	17.47	5.11	0.16	0.24	1.03	7.24	4.14	0.14	99.43	4.62-27.12
sd		0.51	0.07	0.35	0.24	0.10	0.07	0.31	0.18	0.43	0.09	0.99	
5	2	65.66	0.76	16.32	4.71	0.05	0.56	1.70	6.16	0.00	0.07	100.26	10.79-25.59
		0.35	0.09	0.24	0.38	0.15	0.08	0.28	0.45	0.38	0.00	0.70	
GT-R 3, 750°C, 1000 bar													
6	7	66.67	0.24	18.58	0.89	0.05	0.09	0.23	7.95	5.35	0.16	98.38	2.42-28.82
sd		1.01	0.06	0.60	0.20	0.02	0.02	0.32	0.44	0.75	0.22	0.79	
GT-R 11, 950°C, 500 bar													
4	2	64.29	0.21	18.15	0.74	0.20	0.11	1.92	7.55	3.68	0.08	96.93	9.69-21.48
sd		0.27		0.08	0.19	0.06	0.03	0.41	0.45	0.37	0.03	0.10	
5	5	63.85	0.11	19.05	1.39	0.02	0.06	1.88	7.79	3.51	0.10	97.75	9.32-20.72
sd		0.37	0.08	0.27	0.94	0.03	0.03	0.45	0.41	0.40	0.02	0.05	
GT-R 12, 900°C, 500 bar													
3	1	64.33	0.44	18.31	2.30	0.18	0.48	0.48	7.70	4.19	0.03	99.86	9.29-23.90
4	3	64.91	0.50	18.30	2.88	0.09	0.41	0.41	7.50	4.00	0.04	100.32	9.51-25.12
sd		2.14	0.14	0.26	0.63	0.01	0.10	0.10	0.36	0.35	0.02	1.50	
5	2	65.86	0.00	17.82	1.41	0.08	0.36	1.96	7.34	4.00	0.15	100.00	9.82-23.80
sd		1.97	0.03	0.32	0.38	0.03	0.14	0.14	0.54	0.05	0.10	2.09	

Post Cinque Denti (PCD)

	n.	SiO_2	TiO_2	Al_2O_3	FeO_{tot}	MnO	MgO	CaO	Na_2O	K_2O	P_2O_5	Total	An-Or (%)
R1 950°C, 1500 bar													
5	2	65.53	0.17	19.52	0.64	0.00	0.00	1.09	7.60	4.42	0.02	99.21	5.4-26.1
sd		0.37	0.00	1.50	1.16	0.00	0.00	0.27	1.17	0.37	0.00	0.24	
R4 950°C, 1000 bar													
4	3	65.80	0.13	19.52	0.61	0.30	0.80	1.02	7.80	4.91	0.00	100.89	4.9-27.9
sd		0.44	0.07	0.71	0.70	0.09	0.08	0.20	0.34	0.55	0.00	0.40	
5	4	63.29	0.26	17.95	1.63	0.02	0.06	1.19	7.79	4.25	0.04	96.48	4.70-24.7
sd		0.71	0.09	0.44	0.57	0.00	0.01	0.21	0.44	0.62	0.02	0.30	
R3 900°C, 1000 bar													
3	6	64.19	0.10	19.03	0.65	0.04	0.01	1.38	8.30	3.98	0.05	97.72	6.51-22.41
sd		0.64	0.07	0.27	0.18	0.04	0.01	0.20	0.42	0.34	0.06	0.57	
4	3	63.64	0.42	19.31	2.10	0.00	0.01	1.66	7.69	3.87	0.04	98.73	8.20-22.86
sd		0.04	0.07	0.99	0.03	0.03	0.03	0.08	0.47	0.01	0.32	1.08	

n: number of analysis;
sd: standard deviation
FeO_{tot} Total iron reported as FeO
An-Or (%): mole % of anorthite and orthoclase of the alkali feldspar.

Table 6: Table of experimental magnetite and ilmenite

Green Tuff Magnetite (GTT)

	n.	SiO_2	TiO_2	Al_2O_3	FeO_{tot}	MnO	MgO	CaO	Na_2O	K_2O	P_2O_5	Total	% Ulv
GT-R 7, 900°C, 1500 bar													
1	2	0.46	19.58	1.09	66.34	1.54	1.45	0.12	0.04	0.10	0.46	90.58	60.5

sd		0.31	0.40	0.05	0.83	0.08	0.06	0.13	0.04	0.30	0.31	0.00	
2	1	1.16	20.15	1.39	65.66	1.49	1.36	0.20	0.03	0.05	1.16	91.40	64.73
GT-R 8, 850°C, 1500 bar													
1	2	0.82	15.74	1.32	68.73	1.58	0.78	0.07	0.00	0.00	0.00	89.04	50.99
sd		0.06	0.35	0.00	0.50	0.13	0.00	0.03	0.00	0.00	0.00	1.07	
GT-R 10, 950°C, 1000 bar													
1	7	0.26	18.35	1.34	68.38	1.38	1.59	0.05	0.03	0.11	0.01	91.48	57.59
sd		0.04	0.28	0.13	0.93	0.16	0.05	0.01	0.04	0.05	0.01	0.81	
2	8	0.34	21.14	1.35	65.65	1.48	1.82	0.09	0.02	0.12	0.06	92.08	65.29
sd		0.25	0.46	0.09	0.31	0.17	0.02	0.04	0.04	0.03	0.06	0.80	
3	2	1.06	23.17	1.53	64.25	1.44	1.69	0.06	0.13	0.14	0.02	93.50	72.71
sd		0.95	0.04	0.25	0.65	0.11	0.01	0.00	0.03	0.01	0.00	0.37	
5	1	0.44	26.33	0.74	63.47	2.20	1.26	0.05	0.00	0.23	0.10	94.82	78.71
GT-R 2, 900°C, 1000 bar													
1	6	0.66	17.98	1.37	71.09	1.47	1.72	0.08	0.03	0.04	0.02	94.36	53.47
sd		0.68	0.47	0.37	0.55	0.21	0.03	0.04	0.05	0.07	0.09	1.33	
2	2	0.26	19.42	1.22	69.36	1.33	1.56	0.13	0.03	0.04	0.02	93.27	57.83
sd		0.05	0.10	0.04	0.53	0.02	0.11	0.08	0.05	0.09	0.00	0.94	
GT-R 4, 850°C, 1000 bar													
6	1	2.00	15.43	2.20	67.57	1.84	0.90	0.07	0.27	0.38	0.02	90.69	59.3
sd													
7	3	0.24	19.58	1.09	66.34	1.54	1.45	0.12	0.00	0.03	0.02	90.41	61.98
sd		0.10	0.20	0.03	0.40	0.30	0.11	0.02	0.00	0.01	0.00	0.09	
GT-R 11, 950°C, 500 bar													
1	3	0.58	20.13	1.47	65.70	1.36	1.65	0.07	0.01	0.10	0.02	90.97	63.28
sd		0.26	0.34	0.09	1.14	0.28	0.02	0.02	0.20	0.10	0.02	0.00	
2	2	0.44	20.17	1.46	65.26	1.77	1.87	0.10	0.12	0.12	0.00	91.30	67.02
GT-R 12, 900°C, 500 bar													
1	1	0.18	18.24	1.35	69.20	1.40	1.40	0.07	0.00	0.13	0.03	92.00	55.34
3	3	1.98	17.47	1.93	72.48	1.41	1.31	0.19	0.02	0.09	0.06	96.94	55.1
		0.2	1.04	0.34	0.29	0.09	0.01	0.05	0.01	0.02	0.00	0.42	

Post Cinque Denti Magnetite (PCD)

	n.	SiO_2	TiO_2	Al_2O_3	FeO_{tot}	MnO	MgO	CaO	Na_2O	K_2O	P_2O_5	Total	% Ulv
R2 900°C, 1500 bar													
2	3	1.80	16.07	2.94	70.50	1.31	1.00	0.14	0.26	0.29	0.05	94.34	54.91
sd		0.54	0.35	0.17	0.29	0.23	0.06	0.10	0.08	0.06	0.04	0.66	
R4 950°C, 1000bar													
2	2	0.85	21.82	1.61	67.83	1.59	1.48	0.10	0.08	0.12	0.00	96.13	66.86
sd		0.02	0.21	0.01	1.42	0.03	0.02	0.01	0.05	0.10	0.00	1.96	
3	3	0.34	19.65	1.19	70.26	1.23	0.79	0.10	0.07	0.13	0.06	94.39	59.73
sd		0.15	0.07	0.06	0.82	0.31	0.02	0.02	0.03	0.03	0.03	0.60	
R3 900°C, 1000 bar													
3	4	0.98	22.15	1.12	69.09	1.38	1.08	0.10	0.14	0.11	0.01	96.14	67.08
sd		0.25	1.23	0.14	1.26	0.12	0.12	0.06	0.11	0.05	0.02	1.92	

Green Tuff Ilmenite (GTT)

	n.	SiO_2	TiO_2	Al_2O_3	FeO_{tot}	MnO	MgO	CaO	Na_2O	K_2O	P_2O_5	Total	% Ilm
GT-R 7, 900°C, 1500 bar													
1	4	0.14	48.62	0.08	41.14	2.04	2.21	0.07	0.05	0.07	0.00	94.29	96.04
sd		0.15	0.59	0.02	0.88	0.20	0.07	0.04					
2	2	1.31	48.11	0.28	41.40	2.07	2.10	0.17	0.21	0.18	0.00	95.83	96.91
sd		1.73	0.17	0.29	0.76	0.29	0.18	0.01	0.28	0.04	0.00	2.22	
GT-R 10, 950°C, 1000 bar													
3	3	1.76	48.15	0.62	39.73	1.98	2.67	0.12	0.07	0.25	0.00	95.02	98.51
sd		1.25	0.10	0.35	0.01	0.15	0.01	0.02	0.01	0.00	0.00	0.90	

n: number of analysis;
sd: standard deviation
FeO_{tot} Total Iron reported as FeO
% Ulv: mole % of ulvospinel in the oxide; % Ilm: mole % of ilmenite in the oxide

Table 7: Table of experimental glasses

Green Tuff (GTT)

Run	n.	SiO_2	TiO_2	Al_2O_3	FeO_{tot}	MnO	MgO	CaO	Na_2O	K_2O	P_2O_5	Total	P.I
GT-R 9, 950°C, 1500 bar													
1	7	65.23	0.95	15.24	5.34	0.35	0.65	1.54	6.46	4.55	0.29	100.00	1.02
sd		0.36	0.07	0.11	0.23	0.07	0.03	0.04	0.81	0.18	0.09	0.94	
2	7	65.48	0.78	15.70	5.09	0.20	0.58	1.11	6.34	4.38	0.34	100.00	0.97
sd		0.44	0.10	0.22	0.22	0.10	0.04	0.05	0.57	0.14	0.09	0.67	
3	7	66.57	0.85	15.96	3.35	0.18	0.66	1.35	6.35	4.59	0.14	96.97	0.97
sd		0.65	0.09	0.31	0.19	0.09	0.02	0.08	0.38	0.12	0.09	0.63	
4	7	65.97	0.87	15.75	3.89	0.28	0.66	1.43	6.21	4.67	0.27	100.00	0.97
sd		0.12	0.12	0.13	0.33	0.11	0.03	0.04	0.60	0.16	0.10	0.80	
5	7	66.05	0.94	15.84	3.45	0.24	0.69	1.48	6.35	4.77	0.19	100.00	0.98
sd		0.52	0.11	0.10	0.27	0.10	0.03	0.07	0.52	0.13	0.04	0.49	
GT-R 7, 900°C, 1500 bar													
1	20	66.26	0.63	15.34	4.51	0.20	0.59	1.38	6.38	4.59	0.11	100.00	1.01
sd		0.81	0.09	0.33	0.68	0.09	0.10	0.16	0.62	0.11	0.07	0.00	
2	5	67.62	0.47	15.75	3.41	0.13	0.31	0.82	6.49	4.91	0.08	100.00	1.02
sd		0.83	0.06	0.17	0.35	0.06	0.11	0.08	0.94	0.14	0.06	0.92	
3	3	68.52	0.38	14.81	3.79	0.04	0.16	0.68	6.44	5.05	0.14	100.00	1.08
sd		0.17	0.08	0.40	0.28	0.07	0.09	0.05	0.80	0.12	0.03	0.80	
4	1	70.25	0.49	13.34	3.37	0.00	0.33	0.85	6.42	4.80	0.15	100.00	1.18
GT-R 8, 850°C, 1500 bar													
1	1	67.16	0.39	15.60	3.76	0.15	0.15	1.10	6.22	5.07	0.40	100.00	1.01
sd		0.77	0.07	0.43	0.50	0.03	0.00	0.30	0.50	0.18	0.02	0.90	
2	3	68.34	0.56	14.59	3.85	0.17	0.12	0.45	6.74	5.08	0.09	100.00	1.14
sd		0.30	0.04	0.09	0.72	0.02	0.04	0.03	0.20	0.13	0.02	0.55	
3	3	69.85	0.30	13.94	3.10	0.07	0.14	0.82	6.74	4.64	0.38	100.00	1.16
sd		0.80	0.02	0.60	0.22	0.01	0.03	0.04	0.00	0.35	0.08	0.72	

GT-R 10, 950°C, 1000 bar													
1	8	65.62	0.77	15.46	4.79	0.24	0.60	1.33	6.33	4.65	0.21	100.00	0.99
sd		0.55	0.08	0.17	0.25	0.09	0.03	0.05	0.73	0.16	0.07	0.00	
2	7	64.99	0.87	15.28	4.93	0.28	0.64	1.40	6.73	4.66	0.22	100.00	1.05
sd		0.58	0.28	0.19	0.55	0.13	0.04	0.08	0.55	0.14	0.14	0.80	
3	13	65.90	0.77	15.67	3.99	0.16	0.54	1.42	6.70	4.63	0.22	100.00	1.02
sd		0.56	0.06	0.13	0.48	0.08	0.02	0.36	0.58	0.19	0.28	0.00	
4	6	65.87	0.75	15.80	4.30	0.16	0.44	1.35	6.72	4.73	0.19	100.00	1.02
sd		0.35	0.10	0.13	0.35	0.06	0.02	0.09	0.56	0.09	0.07	0.43	
5	1	66.65	0.68	14.68	4.80	0.22	0.35	1.00	6.36	5.09	0.16	100.00	1.09
GT-R 2, 900°C, 1000 bar													
1	5	65.72	0.56	15.72	4.62	0.21	0.59	1.48	6.33	4.57	0.20	100.00	0.97
sd		0.39	0.07	0.12	0.48	0.10	0.03	0.10	0.09	0.04	0.10	0.46	
2	4	66.38	0.42	15.74	4.43	0.23	0.55	1.37	6.22	4.54	0.12	100.00	0.96
sd		0.75	0.10	0.04	0.30	0.08	0.11	0.19	0.37	0.15	0.11	1.08	
3	3	67.61	0.48	15.35	3.35	0.07	0.30	1.13	6.50	4.95	0.26	100.00	1.05
sd		0.16	0.51	15.08	0.39	0.09	0.29	0.10	0.07	0.08	0.09	0.79	
4	3	67.69	0.56	14.59	4.27	0.19	0.27	0.91	6.29	4.98	0.25	100.00	1.08
sd		0.61	0.11	0.42	0.70	0.05	0.03	0.14	0.73	0.15	0.22	0.79	
GT-R 4, 850°C, 1000 bar													
6	4	68.69	0.23	15.83	2.30	0.22	0.14	0.65	7.24	4.67	0.03	100.00	1.07
sd		0.33	0.07	0.30	0.08	0.08	0.01	0.04	1.52	0.62	0.07	1.60	
7	5	69.34	0.19	15.11	3.07	0.04	0.13	0.49	6.80	4.81	0.01	100.00	1.09
sd		0.24	0.02	0.10	0.16	0.05	0.01	0.03	0.20	0.07	0.01	0.10	
8	2	70.21	0.64	13.10	4.13	0.12	0.19	0.53	6.48	4.51	0.09	100.00	1.19
sd		0.45	0.10	0.67	0.44	0.07	0.09	0.10	0.30	0.13	0.04	0.92	
9	2	70.33	0.44	12.80	3.94	0.32	0.38	1.07	6.22	4.22	0.27	100.00	1.16
sd		2.84	0.14	0.77	0.57	0.04	0.19	0.53	0.92	0.37	0.16	0.85	
GT-R 14, 800°C, 1000 bar													
1	8	71.28	0.27	13.52	2.87	0.22	0.11	0.43	6.55	4.72	0.03	93.00	1.17
sd		1.64	0.08	0.46	0.35	0.07	0.15	0.39	0.86	0.50	0.12	2.33	
2	1	71.54	0.34	12.95	2.94	0.15	0.17	0.74	6.52	4.22	0.45	92.59	1.18
5	2	72.75	0.31	11.84	3.61	0.15	0.13	0.78	6.14	3.96	0.33	100	1.22
sd		1.21	0.01	0.58	0.48	0.12	0.01	0.14	0.25	0.04	0.03	1.13	
GT-R 3, 750°C, 1000 bar													
6	8	70.77	0.56	12.10	4.66	0.04	0.20	0.73	6.09	4.29	0.56	100.00	1.21
sd		0.20	0.19	0.80	1.10	0.13	0.18	0.43	0.85	0.52	0.17	4.12	
GT-R 11, 950°C, 500 bar													
1	16	64.92	0.87	15.08	5.29	0.19	0.63	1.44	6.71	4.67	0.21	94.82	1.07
sd		0.62	0.07	0.32	0.31	0.08	0.04	0.06	0.26	0.09	0.09	0.98	
2	7	65.00	0.87	15.18	4.72	0.24	0.63	1.51	6.58	4.60	0.28	100.00	1.04
sd		0.70	0.05	0.19	0.29	0.13	0.03	0.13	0.12	2.17	0.11	1.51	
3	4	65.19	0.86	15.22	4.65	0.22	0.57	1.43	6.94	4.74	0.18	100.00	1.09
sd		0.38	0.04	0.23	0.38	0.11	0.11	0.19	0.09	0.26	0.08	0.58	
4	6	65.20	1.00	14.87	5.05	0.33	0.28	1.49	6.31	5.47	0.00	100.00	1.10
sd		0.35	0.19	0.49	0.27	0.09	0.08	0.14	0.20	0.20	0.20	0.43	
5	2	65.77	0.74	14.31	5.67	0.18	0.38	1.37	6.30	5.00	0.28	100.00	1.10

sd		62.54	0.81	14.61	4.90	0.25	0.61	1.31	6.27	4.29	0.13	95.71	
GT-R 12, 900°C, 500 bar													
1	7	67.17	0.65	16.06	2.94	0.18	0.40	1.04	6.44	4.96	0.16	100.00	0.99
sd		0.78	0.13	0.20	0.76	0.10	0.02	0.14	0.84	0.18	0.10	0.68	
2	5	67.39	0.63	15.83	3.02	0.21	0.33	1.03	6.37	5.05	0.14	100.00	1.01
sd		0.51	0.13	0.16	0.28	0.14	0.01	0.06	0.75	0.12	0.08	0.78	
3	1	66.26	0.69	15.71	4.02	0.15	0.36	0.94	6.37	5.43	0.07	100.00	1.04
4	4	67.91	0.90	14.55	3.62	0.25	0.31	0.77	6.34	5.25	0.11	100.00	1.11
sd		0.11	0.16	0.22	0.04	0.20	0.01	0.09	0.01	0.08	0.06	0.10	
5	2	68.18	0.58	13.24	5.26	0.17	0.21	0.89	6.32	4.92	0.21	100.00	1.19
sd		0.83	0.08	0.70	0.36	0.15	0.29	0.74	0.08	0.20	0.03	0.00	

Post Cinque Denti Caldera (PCD)

Run	n.	SiO_2	TiO_2	Al_2O_3	FeO_{tot}	MnO	MgO	CaO	Na_2O	K_2O	P_2O_5	Total	P.I
R 1 950°C, 1500 bar													
2	10	66.72	0.74	15.55	3.87	0.14	0.56	1.88	6.10	4.37	0.08	100.00	0.95
sd		0.33	0.08	0.28	0.30	0.05	0.01	0.04	0.18	0.09	0.07	0.49	
3	10	67.10	0.70	15.75	3.42	0.18	0.43	1.72	6.49	4.45	0.11	97.49	0.98
sd		0.94	0.10	0.28	0.17	0.07	0.03	0.07	0.11	0.15	0.08	1.06	
4	10	67.35	0.71	15.72	3.26	0.18	0.37	1.52	6.05	4.51	0.11	100.00	0.94
sd		0.23	0.07	0.22	0.23	0.06	0.03	0.09	0.14	0.08	0.08	0.32	
5	3	67.10	0.62	15.29	4.14	0.19	0.25	1.31	6.07	4.93	0.10	98.41	1.00
sd		0.66	0.15	0.62	0.13	0.10	0.06	0.18	0.71	0.13	0.04	0.89	
R2 900°C, 1500 bar													
2	9	67.51	0.41	15.93	3.12	0.12	0.29	1.45	6.42	4.58	0.17	100.00	0.97
sd		0.33	0.06	0.17	0.28	0.10	0.04	0.18	0.74	0.15	0.10	0.91	
R4 950°C, 1000bar													
1	20	66.12	0.74	15.32	4.72	0.19	0.56	1.96	5.87	4.39	0.13	100.00	0.94
sd		0.47	0.10	0.18	0.23	0.09	0.02	0.10	0.73	0.21	0.08	1.03	
2	20	65.23	0.78	15.95	4.65	0.22	0.56	1.93	6.15	4.37	0.16	100.00	0.93
sd		0.80	0.08	0.23	0.24	0.08	0.02	0.25	0.15	0.16	0.14	0.06	
4	10	67.45	0.69	15.12	3.46	0.16	0.37	1.34	6.46	4.81	0.17	100.00	1.05
sd		0.45	0.09	0.17	0.34	0.08	0.03	0.08	0.12	0.19	0.08	0.75	
5	4	68.53	0.79	13.97	3.64	0.18	0.31	0.91	6.07	5.41	0.18	100.00	1.13
sd		0.29	0.11	0.23	0.28	0.06	0.02	0.03	0.11	0.11	0.02	0.59	
R3 900°C, 1000 bar													
2	15	66.84	0.56	15.81	3.81	0.18	0.33	1.41	6.45	4.54	0.09	100.00	0.98
sd		0.96	0.24	0.22	0.63	0.12	0.06	0.16	0.12	0.15	0.07	0.57	
3	12	68.25	0.44	15.02	3.23	0.15	0.24	1.09	6.33	5.11	0.15	100.00	1.06
sd		0.30	0.06	0.22	0.25	0.12	0.06	0.05	0.14	0.01	0.03	0.10	
4	5	69.72	0.39	13.28	4.05	0.13	0.18	0.88	6.16	5.10	0.12	100.00	1.18
sd		0.50	0.07	0.10	0.19	0.11	0.02	0.29	0.09	0.07	0.14	0.43	

n: number of analysis;
sd: standard deviation
FeO_{tot} Total Iron reported as FeO
P.I peralkalinity index

Chapter 5

Crystallisation experiments on two pantellerite starting materials *(how small variations in bulk composition and redox conditions influence phase equilibria)*

5.1 INTRODUCTION

At Pantelleria island peralkaline rhyolites are the most abundant erupted products, occurring mostly as pyroclastic flows then as pumice fall deposits or obsidianaceous-lavas flows (Mahood & Hildreth, 1986). In contrast with the early petrological studies on Pantelleria island (Wolff & Wright 1981; Lowenstern & Mahood 1991), recent analytical, thermodynamic and experimental studies have emphasised several petrological aspects of the peralkaline rhyolite of Pantelleria such as the low temperature equilibration (T≤ 750°C), the reducing redox conditions (White et al., 2005; 2009; Di Carlo et al., 2010) and the relative high melt water content despite the reduced conditions (Gioncada & Landi 2010; Lanzo et al., 2013; Neave et al., 2012).

Although excellent progresses have been made, the precedent phase equilibria experiments were not able to reproduce the **full mineral assemblage** observed in natural pantellerite as well as the relations between peralkalinity index and mineral assemblages observed in natural rocks (White et al., 2005). Moreover, the pre-eruptive conditions of the last caldera forming eruption at Pantelleria (Green Tuff eruption) have been only partially investigated (Wolf & Wright 1981, White et al., 2005; Lanzo et al., 2013) with results not always comparable. On the other hand several research groups have paid attention to different aspects of the Green Tuff eruption such as the emplacement mechanism of the pyroclastic density current (Williams 2010; Williams et al., 2014) as well as the volatiles dissolved in the magma before the eruption (Lanzo et al., 2013).

In this study we present the results of phase equilibria experiments performed on two pantellerites with similar compositions, the first is representative of the Green Tuff eruption while the second belongs to one of the last energetic eruption at Pantelleria, the Fastuca eruption (Orsi et al., 1989; Di Carlo et al., 2010). **Phase relationships** were established at 1 kbar, for temperature in the range 680°C - 900°C and redox condition between around the FMQ (fayalite-magnetite-quartz) buffer. Our attentions were restricted to the role played by variations in **temperature** and the **redox conditions** on the mineral assemblage of pantellerites. By comparing the experimental phase relationships and compositions with

natural products it have been possible constraining the pre-eruptive conditions (P-T-H_2O_{melt}-fO_2) of the Green Tuff Plinian as well as to add new constraints on the stability of mineral phases such as fayalite and amphibole, common mineral phases in peralkaline rhyolites.

5.2 Starting materials and experimental conditions

5.2.1 Experimental strategy and starting materials

We have performed ten phase equilibria experiments choosing the experimental conditions on the base of previous works carried out on the peralkaline rhyolites of Pantelleria. All experiments were performed at pressure of 1 kbar while the range of temperature investigated varied between 680°C and 900°C, covering widely the temperature range inferred for pantellerites by precedent petrological and experimental works (White et al., 2005, 2009; Di Carlo et al., 2010). As regards the fO_2, our experiments were conducted imposing redox conditions around the FMQ buffer and were explored also redox conditions lower than the FMQ buffer.

We have chosen as starting materials **two pantellerites**,

(i) one is representative of the basal pumice fall-out of the *Green Tuff eruption* (Age 45 ka), last caldera forming eruption at Pantelleria and the sole to be chemically zoned from pantellerite at bottom to trachyte at the top of the deposit (see Chapter 4), reflecting a chemical zoning in the magma reservoir,

(ii) the second belongs to a violent strombolian eruption (Fastuca eruption, age ca. 10 ka), the same used by Di Carlo et al., (2010). The pre-eruptive conditions (P-T-H_2O_{melt}-fO_2) of Fastuca eruption were well established experimentally by Di Carlo et al., (2010), therefore, it represents a starting point to explore the effects on phase relationships and compositions of further variations in intensive parameters (T-fO_2).

The detailed description of the eruptive units is contained in chapter 3, here we shortly summarize the description of the two natural samples used as starting materials in order to be able to compare immediately the experimental results and natural products.

The pumice of Green Tuff basal fall-out and Fastuca eruptive unit are both pantelleritic in composition even though small differences in major element and crystal content (Table 1). The Green Tuff pumice has crystal content **≤ 10 vol%** and it is richer in iron and SiO_2 than the Fatsuca pantellerite, which has a crystal content close to the **20 vol%**. The mineral assemblage of both rocks is dominated (in order of abundance) by alkali feldspar, aenigmatite and clinopyroxene, even thought fayalite, amphibole and quartz can be found in the mineral assemblage (White et al., 2005; Rotolo et al., 2007).

Alkali feldspars are homogeneous in compositions ($An_{<0.1}Ab_{65-64}Or_{35-36}$) and they are euhedral to subeuhedral with maximum length of 1 mm in the pumice of Green Tuff basal member and 3 mm in the Fastuca unit; microphenocrysts and microlite of alkali feldspar are present only in the Fastuca pantellerite. *Clinopyroxene* microphenocrysts (maximum length 0.5mm) in the samples studied present a slightly different composition: the clinopyroxene of Green Tuff basal fall-out are Wo_{40}-En_{10}-Fe_{50} whereas those of Fastuca eruptive unit have composition Wo_{43}-En_{4}-Fs_{53}. NaO_2 content in clinopyroxenes of both samples is 1.8± 0.2 wt% and only in the Fastuca eruptive unite were found rare microlite of aegirine (Di Carlo et al., 2010). *Aenigmatite* microphenocrysts in both samples have composition quite homogeneous with XTi [=Ti/(Ti+Fe_{tot})]= 0.15-0.17. Rare microphenocryst of ilmenite have been found in the pumice of Green Tuff basal member, in groundmass or included into aenigmatite crystals. As regard the *amphibole*, the composition varies within the ferrorichterite-arfvedsonite groups (Na-Fe-rich amphibole). Amphiboles of Green Tuff pantellerite and Fastuca pantellerite have composition slightly different, the first are richer in CaO and MgO (White et al., 2005) while the second are richer in FeO and Na_2O and poorer in CaO and MgO (Rotolo et al., 2007; Di Carlo et al., 2010). Fayalite crystals have compositions $Fa_{91-96,}$ typical of the fayalite in peralkaline rhyolites of Pantelleria.

Due to lower crystal content, the pumice of Green Tuff basal fall-out were crushed finely in a 10-30μm powder and the latter was used directly as starting material; this procedure was the same used by Scaillet & Macdonald (2001; 2003; 2006) performing hydrothermal experiments on the peralkaline rhyolites of Kenya rift valley. On the other hand, the Fastuca starting material was prepared following the procedure reported in chapter 2 (paragraph 2.1.1).

In the following paragraphs it will be used Green Tuff pantellerite (GTP) and Fastuca pantellerie (FP) to refer to the experiments performed with the starting materials described previously. The composition of the starting material and mineral phases of the natural rocks are reported in table 5.1

Table 5.1: Composition of the starting glasses Green Tuff Pantellerite *(GTP)* and Fastuca Pantellerite *(FP)* and the respective natural mineral phases in the starting rocks

GTP n:	Starting material 20	Afs 20	sd	Cpx 6	sd	Ol 4	sd	Aenig 9	sd	Ilm 4	sd
SiO_2 (wt%)	72.74	67.16	0.79	49.25	0.41	30.32	0.70	41.38	0.64	0.1	0.00
TiO_2	0.53	0.03	0.00	0.36	0.12	0.00	0.00	8.97	0.23	49.41	0.22
Al_2O_3	9.02	17.73	0.27	0.14	0.05	0.00	0.00	0.66	0.04	0.03	0.01
FeO_{tot}	6.25	0.84	0.1	25.33	0.87	62.01	1.5	39.67	0.61	43.78	0.3
MnO	0.24	0.00	0.00	1.42	0.19	2.00	0.05	1.21	0.13	1.92	0.03
MgO	0.51	0.00	0.00	3.16	0.49	4.05	2.00	0.99	0.37	0.01	0.00
CaO	0.46	0.01	0.01	16.84	0.79	0.43	0.43	0.63	0.08	0.02	0.01
Na_2O	7.31	7.63	0.29	1.96	0.25	0.00	0.00	6.62	0.20	0.00	0.00
K_2O	2.87	6.14	0.23	0.06	0.00	0.00	0.00	0.03	0.00	0.00	0.00
P2O5	0.06	0.00	0.00	0.00	0.0	0.00	0.00	0.00	0.00	0.00	0.00
sum	100.00	99.51	0.81	100.6	0.80	99.11	0.92	98.84	0.88	95.30	0.31
P.I	1.70										
Fa						90.41					
Wo				39.97							
En				10.44							
Fs				49.59							
An		0.1									
Ab		65.3									
Or		34.6									

FP* n:	Starting material	Afs	sd	Cpx	sd	Ol	sd	Aenig	sd	Amph	sd	Na-cpx	sd
SiO_2 (wt%)	69.45	65.00		47.2		29.28		40.5		49.2		52.9	
TiO2	0.48	0.00		0.73		0.07		9.00		1.77		0.22	
Al_2O_3	10.15	18.45		0.42		0.20		0.52		0.65		0.77	
FeO_{tot}	7.87	1.05		27.7		65.15		40.5		34.2		32.3	
MnO	0.21	0.00		1.42		3.93		1.22		1.16		0.84	
MgO	0.10	0.00		1.33		0.90		0.4		0.89		0.08	
CaO	0.53	0.00		17.9		0.47		0.52		3.3		1.36	
Na_2O	6.71	7.42		1.77		0.00		7.11		7.32		11.21	
K_2O	4.46	6.19		0		0.00		0.01		1.48		0.16	
P2O5	0.04	0.00		0.0		0.00		0.00		0.00		0.00	
sum	100.00	98.1		98.5		100.0		99.80		100.0		99.8	
P.I	1.56												
Fa						92.10							
Wo				42.98									
En				4.44									
Fs				52.57									
An		0.01											
Ab		64.56											
Or		35.44											

n, number of analyses; sd, standard deviation; FeOtot total iron reported as FeO. Ol, olivine; cpx, clinopyroxene; afs, alkali feldspar, mt, magnetite; ilm, ilmenite.Fa (mol%)=100(Mg/Mg+FeOtot) in olivine. Wo, En and Fs were calculated as in the study by Morimoto (1989). P.I = peralkalinity index (molar Na_2O+K_2O/Al_2O_3). An=100[Ca/(Ca+Na+K)]; Ab=100[Na/(Ca+Na+K)]; Or=100[K/(Ca+Na+K)]. End-members calculated as in the study by Deer et al., (1992).

*Apart from the starting material, the analyses of mineral phases are taken from Di Carlo et al., 2010

5.2.2 Experimental methods and analytical techniques

The experimental methods and analytical techniques used in this study have been described for extended in **Chapter 2**. Experimental charges were prepared following the procedure described in detail in paragraphs 2.1.2, each experiment consisted of 4-5 capsules and the capsules were prepared with XH_2O in the range 0.3-1. As regard the experimental apparatus, the **internally heated pressure vessel** used for the experiments has been described in paragraph 2.1.3 while the experimental products were analysed by scanning electron microscope and electron microprobe using the analytical conditions reported in paragraph 2.2

In the following paragraph, it will be described in detail only the calculations used to determine the (i) redox conditions into the capsules and (ii) the melt water content of the experimental products.

5.2.3 fH_2, fO_2 and water content in the experimental charges

Knowing the fH_2 in the vessel at experimental conditions (high T and P) is necessary in order to compute the fO_2 within the capsules. Two different Ar/H_2 ration were used to reach (i) redox conditions similar to those explored by Di Carlo et al., 2010 (~ FMQ) and (ii) redox conditions lower than the FMQ buffer. To be sure of the control on the experimental redox conditions, it was replicated an experiment (#GT R14) performed by Di Carlo et al., (2010) and the results in term of phase relation were exactly the same (table 5.2).

In those run where the solid sensor were used, the fH_2 prevailing during the experiments was calculated from the water dissociation equation $K_w = f°H_2O / (fH_2 \times fO_2^{1/2})$ using the water dissociation constant (K_w) from Robie et al., (1979), $f°H_2O$ at P and T of interest from Burnham et al., (1969) and fO_2 from the sensors. Redox conditions lower than FMQ are not recorded by Co-Pd solid sensor (Taylor et al., 1992). Therefore, for those runs aimed to explore redox conditions slightly lower than FMQ buffer, we used an empirical relation reported by Di Carlo et al., (2010). This relationship, extrapolated from numerous experiments performed using H_2 membranes (Scaillet at al., 1992), allows obtaining the fH_2 at P and T of equilibrium during the experiment by multiplying for a factor of 3 (±1) the hydrogen (bar) loaded at room temperature. It is worth to note that if the empirical relation is applied also for those experiments in which solid sensors were used the results are consistent.

The fO_2 specific to each single capsule was calculated in the following way. For H_2O-saurated charges, fO_2 was calculate from the water dissociation equation using the water constant (K_w) from Robie et al., (1979) and $f°H_2O$ at P and T of interest from Burnham et al., (1969) while the fH_2 was obtained as explained before. For the under-saturated charges, instead, fH_2O was derived from the relation $fH_2O = f°H_2O \times XH_2O_{in}$ (moles). In table 5.2 are reported the value of fO_2 also expressed in term of ΔNNO, the redox conditions investigated for the Green Tuff pantellerites range from NNO -0.5 to -2.5 while for the Fastuca pantellerite from -1.25 to 2.5. It is important to note that the most relevant differences in redox conditions regard water rich capsules, for which the control of the redox conditions is better than water poor charges.

Due to the high crystal content of most of the charges, the direct measure of water content resulted difficult or yielded meaningless results, thus the water content dissolved in the melt was computed in the following way. Using the results of a series of water saturated experiments performed on the Fastuca pantellerite, it was first derived an empirical relationships between $f°H_2O$ and the melt water content at saturation conditions: $\boldsymbol{f°H_2O = a(H_2O_{melt}\ wt\%)^b}$. The coefficient obtained are a= 67.72 and b= 1.84, the H_2Omelt was then computed by inverting the precedent equation $\boldsymbol{[H_2O_{melt}\ (wt\%) = (fH_2O/67.72)^{1/1.84}]}$ and considering the fH_2O for the under-saturated charges as calculated before [$fH_2O = f°H_2O \times XH_2O_{in}$ (moles)]. This procedure, used also in other experimental studies (i.e Di Carlo et al., 2010; Andujar et al., 2016) is equivalent to assume an ideal behaviour in the H_2O-CO_2 fluid phase and the values obtained must be considered as maximum dissolved water contents.

Nevertheless, in the crystal-free charges (i.e GTR1-GTR4 and GTR22) the water content was also measured using the **"by-difference"** method (Devine et al., 1995) and the results obtained (table 5.2) are consistent with those computed through the method explained before. As standards for the "by-difference" methods were used four of hydrous glasses with pantelleritic composition and water content from 0 to 5.20 wt% (determined by Karl Fisher Titration). Glassy standards were analysed before each probe session focused to analyse water content in experimental glasses. The accuracy of by-difference method for H_2O_{melt} is estimated to be ± 0.5 at the best.

Table 5.2: Experimental run conditions and results

Green Tuff pantellerite (GTP)

Run	XH_2O_{in} moles [1]	H_2O_{melt} (wt%) [2]	H_2O by-diff (wt%)	log fO_2 [4] (bar)	Δ NNO [5]	Phase assemblage and abundances (wt%)	Crystal (wt%)	R^2
GT-R 2, 900°C, 1000 bar, PH_2 [6]=6 bar (target: FMQ buffer), 96h								
1	1.00	4.52	-	-12.35	-0.41	Gl only	-	-
2	0.81	3.10	-	-12.95	-1.02	Gl only	-	-
3	0.52	1.29	-	-14.35	-2.41	Gl only	-	-
GT-R 4, 850°C, 1000 bar, PH_2= 6 bar, 145h								
1	1.00	4.52	4.65	-13.35	-0.48	Gl only	-	-
2	0.81	4.00	3.60	-13.55	-0.68	Gl only	-	-
3	0.52	3.10	2.23	-13.96	-1.08	Gl only	-	-
4	0.26	2.35	2.11	-14.40	-1.53	Gl (97.6), Cpx (2.4)	2.4	0.68
5	0.1	1.29	-	15.36	2.48	Gl (96.6), Cpx (2.7), afs (0.6)	3.4	0.62
GT-R 1, 800°C, 1000 bar, PH_2=6 bar, 196 h								
1	1.00	4.52	4.25	-14.40	-0.52	Gl (97.9), Cpx (0.9), Amph (1.2)	2.1	0.28
2	0.82	4.01	3.22	-14.59	-0.70	Gl (95.7), Cpx (0.8), Amph (3.6)	4.3	0.34
3	0.51	3.10	-	-14.99	-1.11	Gl (95.1), Cpx (1.0), Amph (3.3), Afs (0.6)	3.9	0.42
4	0.33	2.35	-	-15.44	-1.55	Gl, (88.9) Cpx(0.2), Amph (2.4), Afs (7.8), qz (1.49)	11.9	0.02
5	0.10	1.29	-	-16.39	-2.51	Gl, (69.1) Cpx (4.66), Amph (4.9), Afs (18.1), qz (3.22)	30.8	0.63
GT-R 3, 750°C, 1000 bar, PH_2=5,5bar, 96h								
1	0.99	4.53	-	-15.48	-0.48	Gl (90.2), Cpx (1.1), Amph (8.7)	9.8	0.43
2	0.80	4.00	-	-15.68	-0.68	Gl (85.8), Cpx (1.1), Amph (8.8), Afs (3.9)	14.2	0.29
3	0.48	3.10	-	-16.08	-1.09	Gl (65.5), Cpx (1.6), Amph (6,1), Afs (26.45), aenig (0.4)	34.5	0.82
4	0.30	2.35	-	-16.53	-1.53	Gl, Cpx, Amph, Afs	-	-
5	0.10	1.30	-	-17.48	-2.54	Gl , Cpx, Amph, Afs	-	-

Fastuca Pantellerite (FP)

Run	XH_2Oin moles [1]	H_2O_{melt} (wt%) [2]	H_2O by-diff (wt%)	log fO_2 [4] (bar	Δ NNO [5]	Phase assemblage and abundances (wt%)	Crystal (wt%)	R^2
GT-R 14 800°C, 1000 bar, PH_2=6 bar (target: FMQ buffer), = Run 8 of Di Carlo et al., (2010)								
1	1.00	4.53	-	-14.45	-0.57	Gl only	-	-
2	0.80	4.00	-	-14.63	-0.75	Gl, cpx	-	-
3	0.51	3.10	-	-15.06	-1.17	Gl, cpx, Afs	-	-
4	0.32	2.35	-	-15.40	-1.51	Gl, cpx, Afs, qz	-	-
GT-R22 800°C, 1000 bar, 96 h, PH_2=9,5bar, (target: below FMQ buffer),								
1	1.00	4.52	4.40	-15.14	-1.25	Gl only	-	-
2	0.83	4.09	3.55	-15.33	-1.44	Gl only	-	-
3	0.60	3.10	2.03	-15.74	-1.85	Gl only	-	-
4	0.29	2.35	1.60	-16.18	-2.30	Gl only	-	-
GT-R20 750°C, 1000bar, PH_2=9,5bar, (target: below FMQ buffer),								

1	1.00	4.53	-	-16.31	-1.31	Gl (96.3), cpx (1.8), fa (2.7)	3.7	0.98
2	0.83	4.00	-	-16.51	-1.50	Gl (81.3), Cpx (2.7), fa (1.8), Afs (14.2)	18.8	0.30
3	0.52	3.10	-	-16.92	-1.92	Gl (69.7), Cpx (2.1), fa (2.0) aenig (0.76), Afs (26.1)	30.3	0.10
4	0.30	2.35	-	-17.36	-2.36	Gl (36.4), Cpx (1.2), Aenig (5.5) Afs (47.0), Qz (9.6)	63.3	0.62
GT-R23 680°C, 1000 bar, PH_2=9,5bar, 86 h, (target: below FMQ buffer),								
1	1.00	4.53	-	-18.16	-1.41	Gl (71), Cpx (2.8), Amph (2.3), Aenig(5.4) Afs (18.4)	29	0.05
2	0.82	4.06	-	-18.35	-1.60	Gl (61.9), Cpx (4.0), Amph (0.2), Aenig(6.1) Afs (27.8)	38.1	0.28
3	0.58	3.10	-	-18.76	-2.01	Gl (36.4), Cpx (4.0), Amph (8.0), Aenig (1.3), Afs (43.7), Qz (6.7)	63.4	0.49
4	0.35	2.51	-	-19.21	-2.45	Gl, Cpx,Amph, Aenig, Afs,	60.6	-

[1] $XH_2O_{in,}$ initial mole fraction of H_2O of the C-H-O fluid loaded in the capsule.
[2] H_2O_{melt} (wt%), dissolved melt water content determined following the method of Scaillet & Macdonald (2006) and Andujar et al., (2016).
[3] H_2O_{melt} (wt%), dissolved melt water content calculated following the by-different method of Devine et al., (1995).
[4] $fO_{2,}$ logarithm of the oxygen fugacity (bar) calculated from the experimental fH_2 obtained from the solid sensors (see the text).
[5] Δ NNO log fO_2-logfO_2 of the NNO calculated at P and T respectively from Pownceby & O'Neill (1994).
[6] PH_2, hydrogen pressure loaded in the vessel at room temperature. Crystal content, values indicate the phase abundance in the charge (in wt %). Gl, glass; Cpx, clinopyroxene; fa, fayalitic olivine; Amph, amphibole; Aenig, aenigmatite; Afs, alkali feldspar; Qz, quartz.

5.3 Experimental results

5.3.1 General observations

Crystallization experiments performed in our study show similar textural features already observed in other experiments carried out on similar composition (e.g Scaillet & Macdonald 2001, 2003, 2006; Di Carlo et al., 2010). The achievement of near-equilibrium conditions during the experiments is suggested by several observations, among these: **(i)** the homogeneous distributions of phases within the charges, **(ii)** the euhedral shape of crystals, **(iii)** the regular variations of crystal abundances and composition as function of T, H_2O_{melt} and fO_2. **(iv)** homogenous glass composition probed in different places within the charge. Moreover, the run durations were long enough (> 140 h) to ensure the crystal-melt equilibrium in agreement with other works on silicic rich compositions (Di Carlo et al., 2010; Cadoux et a.2014).

Crystallization experiments reproduced all mineral phases observed in natural pantellerite, indeed, the mineral phases identified are clinopyroxene, olivine, alkali feldspar, ilmenite, aenigmatite, quartz and amphibole. All charges present also residual glass and vesicles, the latter indicating a fluid saturation conditions in the capsules during the experiments.

Chemical analysis of minerals and glasses were used to perform *mass-balance calculation* (Albarède 1995) in order to obtain quantitative phase proportions for each charge (Table 5.2). Square residual of mass-balance calculation are generally ≤ 1 suggesting that during the calculation (i) no major phases were overlooked and (ii) the Na of experimental glasses have been evaluated correctly. As regard the phase composition, the experimental mineral phases produced have homogeneous composition and moreover the variation in T, XH_2O and fO_2 are well displayed in the composition of solid-solution phases (i.e iron-bearing mineral phases).

Microprobe analyses of alkali feldspar in some case resulted difficult because the poor contrast in back-scatter (BSE) electron images between the crystals and residual glass. Moreover, the presence of very small oxides inclusion increased the total iron content of the alkali feldspar, anyhow we reported in the appendix (table 3) only alkali feldspar analysis which iron content is less of 3 wt%. Ilmenite analyses, due to the small size, in some case resulted contaminated by the glass, only the ilmenite analysis with $SiO_2 < 1$ wt% were taken into account. Also clinopyroxene, in the experiment at 680°C, was difficult to analyse

because the very small size (2-7 μm). Phase relations for both compositions are showed in **Fig. 5.1** while phase proportion and composition are listed in table 1 to 6 in appendix and showed in **Fig. 5.2-5.8.**

5.3.2 Phase relationships

Experimental phase relationships of both the starting compositions were established at P= 1 kbar and temperature between 900 and 750°C for the Green Tuff pantellerite and T= 800-680°C for the Fastuca pantellerite. Although the pressure and temperature conditions investigated are similar, the phase diagram in Fig. 5.1 differ for the redox conditions imposed during the experiment; for the Green Tuff pantellerite (GTP) they range between ΔNNO -0.5 to -2.5 while for the Fastuca pantellerite (FP) between ΔNNO -1.5 and -2.5. In both projections the stability field of clinopyroxene, alkali feldspar, aenigmatite quartz and amphibole are well established while olivine and ilmenite were found only a narrow stability field in the experimental products of Fastuca pantellerite.

Green Tuff pantellerite (GTP)

At 1 kbar and 900°C Green Tuff pumice fall charges are at supra-liquidus conditions regardless the melt water content. At 850°C clinopyroxene is the liquidus phase for H_2O melt < 2.5 wt% (Fig. 5.1a) and it is followed by alkali feldspar at H_2O_{melt} close to 1 wt%. At T ≤ 800°C clinopyroxene is liquidus phase at water saturation conditions while alkali feldspar expands its stability field becoming stable when the H_2O_{melt} is close to 4 wt% at 750°C. At T= 800°C and H_2O_{melt} around 2.5 wt% quartz joins the crystallization sequence, whereas aenigmatite becomes stable at 750°C and $H_2O_{melt} \leq 3$ wt%. As regard the amphibole, it is stable in all charge at T < 850°C regardless the water content (Fig. 5.1a).

Fastuca pantellerite (Post Cinque Denti caldera pantellerite) FP

The different redox conditions explored for the Fastuca pantellerite arise in some remarkable differences in the phase relationships established by Di Carlo et al., (2010) as well as with those of the Green Tuff pantellerite. At 800°C all charges are at supra-liquidus conditions regardless the water content (Fig.5.1b). At T= 750°C clinopyroxene and Fe-rich olivine are the liquidus phase at H_2O_{melt} saturation conditions (~ 4.5 wt%). For H_2O melt = 4 wt% alkali feldspar joins the crystallization sequence while at 680°C it becomes stable at H_2O_{melt} saturation condition. As regards fayalitic olivine and ilmente, their stability field is limited at 750°C and for a or a narrow range of melt water content that is between 3- 4.5 wt% for olivine and 3-4 wt% for ilmenite (Fig. 5.1b); both disappear when melt water content is lower than 3 wt%. It is worth to note that, in contrast to the natural rocks, fayalite has not been found coexisting with quartz. Aenigmatite become stable at 750°C and $H_2O_{melt} \leq 3$ wt% and together with amphibole remain stable at 680°C regardless the melt water

content. Lastly, quartz crystalizes only when melt water content is lower than 2.5 wt% at 750°C or lower than 3.5 wt% at 680°C.

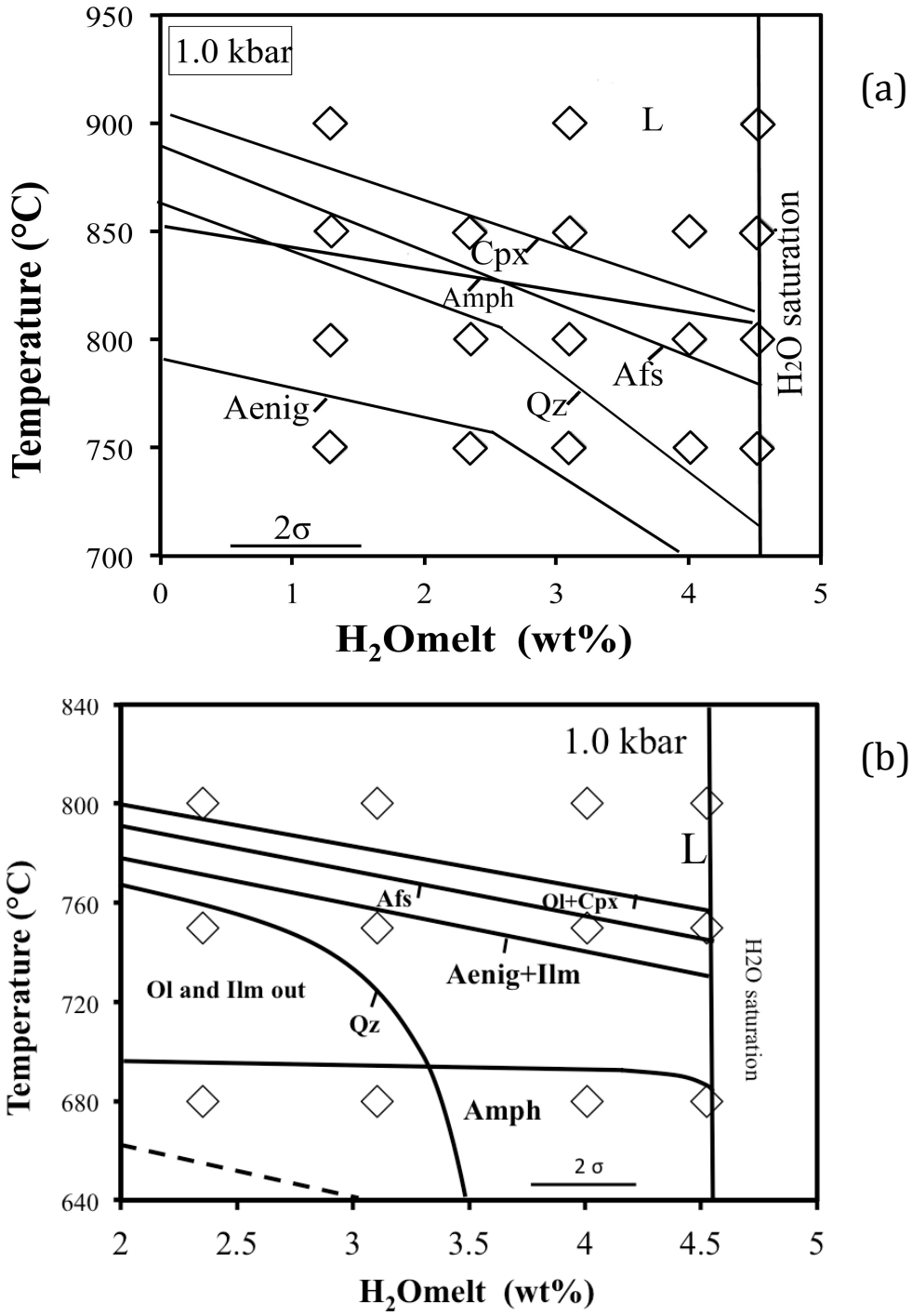

Figure 5.1: a) Phase relationship of the Green Tuff pantellerite (GTP) in the T-H_2Omelt section at 1.0 kbar and fO_2 ~ FMQ. b) Phase relationships of the Fastuca pantellerite (FP) at 1.0 kbar and fO_2 < FMQ buffer (indicare il range). L, liquid; Cpx, clinopyroxene; Ol, olivine; Afs, alkali feldspar; Qz; quartz; Ilm; ilmenite; Aenig, aenigmatite. The tick on a phase boundary marks the side on which an experimental phase is stable. Dashed lines are estimated phase boundary.

5.3.3 Phase proportions

Phase proportions of both compositions obtained from mass-balance calculations are listed in Table 5.2, only for the charge GTR3-4 GTR3-5 and GTR23-4 mass-balance calculation is missing due to the difficulties to probe the residual glass. The amount of liquid varies from 100 % to 36 wt%, decreasing when temperature and melt water content decrease (Fig. 5.2a). Supra-liquidus conditions were attained at 900°C for the Green Tuff pantellerite and 800°C for Fastuca pantellerite while the highest crystallized charges are those at T≤ 750°C (Fig. 5.2a). Decreasing temperature and H_2Omelt alkali feldspar become the most abundant mineral phase reaching a mass proportion of 43wt% in the most crystallized charges (Fig. 5.2b). The sum of iron-bearing mineral phases (clinopyroxene, olivine, aenigmatite and amphibole) never exceeds the 11 wt% while quartz proportion ranges between 3-9 wt%. Mass proportions of alkali feldspar and clinopyroxene are comparable with those obtained by Di Carlo et al., (2010) and Scaillet & Macdonald (2003, 2006) as well as with those of the natural rocks. As regard olivine, this is the first time that it has been synthesized in experimental pantellerite and the mass proportion in the experimental charges results comparable to that of natural rocks. In contrast, as already pointed out by Di Carlo et al., (2010), the lower mass proportion of quartz with respect to the experimental products of Scaillet & Macdonald (2003, 2006) may derive from the lower silica content in pantellerite from Pantelleria. Regarding the amphibole proportion, even if in our experiments it crystallizes in a wide range of temperature (Fig.5.2c), its mass proportion never get the 21 wt% obtained by Di Carlo et al., (2010) in the lower temperature experiments (680°C). It is worth noting that the phase proportions of each mineral phase obtained in our experiments match the proportions of those observed in natural pantellerite.

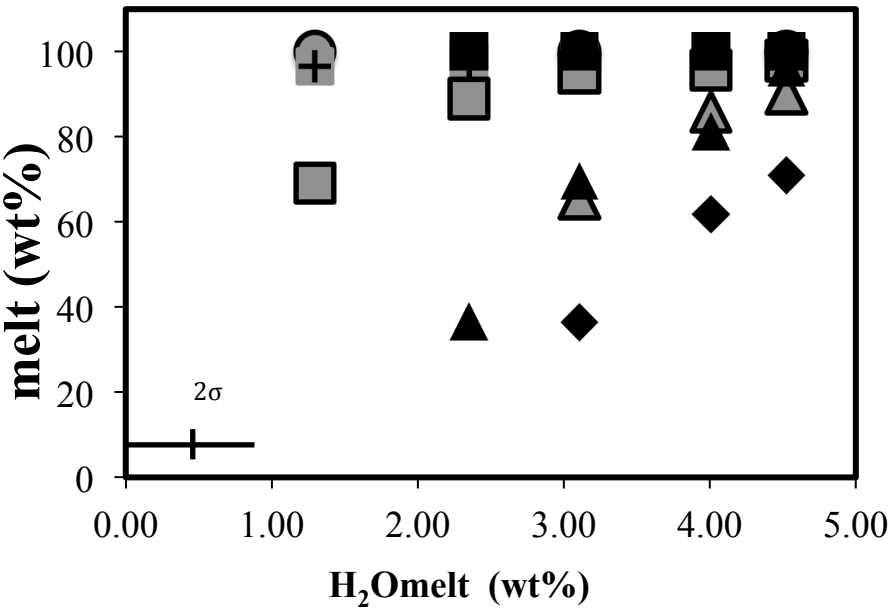
melt (wt%)
100
80
60
40
20
0
2σ
0.00
1.00
2.00
3.00
4.00
5.00
H2Omelt (wt%)

a)

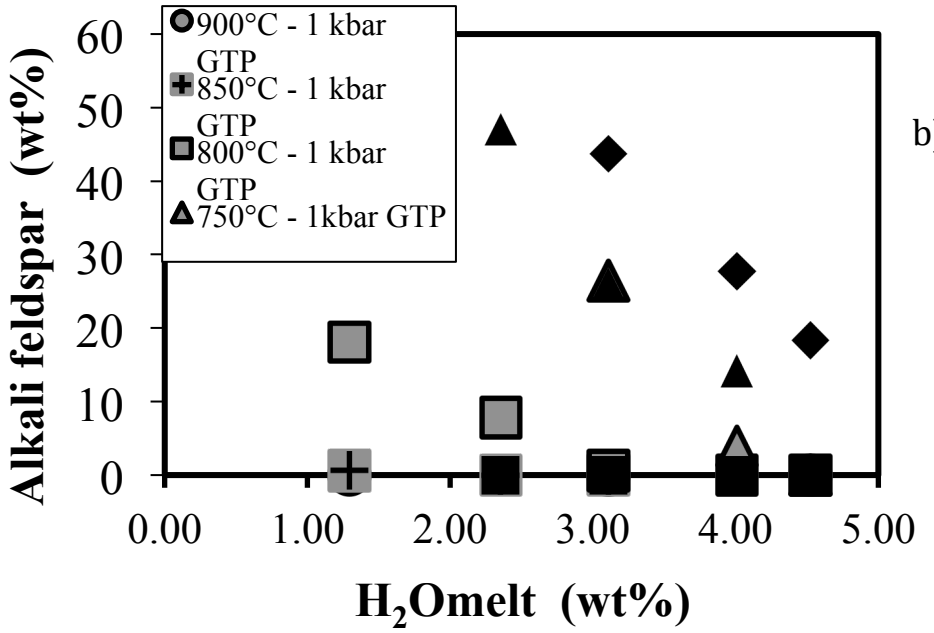
900°C - 1 kbar GTP
850°C - 1 kbar GTP
800°C - 1 kbar GTP
750°C - 1kbar GTP
Alkali feldspar (wt%)
60
50
40
30
20
10
0
0.00
1.00
2.00
3.00
4.00
5.00
H2Omelt (wt%)

b)

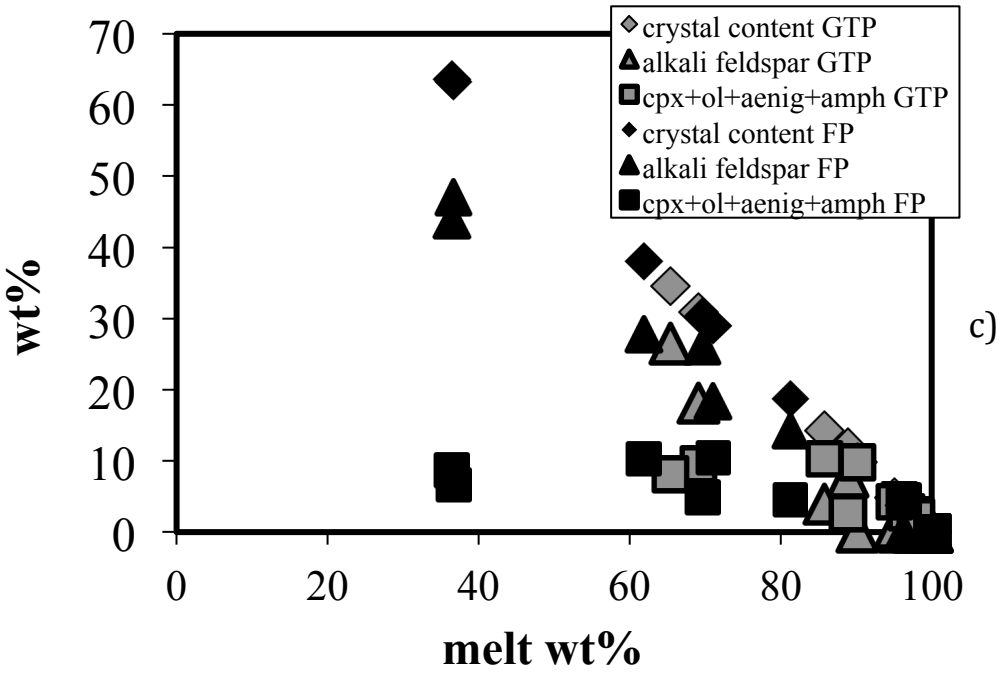

Figure 5.2: Variation of (a) melt content with and (b) alkali feldspar content with water solubilized in the melt (H_2O_{melt}); the legend is common for the two projections. c) variation of crystal content, alkali feldspar content and sum of mafic mineral (clinopyroxene+olivine+aenigmaite+amphibole) as a function of melt content. In all projections black symbols identify the experiment on Fastuca pantellerite (FP) whereas grey symbols those on Green Tuff pantellerite (GTP).

5.3.4 Phase composition

Experimental phases compositions for both starting materials investigated are reported in in appendix (table 1 to 6), whereas the compositional variation with T-fO_2 and H_2O_{melt} are shown from Fig. 5.3 to Fig. 5.8 and discussed below.

Clinopyroxene

Experimental clinopyroxenes have composition falling in the range $En_{2.24\text{-}25.2\text{-}}$ – $Fs_{34.3\text{-}68.81}$ – $Wo_{33.4\ \text{-}38.5}$ and XFe [=Fe/(Fe+Mg), atomic] ranging between 0.54 and 0.97 (appendix, table 1). The Ca and Na contents in the experimental pyroxene show a variation range from augite to aegirine-augite (Fig. 5.3a), pure aegirine end-member does not crystallize in our experiments even though it have been already synthetized on similar composition (Scaillet & Macdonald 2003; Di Carlo et al., 2010) a temperature lower than 750°C. Changes in H_2O_{melt}, and hence in fO_2, at a given temperature influences the XFe_{tot} in clinopyroxene (Fig.5.3b-c). In the Green Tuff pantellerite charges, at constant H_2O_{melt} a decrease in temperature of 50°C increases the XFe from 0.60 to 0.80. In the charge of Fastuca pantellerite, clinopyroxene, which crystallize only at T< 800°C, has XFe included between 0.89 - 0.93 that increases up 0.97 in the charge at 680°C. The Na_2O content in clinopyroxene range between 0.70 and 2.26 wt%, considering all charges it increases with increasing melt peralkalinity index (Fig. 5.3d). It is worth to note that despite the compositional difference of natural clinopyroxene, the experiments were able to reproduce the composition of clinopyroxene at the same temperature but different fO_2. The average coefficient clinopyroxene-liquid exchange ($K_d^{Mg\text{-}Fe}{}_{cpx\text{-}liq}$) calculated using $FeO=FeO_{tot}$ is 0.18±0.03, which is very similar to the value found by and Di Carlo et al., (2010) ($K_d^{Fe\text{-}Mg}{}_{cpx\text{-}liq}$= 0.16± 0.14)

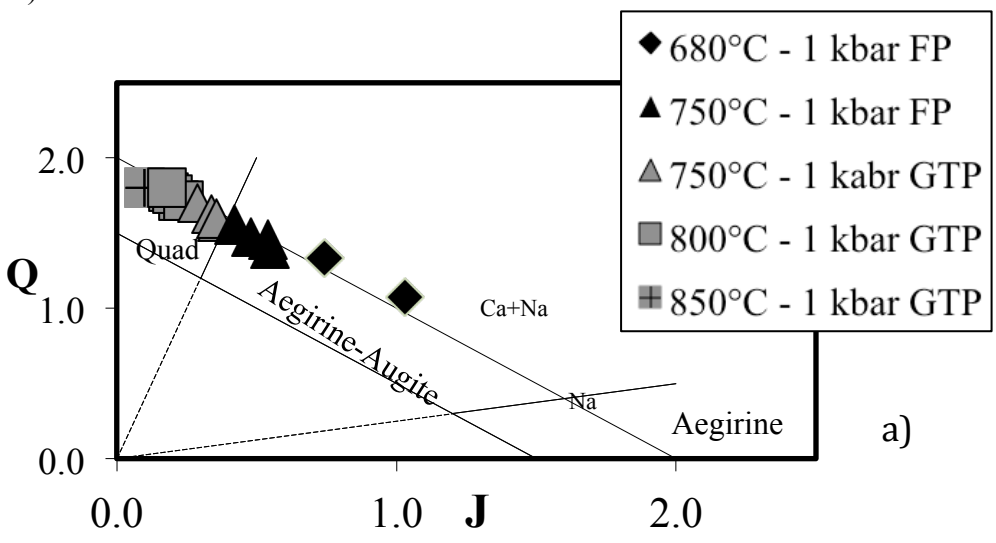

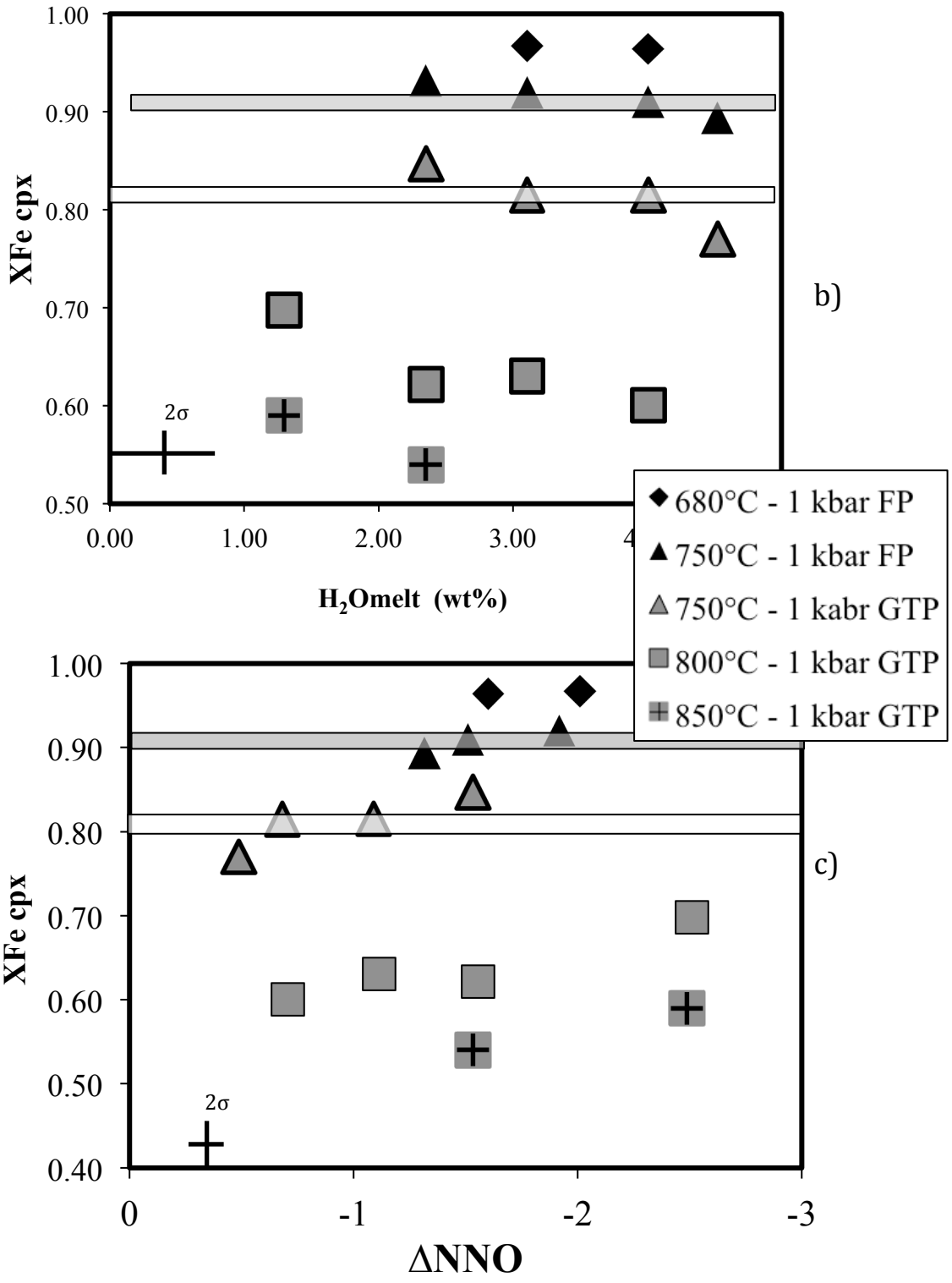
1.00
0.90
0.80
0.70
0.60
0.50
XFe cpx
2σ
0.00
1.00
2.00
3.00
H2Omelt (wt%)
b)
680°C - 1 kbar FP
750°C - 1 kbar FP
750°C - 1 kabr GTP
800°C - 1 kbar GTP
850°C - 1 kbar GTP
1.00
0.90
0.80
0.70
0.60
0.50
0.40
XFe cpx
2σ
0
-1
-2
-3
ΔNNO
c)

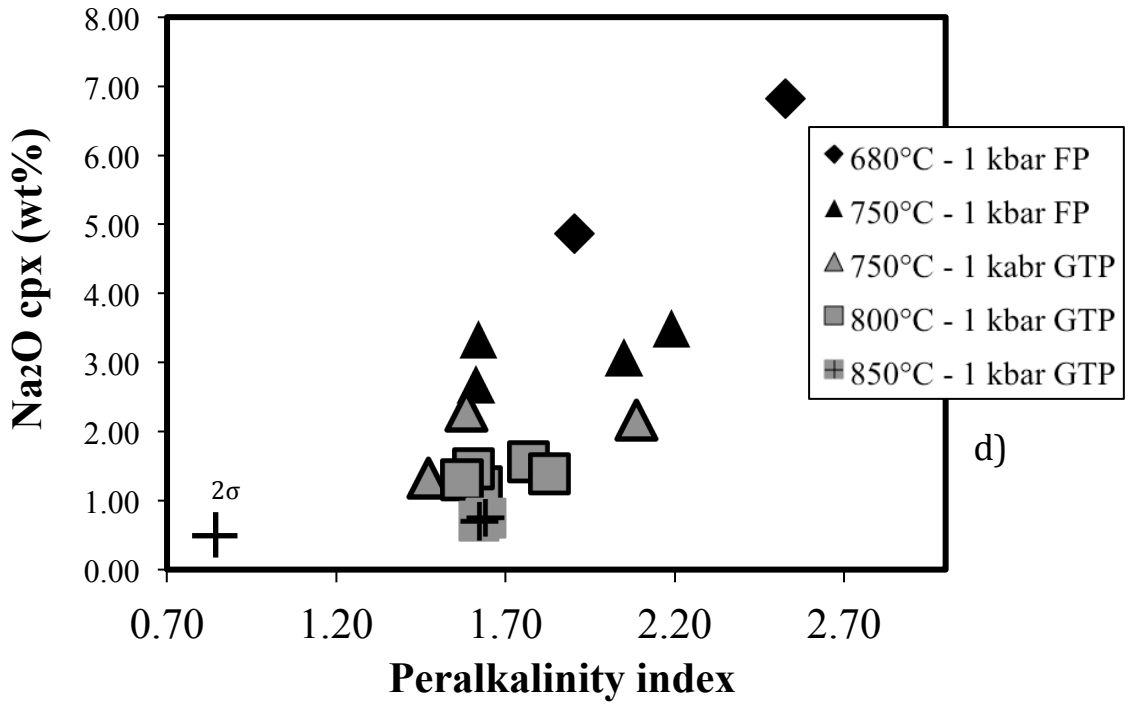

Figure 5.3: Composition of experimental clinopyroxene. (a) classification of experimental clinopyroxene following Morimoto & Kitamura 1983, in this diagram Q is the sum of cations Ca+Mg+Fe^{2+} and J= 2Na. (b) variation of total iron content (expressed as XFe= Fe_{tot} /(Fe_{tot}+Mg) vs melt water content, (c) variation of XFe with oxygen fugacity (expressed as ΔNNO). (d) Variation of Na_2O content in clinopyroxene with melt peralkalinity index. The grey box indicate the composition of natural clinopyroxene in Fastuca pantellerite (FP) whereas the white box that of clinopyroxene in Green Tuff pantellerite (GTP) .

Olivine

Experimental olivine, synthesized only in the experiments performed on Fastuca pantellerite, can be classified as fayalite ranging from Fa_{90} to Fa_{93} (appendix table 2, Fig. 5.4). The composition of experimental olivines perfectly matches that of phenocrysts in pantelleritic rocks (White et al., 2005; Civetta et al., 1998), having, as for the natural crystals, manganese content up to 6.4 wt%. (i.e. Tephroitic compontent as high as 6 mol%). Iron content in the experimental olivines increases with decreasing H_2Omelt and fO_2 (Fig. 5.4a-b), on the contrary Mn content roughly shows the opposite behaviour decreasing till 4.8 wt %. The average exchange coefficient $Kd^{Fe\text{-}Mg}$ $f_{ol\text{-}liq}$, calculated with $FeO=FeO_{tot}$, is 0.58 ± 0.20. Considering instead the Fe^{2+}/Fe^{3+} of the melt estimated with the method of Kress & Carmichael (1991) by using the experimental fO_2, the K_d^{Fe-Mg} is 0.72 ± 0.21. In both case the large standard deviation is associated with low MgO concentration (appendix, table 2) in the melt. The K_d calculated using natural olivine phenocrysts and the glassy groundmass K_d^{Fe-Mg}= 0.40 ±0.1 (this work and data from Neave et al., 2012) is marginally similar to that experimentally determined. Fayalitic olivine synthetized in pantellerites is the most evolved term of Fe-rich olivine found in silicic rocks of Pantelleria (trachyte and pantellerite) and they are stable for temperature ≤ 950°C (Fig. 5.4c)

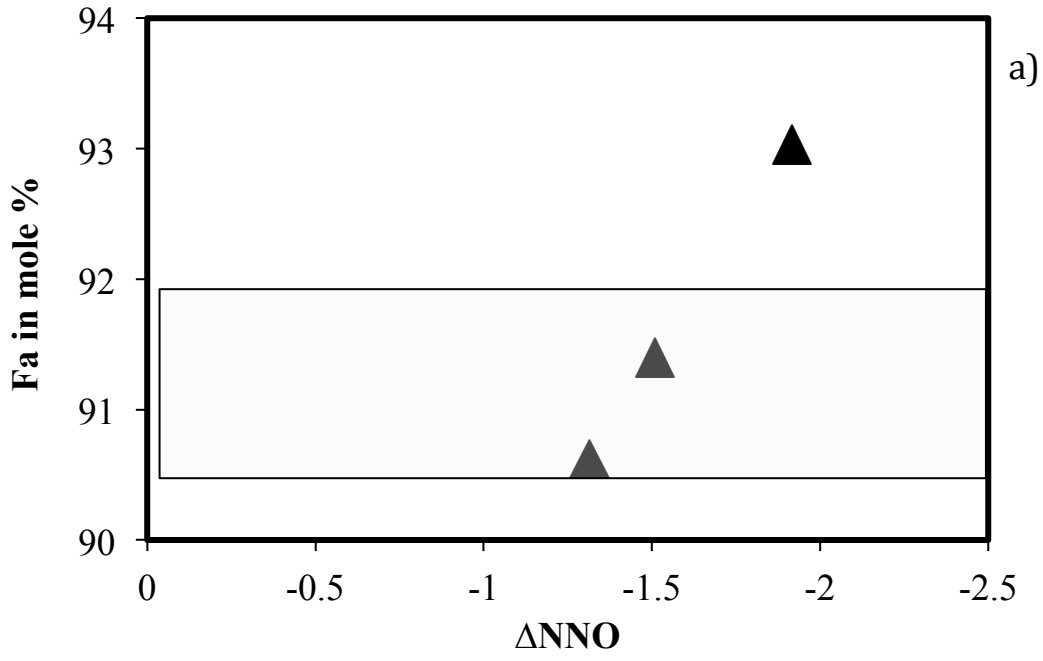

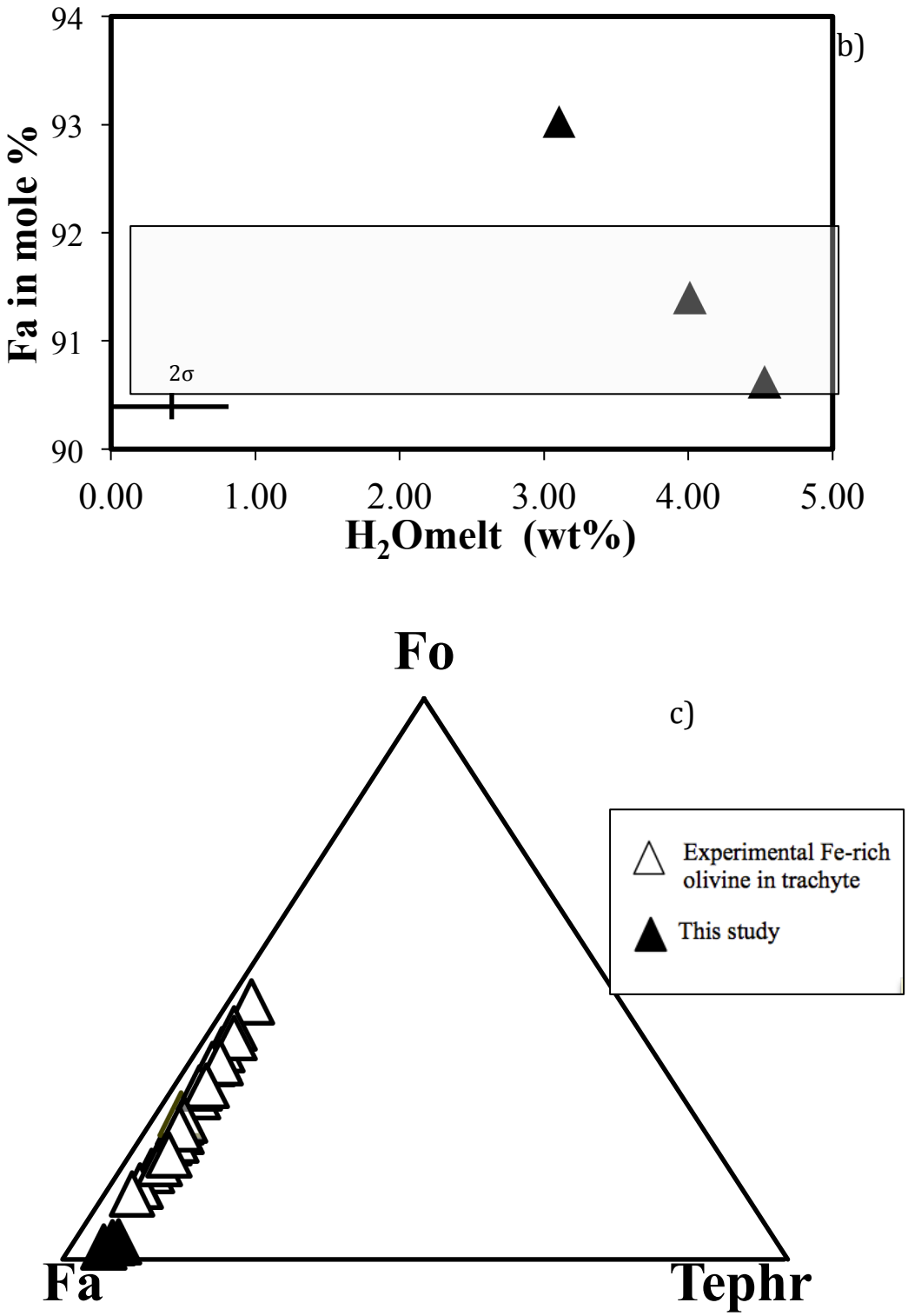

Figure 5.4: Composition of experimental olivine. Variation of fayalite content in olivine with (a) oxygen fugacity (expressed as ΔNNO) and (b) melt water content. (c) Ternary classification diagram of olivine Fo, forsterite; Fa, fayalite; Tephr, tephroite. Black triangles indicate the composition of experimental olivine in this study whereas white triangle indicate the Fe-rich olivine synthetized on trachyte rock of Pantelleria (Romano et al., submitted)

Aenigmatite

Representative analyses of experimental aenigmatite are listed in appendix (table 4). Experimental aenigmatites have fairly constant composition, TiO_2 and Na_2O contents ranges respectively between 7.3- 9.1 wt% and 6.8-7.1. The XTi of aenigmatite, calculated as [Ti/(Fe+Ti)]*100 ranges between 13.83 and 17.08 showing a positive correlation with temperature and a negative correlation with fO_2 (Fig. 5.5). In contrast Na_2O content remain roughly constant in the range 6.7-7.1wt%. Even if the redox conditions explored for the Fastuca pantellerite are slightly lower than those reached by Di Carlo et al., (2010), the lowermost value of XTi obtained in our experiments at 680°C is only marginally lower of that obtained in the previous work. The composition of experimental aenigmatites match those of aenigmatite found in pantelleritic rocks, which usually have XTi and Na_2O respectively of 14.62-16.55 and 6.74-7.02wt%. Considering composition and phase relationships, aenigmatite has a maximum thermal stability around 750°C, at least for pantellerites from Pantelleria.

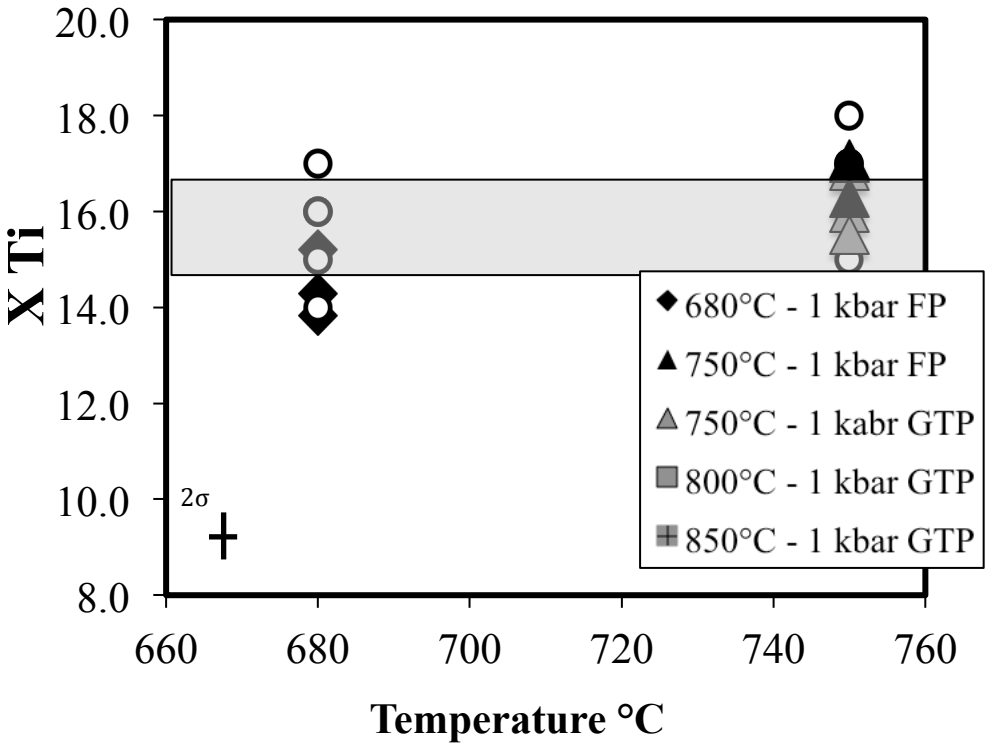

Figure 5.5: Composition of experimental aenigmatite, variation of XTi [=Ti/(Ti+Fe)] with temperature. Black symbols indicate the experiments on Fastuca pantellerite and grey symbols those on Green Tuff pantellerite. White circles are the experimental aenigmatite of Di Carlo et al., (2010) while the grey box indicate the composition of natural aenigmatite of Pantelleria.

Amphibole

Following the classification of Leake et al., (1997), experimental amphibole composition span in the range richterite –ferrowinchite and in few charges also arfvedsonite. Representative analyses of amphiboles are listed in appendix (table 5) and the relation with the experimental parameters is shown in Fig. 5.6 for both compositions. Amphibole crystallizing at 800°C in the Green Tuff pantellerite is ferri-winchite while at 750°C it range between ferri-winchite and ferro-richterite. At fixed temperature with the decrease of melt H_2O content increase the XFe and Na (Fig. 5.6a) while the CaO marginally shows the opposite behaviour. Also Scaillet & Macdonald (2003) and Di Carlo et al., (2010) noted such a positive correlation in which, moreover, the decrease in CaO is usually accompanied by an increase in Na_2O (Fig. 5.6b). In contrast, no evident relations have been found between concentration in Al and K with experimental variables (i.e temperature and H_2O_{melt}). It is worth to note that the composition of the amphibole found in the Green Tuff pantellerite by White et al., (2005) closely match the composition of the experimental amphiboles at 750°C (Fig.5.6c). Considering now the experiments performed on the Fastuca pantellerite, amphibole crystallizes only at T= 680°C (see also Di Carlo et al., 2010). If compared with the amphiboles crystallizing at higher temperature, they represent the most enriched end-member in term of Fe and Na, matching also the composition of amphiboles in the Fastuca pantellerite (Rotolo et al., 2007; Di Carlo et al., 2010). Experimental amphiboles have also high F content (up to 1.7 wt%), but in contrast to Scaillet & Macdonald (2003) we have not observed a clear relation between variation in melt water content and fluorine content in amphibole.

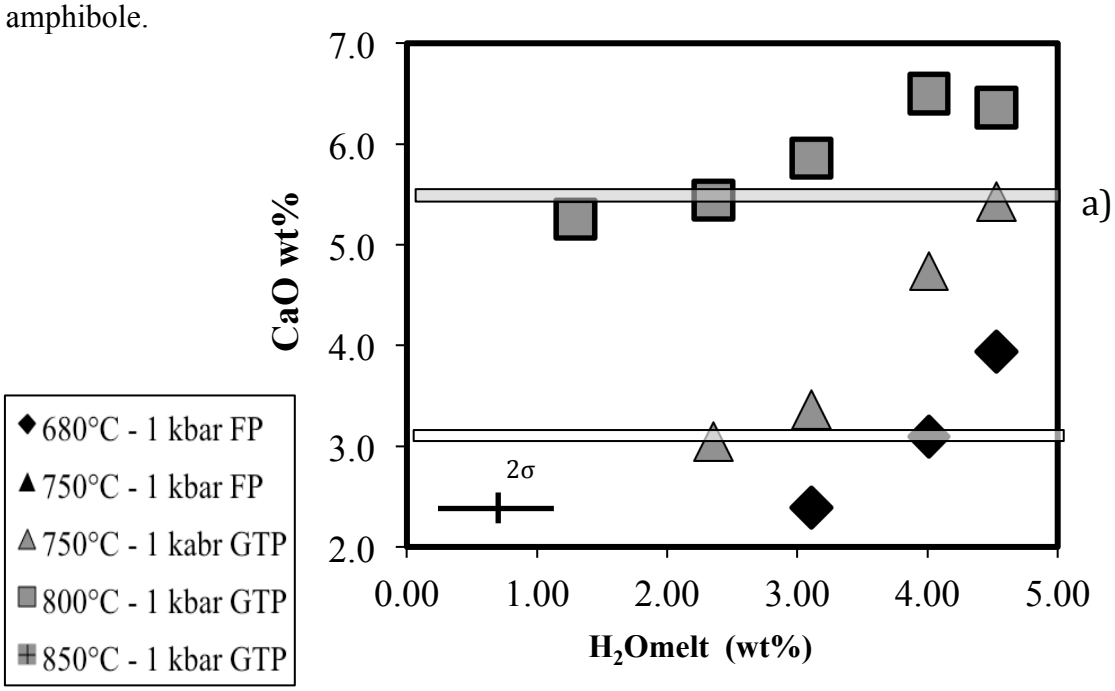

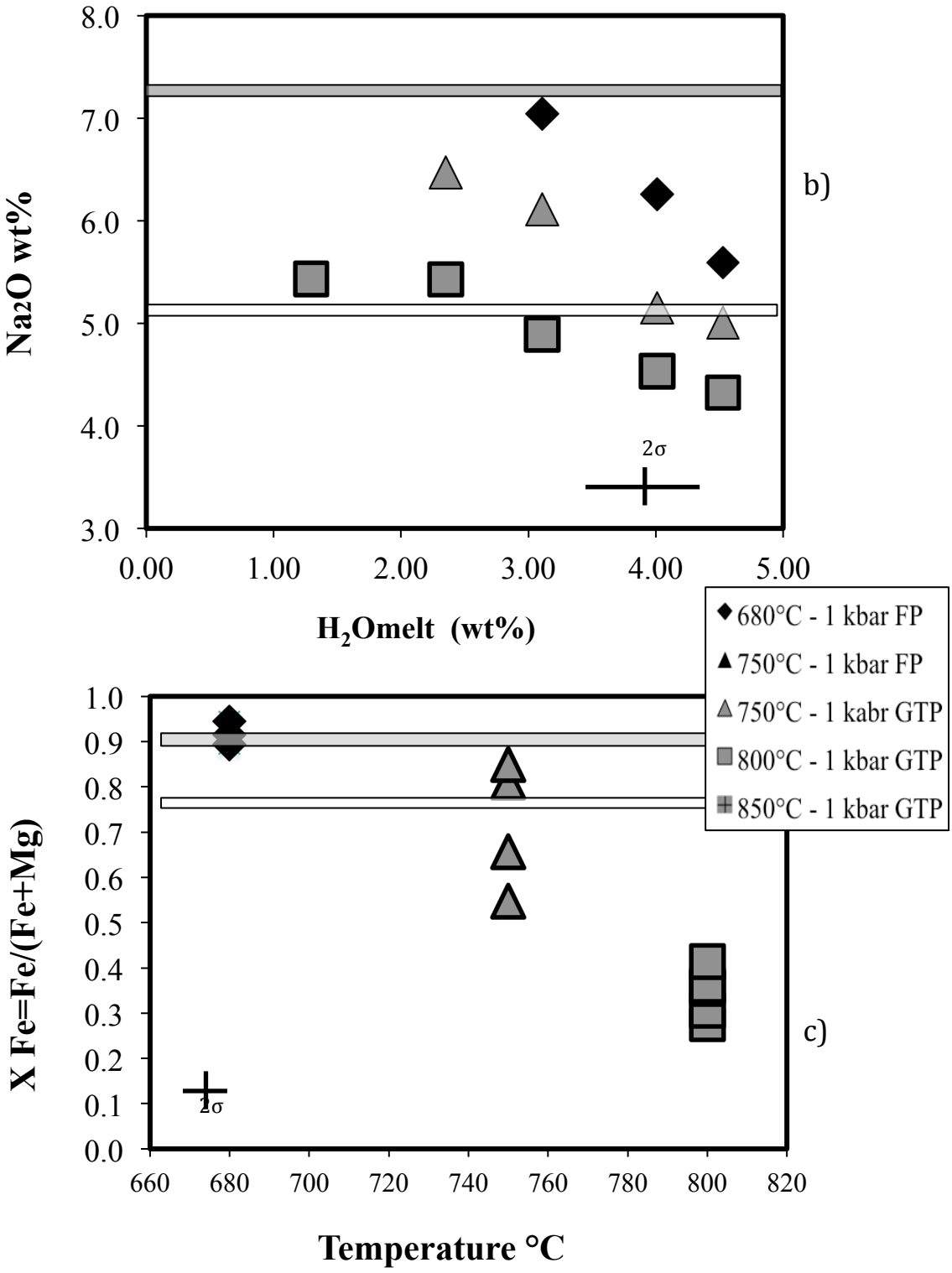

Figure 5.6. Composition of experimental amphibole. a) Na_2O content vs melt water content, b) CaO content vs H_2O_{melt}. c) variation of XFe [=Fe/(Fe+Mg)] as a function of temperature. Grey symbols indicate the experiment on Green Tuff pantellerite and black symbols those on Fatsuca pantellerite.

Alkali feldspar

Analysis of experimental alkali feldspars that fulfilled the criteria [Ca+Na+K]=1.000 ± 0.030 and [Si+Al+Fe]= 4.000 ± 0.050 a.p.f.u (calculated on 8 oxygen basis) are listed in appendix (table 3). Compositionally, alkali feldspars range between $Or_{28.7\text{-}41.7}$-$Ab_{52.8\text{-}70.6}$-$An_{0.0\text{-}0.4}$ covering the compositional range of alkali feldspar found in pantelleritic rocks. Alkali feldspars compositional variations, mostly induced by changes in temperature and H_2O_{melt}, are shown in Fig. 5.7a-b. When all data are plotted together, Or content in alkali feldspar shows a positive correlation with melt water content and a negative correlation with temperature.

The content in Ab and An broadly shows the inverse behaviour, nevertheless it is important to note that the error associated with An content determination could be high due to the very low CaO concentration. However, considering in detail the composition of experimental alkali feldspar, the variation in Or content is appreciable only in the experiments at T≤ 750°C whereas at temperature higher a nearly horizontal in the range $Or_{28.7\text{-}41.7}$-$Ab_{52.8\text{-}70.6}$-$An_{0.0\text{-}0.4}$ is obtained. This lack of a clear correlation is probably due to the difficulties to analyse alkali feldspar in that charges with low H_2O_{melt}, in turn the charge with high crystal content. Anyhow the composition of the natural alkali feldspar has been well reproduced in the experiments at 750°C and H_2Omelt in the range 2.5-4 wt%.

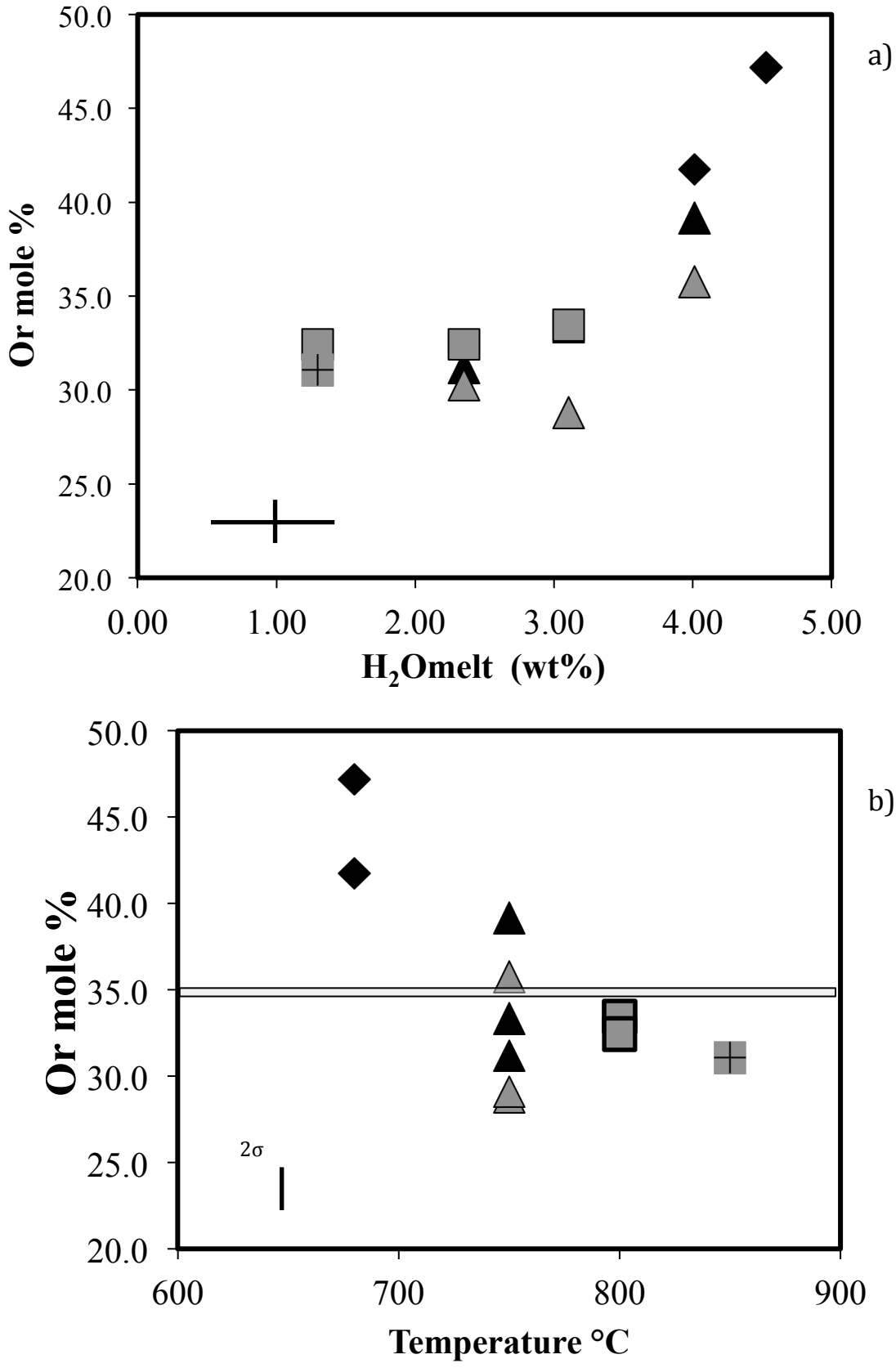

Figure 5.7: Experimental alkali feldspar compositions. Variation of Or content in alkali feldspar as a function of a) melt water content and b) temperature.

Glasses

The composition of experimental glasses recalculated on anhydrous bases are listed in appendix (table 6), following the classification of MacDonald (1974) all glasses have pantelleritic composition, with peralkalinity index from 1.52 to 2.53. The content in SiO_2 range between 71.04 and 74.80, whereas TiO_2, MnO, MgO and CaO have concentration always lower than 1 wt% and especially MgO reaches concentration lower than 0.1 wt%. FeO and Al_2O_3 contents in the residual glasses range respectively between 4.94-9.33 wt% and 6.38-9.95 wt% while as regard Na_2O and K_2O they varies between 6.12-7.57 wt% and 2.70-4.87 wt%.

The variation in glass composition with proceeding crystallization is shown in Fig.5.8. Glass composition in above-liquidus charges is similar to the starting materials composition whereas, as crystallization proceeds, FeO, Al_2O_3 show a greater variation in the residual glasses and lesser extent silica and alkali. In the Green Tuff pantellerite charges, silica and iron content show first a slightly decreases, but increases again when the crystal content is > 10wt%, while aluminium content shows the opposite behaviour (Fig.5.8a-c). The latter in turn affects the peralkalinity index, which first becomes slightly lower of that of the starting material and then it increases up to 2.09 (correlating positively with the crystal content). Di Carlo et al., (2010) explained this behaviour with the crystallization of the sole mafic phases such as clinopyroxene (i.e charges at T≥ 800°C and high melt water content).

In the Fastuca pantellerite charges, silica content remains quite constant (within the error) as crystallization proceed, even though in the charge at 680°C SiO_2 is slight higher of that in charges at 750°C (Fig. 5.8a). Iron content increase with increasing of crystal content and it appears to be higher in the charge at 750°C respect to those at 680°C (Fig. 5.8b). As regard aluminium content, it decreases as crystallization proceeds, consequently, melt peralkalinity index increases reaching a value as high as 2.53 (i.e the most crystallized charge #GT-R22-3). Considering the experiment on Fastuca pantellerite, the differences in experimental mineral assemblage, related principally to the presence of fayalite or amphibole beside alkali feldspar, clinopyroxene, aenigmatite and quartz, influence the composition of the residual glass. In Fig 5.8d, it have been used a ternary diagram FeO-Al_2O_3-(Na_2O+K_2O) to show two different trend in the evolution of glass composition as crystallization proceeds. Crystallization of fayalitic olivine enriches progressively the residual melt in iron, on the contrary, the effect of amphibole crystallization is an increase in alkalis.

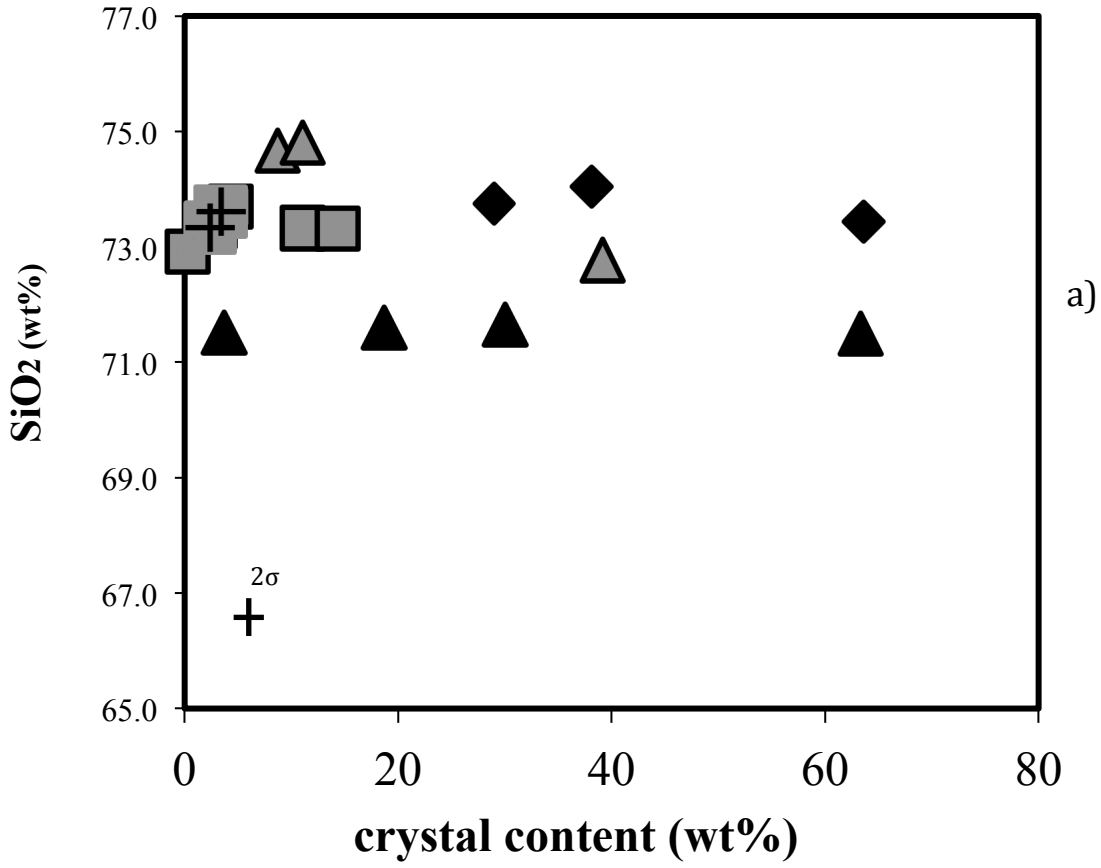
77.0
75.0
73.0
71.0
69.0
67.0
65.0
SiO2 (wt%)
2σ
0
20
40
60
80
crystal content (wt%)

a)

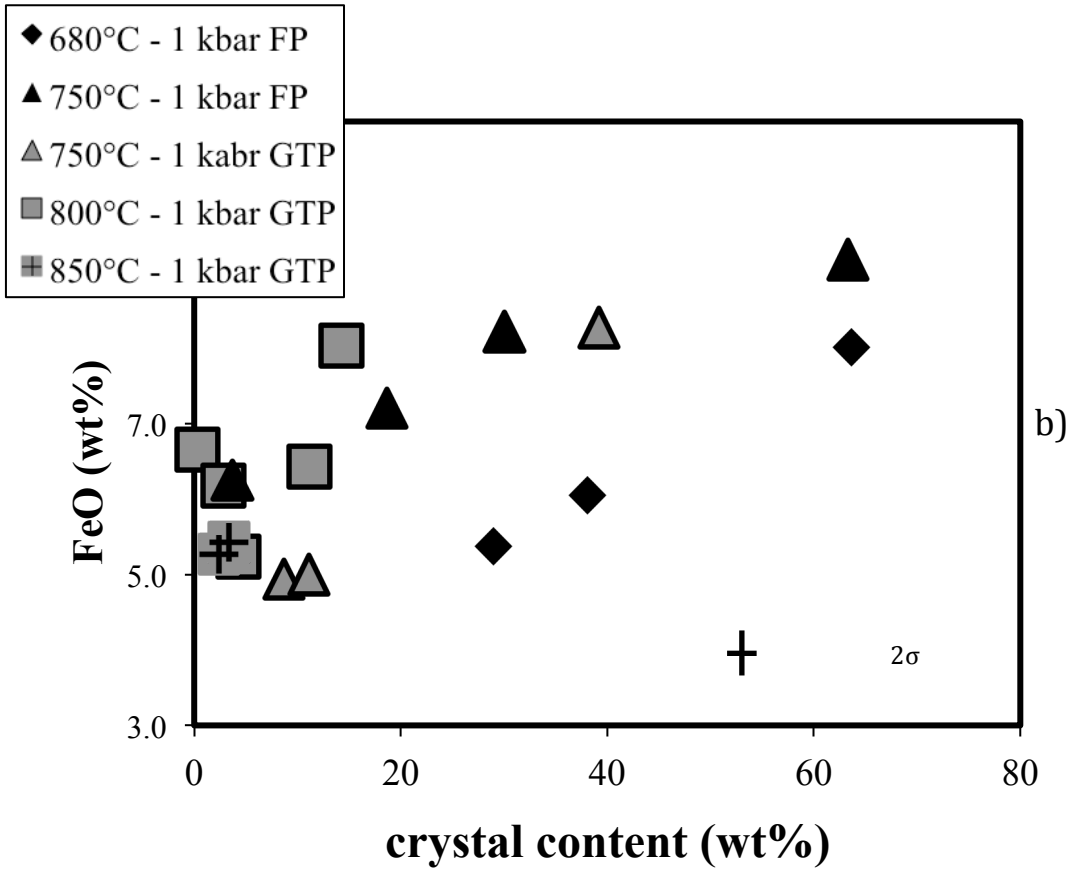
680°C - 1 kbar FP
750°C - 1 kbar FP
750°C - 1 kabr GTP
800°C - 1 kbar GTP
850°C - 1 kbar GTP
FeO (wt%)
7.0
5.0
3.0
2σ
0
20
40
60
80
crystal content (wt%)

b)

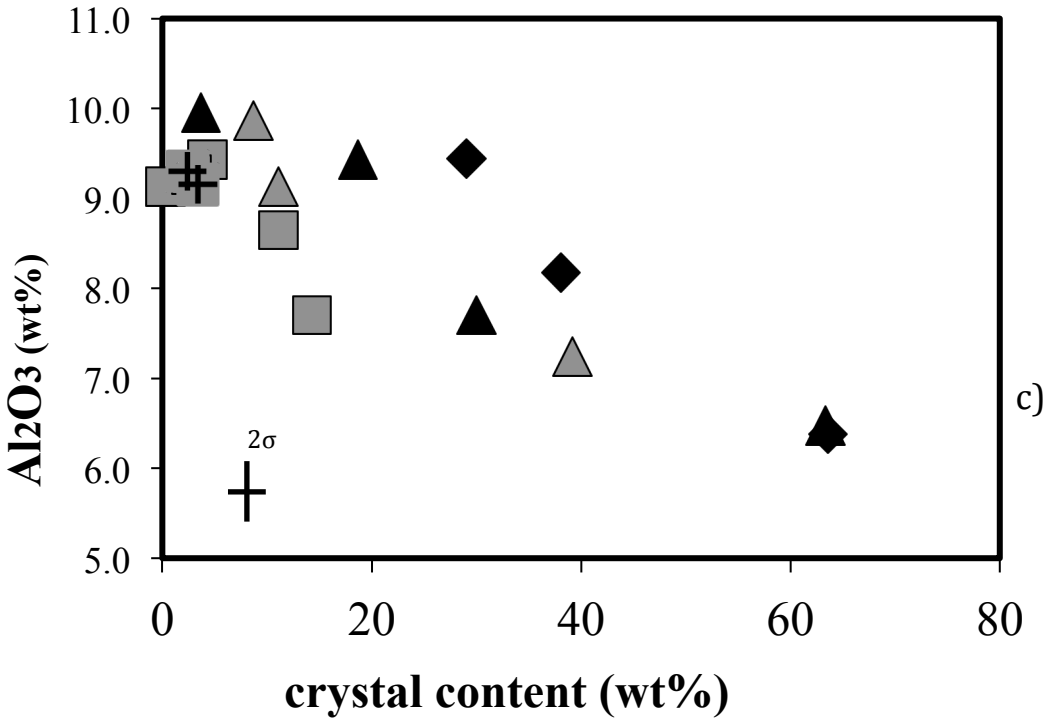
11.0
10.0
9.0
8.0
7.0
6.0
5.0
Al2O3 (wt%)
2σ
0
20
40
60
80
crystal content (wt%)

c)

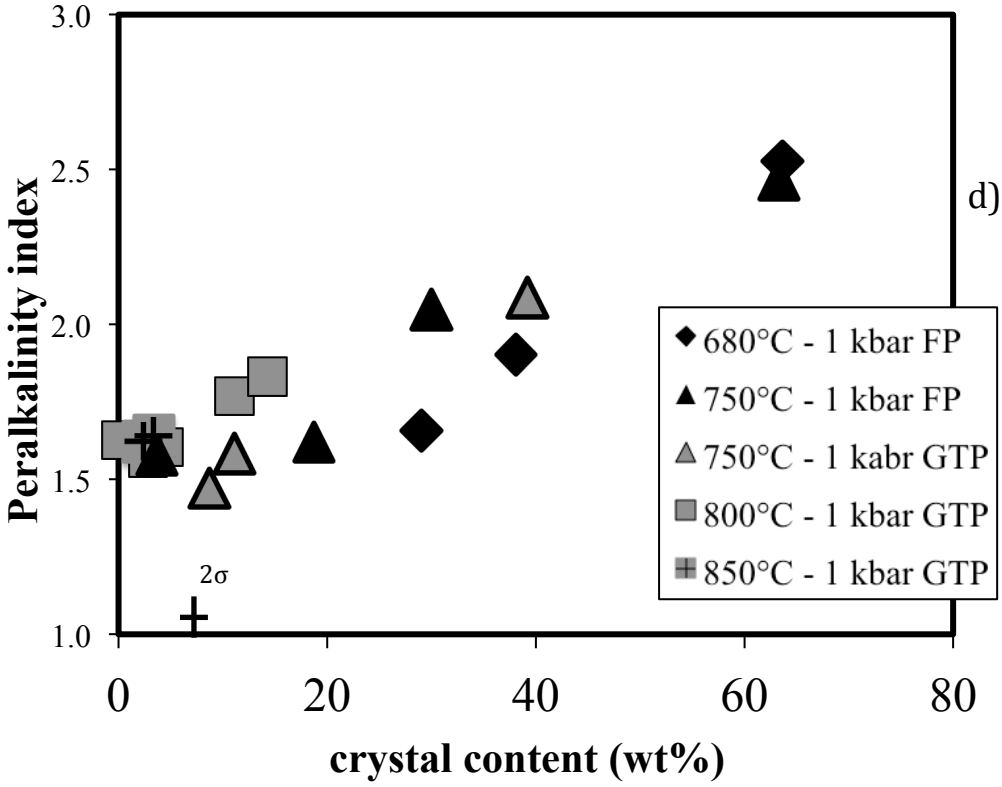
3.0
2.5
2.0
1.5
1.0
Peralkalinity index
2σ
680°C - 1 kbar FP
750°C - 1 kbar FP
750°C - 1 kabr GTP
800°C - 1 kbar GTP
850°C - 1 kbar GTP
0
20
40
60
80
crystal content (wt%)

d)

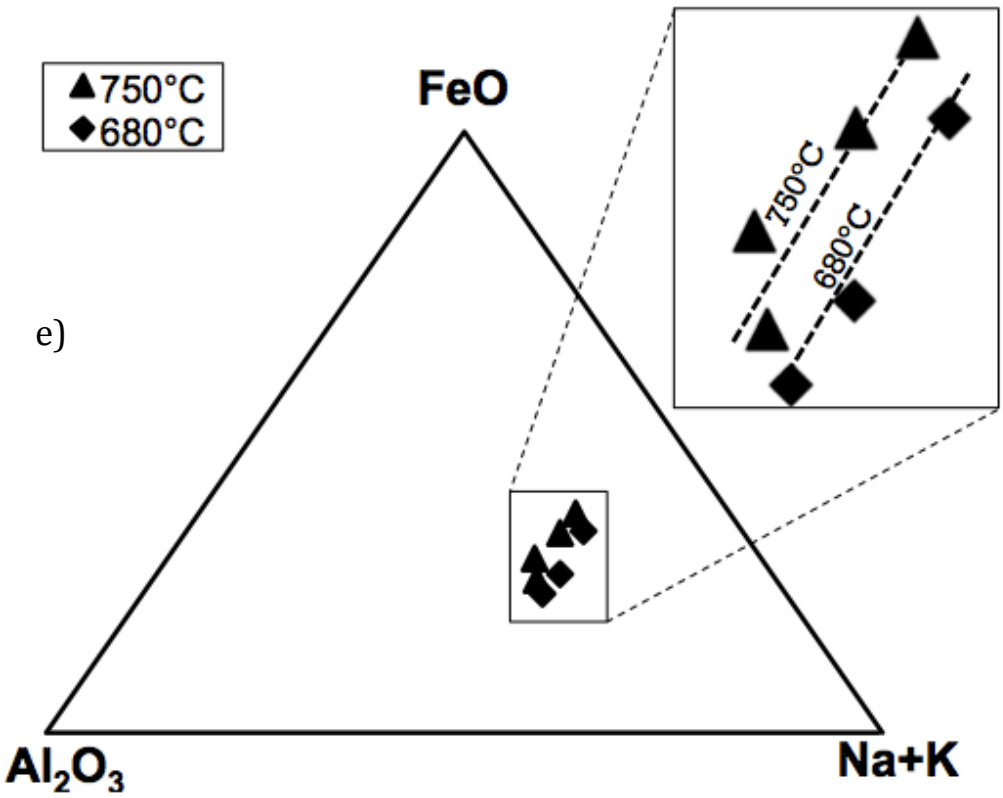

Figure 5.8: Composition of experimental glasses. Variation of crystal content with melt (a) SiO_2 wt%, (b) FeO wt%, (c) Al_2O_3 wt%, (d) peralkalinity index. e) Position of experimental glass of Fatsuca Pantellerite in a ternary projection FeO-Al2O3-(Na_2O+K_2O) illustrating the different trends drawn by the glass composition as consequence of differences in mineral assemblage.

5.4 DISCUSSIONS

5.4.1 Comparison with previous work

We start the discussions by comparing our findings with other experimental results such as those of Scaillet & Macdonald (2001; 2003; 2006) on paralkaline rhyolite of Kenya rift valley and the results of Di Carlo et al., (2010) on Pantelleria Island. The main differences between the experimental phase equilibria established for the rhyolites of Pantelleria and those established for Kenya pantellerites are well resumed in the work of Di Carlo et al., (2010). The most relevant points, that obviously regard also our findings, are: (i) the crystallization sequence and (ii) the stability of the main mineral phases. Kenya pantellerite (Scaillet &Macdonald 2006) and comendite (Scaillet & Macdonald 2001, 2003), being more Si-rich than peralkaline rhyolite of Pantelleria crystallize first quartz and alkali feldspar, whereas pantellerites from Pantelleria, in turn slightly rich in Ca, stabilize first clinopyroxene as liquidus phase. Aenigmatite, although occurs as phenocryst in natural rocks, does not crystallize in the experiments performed on Kenyan rhyolite while in the experiments of Di Carlo et al., (2010) as well as on our experiments aenigmatite is stable at T < 800°C. However, the reason why aenigmatite crystallized in pantellerites from Pantelleria but not in the Kenyan pantellerite, remains still unclear since starting materials have comparable content in Na_2O, FeO and TiO_2 as well as comparable is the peralkalinity of the residual melts. This comparison shows that although the bulk-rock composition appears similar, experimental phase relations are extremely sensitive to small variation in major elements, several authors indeed recommend a case-by-case approach when the main objective is the precise estimations of pre-eruptive conditions (Scaillet et al., 2008; Andujar & Scaillet 2008; Cadoux et al., 2014).

Comparing more closely our results on Green Tuff pantellerite with those of Di Carlo et al., (2010), both performed in a similar range of temperature and fO_2, the differences in the phase topology are appreciable. In the Green Tuff pantellerite experiments clinopyroxene crystallizes at 800°C and melt water content close to the saturation conditions while in the experiments of Di Carlo et al., (2010) clinopyroxene is stable at the same temperature and pressure but melt water content lower than 4 wt%. Moreover, also alkali feldspar and quartz crystallize at melt water content slightly higher respect to experiments of Di Carlo et al., (2010). As regard aenigmatite, in our experiments it crystallizes at T≤ 750°C, while in the experiments of Di Carlo et al., (2010) at 1 kbar it crystallizes only at T< 700°C. However, this difference could be due to a lack of an experiment at 750°C and 1 kbar

because in their experiments at 1.5 kbar aenigmaite crystallizes also at T≤ 750°C. Another important point of difference between our results on Green Tuff pantellerite and the phase relationships established by Di Carlo et al., (2010) is the stability of amphibole. Nicholls & Carmichael (1969) suggested that amphibole in pantellerite (mostly ferrorichterites and arfvedsonite) can be stable at liquidus conditions (900-1000°C) evidencing also that high fF_2 allows the stability at these temperature. In contrast, recent experimental works on pantellerites (Scaillet & Macdonald 2001; 2003; 2006; Di Carlo et al., 2010) suggest that amphibole crystallizes at T≤ 750°C. Scaillet & Macdonald (2003; 2006) moreover remarked that high fF_2 allows the stability of amphibole even in H_2O-poor magmas. In our experiments on Green Tuff pantellerite, amphibole crystallizes at T≤ 800°C regardless the water content and it is stable also at 750°C. How mentioned before, we used the natural rock as starting material, this implies that all volatiles present in the natural rock (Lanzo et al., 2013) were not lost during the preparation of the starting materials (Pichavant et al., 1987). The fluorine content measured in the experimental glasses reaches 1.3 wt%, therefore, it have allowed to stabilize amphibole at temperature higher than 700°C. However, in contrast with the experiments of Nicholls & Carmichael (1969), amphibole does not crystallize at temperature higher than 800°C. The occurrence of amphibole in pantellerite of Pantelleria island has been discussed also by Di Carlo et al., (2010). On the basis of experimental results, they advanced the hypothesis that amphibole represents a mineral phase coming from a wetter, cooler and possibly deeper storage region. In this way, amphibole would coexist with alkali feldspar for crystal content comparable with those observed in natural pantellerite. However, our experimental results show that amphibole can be stable up to 800°C and we ascribe this mostly to the high fF_2 content, which could explain the coexistence of amphibole and alkali feldspar at temperature higher than 680°C. Nevertheless, Charles (1975) constrained experimentally the stability of fluorine rich amphibole (F-ferrorichterite) for temperature lower than 750°C and very reducing conditions, at higher temperature and oxidizing conditions amphibole+clinopyroxene decomposes to aegirine-augite+fayalite+quartz+ vapour.

In our experiments on Fastuca pantellerite at 750°C, besides clinopyroxene, alkali feldspar, aenigmatite and quartz, also fayalitic olivine crystallizes even though in a narrow range of melt water content and fO_2 (Fig.5.1). Although fayalite is common in pantelleritic rocks, the precedent experimental works on pantellerites (Scaillet & Macdonald 2001; 2006; Di Carlo et al., 2010) had some difficulties to synthetize such mineral phase. The sole example of fayalitic olivine synthesized in peralkaline sicilic magmas is reported by Scaillet

& Macdonald (2003) in the Kenyan comendite experiments at 693-729°C and fO_2 between ΔNNO -1.8 and -3.2. However, we will return on the reason of the stability of fayalite in our experiments in the next paragraphs, discussing the relation between occurrence of fayalite and melt peralkalinity.

5.4.2 Role of fO_2 in pantellerite paragenesis and further constraints on pre-eruptive conditions

In the following discussion we will compare the experimental results with the existing petrological and experimental studies on peralkaline rhyolites of Pantellerita in order to infer the origin of the different paragenesis reported in pantellerites (White et al., 2005) as well as to add further constraints on the storage temperature and redox conditions of pantellerites. It is important to remember that the following discussion will focus on temperature, melt water content and fO_2 derived experimentally in our study.

Phase relations and proportions

The application of several themobarometers based on inter-crystalline (clinopyroxene-olivine), or crystal-liquid exchange equilibria (cpx-liquid, feldspar-liquid) led White et al., (2005) to show in detail that peralkaline rhyolites of Pantelleria record temperatures ranging between 680-800°C and redox conditions in the range ΔFMQ -0.55, -1.06. They reported also different mineral assemblages in pantellerites showing that the main variations in the mineral assemblage regard principally the presence of fayalitic olivine and aenigmatite. In particular, they indicated that fayalite is stable only at low medium peralkalinity index (NK/A < 1.63) while when peralkalinity index becomes > 1.75 only aeningmatie (besides alkali feldspar and clinopyroxene) is stable. Furthermore, they showed a strong correlation of mineral assemblage with melt peralkalinity index and whole-rock SiO_2 content, which in turn appears to correlate negatively with T and fO_2. Di Carlo et al., (2010) constraining experimentally temperature and fO_2, reported pre-eruptive temperatures between 680 and 720°C and redox conditions around the FMQ buffer confirming both the low temperature evolution and the reduced redox conditions of Pantelleria rhyolites.

If we now compare the experimental phase relationships obtained from our experiments on Fastuca pantellerite with those of Di Carlo et al., (2010), we observe how an apparently small difference in the redox condition imposed during the experiments have an important impact on the phase topology/relationships of pantellerites. At T= 800°C, indeed, charges of Fastuca starting composition are at supra-liquidus conditions regardless the water content; in the experiments of Di Carlo et al., (2010) and also in the experiments on Green Tuff pantellerite, at the 800°C crystallize in order clinopyroxene, alkali feldspar and quartz. A depression of solidus of ~30°C in peralkaline rhyolite under reducing conditions have been reported by Scaillet & Macdonald (2001), here we document also the effect on liquidus

temperature that decrease of ~ 50°C. Something similar have been observed on metaluminous silicic composition by Dall'Agnoll et al., (1999), indeed, they showed a significant decrease in the thermal stability of the tectosilicates at reduced redox conditions. Although from a purely qualitative point of view, it is worth to note that the reason why we were able to analyse the glass composition also in the charge at 680°C and $XH_2O<1$, contrarily to Di Carlo et al., (2010), is probably related to a further depression of the solidus of pantellerite at more reducing conditions. The variation in fO_2 obviously affects also the Fe^{2+}/Fe^{3+} and hence the iron-bearing phase composition and proportion. In our experiments on Fastuca pantellerite at 750°C coexist alkali feldspar, aenigmatite and clinopyroxene, i.e the three most abundant phases in the natural pantellerites, moreover at this temperature also quartz and fayalite can be stable. Fayalite is often found in the mineral assemble of pantelleritic rocks with alkali feldspar, clinopyroxene ± oxides ± aenigmatite. In our experiments, we have observed that to crystallize fayalitic olivine the redox conditions has to be close to ΔNNO -1.5 (table 5.2). Otherwise, there is not other explanation for non-crystallization of olivine in the experiments of Di Carlo et al., (2010) as well as in GT pantellerite. Indeed, liquids with composition compatible with the stability of fayalite and similar water content have been reproduced experimentally both by Scaillet & Macdonald (2003, 2006) and Di Carlo et al., (2010) but fayalite has not been synthetized. The fact that at 680°C even at low redox conditions olivine does not crystallize is probably due to the low temperatures that constitutes a thermal limit to the stability of such a mineral. At temperature lower than 700°C the mineral that can accommodate large quantity of Fe^{2+} would be the amphibole besides clinopyroxene and aenigmatite.

Extrapolating the information useful to constrain the pre-eruptive redox conditions and temperatures, it worth to note that in the experimental charges at 750°C and H_2O_{melt} ranging between 3 wt% and 4.5 the crystal content remain similar to those observed in natural pantellerites, while at 680°C the crystal content increases from 30 wt% to 63 wt% when melt water content decreases. Moreover, as already pointed out by Di Carlo et al., (2010), the stability of aenigmatite and now also fayalite could represent the main topological argument to limit the pre-eruptive temperature of pantellerites at 750°C maximum and redox conditions between ΔNNO -0.5 and -2.0. However, further constraints on pre-eruptive temperature and oxygen fugacity can be gained by comparing the composition of experimental phases with the natural minerals.

Phase compositions

The composition of iron bearing minerals (i.e clinopyroxene amphibole, olivine and lesser extent aenigmatite) is sensitive to fO_2 changes arising from fH_2O. Contrarily to Di Carlo et al., (2010), the slightly lower redox conditions investigated in our study have allowed reproducing clinopyroxene with XFe perfectly matching to those of the Fastuca sample when temperature is 750°C and melt water content in the range 3-4.5 wt%. The compositional differences observed in natural clinopyroxene belonging to the Green Tuff and Fastuca pantellerites (Table 5.2, Fig. 5.3) thus have been reproduced at the same temperature (i.e 750°C) but a different redox conditions.

In detail, natural clinopyroxenes of Green Tuff pantellerite have XFe=0.83 while in the Fastuca pantellerite has XFe=0.91, this differences can be attributed to a variation in redox conditions from ΔNNO -0.6 to ΔNNO -1.5 for similar melt water content (Fig. 5.3). On the other hand the clinopyroxene crystallizing at 680°C have XFe slightly higher of that of natural phenocrysts, indicating that clinopyroxenes in pantellerites record temperature around 750°C. In the narrow range of stability (750°C, ΔNNO –1.31 and –1.91), experimental fayalite, although it is not comparable with other experiments results, has compositions similar to of natural phenocrysts in pantellerite. As regard experimental amphibole, its composition seems more influenced by crystallization temperature (Fig. 5.6) while aenigmatite composition remain almost constant at 750 and 680°C. The discussion reported until now shed in light how pantellerites can exists even at lower fO_2 conditions than those investigated until now.

5.4.3 Melt inclusions constraints and experimental glass compositions

Water content in Pantelleria rhyolites have been debated for a long time, several researchers have focused their attention on the volatile content dissolved in melt inclusion using different techniques and not always it has been obtained homogeneous results.

Kovalenko et al., (1988) analysing melt inclusions in anorthoclase and quartz found H_2O_{melt} = 4.3±0.3 (SIMS data) wt% while Lowenstern & Mahood (1991) obtained H_2O in the range 1.4-2.1 wt% from the melt inclusions trapped in quartz phenocrysts. In addition, Metrich et al., (2006), again on melt inclusion trapped on quartz phenocryts, reported an average H_2O_{melt} = 2.45±0.3.

Most recent studies, such as Lanzo et al., (2013) for the basal fallout of the Green Tuff eruption or Gioncada & Landi (2010) and Neave et al., (2012) for several of the most recent (< 45 ka) eruptive units, have found a very similar average H_2O_{melt} concentration (2.6 wt%) in a variation range included between 1.25 wt% and 4.88. More in detail, over 80 melt inclusions analysed, the 63.8% of them have water content in the range 2.5-4.5 wt%, the remnant are out of this range. Interpreting the results of melt inclusions studies in the light of the phase relationship determined experimentally, the melt water contents reported in the recent studies are perfectly compatible with the crystallization of clinopyroxene, alkali feldspar, aenigmatite, olivine ± amphibole at 750°C, 1kbar and fO_2 in the range ΔNNO -0.5 to -2.0. Most of the melt inclusions analysed have been found on alkali feldspar with a quite homogeneous composition (Ab_{65}-Or_{35}), which in our experiments crystallizes at 750°C, 1 kbar and water content 3.5 ± 0.5 wt%. As already discussed by Di Carlo et al., (2010), the fact that composition of alkali feldspar remains almost constant while the H_2O_{melt} decreases (Fig. 5.7), it can explain also the variability in melt water content encountered in melt inclusion trapped in alkali feldspar. Otherwise, the other explanation for those melt inclusions with lower water content is the post entrapment modification. In contrast, those melt inclusion with 4.5 wt% or slightly higher hosted in alkali feldspar probably have recorded crystallization pressure conditions marginally higher (~1.2-1.3 kbar). Indeed, following the phase relationship in Fig.5.1 at 1 kbar and 4.5 wt% of water dissolved in the melt, pantellerites are close or at water saturation conditions and alkali feldspar does not crystallize. Gioncada & Landi (2010) reported also analyses of melt inclusions trapped in olivine and aenigmatite phenocrysts, although statistically less significant respect to the data from melt inclusions trapped in alkali feldspar, the water contents found corroborate the crystallization process from a pantelleritic melt with water content between 2.5 and 4.5 wt%.

Indeed, in the melt inclusion trapped in aenigmatite crystals H_2O= 2.57± 0.1 while in fayalite the highest water content measured is 4.33 wt%

As regards the water content found in melt inclusions trapped quartz phenocrysts, we support the idea of Di Carlo et al., (2010) that a polybaric crystallization is required to explain the low melt water content otherwise the simple water lost upon cooling would increase the crystal content of the magma (over the 30 wt%) much more of that observed in natural pantellerites.

If now we consider the composition of the experimental glasses, by comparing it with the composition of melt inclusions or whole rocks data further constraints can be gained. How anticipated before, the most relevant point reported by White et al., (2005) regard the variation in SiO_2 with temperature and the presence of fayalite and aenigmatite in the mineral assemblage. Taking into account the glass composition of the experiments on Fastuca pantellerite at 750°C, in which all the main mineral phases found in pantellerites where synthetized, as the crystallization proceeds the liquid composition become richer in iron and alkali but poorer in Al_2O_3. It is important to note that the evolution of the mineral assemblage of Pantelleria rhyolites as function of peralkalinity index has been well reproduced experimentally. Considering the experimental phases and the glass composition, fayalite is stable when peralkalinity index ranges between 1.58 and 2.05, it coexists also with aenigmatite when the P.I is around 2 while for higher values (i.e GT-R20-4; P.I=2.47) only aenigmatite is stable; in contrast, in our experiments the SiO_2 content remain constant around 71.5 wt%. The important information is that for a similar crystal content, the different mineral assemblages can be originated at the same temperature of 750°C but a different redox conditions or melt water content.

In addition, plotting in a diagram FeO/Al_2O_3 vs P.I the experimental glass with natural products such as whole rock and melt inclusions compositions (Fig. 5.9), the natural products match the experiments at 750°C. Looking in details to the composition of melt inclusions, most of them are close to that charge in which alkali feldspar, clinopyroxene, olivine and aenigmatite crystallize. This in turn imply that these melt inclusions were trapped when the liquid had already crystallized the four above-mentioned mineral phases, in contrast the composition of melt inclusions trapped in olivine appear less evolved. Lastly, the fact that natural products match with experiments at 750°C indicates both the evolution temperature at 750°C and also that amphibole does not fractionate during Pantelleria rhyolite

evolution, explaining also why it is found only rarely in the mineral assemblage of pantellerites from Pantelleria.

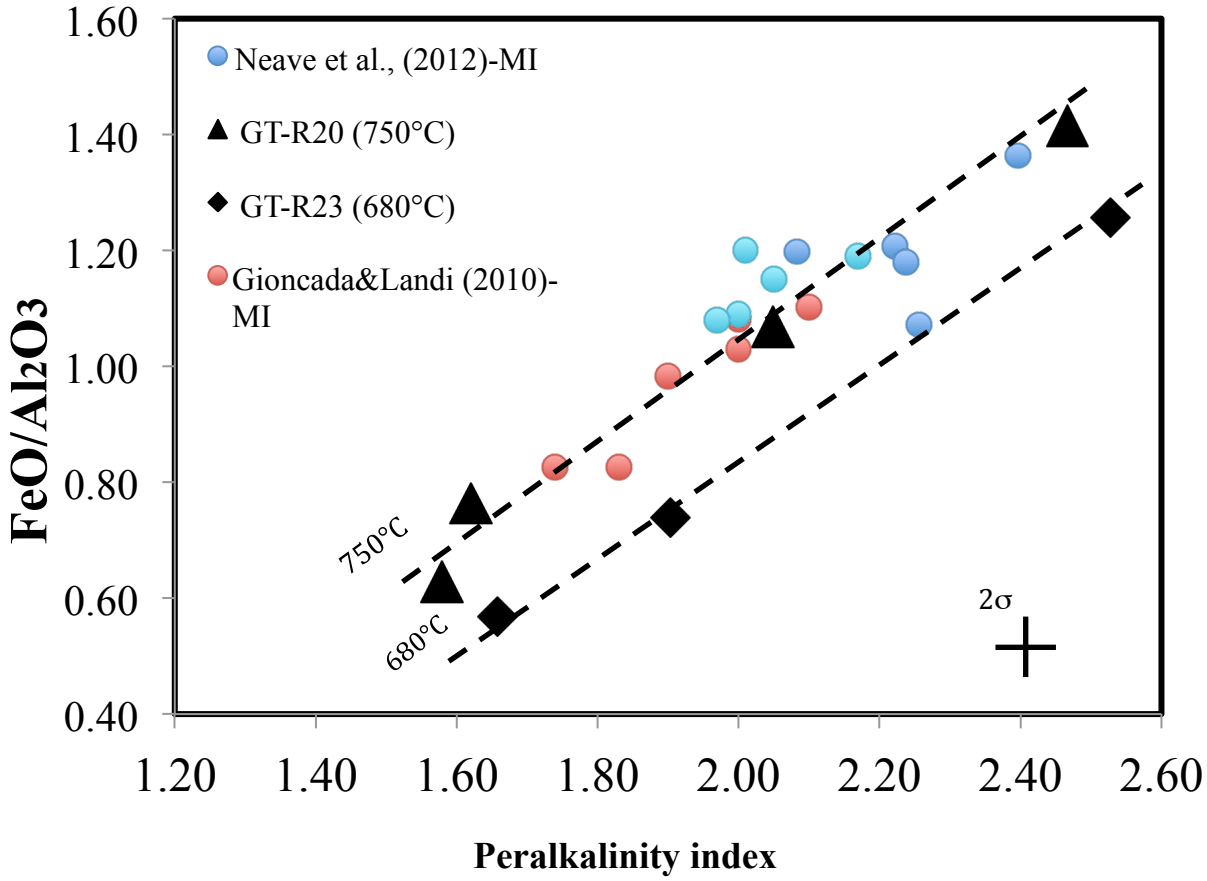

Figure 5.9: Composition of the experimental glasses in the projection FeO/Al_2O_3 vs the melt peralkalinity of Fastuca pantellerite compared with the composition of natural glasses (Melt inclusions, MI). It is worth to note that natural glasses are similar in composition to the experiments at 750°C in which the common mineral assemblage of peralkaline rhyolite of Pantelleria (cpx+fa+afs+aenig+qz) is reproduced.

5.4.4 Phase equilibrium and melt inclusion constraints on the pre-eruptive conditions of Green Tuff zoned ignimbrite

In order to constrain the pre-eruptive condition of Green Tuff eruption, we combine our experimental results on the Green tuff pantellerite with (i) petrological data, (ii) the findings of Lanzo et al., (2013) on melt inclusions and (iii) the experimental results on the GT trachytic top member (Chapter 3). How mentioned before, the Green Tuff eruption is an example of zoned ignimbrite emplaced without significant pause during the eruption (Williams et al., 2014). Regardless the volumes erupted, a common characteristic into the silicic-zoned ignimbrite is the gradation along the eruptive sequence in chemical composition and crystal content. The first erupted magma is indeed more evolved (rhyolitic) and depleted in crystal than the less evolved crystal rich magma erupted lastly.

In the last years, several works have focused on the evidence of temperature and pressure gradient in the magmas prior the eruption (Bachmann & Bergantz, 2004; Evans & Bachmann 2013; Gardner 2014) and on the geochemical expression of the zoning in silicic reservoir (Wolff et al., 2015) as well as several thermo-mechanical numerical modelling have focused on the dynamics underlying the zonation (Huber et al., 2009; Dufek & Bachmann 2010). Here we focus the attention on the pre-eruptive conditions of the compositional end-member (P-T-fO_2-H_2O_{melt}) forming the Green Tuff ignimbrite using the experiments. Considering the large temperature range investigated (750-900°C) only in the experiments at 750°C the mineral assemblage is well reproduced, while at higher temperature (i) aenigmatite does not crystallize and (ii) pantellerites are close to the liquidus temperature to to reproduce the mineral proportion found in GT pantellerites; moreover at 900°C pantellerite are above the liquidus regardless the water content. Moreover, experimental phases have compositions matching those of natural phase at 750°C, H_2O_{melt} between 3 and 4 wt% and fO_2, ΔNNO -0.5 to -1.9. White et al., (2005) for the Green Tuff (unspecified member) reports a temperature slightly lower of 750°C (703 °C) and redox conditions close to that determined in our experiments.

On the contrary, Wolf & Wright (1981b) referring to "the crystalline part of the Green Tuff" reported a temperature of 950°C. Considering the trachytic member, the pre-eruptive temperature inferred experimentally ranges between 900 and 950°C. The decreasing in temperature in the trachytic melt increase considerably the crystal content ~80wt% at 750°C. Moreover the chemical composition of the magma evolves approaching that of pantellerites. This evidences that the zoning in composition and crystal content in the magma

reservoir feeding the Green Tuff eruption could be related with a thermal gradient of ~150°C between the bottom and the top of the magma reservoir. Moreover considering the melt water content inferred from phase equilibria experiments on the trachytic member of the Green Tuff and those measured in melt inclusions belonging to pantelleritic members (Lanzo et al., 2013) the results are only marginally different, 2-3wt% in trachytes and 2.5-4 wt% in pantellerites.

5.5 Conclusions

This study was aimed to explore phase relations and compositions of two pantellerites erupted during the recent history of Pantelleria Island. Our experiments were successful in reproducing all the mineral phases presents in peralkaline rhyolites of Pantelleria. Phase relationships and compositions show notable difference between the eruptions investigated due to subtle differences in whole-rock composition and the redox conditions investigated.

The results confirm that peralkaline rhyolite of Pantelleria evolves at temperature lower than 750°C and redox conditions have fundamental role inthe stability of mineral phase found in pantellerites such as fayalite. The different mineral assemblage reported for pantellerites by White et al., (2005) have been reproduced at 750°C and redox conditions between ΔNNO -0.5 and -2.0. As in natural rock, we have observed that stability of fayalite and aenigmatite in pantellerites is strictly related to the peralkalinity of the melt. In our experiments olivine is stable when the melt in equilibrium has a peralkalinity index ≤ 1.9, for melt peralkalinity > 2 olivine is no longer stable.

Our experiments evidence also that amphibole in peralkaline rhyolite of Pantelleria can be stable for temperature ≤ 800°C and it is strictly dependent on the fluorine content. Furthermore, our results suggest that the pre-eruptive conditions of pantelleritic members of Green Tuff eruption can be inferred at temperature of 750°C and redox conditions between ΔNNO -0.5 and -2.0. Melt water content inferred from our study and melt inclusion (Lanzo et al., 2010) is around 4 wt%. Considering the experimental results (Chapter 4) obtained on the trachytic member of the Green Tuff highlights a compositional gradient in magma chamber (trachyte to pantellerite) related to a thermal gradient from 900°C (trachyte) to 750°C (pantellerite)

Chapter 6

Water solubility in trachytic melts of Pantelleria island: an experimental study

6.1 Introduction

Solubility of water in silicate melts have been widely investigated because of the important effects that water has on magmas properties, such as viscosity and density (Dingwell et al., 1996; Richet et al., 1996), liquidus and solidus temperature, mineral phases compositions (e.g. Sisson & Grove 1993), mineral phase stability (Housh and Luhr, 1991; Holtz et al., 1992) crystallization kinetics (Watson 1994; Cashman & Mangan 1994) and eruptive dynamics. Water solubility has been largely experimentally investigated in basaltic and rhyolitic compositions (Hamilton et al., 1964; Silver et al., 1990; Dixon et al., 1995; Moore et al., 1998; Beherens & Jantos, 2001; Tamic et al., 2001; Liu et al., 2005; Lesne et al., 2011c). Besides the major control of composition and pressure a less intense role is played by temperature (e.g. Holtz et al., 1992; 1995; Behrens et al., 2001). As regards the primary control of melt composition, besides the well known positive correlation of H_2O solubility with silica content, several studies on silica-rich systems showed that increasing the Na/K ratio, or peralkalinity ((Na+K)/Al>1)) have a positive effect on water solubility (Johannes & Holtz 1996; Romano et al., 1996; Dingwell et al., 1997; Holtz et al., 2000; Behrens et al., 2001). Recently several works have started to pay attentions to intermediate compositions such as andesite (Mandeville et al., 2002, Botcharnikov et al., 2006), phono-tephrite (Behrens et al., 2009), phonolite melts (Carrol & Blank 1997; Larsen & Gardner 2004; Iacono-Marziano et al., 2007; Schmidt & Behrens, 2008). In this rapidly growing amount of studies little attention has been paid to trachytic melts, a crucial composition because represents the transition to peraluminous or peralkaline rhyolite derivative melts, with only two studies on trachytic melts from Phlegrean Field magmas (Di Matteo et al., 2004; Fanara et al., 2015). Moreover, detailed or systematic studies on the effects of melt composition and temperature on the water solubility in basaltic and intermediate melts are almost completely absents. Di Matteo et al., (2004) partially showed an increase in H_2O solubility concordantly to an increase in melt Na/K ratio while Schmidt & Behrens (2008) reported that variation of (Na/Na+K) and (Na+K)/(Ca+Mg) in phonolitic melts has only a minor effect on H_2O solubility.

Here we present experimental data on water solubility in natural trachytic melts from Pantelleria island, for an explored pressure range between 0.5 and 3.0 kbar, supra-liquidus conditions (T= 950°C-975°C) and fO_2 around the FMQ buffer. The necessity to perform this experimental study generates from the compositional dependence of water solubility, where even slight variations in melt composition (e.g. same silica but different alkali content with the existing experimental data set) may cause substantial variations in H_2O solubility; precise knowledge of water solubility is essential to tightly constrain pre-eruptive conditions.

Dissolved H_2O in experimental trachytic glasses has been investigated by FT-IR spectroscopy and Elemental analyser, solubility data were then compared with experimental results on similar compositions (Di Matteo et al., 2004; Fanara et al., 2015) as well as with the results of existing thermodynamic models (e.g. Papale et al., 2006). The aim of this study is to enlarge the limited existing dataset of water solubility in trachytic melt and to provide a solubility model for metaluminous trachyte melts, particularly useful for melt inclusions studies on similar compositions worldwide.

6.2 Starting material and experimental strategy

The chemical composition of the starting material used in this study is representative of the trachytic rocks of Pantelleria Island (table 6.1). The staring material was prepared from the Green Tuff trachyte (GTT) described in Chapter 3, the same starting rock used for the experimental work presented in chapter 4. The description of the Green Tuff eruption is reported in Chapter 3 (paragraph 3.2.2) while the starting material have been prepared following the procedure described in chapter 2. The composition of the starting material is reported in table 1 and a comparison with the composition of Plegreaen field trachytes is also reported.

Experimental charges preparation was described in paragraph 2.1.2, it is worth remembering that solubility experiments performed in this study were realized loading in the capsules a fluid phase with $XH_2O= [H_2O/(H_2O+CO_2)]=1$. Experiments were performed using the Internally Heated Pressure Vessels described in paragraph 2.1.3; all solubility experiments were terminated using the fast quench device (quench rate >100°C s^{-1}.)

Table 6.1: Chemical composition of the starting material (GTT), fro comparison the compostion of the starting materials of Di Matteo et al., (2004) and Fanara et al., (2015).

Acronym	This study GTT	Di Matteo et al., (2004) ZAC	Di Matteo et al., (2004) PR38S	Di Matteo et al., (2004) PR38P	Fanara et al., 2015 Trachyte
SiO_2 (wt%)	64.12	61.71	58.35	59.9	60.31
TiO2	0.85	0.45	0.47	0.41	0.42
Al_2O_3	15.04	18.56	19.07	18.94	18.32
FeO_{tot}	6.27	3.17	3.70	3.27	5.21
MnO	0.27	0.27	0.13	0.15	0.00
MgO	0.62	0.23	1.84	1.11	1.31
CaO	1.48	1.64	3.21	2.43	4.11
Na_2O	6.58	6.11	2.75	3.78	2.81
K_2O	4.60	7.09	9.29	9.02	7.47
P2O5	0.17	0.02	0.33	0.22	0.00
sum	100.00	99.25	99.14	99.23	100.08
P.I*	1.05	0.96	0.76	0.84	0.69

*P.I: peralkalinity index molar $(Na+K)/Al_2O_3$

After the experiments, capsule were weighed to check for leaks; the post run weight difference was always < 0.4 mg, capsules with higher difference were discarded. An excess of H_2O (small liquid drop) within the capsule was observed during the opening of the

capsules, to confirm that saturation conditions were reached during the experiment. For each capsule one third of the run product was embedded in epoxy resin for qualitative analysis by scanning electron microscope (SEM) and chemical analysis by electron microprobe (EMP) while the remaining part was used for the determination of water content.

6.3 Analytical techniques

Scanning electron microscope and electron microprobe analyses

The fragments of glass mounted in epoxy resin were first observed under scanning electron microscope and then analysed by electron microprobe to check glass composition and homogeneity. Analytical conditions are those described in Chapter 2, paragraph 2.2.1

6.3.1 H_2O determination by the Elemental analyser

Total water content in experimental glasses was determined through an Elemental Analyser (EA) Thermo Scientific Flash 2000 housed at CNRS-ISTO laboratory. The elemental analyser allows determining the concentration of H-C-N in a given sample. In our case only H_2 was measured. The glass in the Elemental analyser is first combusted at 1800°C, oxidizing the substance into simple compounds, which were in turn quantified by thermal conductivity detection. Elemental analyser was calibrated before each analytical session using pure pyrophyllite, which is well known to contain 5 wt% of stoichiometric H_2O in its crystalline structure. The experimental samples for the analyses were prepared grinding 1 to 10 mg of experimental glass in a fine powder and then loading it in a tin capsule folder. The instrument was tested repeatedly using an international standard with kwon amount of carbon, hydrogen and nitrogen. We used also other hydrated glass samples prepared for this purpose and for which the solubility of water have been already investigate (i.e haplogranite composition) as well as hydrated glasses already analysed with other techniques (i.e KFT). In Fig. 6.1 are compared the results of the melt water content determined with the Elemental Analyser with (i) water content reported in literature (table 2) for haplogranite composition (Dingwell et al., 1997) and (ii) water content in pantellerites determined by KFT analysis (Scaillet & MacDonald 2006; Di Carlo et al., in prep).

Table 6.2: Comparison between the water content measured with CHNS- Elemental analyser and references values of several internal standards.

Run	T (°C)	P (kbar)	Duration (h)	$X^{fl}_{H_2O}$	H_2O	Referene values
HPG8*	975	2	125	1	5.71	5.94
HPG8	975	2	125	1	5.69	5.94
HPG8	975	2	125	1	5.59	5.94
HPG8	975	3	130	1	6.98	7.19
HPG8	975	3	130	1	6.99	7.19
HPG8	975	3	130	1	7.02	7.19
RUN H**	850	1	125	1	4.70	4.53
RUN H	850	1	125	1	4.58	4.53
RUN H	850	1	125	1	4.60	4.53
RUN B	850	1.5	140	1	5.06	5.22
RUN B	850	1.5	140	1	5.49	5.22
RUN B	850	1.5	140	1	5.36	5.22
RUN C	850	0.5	172	1	2.61	2.59
EBU***	-	-	-	-	0.16	0.15

References values of: * Dingwell et al., (1997); ** Di Carlo et al., *in prep.* ***Scaillet & MacDonald (2006

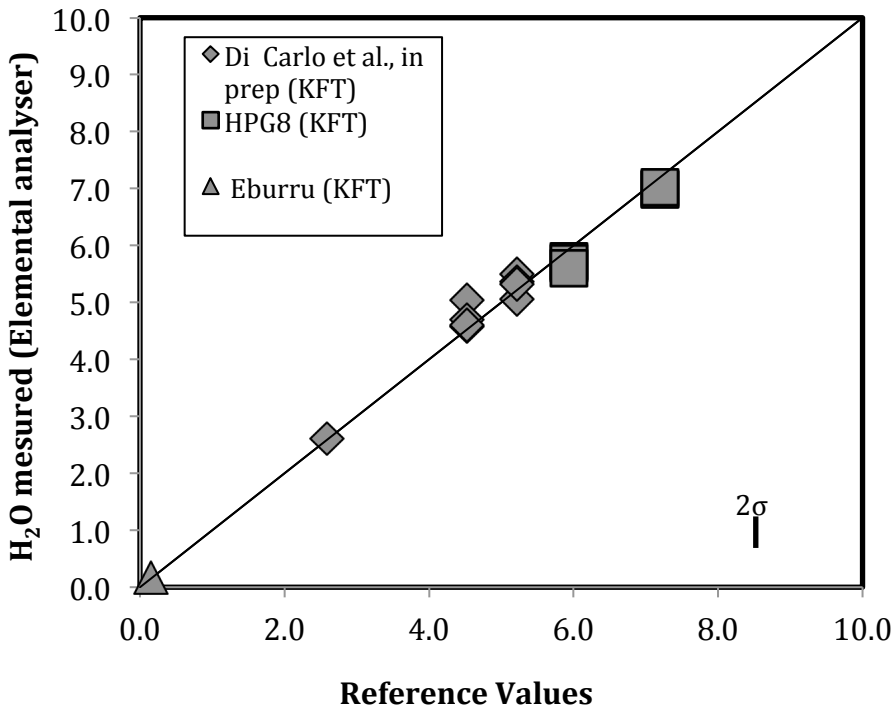

Figure 6.1: Comparison between water content in silica-rich melts analysed by CNHS-Elemental analyser and reference values for: peralkaline rhyolite (Di Carlo et al., in prep), haplogranite (HPG8) composition (Dingwell et al., 1997), Eburru obsidian (Scaillet & MacDonald 2006).

6.3.2 H_2O determination by FT-IR

Fourier Transform Infra Red analyses were performed using a Nicolet 760 Magna spectrometer equipped with an IR microscope (fluxed with H_2O-free compressed air). The spectrometer was equipped with a MCT detector and a Globar light source and a KBr beam splitter. Absorption spectra were acquired for each sample in the range 1000-6000 cm^{-1} with 128 scans and a resolution of 4 cm^{-1}. Experimental glass chips samples were placed on a NaCl crystal plate, which is transparent to the infrared beam; for each sample 3-7 points (50x50 μm spot size) were analysed. Glass chips were double-polished to obtain 50 – 100 μm thin wafers, and then carefully washed before the analysis under acetone and ethanol, in order to remove any impurities. The area of the sample analysed were always checked optically before the measurement to avoid bubble or impurities. The main advantage of FT-IR technique is the possibility to know the water speciation (H_2O_{mol} and OH^-) in the silicate melt (Stolper 1982a).

Water determination

After FT-IR analyses the absorbance was converted in H_2O concentration according to the Beer- Lambert equation:

$$C = (PM * A)/t * \rho * \varepsilon \quad \textbf{(eqtn. 1)}$$

The Beer- Lambert equation put in relation the total amount of water content (*C*) dissolved in the melt (eq 1): *PM:* molecular weight of the given volatile species; A: the height of the absorbance peak ; (t): thickness (cm) of the glass wafer, *(ρ):* density (g/l) of the glass; (*ε*) the molar absorption extinction coefficient (L mol^{-1} cm^{-1}). To calculate the H_2O content were considered the combination of absorption bands of the IR spectra basically at 2 wavenumbers: 5200 cm^{-1} (molecular H_2O, H_2O_{mol}) and at 4500 cm^{-1} (hydroxyl), applying a straight baseline correction (TT method, Ohlhorst et al., 2001), to measure the peak height.

These bands provide information about the concentration of hydrous species in the glass and the total water content results as the sum of these two species. For a few samples was also measured the absorbance of the fundamental OH^- stretching vibration at about 3530 cm^{-1} ($H2O_{total}$. In fact, for the vast majority of samples this latter band resulted saturated due to the combination of high H_2O concentrations and sample thickness, which needed to be thinner than 25μm to avoid peak saturation. The difficulties due to the preparation of an ultra-thin glass wafers, and the error associated with the wafer thickness determination

discouraged the measurement of the H_2O_{total} band. The thickness of glass wafers was measured using a Mitutoyo digital micrometer with an accuracy of ± 3μm (an error of 2μm in thickness measurement, propagates in an error on H_2O concentration of ~ 0.3 wt%.).

The density of experimental glasses was (i) calculated using the Ochs & Lange (1999) algorithm and also (ii) measured by the Archimedean method, which consists of weighting in air and in a liquid with a known density (i.e ethanol) the glass fragments.

Due to the small dimension of the glass chips, the Archimedean method was subject to large error during the measure. A minimum weight of 15 mg is indeed required to perform Archimedean density measure. Only for two hydrous glass fragments was measured the density with reasonable standard deviations. Considering also the density measured for the anhydrous starting material, it has been extracted an empirical relation of the form $\rho = -4.4032(H_2O_{melt}) + 2329$ (Fig. 6.2), where (ρ) is the density and H_2O_{melt} is the melt water content of the experimental glasses. The density calculated using this empirical relation differs notably from that obtained with the algorithm of Ochs & Lange (1999); the latter is 100-200 (g/L) larger, that means a difference of ~0.2-0.3 wt% in water concentration calculated using the Beer- Lambert equation (see below). To maintain an internal consistency, we preferred to use the density calculated using the empirical relationship obtained from Archimedean density measures. Molar absorption extinction coefficients (ε) for the bands of molecular H_2O (5200 cm^{-1}) and OH^-groups (4500 cm^{-1}) were calibrated using the water content determined by means of the CHNS Elemental Analyser.

As mentioned before total water content dissolved in the melt derive from the sum of the hydrous species in the glass, thus equation 1 can be rewritten as follows:

$$C = 18.01 * A_{4500} / \rho * t * \varepsilon_{4500} + 18.01 * A_{5200} / \rho * t * \varepsilon_{5200} \quad (\textbf{eqtn.2})$$

Normalizing the absorption value by density, thickness and water content the eq. 2 becomes an equation of a straight line y=-*m*x+q (Fig. 6.3) with the intercepts on x and y axes representing the ε_{4500} and ε_{5200} values, in our case the first is 0.71 and the second 1.94 L/mol*cm. With this method is assumed that molar absorptivity is constant for the range of water content investigated. The validity of this method is confirmed by the good agreement found between the water content measured with CHNS-Elemental Analyser and values determined by FT-IR (Fig. 6.4; table 6.2). The molar absorptivity coefficients found in our study differ slightly from those calculated for similar composition (Di Matteo et al., 2004; Fanara et al., 2015) although using the value of Di Matteo et al., (2004) the final water

content results very close (± 0.3 wt%), while if the values of Fanara et al. (2015) are used the water content is overestimated of ~ 2wt%.

Table 6.3: Experimental conditions and water concentration in the experimental glasses

Run	T (°C)	P (kbar)	Duration (h)	A_{5200}	A_{4500}	ρ (g/l)	t (µm)	H_2Om (wt%)	OH (wt%)	H_2O (EA)
GT-R16	975	3	96	0.33	0.06	2298	286.8	4.64	2.48	6.87
GT-R15	975	2	96	0.15	0.04	2302	193.4	3.16	2.34	5.97
GT-R9	950	1.5	125	0.11	0.04	2307	177.3	2.45	2.38	4.97
GT-R10	950	1	130	0.12	0.05	2312	264.3	1.87	2.24	3.83
GT-R11	950	0.5	135	0.08	0.04	2316	270.1	1.14	1.68	2.85
GT-R19	950	3	115	0.20	0.04	2298	211.3	3.76	2.17	6.92
GT-R18	950	2	115	0.18	0.04	2302	208.0	3.45	2.25	6.00

A_{5200} and A_{4500}: height of the of the absorbance peak at
ρ: density of the hydrated glasses
t: thickness of the glass wafers
H_2O and OH: concentration molecular water and hydroxyl group deter

H_2O (EA): concentration of water content measured with CHNS-Elemental analyser

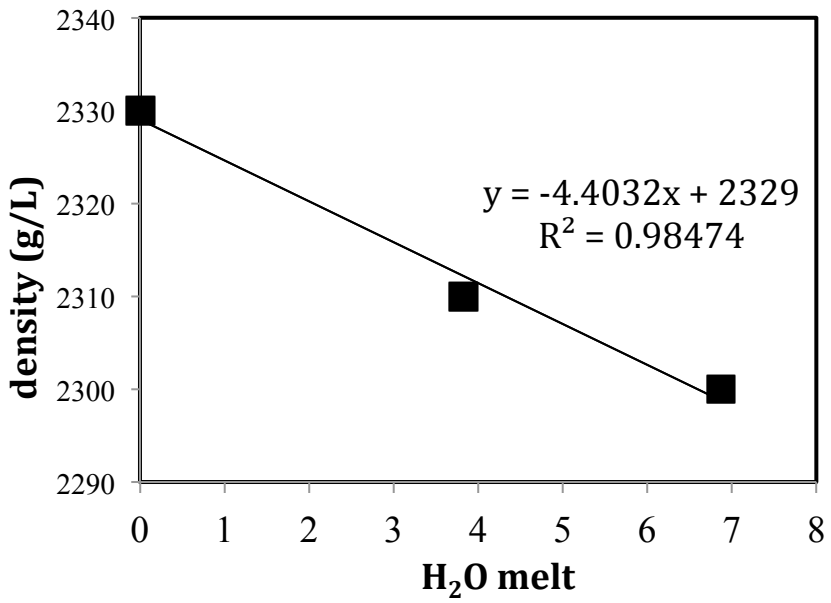

Figure 6.2: Dissolved H_2O vs. melt density correlation. The water content of experimental glasses was measured by with CHNS-elemental analyser, while the density was measured using the Archimedean method (see text for details).

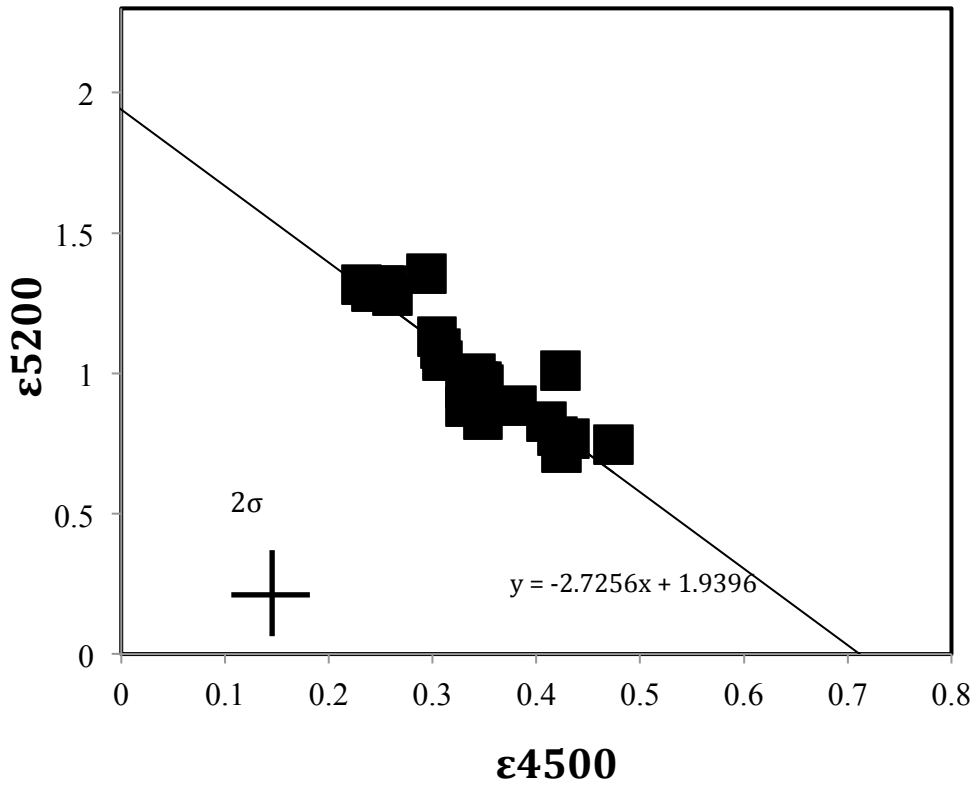

Figure 6.3: Resolution of Eqtn 2 (see text) results in a series of values whose regression is a straight-line (R= 0.80) intercepting abscissa and ordinate axes at the ε4500 (0.71) and ε5200 (1.94), respectively.

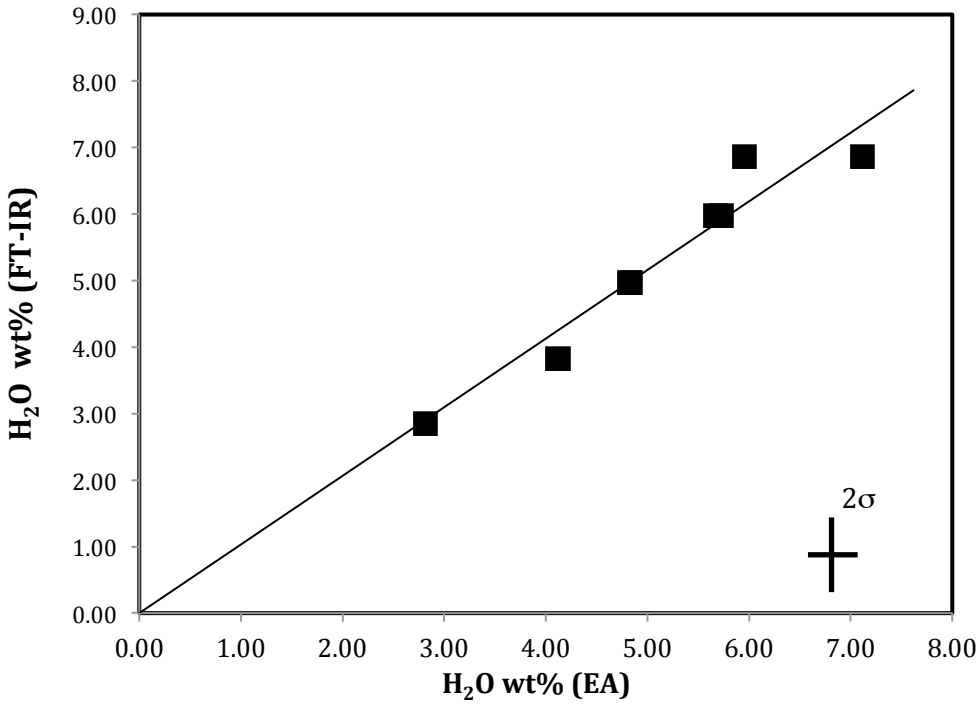

Figure 6.4: Comparison between the total H_2O measured by CHNS- Elemental analyser (EA) and FT-IR spectroscopy.

6.4 Experimental results

6.4.1 Microscopic observation and major element composition

The run products consist of brownish microlite-free glasses. Most of the quenched glasses present also bubble at the melt/capsule interface, indicative of fluid saturation condition during the experiment; however bubble content never exceeded the 0.1 %. Major element analyses of experimental glasses are listed in appendix (table 7). Experimental glasses are compositionally similar to the starting materials (table 6.1), some difference in major elements with respect to the starting material are an effect of the use of a defocused beam (Morgan & London 2005)

6.4.2 Water solubility in trachyte melts

The H_2O content dissolved in experimental glasses is reported in table 6.3. Water content ranges from 2.83± 0.3 at 0.5 kbar to 6.89 ± 0.6 at 3.0 kbar. At 2 and 3 kbar were performed two additional experiments to check the reproducibility of the H_2O solubility at high pressure. In Fig. 6.5 is shown the variation of melt water content dissolved in trachytic melt with pressure confirming the trend observed in all hydrous silicate melts that is the increasing of water solubilized in the melt with pressure. For comparison has been reported the experimental results of two recent studies on trachytes from Phlegraean field (Di Matteo et al., 2004; Fanara et al., 2015). In detail, Di Matteo et al., (2004) performed water solubility experiments (as in this study) on three Plegreaen field trachytic melts with different Na/K melt ratio. Only for the sample with the highest Na/K ratio was explored a pressure range included between 0.25 and 2 kbar while for the other compositions only the results at 2 kbar and one at 1.5 kbar were presented. Fanara et al., (2015) performed solubility experiments loading in the capsules a mixture of H_2O and CO_2, we compared our results only with the data of Fanara et al., (2015) obtained from experiments performed at water saturation conditions.

Water species (OH- and H_2Om) in trachytic melt as a function of total water content are shown in Fig. 6.6, in which, as already shown for other quenched hydrous glasses, the OH group concentration is higher at low water content whereas molecular H_2O dominates at higher water content (Stolper 1982a; Xue & Kanzaki, 2004). Linear regression of water solubility data in GTT trachyte melt as a function of pressure, can be described through an equation of the form $H_2O_{melt} = -8*10^{-7}P + 0.0047P$ ($R^2 = 0.9798$) where P is the pressure in bars.

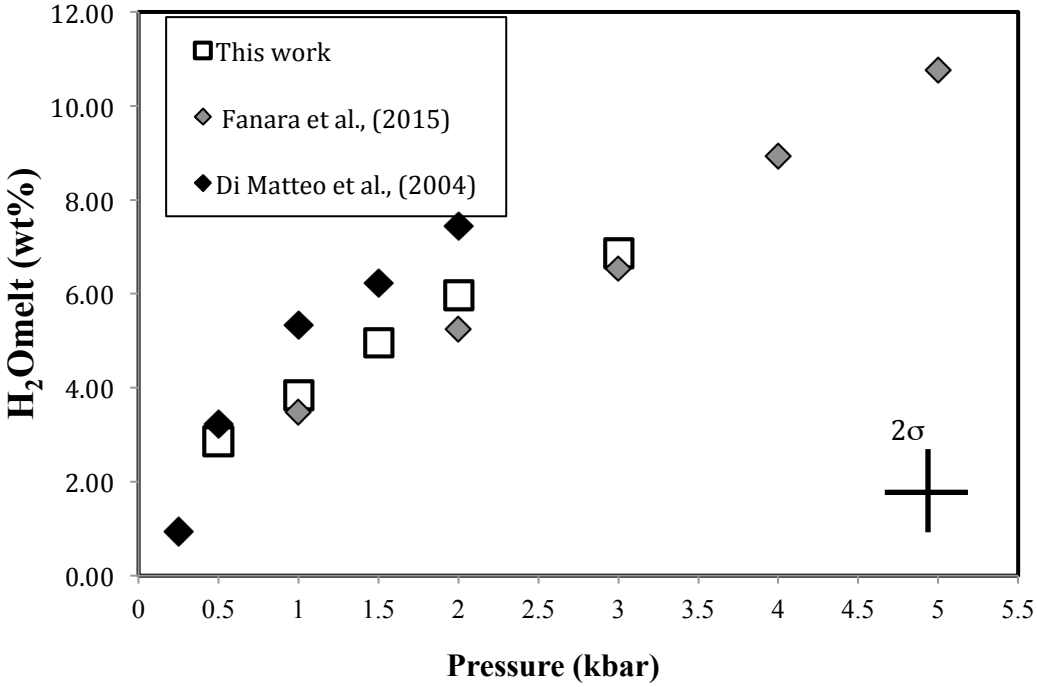

Figure 6.5: Water contents solubilized in the melt as a function of pressure obtained for in this study for the trachytic composition of Pantelleria island. For comparison have been reported the experimental result on Plegraean field trachytes of Di Matteo et al., (2004) and Fanara et al., (2015).

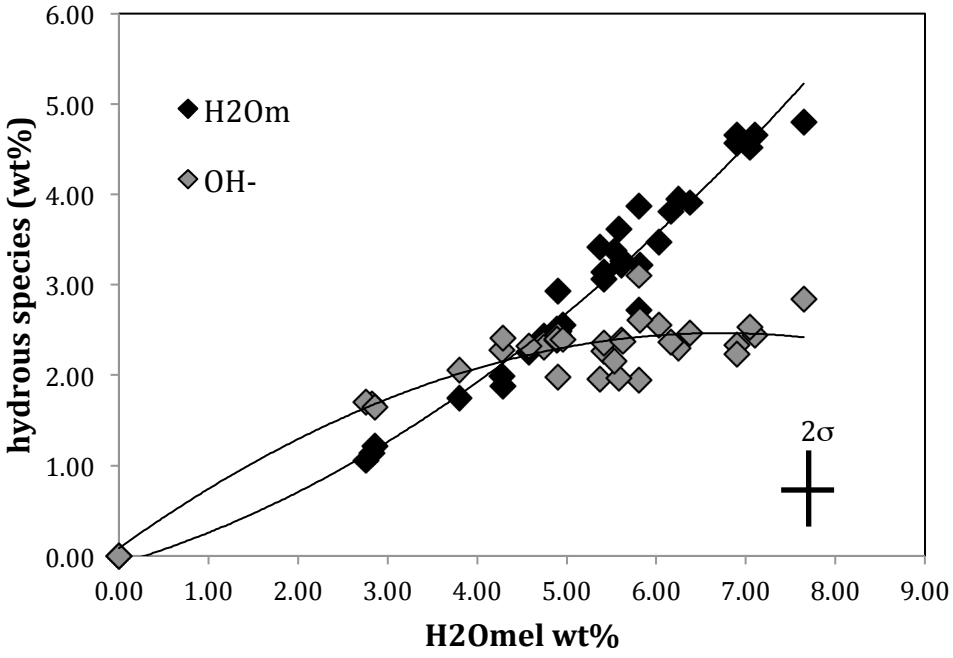

Figure 6.6: Measured concentrations of molecular water groups (H_2O_m) and hydroxyl (OH) vs. total water content in the experimental GTT trachyte glasses, molecular water becomes dominant over OH groups for total $H_2O \geq 4.2$ %

6.5 DISCUSSION

6.5.1 Comparison with previous works

In this paragraph we will discuss the comparison of the experimental results obtained in our study with other experimental solubility models obtained for other similar and roughly similar composition. We compared also our experimental results with those obtained through the thermodynamic solubility model of Papale et al., (2006), which calculates the water solubility as a function of temperature pressure and melt composition.

The comparison with previous works on trachyte composition of Di Matteo et al. (2004); Fanara et al., 2015 evidenced how the water solubility on silicate melt compositionally similar can be rather different. The experimental results presented in this study are broadly similar to the results of Fanara et al., (2015) but both differ considerably with part (ZAC series) of the results of Di Matteo et al., (2004) (Fig. 6.5).

In detail, the water dissolved at 1 kbar in GTT melt is ~ 1.20 wt % lower and this difference increases with increasing pressure. On the contrary, considering the trachyte composition of Di Matteo et al., (2004) with the lowest Na/K among their three starting compositions (for which only one experimental datum is reported) the water content dissolved is similar. Di Matteo et al., (2004) attributed this difference in their dataset principally to the variations in the Na_2O content of the starting materials. Despite the similarity in sodium content between GTT and the composition of Di Matteo et al. (2004) with highest Na/K (their sample ZAC) the differences in water solubility are considerable (Fig 6.5). However, this differences can ben ascribed to the general difference in the chemical composition between the two staring materials considered. Nevertheless, the dependence of water solubility in trachyte melts respect to small variation in chemical composition has not been fully investigated. It is noteworthy that being different the temperature at which experiments were performed, this difference in water solubility could be due to an effect of temperature; in fact, as shown by experiments on rhyolite composition of Yamashita (1999), a decrease in temperature of 300°C at 1 kbar increases the water solubility up to 1wt%.

If instead, our experimental data are compared with water solubility studies for silicate melts of different compositions, these almost coincide with data for rhyolitic melt of Tamic et al., (2001), but also with strikingly different starting composition such as the phonolite of Schmidt & Behrens (2008) (Fig. 6.7).

Finally, the comparison with water solubility inferred trough the thermodynamical model of Papale et al., (2006), shows that the water solubility calculated is overestimated. At 1 kbar (T= 950°C the water content calculated for GTT is 1wt % higher with respect to the experimental solubility at the same conditions and this difference becomes increasingly higher with increasing pressure (Fig. 6.8). It is worth to note that the solubility model of Papale et al., (2006) has been successfully tested on phonolitic melts by Schmidt & Behrens (2008) but failed to reproduce the water solubility in GTT trachytic melt.

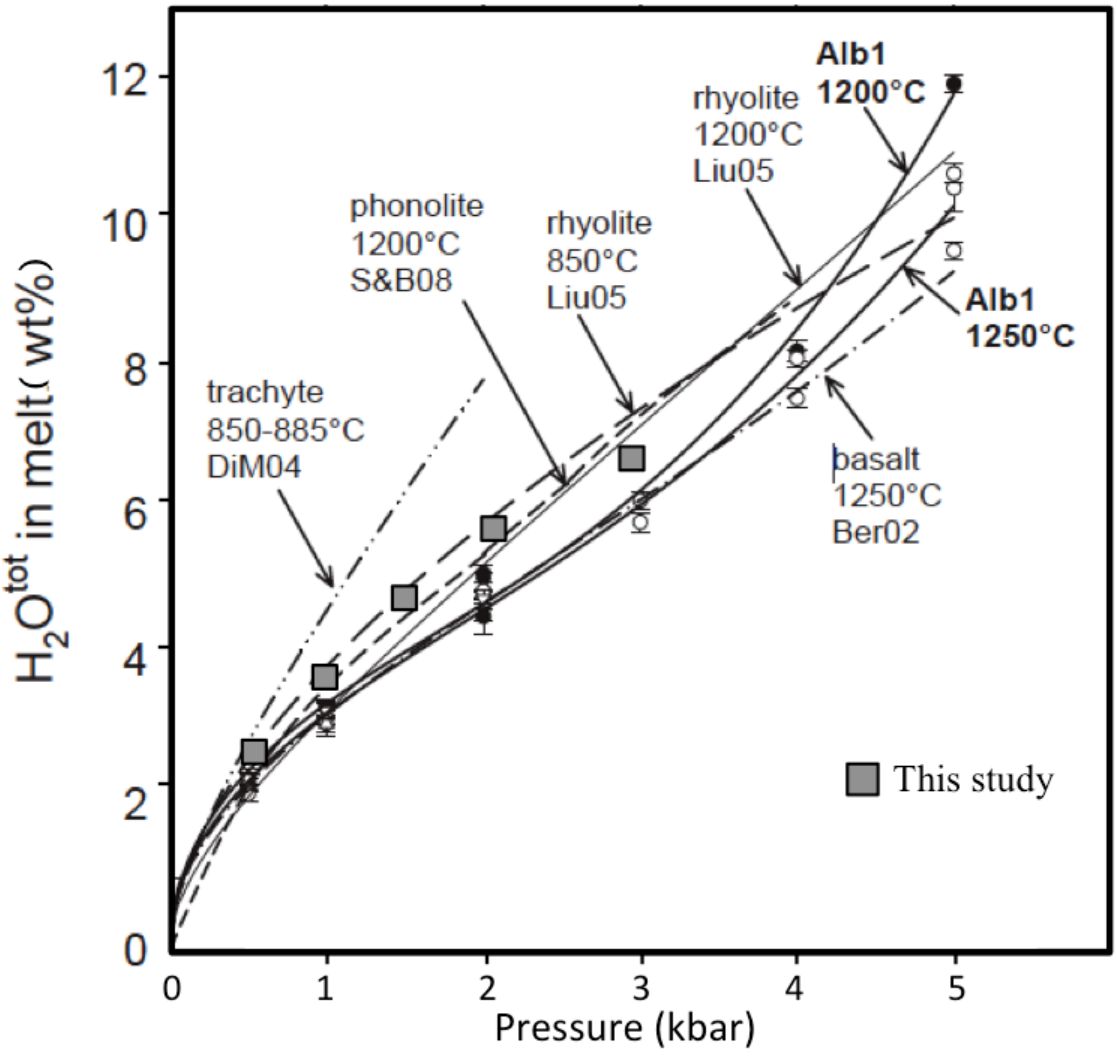

Figure 6.7: Comparison between the experimental results on the water solubility in trachytic melt as a function of pressure obtained in this study (colored squares) and experimental studies on mafic to silica-rich compositions. Literature values from: rhyolites: Liu et al., (2005), Tamic et al., (2001); for phonolites: Schmidt & Behrens (2008); trachytes: Di Matteo et al., (2004); basalts: Berndt et al., (2002) and Behrens et al., (2009).

6.5.2 Volcanological implications

The study of water solubility in silicate melts has several implications on melt inclusion study. In ideal conditions, melt inclusion studies allow to assess the pre-eruptive volatiles content of a magma, hence, through adequate solubility models, to infer the entrapment pressure (i.e. storage conditions). In the case of Pantelleria magmatism, several recent studies have paid attention on the volatile content in melt inclusion trapped in phenocrysts of pantelleritic rocks, of some key pantellerite explosive eruptions. Studies on volatiles in trachytic melts instead are completely lacking, despite the evidence that trachyte magma –though less abundant than pantellerite ones- were erupted either explosively or effusively.

The maximum water content measured in melt inclusion with pantelleritic composition is 4.5wt% while the water content estimated for trachytic melt through thermodinamical modelling and mass balance by White et al., (2009) range between 3.40 and 4.0wt %. Assuming such as water content dissolved in the trachytic melt of Pantelleria and water as the unique volatile component (no CO_2), if the thermodynamical model of Papale et al., (2006) is used to derive the saturation pressure, the obtained inferred P ranges between 0.55 and 0.75 kbar.

If instead the experimental data presented in this study are used, the pressure values obtained range between 0.70 and 1.0 kbar. Although this pressure difference might appear small, the translation in depth of the magma storage region (calculated assuming a crustal density of 2600 kg m^{-3}) results underestimated for ~ 1 km. To underestimate of ~1 km the depth of magma storage region in volcanic system such as Pantelleria or other volcanic system in which the magma reservoir evolves at low pressure (< 2 kbar) could have important consequence as regard the consideration on the volcanic hazard.

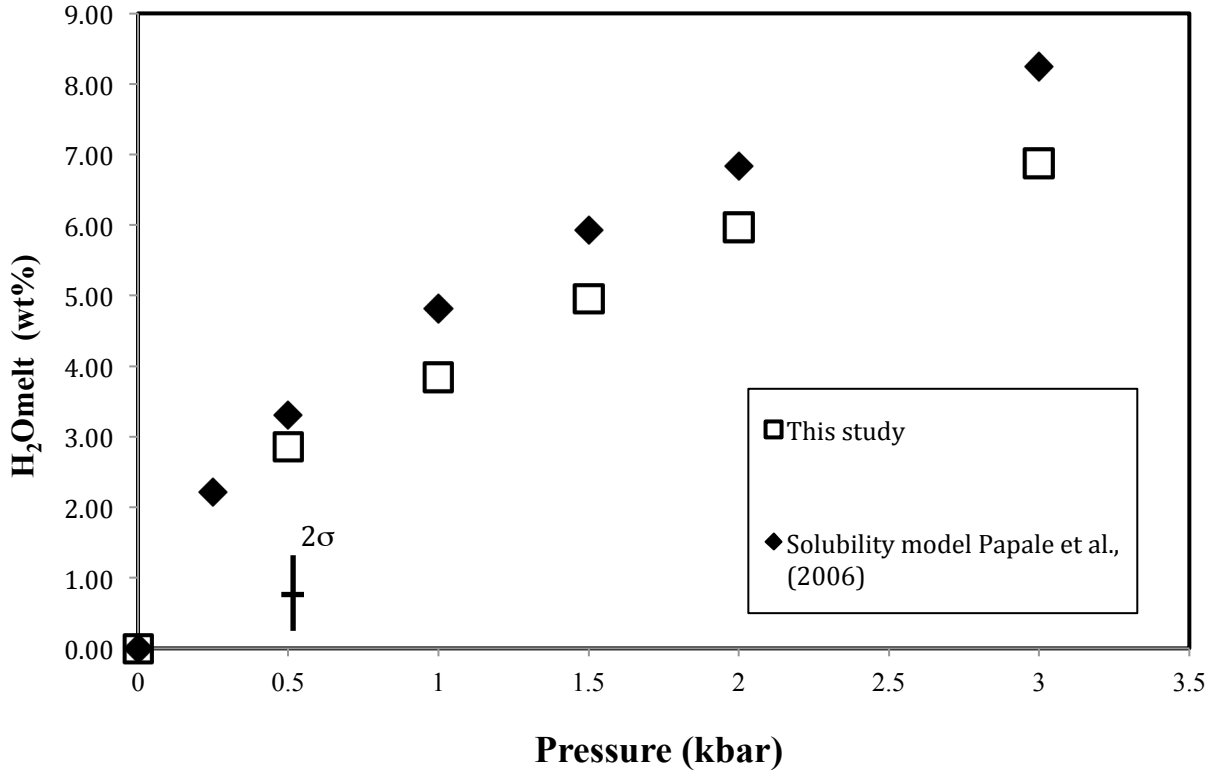

Figure 6.8: Comparison between the experimental results on the GTT trachyte and the results obtained from the calculation according to the solubility model of Papale et al., (2006) for the same bulk composition.

6.6 Conclusions

This study evidences how the solubility of water in silicate melts is composition-specific not only at the broad scale (silica-rich, silica-poor magmas) but also for tiny variations in major element abundance (alkalis overall) within the same magma typology, for instance Pantelleria and Phlegrean Fields trachytes..

We thus performed this experimental study in order to add to the existing experimental data set on water solubility in felsic magmas, the missing data for trachytes straddling the chemical divide that separates metaluminous with peralkaline magmas: those trachytes which are parental to pantellerite magmas.

Our results place tighter constraints in all the water solubility-related arguments (e.g. petrology, eruption style, pre-eruptive conditions, magmatic outgassing) and can be applied

to all the comparable magmatological situations (i.e liquid line of descent oriented towards pantellerite melts).

Experiments were carried out in a pressure range 0.5 – 3 kbar in an IHPV equipped with fast quench device, with only H_2O as volatile component. FT-IR study of experimental glasses resulted also in derivation of molar absorptivity coefficients different from those estimated in other intermediate trachyte (Di Matteo et al., 2004, Fanara et al., 2015) or phonolite melts Carroll & Blank (1997), and hence contribute to define an important composition-specific variable, needed for FT-IR studies in such a type of melts.

Our experimental data were tested against the thermodynamic solubility model of Papale et al., (2006), that takes in account the magma composition. Thermodynamic calculation resulted in consistent differences with our experimentally determined water solubility. In particular Papale (2006) model overestimates the H_2Omelt content for Na-rich magma, such as Pantelleria felsic magmas. This bias has significant inferences when applied to the study of melt inclusions, whose volatile abundances are used to derive the depth of magma storage region; this is allowed in the assumption of melt volatile saturation whose precise value is therefore essential.

In the specific case of Pantelleria trachyte melt the pressure derived from the model of Papale et al., (2006) , for a H_2Omelt = 3.4-4.0 wt%, allows to estimate the magma storage region at depth of ~2.4 km. Through our experimental solubility model, the depth value estimated is ~ 3.5 km, a difference of 30 % not trivial for these shallow magma depths, and furthermore closer to the value of ~ 4km estimated from geophysical studies by Mattia et al., (2007) for the felsic magma residence depth at Pantelleria.

Chapter 7

Conclusive remarks

This study was focused on the felsic magmas of Pantelleria Island, trachyte and pantellerite, which constitute the almost totality of the outcropping rocks.

We used an experimentally approach simulating the P-T-H_2O_{melt}-fO_2 magma conditions in the laboratory, to constrain the thermodynamic parameters at which peralkaline silicic magmas evolve. To do this, we have performed several *phase equilibrium* (crystallisation) and *water solubility* experiments on trachyte and pantellerite magmas, representative of key eruptions of the island's eruptive history.

The first set of experiments was performed in a pressure range of 0.5-1.5 kbar, temperature 680-950°, fluid saturation conditions (H_2O+CO_2) and redox conditions around the FMQ buffer; solubility experiments instead were realized at supraliquidus conditions (T≥ 950°C), pressure range 0.5 kbar- 3 kbar, water saturation conditions and fO_2 ~ FMQ buffer.

The main findings of this experimental work, outlined at the end of the specific chapters through the text body, can be further summarized as follows:

1) Phase equilibrium experiments on trachytic top member of the Green Tuff zoned eruption (age: 45 ka), and (ii) Post Cinque Denti Caldera Montagna Grande trachyte (age: 37-44 ka) allowed us to constrain the pre-eruptive conditions of intermediate (metaluminous) magmas at Pantelleria that bridge the compositional gap of basaltic mafic end member with the peralkaline (pantellerite) one.

Purposes were two-fold: (i) to infer the storage conditions and these were constrained at pressure 1.0-1.5 kbar, temperature 900-950°C redox conditions around FMQ buffer, (ii) to outline a petrogenetic relationship between trachytes (parent) and pantellerites (derivative), a process that with a general concordance is highly likely to occur at shallow crustal level, but was never experimentally demonstrated. To the best of our knowledge, this is the first time that the transition between a metaluminous magma and a peralkaline derivative is experimentally achieved at low pressure, confirming previous suggestions regarding the origin of peralkaline rhyolite by low-pressure fractional crystallization of a metaluminous, more mafic, parental magma.

2) Phase equilibrium experiments on pantelleritic samples of *Green Tuff eruption (age: 45 ka)* and *Fastuca eruption* (age: 9.7 ka) allowed bringing further (and tighter) constraints on pre-eruptive conditions of pantelleritic magmas of Pantelleria already investigated by Di Carlo et al., (2010). In particular, this work supports the low-pressure evolution of peralkaline rhyolite of Pantelleria as well as their H_2O-rich character, fixing pre-eruptive conditions at T=750°C, P=1 kbar redox conditions slightly below the FMQ buffer and H_2O melt ~ 4wt%.

Crystallisation experiments better defined the stability fields of some crucial mineral phases such as fayalite, a mineral common in pantellerite but never reproduced experimentally in these magmas. Fayalite stability requires precise redox conditions and melt peralkalinity to be stable in paragenisis with other minerals of pantellerite. The different paragenesis of Pantelleria peralkaline rhyolite described by White et al., (2005) are thus related with a different degree of evolution of pantellerites.

3) H_2O solubility experiments on trachyte melt evidenced that silicate melts with similar chemical composition (i.e a trachyte from the Phlegrean Fields) can dissolve different amounts of water at the same T-P conditions. One immediate consequence is that some popular thermodynamic models (e.g. Papale et al., 2006) used to determine the water solubility in magmas as a function of pressure, temperature and chemical composition, failed to reproduce the exactly H_2O solubility in these peculiar trachytes; in particular there is a tendency to overestimate the H_2O content potentially soluble at each pressure.

This experimental achievement has relevant consequences on the calculation of crystallization pressure as could be inferred from H_2O content determined in melt inclusions, that can propagate in an error in depth determination (underestimation of thermodynamic models). Our experiments fill the scarcity of experimental data particularly evident for intermediate magmas close to the metaluminous-peralkaline chemical divide, a region where subtle compositional variations result in ample solubility differences.

Acknowledgements

I would like to express my special thanks to my PhD supervisor Prof. Silvio G. Rotolo for receiving the project, supporting and encouraging me during the last three years.

Special and sincere thanks go to Dr. Bruno Scaillet, for the kind hospitality at Institut des Sciences de la Terre d'Orleans (ISTO) and his enormous scientific and human contribution during my long research periods spent in Orleans.

I am particularly grateful also to Dr. Juan Andujar and Dr. Ida di Carlo for the long and constructive discussions but above all for their friendship, your human contribution has been very important for me in the last years.

Thanks are also due to Arnaud Villaros, Claudie Hulin, Malcolm Massuyeau, David Sifré, and all people of "Magma Team" at ISTO, during my stay in Orleans I felt like at home.

A big thank you goes to Alessandro Bonfardeci my fellow PhD student, you have been a colleague and a friend in the last ten years of geological studies.

Thanks go also to the student Alessandro Ciulla, Giovanni Longo and Marco Caruso, working with you has been a great human experience.

Finally, but most important, I would like to thank my family, Mum, Dad and Mauro, without you and your constant support, encouragement and love, I couldn't have actually done it.

Thank you

Appendix

Table 1: Composition of experimental clinopyroxenes (wt%)

Green Tuff pantellerite (GTP)

Run	n.	SiO_2	TiO_2	Al_2O_3	FeO_{tot}	MnO	MgO	CaO	Na_2O	K_2O	P_2O_5	Total	XFe
GT-R 4, 850°C, 1000 bar													
4	1	49.89	0.35	0.18	19.20	1.41	9.20	17.22	0.70	0.02	0.00	98.17	0.54
sd													
5	1	49.99	0.36	0.16	20.20	1.41	8.01	17.32	0.75	0.06	0.00	98.26	0.59
sd													
GT-R 1, 800°C, 1000 bar													
1	4	50.05	0.41	0.16	20.67	1.11	8.10	16.80	1.21	0.01	0.00	98.49	0.59
sd													
2	3	50.46	0.50	0.18	22.21	1.27	8.28	15.84	1.46	0.30	0.00	100.52	0.60
sd		0.59	0.16	0.02	1.03	0.18	0.23	0.88	0.25	0.00	0.00	0.21	
3	5	50.27	0.51	0.26	23.80	1.42	7.83	13.73	1.31	0.10	0.00	99.13	0.63
sd		0.68	0.11	0.06	0.69	0.24	0.26	0.27	0.10	0.00	0.00	0.52	
4	3	50.28	0.47	0.24	24.80	1.51	6.02	15.00	1.55	0.10	0.00	99.87	0.69
sd		0.72	0.15	0.13	1.70	0.19	0.31	1.96	0.35	0.00	0.00	0.84	
5	2	51.19	0.61	0.28	25.62	*1.68*	7.20	12.96	1.28	0.30	0.00	101.1	0.70
sd		0.41	0.05	0.14	0.00	0.04	0.18	0.40	0.15	0.02	0.91	0.41	
GT-R 3, 750°C, 1000 bar													
1	3	51.85	0.446	0.51	23.5	1.47	3.80	18.714	1.32	0.00	0.04	101.61	0.77
sd		0.16	0.20	0.15	1.70	0.19	0.43	0.32	0.17	0.01	0.00	0.84	
2	4	50.20	0.37	0.14	23.80	1.48	2.99	16.06	2.29	0.08	0.00	97.43	0.82
sd		0.91	0.09	0.09	0.69	0.34	0.23	0.28	0.23	0.00	0.00	0.21	
3	3	49.40	0.40	0.24	24.83	1.18	3.16	17.14	2.17	0.20	0.02	98.52	0.82
sd	5	0.45	0.11	0.14	0.7	0.22	0.32	0.41	0.50	0.02	0.00	0.43	
4	2	49.30	0.19	0.11	26.64	1.57	2.70	16.81	2.26	0.09	0.08	99.67	0.85
sd		0.77	0.17	0.06	0.3	0.35	0.26	0.10	0.10	0.00	0.00	0.82	

Fastuca Pantellerite (FP)

Run	n.	SiO_2	TiO_2	Al_2O_3	FeO_{tot}	MnO	MgO	CaO	Na_2O	K_2O	P_2O_5	Total	XFe
GT R 20 750°C, 1000 bar													
1	5	49.71	0.70	0.83	26.45	1.45	1.78	15.50	2.68	0.3	0.00	99.33	0.89
sd		1.89	0.68	0.36	1.11	0.21	0.10	1.03	0.64	1.89	0.00	0.90	
2	4	51.33	0.52	1.40	26.81	1.45	1.45	13.61	3.33	0.02	0.00	99.19	0.91
sd		0.92	0.11	0.71	1.29	0.14	0.25	1.05	0.59	0.00	0.00	1.58	
3	5	48.54	0.75	0.57	29.48	1.46	1.37	13.50	3.07	0.08	0.00	98.38	0.92
sd		1.30	5.23	1.93	4.58	0.22	0.43	4.21	0.51	0.03	0.00	1.30	
4	6	48.25	0.63	0.26	30.80	1.56	1.27	13.25	2.61	0.00	0.00	98.63	0.93
sd		0.65	0.31	0.07	1.33	0.14	0.05	0.20	0.88	0.00	0.00	0.56	
GT R23 680°C, 1000bar													
2	3	54.23	0.71	2.25	25.59	1.06	0.53	10.93	4.87	0.60		100.76	0.96
sd		1.98	0.07	0.69	0.98	0.29	0.09	0.94	0.10			1.63	
3	1	49.32	2.06	0.68	33.67	1.23	0.90	2.22	6.91	1.01	0.091	98.10	0.97

sd													

n: number of analysis;
sd: standard deviation;
FeOtot: Total Iron reported as FeO;
XFe is molar Fe/(Fe+Mg) in clinopyroxene

Table 2: Composition of experimental olivines (wt%)

Fastuca Pantellerite (FP)

Run	n.	SiO_2	TiO_2	Al_2O_3	FeO_{tot}	MnO	MgO	CaO	Na_2O	K_2O	P_2O_5	Total	Fa mole%
GT-R 20, 750°C, 1000 bar													
1	2	29.56	0.00	0.05	63.30	4.40	1.17	0.25	0.00	0.03	0.06	98.84	90.62
sd		0.11	0.00	0.00	1.16	0.10	0.09	0.04	0.00	0.04	0.03	0.39	
2	6	29.32	0.03	0.02	62.72	3.82	1.13	0.23	0.05	0.04	0.08	97.45	91.40
sd		0.45	0.04	0.02	1.55	0.39	0.06	0.04	0.04	0.03	0.05	0.83	
3	3	29.48	0.04	0.00	64.78	3.52	0.94	0.21	0.05	0.03	0.10	99.16	92.46
sd		0.22	0.04	0.01	1.54	0.22	0.05	0.03	0.06	0.03	0.06	1.58	

n: number of analysis;
sd: standard deviation;
FeO_{tot} Total Iron reported as FeO;
Fa mol(%)=100 $Fe/(Fe_{tot}+Mg+Mn)$ in olivine

Table 3: Composition of experimental alkali feldspars (wt%)

Green Tuff pantellerite (GTP)

	n.	SiO2	TiO_2	Al_2O_3	FeO_{tot}	MnO	MgO	CaO	Na_2O	K_2O	P_2O_5	Total	An-Or (%)
GT-R 4, 850°C, 1000 bar													
5	1	67.58	0.00	18.59	1.43	0.00	0.00	0.01	7.62	5.23	0.00	100.40	68.9-31.1
sd													
GT-R 1, 800°C, 1000 bar													
3	4	68.37	0.03	18.21	1.04	0.03	0.01	0.02	7.72	5.04	0.03	100.50	66.5-33.5
sd		0.90	0.04	0.21	0.24	0.04	0.01	0.02	1.06	1.68	0.04	0.73	
4	6	68.28	0.06	17.85	1.38	0.02	0.02	0.02	7.28	5.32	0.02	100.28	67.5-32.43
sd		0.71	0.07	0.68	0.49	0.02	0.03	0.03	0.47	1.77	0.02	0.80	
5	5	68.10	0.03	18.19	1.15	0.00	0.00	0.01	7.53	5.52	0.01	100.58	67.5-32.43
sd		0.38	0.04	0.28	0.29	0.00	0.01	0.01	0.65	0.95	0.02	0.24	
GT-R 3, 750°C, 1000 bar													
2	5	67.79	0.02	17.68	1.12	0.01	0.00	0.00	7.30	6.25	0.00	100.24	64.2-35.8
sd		0.41	0.02	0.23	0.18	0.02	0.00	0.01	0.20	0.18	0.00	0.61	
3	4	67.92	0.04	17.81	1.09	0.02	0.01	0.06	8.17	5.04	0.00	100.16	70.9-28.7
sd		0.55	0.02	0.36	0.23	0.03	0.01	0.10	1.08	1.19	0.00	0.71	
4	8	67.41	0.02	17.97	0.95	0.06	0.10	0.02	7.32	4.85	0.00	98.53	64.8-30.3
sd		0.78	0.04	0.13	0.22	0.08	0.19	0.02	0.23	0.08	0.01	0.74	

Post Cinque Denti (PCD)

	n.	SiO_2	TiO_2	Al_2O_3	FeO_{tot}	MnO	MgO	CaO	Na_2O	K_2O	P_2O_5	Total	An-Or (%)
GT R20 750°C, 1000 bar													
2	6	66.38	0.04	17.54	1.16	0.03	0.01	0.02	7.05	6.90	0.01	99.14	60.7-39.2
sd		0.64	0.05	0.21	0.20	0.05	0.02	0.02	0.22	0.30	0.02	1.12	
3	5	67.06	0.05	17.09	1.77	0.01	0.01	0.07	7.89	5.79	0.01	99.74	66.4-33.4
sd		0.68	0.05	0.25	0.30	0.01	0.01	0.09	0.28	0.27	0.01	1.00	
4	1	65.28	0.03	15.35	3.15	0.00	0.04	0.27	8.01	5.55	0.00	97.68	68.4-31.2
sd													
GT R23 680°C, 1000 bar													
3		66.37	0.00	17.55	1.61	0.07	0.01	0.05	6.03	8.30	0.02	100.02	52.8-47.2
sd		0.39	0.01	0.15	0.25	0.06	0.01	0.07	0.52	0.49	0.03	0.61	
4		67.28	0.02	16.92	2.22	0.08	0.00	0.00	6.61	7.11	0.01	100.26	58.3-41.7
		0.46	0.04	0.57	0.65	0.08	0.00	0.01	0.24	0.30	0.02	0.67	

n: number of analysis;
sd: standard deviation
FeO_{tot} Total iron reported as FeO
An-Or (%): mole % of anorthite and orthoclase of the alkali feldspar.

Table 4: Composition of experimental aenigmatites (wt%)

Green Tuff Pantellerite (GTP)

	n.	SiO_2	TiO_2	Al_2O_3	FeO_{tot}	MnO	MgO	CaO	Na_2O	K_2O	P_2O_5	Total	XTi
GT-R 3 750°C, 1000 bar													
2	4	40.71	8.80	0.54	39.01	1.20	1.17	0.53	7.03	0.03	0.00	99.01	16.84
sd		0.20	0.10	0.09	0.96	0.11	0.08	0.07	0.14	0.03	0.00	0.93	
3	5	41.25	8.66	0.98	37.98	1.04	1.16	0.57	6.89	0.06	0.00	98.58	17.02
sd		0.82	0.86	0.63	1.90	0.25	0.11	0.03	0.20	0.09	0.00	1.97	
4	7	40.74	8.24	0.53	38.98	1.09	0.93	0.58	6.83	0.03	0.00	97.95	15.97
sd		0.51	0.72	0.13	1.04	0.10	0.23	0.11	0.20	0.03	0.00	0.88	
5	4	40.40	7.95	0.76	38.95	1.16	0.94	0.67	6.80	0.06	0.00	97.70	15.50
sd		0.41	1.00	0.09	0.35	0.28	0.24	0.28	0.69	0.05	0.00	0.52	

Fatuca Pantellerite (FP)

	n.	SiO_2	TiO_2	Al_2O_3	FeO_{tot}	MnO	MgO	CaO	Na_2O	K_2O	P_2O_5	Total	XTi
GT 20 750°C, 1000 bar													
2	4	40.95	9.04	0.50	39.48	1.01	0.63	0.52	6.96	0.05	0.00	99.15	17.08
sd		0.79	1.39	0.12	2.99	0.31	0.14	1.80	0.98	0.04	0.00	2.23	
2	3	40.43	8.73	0.47	40.72	1.07	0.59	0.45	6.78	0.06	0.00	99.30	16.29
sd		0.49	0.14	0.14	0.86	0.07	0.03	0.05	0.94	0.05	0.00	0.81	
GT 23 680°C, 1000 bar													
1	6	40.39	7.50	0.67	40.41	1.27	0.48	0.75	6.84	0.09	0.00	98.39	14.29
		0.64	0.43	0.21	1.33	0.14	0.04	0.46	0.44	0.05	0.00	1.22	
2	4	41.99	7.32	0.86	40.97	1.15	0.44	0.59	6.94	0.03	0.00	100.26	13.83
		1.14	0.83	0.32	0.39	0.19	0.04	0.31	0.07	0.02	0.00	0.36	
3	3	40.78	8.63	0.40	40.14	1.60	0.22	0.21	7.05	0.01	0.00	99.04	15.20
		0.40	0.69	0.04	0.88	0.15	0.00	0.02	0.16	0.03	0.00	0.15	

n: number of analysis;
sd: standard deviation
FeO_{tot} Total iron reported as FeO
XTi: is molar [(Ti/(Fe+Ti))*100] in aenigmatite.

Table 5: Composition of experimental amphiboles (wt%)

Green Tuff pantellerite (GTP)

	n.	SiO_2	TiO_2	Al_2O_3	FeO_{tot}	MnO	MgO	CaO	Na_2O	K_2O	P_2O_5	Total	XFe
GT-R 1, 800°C, 1000 bar													
1	4	51.66	1.31	1.31	18.48	0.59	12.88	6.36	4.33	0.36	0.00	97.27	0.28
sd		0.91	0.21	0.15	0.99	0.09	0.30	0.32	0.17	0.03	0.00	0.67	
2	4	51.60	1.36	1.16	18.53	0.76	12.69	6.50	4.53	0.40	0.00	97.53	0.31
sd		0.68	0.21	0.16	0.91	0.12	0.32	0.23	0.19	0.10	0.00	0.65	
3	6	51.22	1.66	1.41	20.40	0.69	11.51	5.86	4.89	0.41	0.00	98.06	0.35
sd		0.44	0.19	0.25	0.77	0.19	0.51	0.38	0.15	0.08	0.00	0.65	
4	4	51.73	2.07	1.23	19.14	0.61	11.79	5.95	5.26	0.46	0.00	98.23	0.36
sd		0.70	0.20	0.24	1.64	0.05	0.66	0.44	0.18	0.05	0.00	0.71	
5	5	51.81	2.15	1.15	20.87	0.59	10.82	5.26	5.43	0.03	0.00	98.08	0.41
sd		1.06	0.22	0.14	1.07	0.10	0.49	0.29	0.15	0.01	0.00	0.70	
GT-R 3, 750°C, 1000 bar													
1	5	50.80	1.62	1.47	24.05	1.00	8.03	5.43	5.01	0.51	0.00	97.92	0.55
		1.80	0.26	0.64	1.47	0.15	0.78	0.48	0.32	0.08	0.00	1.28	
2	4	50.31	2.03	1.38	26.47	0.87	6.00	4.74	5.15	0.57	0.00	97.52	0.66
		1.00	0.16	0.17	0.08	0.26	0.20	0.35	0.19	0.10	0.00	1.70	
3	5	49.34	3.00	1.15	28.85	1.10	3.27	3.36	6.11	1.11	0.00	97.29	0.81
		2.38	1.40	0.51	1.79	0.00	2.24	0.29	0.13	0.41	0.00	1.94	
4	3	50.52	1.81	0.94	29.07	1.25	2.91	5.79	6.10	0.95	0.00	99.36	0.85
sd		0.12	1.31	0.68	0.32	0.33	0.14	3.88	0.51	0.67	0.00	0.73	

Fastuca pantellerite (FP)

	n.	SiO_2	TiO_2	Al_2O_3	FeO_{tot}	MnO	MgO	CaO	Na_2O	K_2O	P_2O_5	Total	% Ilm
GT-R 23, 680°C, 1000 bar													
1	4	47.49	1.81	1.09	32.93	1.22	1.76	3.94	5.59	1.08	0.01	96.93	0.89
sd		0.53	0.37	0.18	0.45	0.22	0.11	0.22	0.26	0.13	0.01	0.63	
2	5	48.00	2.38	1.17	32.98	1.29	1.39	3.09	6.26	1.05	0.01	97.62	0.92
sd		0.87	1.16	0.55	1.09	0.26	0.41	1.07	0.41	0.14	0.03	1.13	
3	7	48.76	2.57	0.68	32.36	1.33	1.04	2.39	6.88	1.23	0.02	97.26	0.94
sd		0.60	0.35	0.16	1.02	0.15	0.13	0.25	0.24	0.12	0.04	0.95	

n: number of analysis;
sd: standard deviation
FeO_{tot} Total Iron reported as FeO
XFe is molar Fe/(Fe+Mg) in amphibole

Table 6: Composition of experimental glasses (wt%)

Green Tuff pantellerite (GTP)

Run	n.	SiO_2	TiO_2	Al_2O_3	FeO_{tot}	MnO	MgO	CaO	Na_2O	K_2O	P_2O_5	Total	P.I
GT-R 2, 900°C, 1000 bar													
5	7	72.89	0.52	9.04	6.01	0.19	0.50	0.51	7.57	2.70	0.06	100	1.70
sd		0.36	0.07	0.11	0.23	0.07	0.03	0.04	0.81	0.18	0.09	0.94	
6	7	73.57	0.53	9.06	5.34	0.29	0.53	0.44	7.27	2.91	0.07	100	1.67
sd		0.44	0.10	0.22	0.22	0.10	0.04	0.05	0.57	0.14	0.09	0.67	
7	7	73.56	0.54	9.18	5.09	0.26	0.51	0.45	7.27	3.08	0.06	100	1.67
sd		0.65	0.09	0.31	0.19	0.09	0.02	0.08	0.38	0.12	0.09	0.63	
GT-R 4, 850°C, 1000 bar													
1	20	71.74	0.55	9.34	6.94	0.13	0.56	0.46	7.39	2.88	0.01	100	1.64
sd		0.81	0.09	0.33	0.68	0.09	0.10	0.16	0.62	0.11	0.07	0.00	
2	5	72.66	0.54	9.39	6.21	0.18	0.41	0.45	7.25	2.91	0.01	100	1.61
sd		0.83	0.06	0.17	0.35	0.06	0.11	0.08	0.94	0.14	0.06	0.92	
3	3	72.64	0.50	9.42	5.58	0.16	0.55	0.41	7.61	3.09	0.04	100	1.69
sd		0.17	0.08	0.40	0.28	0.07	0.09	0.05	0.80	0.12	0.03	0.80	
4	5	73.34	0.47	9.30	5.27	0.21	0.55	0.69	7.28	2.88	0.02	100	1.62
		0.55	0.07	0.10	0.18	0.03	0.03	0.03	0.40	0.16	0.09	0.30	
5	7	73.62	0.52	9.16	5.43	0.07	0.47	0.53	7.06	3.16	0.00	100	1.64
		0.73	0.09	0.33	0.38	0.05	0.07	0.09	0.50	0.19	0.05	0.70	
GT-R 1, 800°C, 1000 bar													
1	4	72.91	0.52	9.14	6.65	0.07	0.37	0.36	7.23	2.75	0.00	100	1.63
sd		0.77	0.07	0.43	0.50	0.03	0.00	0.30	0.50	0.18	0.02	0.90	
2	5	73.69	0.59	9.43	5.23	0.22	0.29	0.34	7.26	2.94	0.00	100	1.60
sd		0.30	0.04	0.09	0.72	0.02	0.04	0.03	0.20	0.13	0.02	0.55	
3	7	73.36	0.45	9.27	6.17	0.26	0.27	0.29	6.79	3.13	0.00	100	1.57
sd		0.80	0.02	0.60	0.22	0.01	0.03	0.04	0.00	0.35	0.08	0.72	
4	8	73.32	0.55	8.65	6.43	0.16	0.27	0.30	7.40	2.89	0.03	100	1.77
sd		0.55	0.08	0.17	0.25	0.09	0.03	0.05	0.73	0.16	0.07	0.00	
5	7	73.31	0.47	7.70	8.03	0.34	0.29	0.30	6.66	2.90	0.04	100	1.83
sd		0.58	0.28	0.19	0.55	0.13	0.04	0.08	0.55	0.14	0.04	0.80	
GT-R 3, 750°C, 1000 bar													
1	13	74.66	0.24	9.87	4.94	0.19	0.11	0.14	6.94	2.87	0.04	100	1.47
sd		0.56	0.06	0.13	0.48	0.08	0.02	0.36	0.58	0.19	0.28	0.00	
2	6	74.80	0.27	9.13	5.00	0.17	0.12	0.27	6.67	3.22	0.04	100	1.58
sd		0.35	0.10	0.13	0.35	0.06	0.02	0.09	0.56	0.09	0.07	0.43	
3	1	72.77	0.21	7.24	8.27	0.48	0.18	0.26	6.72	3.74	0.12	100	2.09
		0.70	0.05	0.19	0.29	0.13	0.03	0.13	0.12	2.17	0.11	1.51	

Post Cinque Denti Caldera (PCD)

Run	n.	SiO_2	TiO_2	Al_2O_3	FeO_{tot}	MnO	MgO	CaO	Na_2O	K_2O	P_2O_5	Total	P.I
GT R 22 800°C, 1000 bar													
1	10	71.59	0.47	9.69	6.77	0.31	0.08	0.56	6.05	4.44	0.04	100.00	1.52
sd		0.33	0.08	0.28	0.30	0.05	0.01	0.04	0.18	0.09	0.07	0.49	
2	10	71.86	0.48	9.77	6.20	0.27	0.09	0.56	6.25	4.49	0.02	100.00	1.55
sd		0.94	0.10	0.28	0.17	0.07	0.03	0.07	0.11	0.15	0.08	1.06	

3	10	71.44	0.47	9.75	6.10	0.28	0.08	0.54	6.75	4.56	0.03	100.00	1.65
sd		0.23	0.07	0.22	0.23	0.06	0.03	0.09	0.14	0.08	0.08	0.32	
4	3	71.04	0.48	9.79	6.00	0.26	0.09	0.56	7.21	4.54	0.03	100.00	1.71
sd		0.66	0.15	0.62	0.13	0.10	0.06	0.18	0.71	0.13	0.04	0.89	
GT R20 750°C, 1500 bar													
2	9	71.52	0.41	9.95	6.25	0.23	0.08	0.24	6.55	4.56	0.00	100.00	1.58
sd		0.33	0.06	0.17	0.28	0.10	0.04	0.18	0.74	0.15	0.10	0.91	
1	20	71.61	0.33	9.43	7.20	0.21	0.05	0.26	6.33	4.50	0.09	100.00	1.62
sd		0.47	0.10	0.18	0.23	0.09	0.02	0.10	0.73	0.21	0.08	1.03	
2	20	71.64	0.55	7.70	8.22	0.39	0.08	0.30	6.73	4.35	0.00	100.00	2.05
sd		0.80	0.08	0.23	0.24	0.08	0.02	0.25	0.15	0.16	0.14	0.06	
4	10	71.49	0.55	6.47	9.16	0.64	0.07	0.45	6.92	4.24	0.01	100.00	2.47
sd		0.45	0.09	0.17	0.34	0.08	0.03	0.08	0.12	0.19	0.08	0.75	
GT R23 680°C, 1000 bar													
2	15	73.75	0.12	9.44	5.37	0.22	0.02	0.09	6.74	4.22	0.04	100.00	1.66
sd		0.96	0.24	0.22	0.63	0.12	0.06	0.16	0.12	0.15	0.07	0.57	
3	12	74.05	0.24	8.17	6.04	0.27	0.02	0.17	6.41	4.61	0.00	100.00	1.90
sd		0.30	0.06	0.22	0.25	0.12	0.06	0.05	0.14	0.01	0.03	0.10	
4	5	73.44	0.22	6.38	8.01	0.26	0.03	0.17	6.59	4.87	0.04	100.00	2.53
sd		0.50	0.07	0.10	0.19	0.11	0.02	0.29	0.09	0.07	0.14	0.43	

n: number of analysis;
sd: standard deviation
FeO_{tot} Total Iron reported as FeO
P.I peralkalinity index

Table 7: Composition of experimental glasses (wt%)

Run	n.	SiO_2	TiO_2	Al_2O_3	FeO_{tot}	MnO	MgO	CaO	Na_2O	K_2O	P_2O_5	Total
GT R 16 975°C, 3000 bar												
1		65.28	0.87	15.55	5.64	0.21	0.60	1.50	5.39	4.57	0.39	65.28
sd		0.74	0.09	0.65	0.26	0.10	0.03	0.05	0.20	0.16	0.12	0.74
GT R 15 975°C, 2000 bar												
1		65.60	0.88	14.86	5.58	0.22	0.62	1.50	6.17	4.37	0.20	100.00
sd		0.36	0.10	0.18	0.26	0.12	0.03	0.06	0.62	0.14	0.09	0.67
GT R 9 955°C, 1500 bar												
1	7	65.23	0.95	15.24	5.34	0.35	0.65	1.54	6.46	4.55	0.29	100.00
sd		0.36	0.07	0.11	0.23	0.07	0.03	0.04	0.81	0.18	0.09	0.94
GT R 10 950°C, 1500 bar												
1	8	65.62	0.77	15.46	4.79	0.24	0.60	1.33	6.33	4.65	0.21	100.00
sd		0.55	0.08	0.17	0.25	0.09	0.03	0.05	0.73	0.16	0.07	0.00
GT R 11 950°C, 500 bar												
1	16	64.92	0.87	15.08	5.29	0.19	0.63	1.44	6.71	4.67	0.21	10.00
sd		0.62	0.07	0.32	0.31	0.08	0.04	0.06	0.26	0.09	0.09	0.98
GT R 19 950°C, 3000 bar												
1	20	65.06	0.80	15.04	5.25	0.23	0.61	1.42	7.14	4.28	0.18	100.00
sd		0.33	0.11	0.15	0.29	0.11	0.03	0.04	0.35	0.11	0.09	0.57
GT R 18 950°C, 3000 bar												
2	20	65.38	0.83	14.91	5.40	0.23	0.62	1.46	6.50	4.50	0.17	100.00
sd		0.50	0.12	0.20	0.19	0.09	0.02	0.05	0.36	0.12	0.07	0.76

REFERENCES

Albarède, F. (1995). *Introduction to Geochemical Modelling*. Cambridge: Cambridge Univeristy Press, 543p.

Almeev, R.R., Bolte, T., Nash, B.P., Holtz, F., Erdmann, M., & Cathey, H. (2012). High-temperature, low-H_2O silicic magmas of the Yellostone Hotspot: an experimental study of rhyolite from the Bruneau–Jarbidge eruptive center, central Snake River Plain, U.S.A. *Journal of Petrology*, **53**, 1837–1866.

Andujar, J., Scaillet, B., Pichavant, M. & Druitt, T. H. (2015). Differentiation Conditions of a basaltic magma from Santorini, and its bearing on the production of andesite in arc settings. *Journal of Petrology* **56**, 765-794.

Avanzinelli, R., Bindi, L., Menchetti, S. & Conticelli, S. (2004). Crystallization and genesis of peralkaline magmas from Pantelleria volcano: an integrated petrological and crystal-chemical study. *Lithos* **73**,41-69.

Bachmann, O., & Bergantz, G.W., 2004. On the origin of crystal-poor rhyolites: extracted from batholithic crystal mushes. *Journal of Petrology* **45** ,1565–1582.

Bailey, Cvile, D., Lodolo, E., Tortorici, L., Lanzafame, & G., Brancolini, G. (2008). Relationships between magmatism and tectonics in a continental rift: the Pantelleria Island region (Sicily Channel, Italy). *Marine Geology* **251**, 32–46.

Bailey, D. K. & Macdonald, R (1975). Fluorine and chlorine in peralkaline liquids and the need for magma generation in an open system. Mineralogical Magazine **40**, 405–414.

Bailey, D. K. & Macdonald, R (1987). Dry peralkaline felsic liquids and carbon dioxide flux throught the Kenya rift zone. In: Maysen, B (ed) *Magmatic Processes: Physicochemical Principles. Geochemical Society, Special Publication* **1**, 91-105

Bailey, D.K. & Schairer, J.F. (1964). Feldspar-liquid equilibria in peralkaline liquids – the orthoclase effect. *American Journal of Science* **262**, 1198-1206.

Barberi, F., Santacroce, R., Ferrara, G., Treuil, M. & Varet, J. (1975). A transitional basalt-pantellerite sequence of fractional crystallisation, the Boina centre (Afar Rift, Ethiopia). *Journal of Petrology* **16**, 22-56.

Barberi, F., Santacroce, R., Ferrara, G., Treuil, M. & Varet, J. (1975). A transitional basalt-pantellerite sequence of fractional crystallisation, the Boina centre (Afar Rift, Ethiopia). *Journal of Petrology* **16**, 22-56.

Beccaluva, L., Colantoni, P., Di Girolamo, P., & Savelli, C., (1981). Upper Miocene submarine volcanism in the Strait of Sicily (Banco Senza Nome). *Bulletin of Volcanology* **44**, 573–581.

Behrens H, Misiti V, Freda C, Vetere F, Botcharnikov R. &, Scarlato P (2009) Solubility of H_2O and CO2 in ultrapotassic melts at 1200 and 1250 & #xB0;C and pressure from 50 to 500 MPa. *American Mineralogist* **94**, 105–120

Behrens, H., Jantos, N., (2001). The effect of anhydrous composition on water solubility in granitic melts. *American Mineralogist* **86**, 14– 20.

Behrens, H., Meyer, M., Holtz, F., Benne, D., & Nowak, M., (2001). The effect of alkali ionic radius, temperature and pressure on the solubility of water in MAlSi3O8 melts (M=Li, Na, K, Rb). *Chemical Geology* **174**, 275–289.

Berndt, J., Liebske, C., Holtz, F., Freise, M., Nowak, M., Ziegenbein, D., Hurkuck, W., & Koepke, J., (2002). A combined rapid-quench and H2-membrane setup for internally heated pressure vessels: description and application for water solubility in basaltic melts. American Mineralogist **87**, 1717–1726.

Black, S., Macdonald, R., Barreiro, B.A., Dunkley, P.N., Smith, M., 1998. Open system alkaline magmatism in northern Kenya: evidence from U-series disequilibria and radiogenic isotopes. Contributions to Mineralogy and Petrology **131**, 364–378.

Bohrson, W. A. & Reid, M. R: (1997). Genesis of silicic peralkaline volcanic rocks in an ocean island setting by crustal melting and open-system processes: Socorro Island, Mexico. *Journal of Petrology* **12**, 2405-2431.

Botcharnikov, R.E., Behrens, H., & Holtz, F. (2006). Solubility and speciation of C-O-H fluids in andesitic melt at T = 1100–1300 °C and P = 200 and 500 MPa. *Chemical Geology* **229**, 125–143.

Bowen, N.L. 1937. Recent high temperature research on silicates and its significance in igneous geology, *American Journal of Science* **33**, 1-21.

Burnham C.W., Holloway, J. R. & Davis, N. F. (1969). Thermodynamic properties of water to 1000°C and 1000 bars. *Geological Society of America, Special Papers* **132**, 1-96.

Cadoux, A., Scaillet, B., Druitt, T. H. & Deloule, E. (2014). Magma storage conditions of large Plinian eruptions of Santorini. *Journal of Petrology* **55**, 1129–1171.

Carapezza, M., Ferla P., Nuccio, M., & Valenza, M. (1979) Caratteri petrologici e geochimici delle vulcaniti dell Isola "Ferdinan-dea". *Rendicondi Società Italiana di Mineralogia Petrologia* **35,** 277-388.

Caricchi, L. & Blundy, J. (2015a). Experimental petrology of monotonous intermediate magmas. In Caricchi, L. & Blundy, J. D. (eds) Chemical, Physical and Temporal Evolution of Magmatic Systems. Geological Society, London, Special Publication **422**

Caricchi, L., Ulmer, P. & Peccerillo, A. (2006). A high-pressure experimental study on the evolution of the silicic magmatism of the main Ethiopian Rift. Lithos **91**, 46-58.

Carroll, M.R., & Blank, J.G., (1997). The solubility of H2O in phonolitic melts. *American Mineralogist* **82**, 1111–1115.

Cashman, K. V., & M. T. Mangan (1994), Physical aspects of magmatic degassing II: Constraints on vesiculation processes from textural studies of eruptive products, in Volatiles in Magmas, edited by M. Carroll, pp. 447–478, Mineralogical Society of America.

Catalano, S., De Guidi, G., Lanzafame, G., Monaco, C. & Tortorici, L. (2009). Late Quaternary deformation on the island on Pantelleria: New constraints for the recent tectonic evolution of the Sicily Channel Rift (southern Italy). Journal of Geodynamics **48**, 75-82.

Catalano, S., Tortorici, L., & Viccaro, M. (2014). Regional tectonic control on large size explosive eruptions: Insights into the green tuff ignimbrite unit of Pantelleria. *Journal of Geodynamics* **73,** 22-33.

Charles, R.W. (1975): The phase equilibria of richterite and ferrorichterite. *American Mineralogist* **60**, 367-374.

Chou, I.-M. (1978). Calibration of oxygen buffers at elevated P and T using the hydrogen fugacity sensor. American Mineralogist **63**, 690–703.

Chou, I.M. (1986). Permeability of precious metals to hydrogen at 2 kb total pressure and elevated temperatures. American Journal of Science **286**, 638-658.

Civetta, L., Cornette, Y., Gillot, P. Y. & Orsi, G. (1988). The eruptive history of Pantelleria (Sicily Channel) in the last 50 ka. *Bulletin of Volcanology* **50**, 47-57.

Civetta, L., D'Antonio, M., Orsi, G. & Tilton, G.R. (1998). The geochemistry of volcanic rocks from Pantelleria, Sicily Channel: petrogenesis and characteristics of the mantle source region. *Journal of Petrology* **39**, 1453-1491.

Clemens, J.D. & Wall, V.J. (1981). Origin and crystallization of some peraluminous (S-type) graniticmagmas. Canadian Mineralogist **19**, 111-131.

Conte, A.M., Martonelli, E., Calarco, M., Sposato, A., Perinelli, C., Coltelli, C., & Chiocci, F.L. (2014) The 1891 submarine eruption offshore Pantelleria Island (Sicily Chennel, Italy): Identification of the vent and characterization of the products and eruptive style. Geochemistry, Geophysics, Geosystems **15**, 2555-2574.

Costa, F. Scaillet, B. & Pichavant, M. (2004). Petrological and experimental constraints on the pre-eruptive conditions of Holocene dacite from Volcan San Pedro (36°S, Chilean Andes) and the importance of sulphur in silicic subduction-related magmas. *Journal of Petrology* **45**, 855-881.

Dall'Agnol, R., Scaillet, B. & Pichavant, M. (1999). An experimental study of a lower Proterozoic A-type granite from the eastern Amazonian craton, Brazil. *Journal of Petrology* **40**, 1673-1698.

Davies, J. R. & Macdonald, R. (1987). Crustal influence in the petrogenesis of the Naivasha basal-comendite complex: combined trace element and Sr-Nd-Pb isotope constraints. *Journal of Petrology* **28**, 1009-1031.

Deer, W. A., Howie, R, A. & Zussman, J. (1992). An Introduction To The Rock-Forming Minerals, 2nd eds. Harlow: Longman, 696 pp.

Devine, J. D., Gardner, J. E., Brack, H. P., Layne, G. D. & Rutherford, M. J. (1995). Comparison of microanalytical methods for estimating H2O contents of silicic volcanic glasses. *American Mineralogist* **80**, 319-328.

Di Carlo, I., Pichavant, M., Rotolo, S. G. & Scaillet, B. (2006). Experimental crystallization of a high-K arc basalt: the golden pumice, Stromboli volcano (Italy). *Journal of Petrology* **47**, 1317–1343.

Di Carlo, I., Rotolo, S. G., Scaillet, B., Buccheri, V. & Pichavant M. (2010). Phase equilibrium constraints on pre-eruptive conditions of recent felsic explosive volcanism at Pantelleria Island, Italy. *Journal of Petrology* **51,** 2245-2276

Di Matteo, V., Carroll, M.R., Behrens, H., Vetere, F., & Brooker, R.A., (2004).Water solubility in trachytic melts. Chemical Geology **213**, 189–196.

Dingwell, D.B., Holtz, F., & Bherens, H., (1997). The solubility of H2O in peralkaline and peraluminous melts. *American Mineralogist* **82**, 434– 437.

Dingwell, D.B., Romano, C., & Hess, K.U., (1996). The effect of water on the viscosity of haplogranitic melt under P–T–X conditions relevant to silicic volcanism. *Contribution to Mineralogy and Petrology* **124**, 19– 28.

Dixon, T.E., Stolper, E., & Holloway, J.R., (1995). An experimental study of water and carbon dioxide solubilities in mid-ocean basalt liquids: Part I. Calibration and solubility models. *Journal of Petrology* **36**, 1607–1631.

Dufek, J., £ Bachmann, O. (2010) Quantum magmatism: Magmatic compositional gaps generated by melt-crystal dynamics. *Geology*, **38**, 687–690.

Esperança, S. & Crisci, G. M. (1995). The island of Pantelleria: A case for the development of DMM-HIMU isotopic compositions in a long-lived extensional setting. *Earth and Planetary Science Letters* **136,** 167-182.

Evans, B.W., & Bachmann, O., 2013. Implications of equilibrium and disequilibrium among crystal phases in the Bishop Tuff. *American Mineralogist* **98**, 271–274.

Fanara, S., Botcharnikov, R.E., Palladino, D. M., Adams, F., Buddensieck, J.,Mulch, A., & Behrens, H., (2015). Volatiles in magmas related to the Campanian Ignimbrite eruption: Experiments vs. natural findings. *American Mineralogist* **100**, 2284-2297.

Ferla, P. & Meli, C. (2006). Evidences of magma mixing in the 'Daly gap' of alkaline suites: a case study from the enclave of Pantelleria (Italy). *Journal of Petrology* **147**, 1467-1507.

Gardner, J.E., Befus, K.S., Gualda, G.A.R., & Ghiorso, M.S., 2014. Experimental constraints on rhyolite–MELTS and the late Bishop Tuff magma body. *Contributions to Mineralogy and Petrology* **168**, 1051-1065.

Gasparon, M., Innocenti, F., Manetti, P., Peccerillo, A., Tsegaye, A., (1993). Genesis of the Pliocene to recent bimodal mafic-felsic volcanism in the Debre Zeit area, central

Ethiopia: volcanological and geochemical constraints. *Journal of African Earth Sciences* **17**, 145–165.

Geist, D., Howard, K. A. & Larson, P. (1995). The generation of oceanic rhyolites by crystal fractionation: the basalt-rhyoliteassociation at Volcan Alcedo, Galapagos Archipelago. *Journal of Petrology* **36**, 965-982.

Ghiorso, M. S. & Evans, B. W. (2008). Thermodynamics of rhombohedral oxide solid solutions and a revision of the fe-ti two-oxide geothermometer and oxygen-barometer. American Journal of Sciece **308**, 957.1039.

Gioncada, A. & Landi, P. (2010). The pre-eruptive volatile contents of recent basaltic and pantelleritic magmas at Pantelleria (Italy). *Journal of Volcanology and Geothermal Research* **189**, 191-201.

Green, D.H. & Ringwood, A. E. (1967). The genesis of basaltic magmas. *Contributions to Mineralogy and Petrology* **15**, 103-109.

Hamilton, D.L., Burnham, C.W. & Osborn, E.F., (1964). The solubility of water and effects on fugacity and water content oncrystallization in mafic magmas. *Journal of Petrology* **5**, 21– 39.

Hanson, B., Delano, J.W. & Lindstrom, D.J. (1996). High-precision analysis of hydrous rhyolitic glass inclusions in quartz phenocrysts using the electron microprobe and INNA. *American Mineralogist* **81**, 1249−1262.

Holtz, F., Behrens, H., Dingwell, D.B., & Johannes, W., (1995). H_2O solubility in haplogranitic melts: compositional, pressure and temperature dependence. *American Mineralogist*. **80**, 94–108.

Holtz, F., Behrens, H., Dingwell, D.B., & Taylor, R.P., (1992). Water solubility in aluminosilicate melts of haplogranite composition at 2 kbar. *Chemical Geolology* **96**, 289–302.

Holtz, F., Roux, J., Behrens, H., & Pichavant, M., (2000). Water solubility in silica and quartzofeldspathic melts. *American Mineralogist* **85**, 682–686.

Housh, T.B. & Luhr, J.F. (1991). Plagioclase-melt equilibria in hydrous systems. *American Mineralogi*st **76**, 477–492.

Huber, C., Bachmann, O., and Manga, M. (2010b) Two competing effects of volatiles on heat transfer in crystal-rich magmas: Thermal insulation vs. defrosting. *Journal of Petrology* **51**, 847–867.

Iacono-Marziano, G., Schmidt, B.C., Dolfi, D., 2007. Equilibrium and disequilibrium degassing of a phonolitic melt (Vesuvius A.D. 79 "White Pumice") simulated by decompression experiments. *Journal of Volcanology and Geothermal Research* **161**, 151–164.

Johannes,W., & Holtz, F., (1996). Petrogenesis and experimental petrology of granitic rocks. Minerals and Rocks, vol. 22. Springer Verlag, Berlin. 335 pp.

Johnson, M. C. & Rutherford, M. J. 1989. Experimentally determined conditions in the Fish Canyon Tuff, Colorado, Magma Chamber. *Journal of Petrology* **30**, 711–737.

Kawamoto, T. & Hirose K. (1994). Au-Pd Sample Containers of Melting Experiments on Iron and Water Bearing Systems. *European Journal of Mineralogy* **6**, 381–385

Kovalenko, V. I., Hervig, R. L. & Sheridan, M. F. (1988). Ionmicroprobe analyses of trace elements in anorthoclase, hedenbergite, aenigmatite, quartz, apatite and glass in pantellerite: evidence for high water contents in pantellerite melts. *American Mineralogist* **73**, 1038-1045.

Kress, V.C. & Carmichael, I.S.E. (1991). The compressibility of silicate liquids containing Fe_2O_3 and the effect of composition, temperature, oxygen fugacity and pressure on their redox states. *Contributions to Mineralogy and Petrology* **108**, 82-92.

Landi, P. & Rotolo, S. G. (2015). Cooling and crystallization recorded in trachytic enclaves hosted inpantelleritic magmas (Pantelleria, Italy): Implications for pantellerite petrogenesis. *Journal of Volcanology and Geothermal Research* **301**, 169-179.

Lanzo, G., Landi, P., & Rotolo S. G. (2013). Volatiles in pantellerite magmas: A case study of the Green Tuff Plinian eruption (Island of Pantelleria, Italy). *Journal of Volcanology and Geothermal Research* **262**, 153-163

Larsen, J.F., Gardner, J.E., 2004. Experimental study of water degassing from phonolite melts: implications for volatile oversaturation during magmatic ascent. Journal of Volcanology and Geothermal Research **134**, 109–124.

Leake, B.E., Woolley, A.R., Arps, C.E.S., Birch, W.D., Gilbert, M.C., Grice, J.D., Hawthorne, F.C., Kato, A., Kisch, H.J., Krivovichev, V.G., Linthout, K., Laird, J., Mandarino, J.A., Maresch, W.V., Nickel, E.H., Rock, N.M.S., Schumacher, J.C., Smith, D.C., Stephenson, N.C.N., Ungaretti, L., Whittaker, E.J.W., & Youzhi, G. (1997) Nomenclature of amphiboles: *Report of the Subcommittee on Amphiboles of the International Mineralogical Association, Commission on New Minerals and Mineral Names. American Mineralogist* **82**, 1019–1037.

Lesne, P., Scaillet, B., Pichavant, M., Iacono-Marziano, G., & Beny, J.M. (2011c). Contribution to . Mineralogy and Petrology **162**, 133-151.

Lightfoot, P. C., Hawkesworth, C. J. & Setnha, S. F. (1987). Petrogenesis of rhyolites and trachytes from the Deccan Trap: Sr, Nd and Pb isotope and trace element evidence. *Contributions to Mineralogy and Petrology* **95**, 44-54.

Liu, Y., Zhang, Y., & Behrens, H., (2005). Solubility of H2O in rhyolitic melts at low pressures and a newempirical model for mixed H2O–CO2solubility in rhyolitic melts. *Journal of Volcanalogy and Geothermal Reserch* **143**, 219-235

Lowenstern, J. B. & Mahood, G. A. (1991). New data on magmatic H_2O contents of pantellerites, with implications for petrogenesis and eruptive dynamics at Pantelleria. *Bulletin of Volcanology* **54**, 78-83.

MacDonald R., Baginski B., Ronga F., Dzierzanowski P., Lustrino M., Marzoli A. & Melluso L. (2012). Evidence for extreme fractionation of peralkaline silicic magmas, the Boseti volcanic complex, Main Ethiopian Rift. *Mineralogy and Petrology* **104**, 163-175

MacDonald, R. (1974). Nomenclature and petrochemistry of the peralkaline oversaturated extrusive rocks. *Bulletin of Volcanology* **38**, 498-505.

MacDonald, R. (2012). Evolution of peralkaline silicic complexes: Lessons from the extrusive rocks. *Lithos* **152***,* 11-22.

MacDonald, R., Davies, G.R., Bliss, C.M., Leat, P.T., Bailey, D.K. & Smith, R.L. (1987). Geochemistry of high-silica peralkaline rhyolites, Naivasha, Kenya Rift Valley. *Journal of Petrology* **28**, 979-1008.

Mahood G. A (1984). Pyroclastic rocks and calderas associated with strongly peralkaline magmatism. *Journal of Geophysical Research* **89,** 8540-8552**.**

Mahood G.A., & Baker D (1986) Experimental constraints on depths of fractionation of mildly alkalic basalts and associated felsic rocks: Pantelleria, Strait of Sicily. Contribution to Mineralogy and Petrology **93**, 251-264.

Mahood, G. A. & Hildreth, W. (1986). Geology of the peralkaline volcano at Pantelleria, Strait of Sicily. *Bulletin of Volcanology* **48**, 143-172.

Mahood, G., & Hildreth, W. (1983). Nested calderas and trapdoor uplift at Pantelleria, Strait of Sicily. *Geology* **11**, 722–726.

Mandeville, C.W., Webster, J.D., Rutherford, M.J., Taylor, B.E., Timbal, A., & Faure, K. (2002). Determination of molar absorptivities for infrared absorption bands of H_2O in andesitic glasses. *American Mineralogist* **87**, 813–821.

Martel, C., Champallier, R., Prouteau, G., Pichavant, P., Arbaret, L., Balcone-Boissasard, H., Boudon, G., Boivin, P., Bourdier, J.-L. & Scaillet, B. (2013). Trachyte Phase Relations and Implication for Magma Storage Conditions in the Chaîne des Puys (French Massif Central). *Journal of Petrology* **0**, 1-37.

Martel, C., Pichavant, M., Holtz, F., Scaillet, B., Bourdier, J.-L. & Traineau, H. (1999). Effects of fO_2 and H_2O on andesitic phase-relationships between 2 and 4 kbar. *Journal of Geophysical Research* **104**, 29453-29470.

Mattia, M., Bonnaccorso, A. & Guglielmino, F. (2007). Ground deformations in the island of Pantelleria (Italy): insights into the dynamic of the current intereruptive period. *Journal of Geophysical Research* **112,**

McMillan, P.F. & Wolf, G.H. (1995). Vibrational spectroscopy of silicate liquids. In: Stebbins, J.F., McMillan, P.F., and Dingwell, D.B. Eds., *Structure, Dynamics and Properties of Silicate Melts* **32**, 247−316.

Moore, G., Vennemann, T., Carmichael, I.S.E., (1998). An empirical model for the solubility of H2O in magmas to 3 kilobars. *American Mineralogist* **83**, 36– 42.

Morgan, G.B. VI & London, D. (1996). Optimizing the electron microprobe analysis of hydrous alkali aluminosilicate glasses. *American Mineralogist* **81**, 1176−1185.

Morgan, G.B. VI & London, D. (2005). Effect of current density on the electron microprobe analysis of alkali aluminosilicate glasses. *American Mineralogist* **90**, 1131-1138.

Morimoto, N. (1989). Nomenclature of pyroxenes. Subcommittee on pyroxenes. Commission on newminerals and mineral names. *Canadian Mineralogist* **27**, 143–156.

Mungall, J.E. & Martin, R.F. (1995). Petrogenesis of basalt-comendite and basalt-pantellerite suites, Terceira, Azores, and some implications for the origin of ocean-island rhyolites. *Contributions to Mineralogy and Petrology* **119**, 43-55.

Mysen, B.O. (1983) The structure of silicate melts. *Annual Reviews of Earth and Planetary Science* **11**, 75−97.

Neave, D.A., Fabbro, G., Herd, R.A., Petrone, C.M. & Edmonds, M. (2012). Melting, differentiation and degassing at the Pantelleria volcano, Italy. *Journal of Petrology* **53**, 637–663.

Nicholls, J. & Carmichael, I. S. E. (1969). Peralkaline acid liquids: a petrological study. *Contributions to Mineralogy and Petrology* **20**, 268-294.

Ochs, F.A., & Lange, R.A., (1999). The density of hydrous magmatic liquids. *Science* **283**, 1314–1317

Ohlhorst, S., Behrens, H., & Holtz, F., 2001. Compositional dependence ofmolar absorptivities of near-infrared OH- and H_2O bands in rhyolitic to basaltic glasses. *Chemical Geology* **174**, 5–20.

Orsi G & Sheridan MF (1984) The Green Tuff of Pantelleria: a rheoignimbrite or rheomorphic fall? *Bulletin Volcanologique* **47**, 611-626

Orsi, G., Ruvo, L. & Scarpati, C. (1989). The Serra della Fastuca Tephra at Pantelleria: physical parameters for an explosive eruptionof peralkaline magma. *Journal of Volcanology and Geothermal Research* **39**, 55-60.

Papale, P., Moretti, R., Barbato, D., 2006. The compositional dependence of the saturation surface of H_2O+CO_2 fluids in silicate melts. *Chemical Geology* **229**, 78–95.

Parello, F., P. Allard, W. D'alessandro, C. Federico, P. Jean-Baptiste & O. Catani. (2000): Isotope geochemistry of the Pantelleria volcanic fluids, Sicily Channel rift: a mantle volatile end-member for volcanism in Southern Europe. Earth Planetary Science Letters **180**, 325-339.

Parker, D. (1983). Origin of the trachyte–quartz trachyte–peralkalic rhyolite suite of the Oligocene Paisano volcano, Trans-Pecos Texas. Geological Society of America Bulletin **94**

Peccerillo, A., Barberio, M.R., Yirgu, G., Ayalew, D., Barbieri, M., & Wu, T.W., (2003). Relationships between mafic and peralkaline acid magmatism in continental rift

settings: a petrological, geochemicaland isotopic study of the Gedemsa volcano, central Ethiopian rift. *Journal of Petrology* **44**, 2003–2032.

Pichavant, M. (1987). Effects of B and H_2O on liquidus phase relations in the haplogranite system at 1 kbar. *American Mineralogist* **72**, 1056-1070.

Pichavant, M., Costa, F., Burgisser, A., Scaillet, B., Martel, C. & Poussineau, S. (2007). Equilibration scales in silicic to intermediate magmas-implication for experimental studies. *Journal of Petrology* **48**, 1955-1972.

Pownceby, M. I. & O'Neill, H. St. C. (1994). Thermodynamic data redox reactions at high temperatures. III. Activity–composition relations in Ni–Pd alloys from EMF measurements at 850–1250 K, and calibration of the NiO-Ni–Pd assemblage as a redox sensor. Contributions to Mineralogy and Petrology **116**, 327–339.

Prosperini, N., Perugini, D., Poli, G. & Manetti, P. (2000). Magmatic enclaves distributionwithin the Khaggiar lava dome (Pantelleria, Italy): implication for magma chamber dynamics and eruption. *Acta Vulcanolgica* **12**, 37–47.

Ratajeski, K., & Sisson, T. W. (1999). Loss of iron to gold capsules in rock-melting experiments. *American Mineralogist*, **84**, 1521–1527.

Riccò, A. *(*1892*),* Terremoti, sollevamento ed eruzione sottomarina a Pantelleria nella seconda metà dell'ottobre 1891. Annali dell'Ufficio Centro Meteorologico e Geodinamico Italiano ***vol. XI****,* 7–27.

Robie, R. A., Hemingway, B. S. & Fisher, J. R. (1979). *Thermodynamic properties of minerals and related substances at 298.15 K and 1 bar (105 Pascals) pressure and at higher temperature. US Geological Survey Bulletin* **1452**

Romano, C., Dingwell, D.B., Behrens, H., & Dolfi, D., (1996). Compositional dependence of H_2O solubility along the joins $NaAlSi_3O_8$–$KAlSi_3O_8$, $NaAlSi_3O_8$–$LiAlSi_3O_8$, and $KAlSi_3O_8$–$LiAlSi_3O_8$. *American Mineralogist* **81**, 452–461.

Romengo N. (2011) - *Relationships between mafic and felsic magmatism at Pantelleria: a petrological study on intermediate trachyte magmas*. PhD Thesis, University of Palermo.

Romengo, N., Landi, P. & Rotolo, S.G. (2012). Evidence of basaltic magma intrusions in atrachytic magma chamber at Pantelleria (Italy). *Periodico di Mineralogia* **81**, 163–178.

Rossi, P.L., Tranne, C.A., Calanchi, N., & Lanti, E., 1996. Geology, stratigraphy and volcanology evolution of the Island of Linosa (Sicily Channel). *Acta Vulcanologica* **8**, 73–90.

Rotolo, S. G., Castorina, F., Cellura, D. & Pompilio, M. (2006). Petrology and geochemistry of submarine volcanism in the Sicily Channel Rift. *Journal of Geology* **114**, 355-365.

Rotolo, S. G., La Felice, S., Mangalaviti, A. & Landi, P. (2007). Geology and petrochemistry of recent (<25 ka) silicic volcanism at Pantelleria Island. *Bollettino della Società Geologica Italiana* **126**, 191-208

Rotolo, S. G., Scaillet, S., La Felice, S. & Vita-Scaillet, G. (2013). A revision of the structure and stratigraphy of pre-Green Tuff ignimbrites at Pantelleria (Strait of Sicily). *Journal of Volcanology and Geothermal Research* **250**, 61–74.

Roux, J. & Lefèvre, A. (1992). A fast-quench device for internally heated pressure vessels. *European Journal Mineralogy* **4**, 279–281.

Sauerzapf, U., Lattard, D., Burchard, M. & Engelmann R. (2008). The titanomagnetite-ilmenite equilibrium: New experimental data and thermo-oxybarometric application to the crystallization of basic to intermediate rocks. *Journal of Petrology* **49**, 1161-1185.

Scaillet, B. & Evans, B. W. (1999). The 15 June 1991 eruption of Mount Pinatubo. I. Phase equilibria and pre-eruption P-T-fO_2-fH_2O conditions of the dacite magma. *Journal of Petrology* **40**, 381-411.

Scaillet, B. & Macdonald, R. (2001). Phase relations of peralkaline silicic magmas and petrogenetic implications. *Journal of Petrology* **42**, 825-845.

Scaillet, B. & Macdonald, R. (2003). Experimental constraints on the relationships between peralkaline rhyolites of the Kenya rift valley. *Journal of Petrology* **44**, 1867-1894.

Scaillet, B. & Macdonald, R. (2006). Experimental constraints on pre-eruption conditions of pantelleritic magmas: Evidence from the Eburru complex, Kenya Rift. *Lithos* **91**, 95-108.

Scaillet, B., Holtz, F. & Pichavant, M. (2016). Experimental Constraints on the Formation of Silicic Magmas. *Elements* **12**, 109-114.

Scaillet, B., Pichavant, M. & Roux, J. (1995). Experimental crystallization of leucogranite magmas. *Journal of Petrology* **36**, 635-705.

Scaillet, B., Pichavant, M. & Roux, J. (1995). Experimental crystallization of leucogranite magmas. *Journal of Petrology* **36**, 663-705.

Scaillet, B., Pichavant, M., Roux, J., Humbert, G. & Lefèvre, A. (1992). Improvements of the Shaw membrane technique for measurement and control of fH_2 at high temperatures and pressures. *American Mineralogist* **77**, 647-655.

Scaillet, S., Rotolo, S.G, La Felice, S., Vita, G., 2011. High-resolution 40Ar/39Ar chronostratigraphy of the post-caldera (< 20 ka) volcanic activity at Pantelleria, Sicily Strait. *Earth and Planetary Science Letters* **309**, 280-290.

Scaillet, S., Vita-Scaillet, G. & Rotolo, S. G. (2013). Millenial-scale pahse relationships between ice-core and Mediterranean marine records: insights from high-precision 40Ar/39Ar dating of the Green Tuff of Pantelleria, Sicily Strait. *Quaternary Science Reviews* **78**, 141-154.

Schiano, P., Clocchiatti, R., Ottolini, L., & Sbrana, A. (2004). The relationship between potassic, calc-alkaline and Na-alkaline magmatism in South Italy volcanoes: A melt inclusion approach. *Earth and Planetary Science Letters* **220**, 121-137.

Schmidt B. C., Behrens, H. (2008). Water solubility in phonolite melts: Influence of melt composition and temperature. *Chemical Geology* **256**, 258-267.

Schmincke, H.U. (1974). Volcanological aspects of peralkaline silicic welded ash-flow tuffs *Bullettin of Volcanology* **38**, 594-636

Selbekk, R. S. & Tronnes, R. G. (2007). The 1362 AD Oraefajokull eruption, Iceland: Petrology and geochemistry of large-volume homogenous rhyolites. *Journal of Volcanology Geothermal. Research*, 160, 42-58.

Silver, L.A., Ihinger, P.D.,& Stolper, E., (1990). The influence of bulk composition on the speciation of water in silicate glasses. Contribution to Mineralogy and Petrology **104**, 142–162.

Sisson T.W. & Grove T.L. (1993/a). Experimental investigation of the role of H_2O in calcalkaline differentiation and subduction zone magmatism. *Contributions to Mineralogy and Petrology* **113**, 143-166.

Speranza, F., Landi, P., D'Ajello Caracciolo, F. & Pignatelli A. (2012). Paleomagnetic dating of the most recent silici eruptive activity at Pantelleria (Strait of Sicily). *Bulletin of Volcanology* **72**, 847-858.

Spray, J.G. & Rae, D.A. (1995). Quantitative electron-microprobe analysis of alkali silicate glasses: A review and user guide. *Canadian Mineralogist* **33**, 323−332.

Stabile, P., Webb, S., Knipping, J.L., Behrens, H., Paris, E., & Giuli, G., (2016). Viscosity of Pantelleritic and alkali-silcate melts: Effect of Fe redox state and Na/(Na+K) ratio. *Chemical Geology* **442**, 73-82.

Stolper E. (1982a). The speciation of water in silicate melts. *Geochimica et Cosmochimica Acta* **46**, 2609-2620.

Tamic, N., Behrens, H., & Holtz, F., (2001). The solubility of H_2O and CO_2 in rhyolitic melts in equilibrium with a mixed CO2–H2O fluid phase. Chemical Geology **174**, 333– 347.

Taylor, J. R., Wall, V. J. & Pownceby, M. I. (1992). The calibration and application of accurate redox sensors. *American Mineralogist* **77**, 284–295.

Trua, T., Deniel, C., & Mazzuoli, R., (1999). Crustal control in the genesis of Plio-Quaternary bimodal magmatism of the Main Ethiopian Rift (MER): geochemical and isotopic (Sr, Nd, Pb) evidence. Chemical Geology **155**, 201-231.

Villari, L. (1974). The island of Pantelleria. *Bulletin of Volcanology* 38, 680-724.

Villari, L. (1974). The island of Pantelleria. *Bulletin of Volcanology* **38**, 680-724.

Washington HS (1909). The submarine eruptions of 1831 and 1891 near Pantelleria. *American Journal of Science* **27**,131–150.

Watson, E.B., (1994). Diffusion in volatile-bearing magmas. In: Carroll, M.R., Holloway, J.R. (Eds.), Volatiles in magmas. *Review in Mineralogy* **30**, 371– 411.

White, J. C., Parker, D. F. & Ren, M. (2009). The origin of trachyte and pantellerite from Pantelleria, Italy: insights from major element, trace element, and thermodynamic modelling. *Journal of Volcanology and Geothermal Research* **179**, 33-55.

White, J. C., Ren, M. & Parker, D. F. (2005).Variation in mineralogy, temperature, and oxygen fugacity in a suite of strongly peralkaline lavas and tuffs, Pantelleria, Italy. *Canadian Mineralogist* **43**, 1331-1347.

Williams, R. (2010). *Emplacement of radial pyroclastic density currents over irregular topography: the chemically zoned, low aspect-ratio Green Tuff ignimbrite, Pantelleria, Italy*. PhD Thesis 232p, University of Leicester.

Wolff, J.A., & Wright, J.V. (1981a). Rheomorphism of welded tuff. *Journal of volcanology and geothermal research* **10**, 13-34.

Wolff, J.A., & Wright, J.V. (1981b). Formation of the Green Tuff, Pantelleria. *Bulletin of Volcanology* **44**, 681–690.

Wolff, J.A.,. Ellis, B.S., Ramos, F.C., Starkel, W.A., Boroughs, S., Olin, P.H., & Bachmann, O. (2015). Remelting of cumulates as a process for producing chemical zoning in silicic tuffs: A comparison of cool, wet and hot, dry rhyolitic magma systems. *Lithos* **236**, 275-286.

Xue, Y., & Kanzaki, M. (2004). Dissolution mechanism of water in depolymerised silicate melts: constraints from H and Si NMR spectroscopy and ab initio calculations. *Geochimica et Cosmochimica Acta* **68**, 5027–5058.

Yamashita, S. (1999). Experimental Study of the Effect of Temperature on Water Solubility in Natural Rhyolite Melt to 100 MPa. *Journal of Petrology* **40,** 1497–1507.